Computational Techniques Applied to the Study and Development of Nanoporous Materials

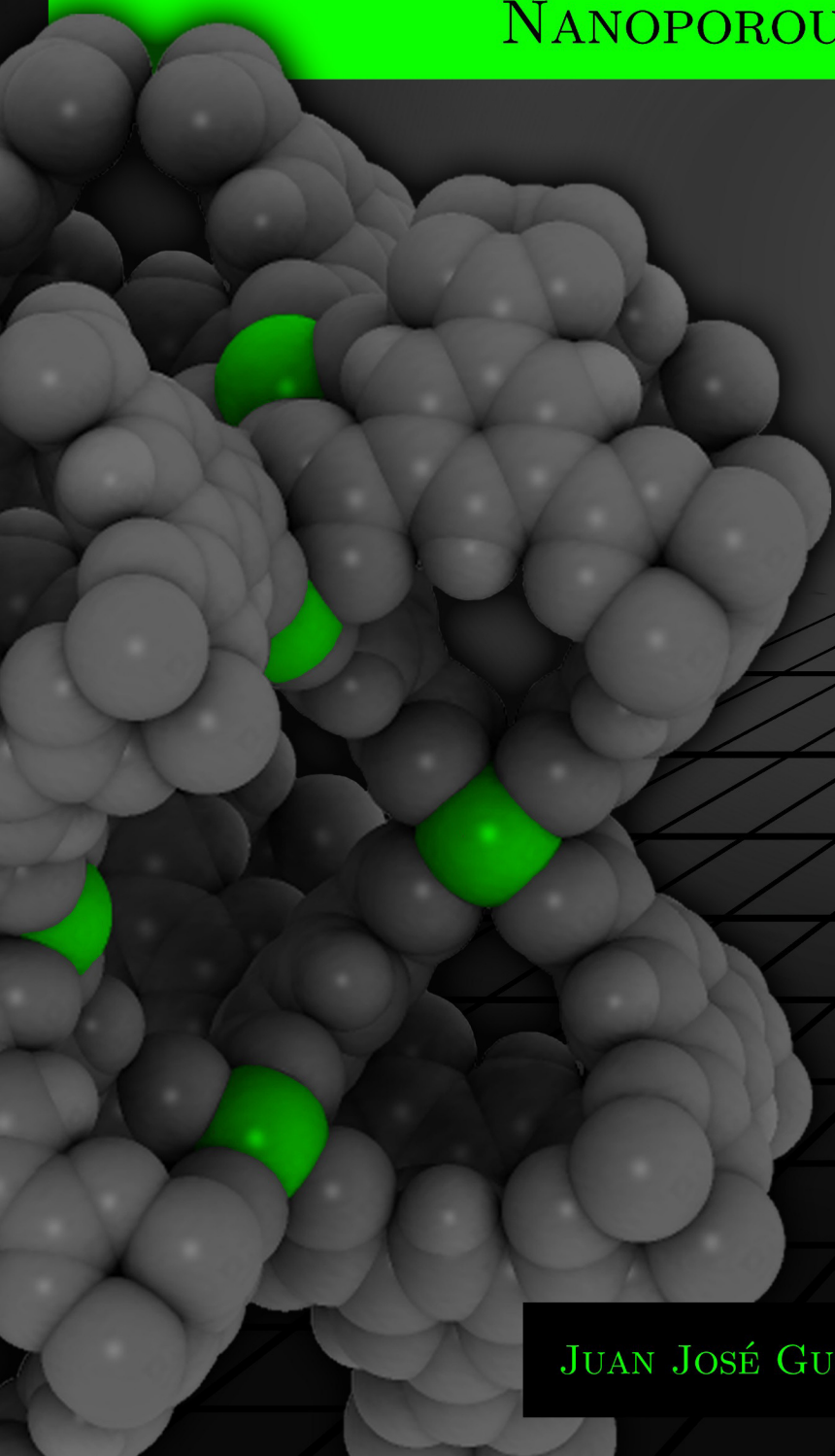

Juan José Gutiérrez Sevillano

Department of Physical, Chemical,
and Natural Systems

University Pablo de Olavide

COMPUTATIONAL TECHNIQUES APPLIED TO THE STUDY AND DEVELOPMENT OF NANOPOROUS MATERIALS

Juan José Gutiérrez Sevillano

Seville, July 2013

COMPUTATIONAL TECHNIQUES APPLIED TO THE STUDY AND DEVELOPMENT OF NANOPOROUS MATERIALS

DIRECTORES

Sofía Calero Díaz

Profesora Titular del Departamento de
Sistemas Físicos, Químicos y Naturales de la
Universidad Pablo de Olavide

David Dubbeldam

Assistant Professor
Computational Chemistry Group,
University of Amsterdam

Said Hamad

Profesor Contratado Doctor del
Departamento de Sistemas Físicos,
Químicos y Naturales de la Universidad
Pablo de Olavide

Trabajo presentado para la obtención del título de Doctor con Mención Internacional

Juan José Gutiérrez Sevillano

Licenciado en Física

Department of Physical, Chemical, and Natural Systems

University Pablo de Olavide

Sofía Calero Díaz, profesora titular del Departamento de Sistemas Físicos, Químicos y Naturales de la Universidad Pablo de Olavide

CERTIFICA:

Que la presente memoria titulada "Computational Techniques Applied to the Study and Development of Nanoporous Materials", que presenta Juan José Gutiérrez Sevillano para la obtención del título de Doctor, ha sido realizada bajo mi dirección en este departamento dentro del programa de Biotecnología y Tecnología Química y que cumple con los requisitos para poder optar a la Mención Internacional.

Sevilla, Julio de 2013

Sofía Calero Díaz

Doctoral advisors

Prof. Sofía Calero Díaz
Dr. David Dubbeldam
Dr. Said Hamad Gómez

PhD evaluation committee

Chair: Prof. J.B. Parra Soto
Secretary: Prof. Mª Carmen Gordillo Bargueño
Member: Prof. T.J.H. Vlugt

External committee

Dr. Flor R. Siperstein
Dr. Juan M. Castillo

The research reported in this thesis was carried out at the Department of Physical, Chemical, and Natural Systems, University Pablo de Olavide (Seville, Spain), with financial support from the European Research Council –ERC Consolidator Grant–, from the Spanish "Ministerio de Ciencia e Innovación" –predoctoral fellowship–, and from the Spanish "Junta de Andalucía" –Proyecto de Excelencia–.

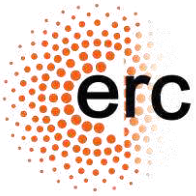

ISBN: 978-84-940260-8-9

Printed by: LLARdigital

AGRADECIMIENTOS

Llegar a este punto supone culminar un trabajo que ha sido un aspecto central, tanto en horas como en ilusión, de esta etapa de mi vida. Ha sido mucho el tiempo, el esfuerzo y el empeño dedicados a esta tarea y sería falso decir que todo han sido buenos momentos. Pero hoy puedo decir que ha valido la pena. Y mucho. Por múltiples razones, al menos una por cada persona que me ha acompañado en este período. Desde la primera persona que me puso en contacto con la investigación y me abrió las puertas de esta universidad, a la última que ha estado a mi lado revisando cada línea de esta tesis. A todas ellas, a las que nombro y a las que no, mi más sincero agradecimiento.

Gracias especialmente a **Sofía**. Nada, absolutamente nada, hubiera sido posible sin su ayuda, sin su guía y sin su apoyo. Ella es la principal responsable de que yo sienta que he crecido, científica y personalmente. Muchas gracias por enseñarme, por escucharme cuando lo he necesitado, y sobre todo, gracias por confiar en mí. Thanks to **David**, for his patience with me, for his immense generosity, for always being willing to help and because without him, my memories from Amsterdam would be much more cold and gray. Gracias a **Said**, por compartir conmigo las claves de su filosofía de vida (*la gente es tonta*), por su ayuda, –al límite, pero siempre a tiempo– y por su amistad.

Gracias a todos con los que he compartido laboratorio. Porque tenerlos a mi lado ha hecho que muchas veces las horas de trabajo pareciesen de ocio. A **Manolo**, por los buenos momentos que pasamos compartiendo piso. A **Elena**, **Juanma**, **Almudena**, **José Fernando** y **María**, que ya estaban cuando llegué y me hicieron sentir como si siempre hubiese estado. A **Paula**, **Ana Hortal**, **Paola**, **Paco**, **Javi**, **Carlos**, **Pablo**, **Jesús**, **Elena Guillén**, **Tom**, **José María**, **Tania**, **Patrick**, **Paula** y **Juan Antonio**, por todos los momentos que hemos pasado juntos y las risas que nos hemos echado. A **Bruno** y **Alejandro**, por sus discusiones en nuestra particular *survey*. A **Rocío**, porque la poesía reside en las magdalenas. A **Ana**, porque si me ofreces un té, se acaban las magdalenas. A **Vicent**, entre otras cosas, por los grandes ratos de Carnaval que hemos vivido juntos. To **Katie** (and her mom) for, among others, their giga-enormous logistic support in N.Y. A **Jesús**, **Salva**, **Julio**, **Paco**, **Ismael**, **Vanesa**, **Chema**, **Paula** y **Rabdel**, porque sin ellos el último año hubiese sido mucho más difícil.

Gracias a **Juan** y **María**, porque la mejor herencia me la han dado en vida. Gracias a **M. Luisa** y **Manoli** y a **Lourdes**, **Maite**, **Nerea** y **Alejandro**, por poner una sonrisa en todos y cada uno de mis fines de semana (y por aceptar que el *tato* siempre esté fuera). Gracias a **Alberto**, **J. Alberto**, **María del Mar** y **Rosario**, porque no les he podido dedicar todo el tiempo que merecen y a pesar de ello siempre están cuando los necesito. A ***Los Granujas***, ***Los Colgaos*** y ***Los Divinos***, por convertirse en una segunda familia con la que reír, llorar y desconectar de los problemas mundanos.

Especialmente le doy las gracias a mi madre, porque hay tantas razones para dárselas que me alcanzaría para escribir otra tesis entera. Tan solo diré que por más que piense, busque o haga memoria, no encuentro un solo motivo por el que no estarle agradecido todos los días de mi vida. Gracias.

Quiero dedicar esta tesis a D. José Sevillano Fernández. Esté donde esté, sé que estará orgulloso.

Al final de la batalla
veintitrés quedaron boca abajo.
Fuéronse rojos, y amarillos,
mas nueve negros se quedaron.
Y todos portaban picas...

...menos un trébol de cuatro.

1

Introduction

The relevance and application of nanoporous materials such as zeolites, Metal Organic Frameworks, and Zeolitic Imidazole Frameworks (see Figure 1) has been growing steadily during the last decades. These materials are characterized by the sizes of the pores, which can be classified into three categories:

- Microporous materials, with pore size of 0.2 - 2 nm
- Mesoporous materials, with pore size of 2.0 - 50 nm
- Macroporous materials, with por size of 50 -100 nm

There is a large variety of nanoporous materials whith a wide range of properties and characteristics. These ordered materials are charaterized by high surface areas. The different sizes, shapes, and distributions of the pores give them unique properties such as the capability to selectively adsorb molecules.

Figure 1*. Natural and synthesized nanoporous materials: Mordenite (left), chabazite (center top), and stilbite (center bottom) from the Smithsonian Institution National Museum of Natural History and Cu-BTC (right) from Centre for Surface Chemistry and Catalysis (KU Leuven).*

Since the advent of computers in the second half of the 20th century, molecular simulation has emerged as a new field of science. This *new* approach based on statistical mechanics allows us to obtain a better understanding at a molecular level of the systems.

The goal of this thesis is to otain a deeper understanding, from a theoretical point of view, of the mechanisms of adsorption and diffusion of gases in zeolites, MOFs, and ZIFs by applying molecular simulations. Simulation techniques not only help to characterize the structures or to obtain a better knowledge of the mechanisms taking place inside the materials, but can also be used as a tool to improve the properties of the frameworks. Furthermore, molecular simulations allow us to predict the behavior of gases inside these materials. In this sense, molecular simulations can act as a cutting edge tool to explore the potential uses and applications of crystalline nanoporous materials.

In this work we study the potential role that nanoporous materials can play in processes of industrial and acedemic interest. We focus on applications such as methane/carbon dioxide, water/alcohol, and propane/propylene separation, and capture of air pollutants such as hydrogen sulfide. We use molecular simulation techniques to study the adsorption and diffusion processes of a variety of gases in nanoporous materials. In particular, we compute adsorption isotherms, adsorption energies, and entropies using Monte Carlo (MC) simulations and diffusion coefficients using Molecular Dynamics (MD) simulations and Transition State Theory (TST).

1. Nanoporous Materials

This section contains a brief overview about the three groups of nanoporous materials used in this thesis: zeolites, Metal Organic Frameworks (MOFs), and Zeolitic Imidazole Frameworks (ZIFs).

1.1. Zeolites

Zeolites are a group of crystalline porous solids based on silica. The name was firstly used by Axel F. Cronsted when he described the unique ability of "an unknown species of rock" which was able to lose water when heated in a blow-pipe flame.

Basically, zeolite frameworks are made of silicon atoms connected to four oxygen atoms forming tetrahedra. These tetrahedra are the Primary Building Units (PBUs). The silicon atoms are placed at the center of the tetrahedra surrounded by the oxygen atoms. Each oxygen atom, placed at the corners of the thetraedra, is linked to two silicon atoms. In this way, the connected PBUs can generate many different topologies. As mentioned before, there are some type of zeolites that can be found in nature but most types are synthesized in the laboratories. Up to date there are around two hundred zeolite types registered in the Database of Zeolites Structures. There is a large variety in pore-shape and size, i.e. we can find structures with straight channels, zig-zag channels, interconnected channels, cages connected by windows, etc.

Some of the silicon atoms can be replaced by aluminium atoms. Since the SiO_4 tetrahedra are neutral these substitutions result in a negative charge per aluminium atom. To balance the net charge, non-framework cations such as sodium, cesium, or calcium are added to the structure. The Löwenstein rule restraints the distribution of aluminium atoms in the structure. This rule states that an aluminium tetrahedron can be only bonded to a silicon tetrahedron, i.e. the configuration Al-O-Al is forbidden.

The chemical formula of aluminosilicates zeolites with cations, is:

$$M_{x/n}\left[\left(AlO_2\right)_x\left(SiO_2\right)_y\right]wH_2O$$

where M are the cations, n their valence, x the number of aluminium atoms, and w the number of water molecules in a unit cell.

Besides aluminosilicates, there are also types of zeolites based on the exchange of silicon atoms by other species, such as titanosilicates, aluminophosphates, silicoaluminophosphates, and germanates (see Figure 2).

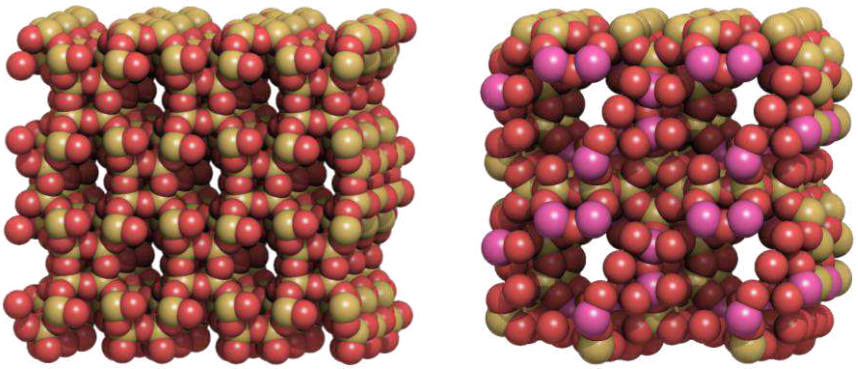

Figure 2. *Molecular representation of two zeolites. On the left, pure silica ITQ-12 and on the right, Ge-ITQ-29.*

Zeolites exhibit high surface area, high thermal stability, and high exchange capacity. Pure silica zeolites are hydrophobic, but the presence of cations can change this nature. The combination of these properties makes them good materials for adsorption and catalysis processes[1-2]. They are able to selectively adsorb gases as a function of the shape, size or polarity of the guest molecules. They can also act as "molecular sieves", materials that selectively adsorb certain gases and avoid the adsorption of others. Zeolites have found widespread industrial applications[3-6], being used as highly selective adsorbents[6], ion exchangers[7-8], and catalysts[9-11] of exceptionally high activity and selectivity in a wide range of reactions. These applications include the drying of refrigerants, removal of atmospheric pollutants such as sulphur dioxide, cryo pumping, separation of air components, separation and recovery of normal paraffin hydrocarbons, recovering radioactive ions from waste solutions, catalysis of hydrocarbon reactions, and the curing of plastics and rubber.

1.2. Metal Organic Frameworks (MOFs)

Metal organic frameworks for use in adsorption applications were first reported in 1999 by Yaghi *et al*[12]., and they have become one of the types of crystalline nanoporous materials more studied in the last years[13]. They are basically composed by metallic centers connected by organic linkers (see Figure 3). Among their main characteristics we can point out the high surface area, pore volume, and storage capacity. However is the high versatility to tailor and to modify these materials

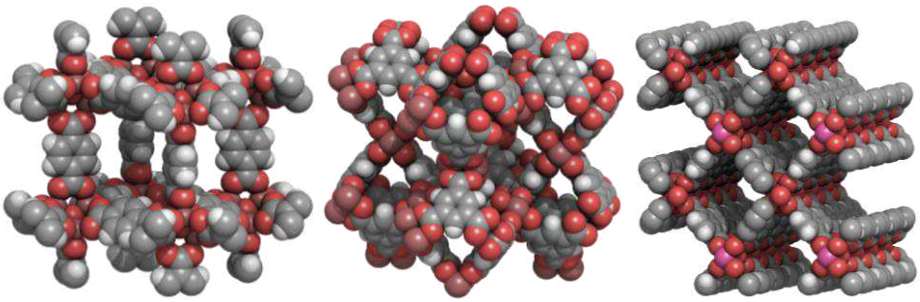

Figure 3. *Molecular representation of three Metal Organic Frameworks: IRMOF-1 (left), Cu-BTC (center), and MIL-47 (right).*

what gives them a huge potential to be used in many different applications[14]. These properties make MOFs good candidates to be used in important industrial applications, such as the capture of greenhouse gases[15-16], hydrogen storage[17], catalysis[18-20], gas separation[21-22], biomedical applications[23], or biofuel separations[24-25] among others.

In contrast to zeolites, MOFs are not found in nature but they are synthesized in the laboratory. There are more than ten thousand MOFs in the Cambridge Structural Database, although only a small percentage are stable when the solvent is removed and most of them are unstable in moist environment.

It is possible to obtain new MOFs by combining different metal clusters with different organic ligands. Moreover, the organic linkers can be functionalized during the synthesis, opening new posibilities. If we find the appropriate combination of these elements (metals, linkers and functional groups) we can obtain solids with cavities of predefined shapes, sizes, and functionalities tailored for specific applications. The possibility to work with a large number of combinations of metal centers with organic linkers and functional groups make molecular simulations a very useful and efficient tool to study MOFs. In this way molecular simulation can be used not only to study the synthesized MOFs but also to explore the theoretical modifications and functionalizations that would improve their properties.

1.3. Zeolitic Imidazole Frameworks (ZIFs)

The last group of nanomaterials that have been studied in this work are Zeolitic Imidazole Frameworks (see Figure 4). These materials can be regarded as hybrids between the two previous groups. On the one hand they are made up of organic linkers connected by metal atoms, on the other hand they have zeolitic structure. This implies that they are composed of tetrahedral structural building units[26]

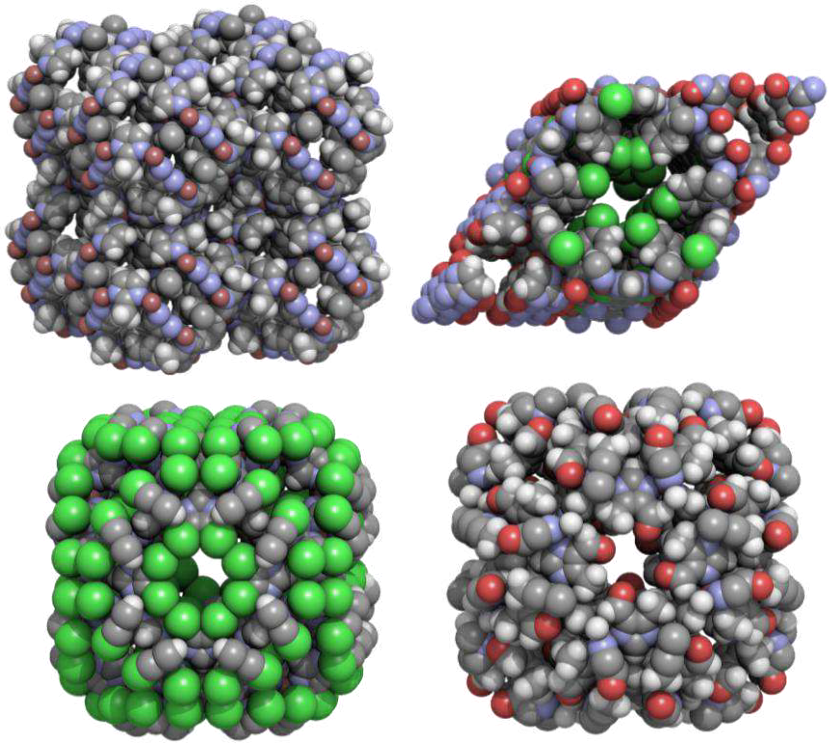

Figure 4. *Molecular representation of four Zeolitic Imidazolate Frameworks (ZIFs). From left to right and top to bottom: ZIF-8, ZIF-69, ZIF-71, and ZIF-93.*

(SBU). Instead of silicon and oxygen atoms the thetraedra are made of metal atoms and organic linkers. The centers are occupied by metal atoms and the role of the oxygen atoms is played by imidazolate molecules. In this way the hybrid nature of MOFs is combined with the stability of zeolitic frameworks. ZIFs were first synthesized[27-31] in the early years of this century, and since then the number of studies on these materials has grown exponentially. ZIFs possess higher thermal and chemical stability than many MOFs, which increase their range of possible applications[32-33]. The main feature that differentiates these structures from other MOFs is that the metal nodes (typically Zn or Co) are tetrahedrically coordinated to imidazolates (im) or functionalized imidazolate ligands, which are shared between two adjacent SBUs. Due to the topological similarity between zeolites and ZIFs, several structures in which the disposition of the tetrahedra is the same are found for both types of materials. The greater flexibility of the metal−imidazolate bonds allows the synthesis of a larger number of ZIF structures. It might be therefore possible to synthesize ZIFs with many of the hypothetical zeolite frameworks predicted with topological tools, which have not been synthesized yet as zeolites.

2. Methods

In the previous section we gave a general overview about nanoporous materials. In this section we describe the main techniques that we use to study these systems.

Molecular simulation has become an efficient and widely used technique for studying properties of systems. Nowadays there are many methods and techniques available to study systems at the molecular level. The selection of the desired techniques depends on the properties that we want to study and the way that we describe our systems. In this work we mainly use classical methods to embark on the study of confined systems. Nevertheless in some parts of our study we also use quantum mechanics. We mainly describe our systems using classical force fields for modeling a) the adsorbents, b) the adsorbates, and c) the interactions between adsorbate-adsorbate and adsorbate-adsorbent. This means that we know the positions of all the atoms involved in our simulations as well as all the interactions between them. Based on that, we are able to compute different properties like Henry coefficients, energies and entropies of adsorption, adsorption isotherms, and diffusion coefficients among others. Therefore the quality of the force field is the key to obtain accurate results. The parameters of the force field can be obtained by fitting to experimental data, but they can also be derived from quantum calculations.

Once we have a force field that is able to describe the interactions, we can use different methods to compute static and dynamic properties of our systems:

- **Monte Carlo (MC).** Statistical methods that use random numbers and probabilities. They are based on computing space phase averages instead of time averages.
- **Molecular Dynamics (MD).** A deterministic method based on the integration of Newton's motion equations.

In addition to these two methods in this chapter we introduce briefly the basis of quantum calculations as well as two more techniques used in this work, the Ideal Adsorption Solution Theroy (IAST) and the Transition State Theory (TST).

2.1. Monte Carlo

In classical mechanics a given system can be described by knowing the positions and the momenta of all its components. Once we have these variables at a single instant in time we can predict the evolution of the system. All this information is included in a single quantity, the Hamiltonian, as a function of the coordinates and momenta of all the components. Based on this, we could apply the classical mechanics to macroscopic systems and then we will obtain a basis for the thermodynamic description. However this approach has two main problems: first, the number of

particles involved is huge (~10^{23} particles), second, the interactions between particles in a real system are very complex. Thus, although classical mechanics encodes all the information needed to predict the properities of a system, the problem of extracting that information is intractable. Furthermore, thermodynamic describes the systems using only a few variables (pressure, temperature, volume, etc.). The connection between classical mechanics and thermodynamics requires a new field of physics: statistical mechanics.

In statistical mechanics we assume that there are a lot of microscopic states (*microstates*) that are compatible with a macroscopic state (*macrostate*). The collection of these different configurations of a system that share macroscopic properties is named "ensemble". Once we have a macrostate we can wonder in which of all compatible microstates is the system. Neither classical mechanics nor thermodynamics can address this question. What statistical mechanics does is to assign *a priori* probabilities to each microstate (e.g. all microstates are equally likely in the microcanonical ensemble). All incompatible microstates with a given macrostate have a vanishingly low probability while the accessible microstates have dominating contributions in such a way that the integration over all the microstates is equal to one. The relationship between microscopic states and macroscopic states is postuled as:

Macroscopic properties of a system are the average of the microscopic states associated to that macrostate:

$$\langle A \rangle = \int \rho(r^N) A(r^N) dr^N \qquad 1.1$$

where A is a macroscopic property, ρ the probability density, and r^N denotes the positions and velocities of the N particles in the system.

The functional form of ρ depends on how we select the microstates. For instance, a system in equilibrium will have a well-defined internal energy. We can assign probability equal to zero to all microstates whose internal energy is not exactly the value of the macroscopic. Other option is to assign probabilities to microstates with different internal energy in such a way that the average matches with the macrostate. Depending on the system and the properties to compute we will have different ρ and therefore different sets of microstates. In other words, we have different ensembles. In all cases averages performed over an ensemble yield the thermodynamic quantities of a system as well as other equilibrium and dynamic properties.

When we use Monte Carlo methods we are computing those averages using a selected ensemble. The problem arises when the number of microstates is too large

to be computed and the majority of them have a weight close to zero. This is solved by using importance sampling, which consists in generating configurations with a probability proportional to the Boltzman weight. The averages can then be computed without computing all the microstates.

The Markov Chain Monte Carlo method (MCMC) is used to estimate the average properties of systems with a very large number of accessible states. The macroscopic magnitudes in which we are interested are usually calculated employing weighted averages, where the probability of a microstate is given by the Bolztman factor:

$$\langle A \rangle = \frac{\int e^{-\beta U(r^N)} A(r^N) dr^N}{\int e^{-\beta U(r^N)} dr^N} \qquad 1.2$$

where $\beta=1/(k_B T)$, with k_B the Boltzmann constant, and $U(r^N)$ is the total energy of the system with N particles at positions r^N. The configurational part of the partition function is denoted by Z.

$$Z \equiv \int e^{-\beta U(r^N)} dr^N \qquad 1.3$$

The ratio e^{β_u}/Z is the probability density of finding the system in a configuration around r^N. The Monte Carlo scheme makes use of the fact that only the relative probability of visiting points in configuration space is needed (not the absolute probability of visiting points with the correct frequency). The MCMC algorithm generates random trial moves from the current "old" state *(o)* to a "new" state *(n)*. To show that an arbitrary initial distribution eventually relaxes to the equilibrium distribution, it is often convenient to apply the condition of detailed balance (as it is used in the original Metropolis scheme). If $P_B(o)$ and $P_B(n)$ denote the probability of finding the system in state *(o)* and *(n)*, respectively, and $(o \rightarrow n)$ and $(n \rightarrow o)$ denote the conditional probability to perform a trial move from o to n and n to o respectively, then the probability of accepting the trial move $P_{acc}(o \rightarrow n)$ to accept is related to the probability of accepting the trial move $n \rightarrow o$, $P_{acc}(n \rightarrow o)$, by:

$$P_B(o)\alpha(o \rightarrow n)P_{acc}(o \rightarrow n) = P_B(n)\alpha(n \rightarrow o)P_{acc}(n \rightarrow o) \qquad 1.4$$

Metropolis *et al.*[34] assumed that:

$$\alpha(o \rightarrow n) = \alpha(n \rightarrow o) \tag{1.5}$$

The acceptance probability is calculated using the following formula:

$$P_{acc}(o \rightarrow n) = \min\left(1, \frac{P_B(n)}{P_B(o)}\right) \tag{1.6}$$

In the Metropolis scheme, the rejected trial states should be counted again and are only contributing to the average via the normalization. Conventional Monte Carlo algorithms become then inefficient, since they tend to generate many trial states that do not contain new information for averages and distributions. To improve efficiency, the properties of the rejected states can be included in the sampling by using the Waste-Recycled Monte Carlo (WRMC) method[35-36]. However, it is important to note that this scheme is only correct when the method used for generating configurations obeys detailed balance.

Conventional Monte Carlo is time consuming for long molecules because the fraction of successful insertions into the systems is normally too low. The Configurational-Bias Monte Carlo (CBMC) technique improves the conformational sampling of molecules[37] and increases the efficiency for successful inserted molecules by many orders of magnitude. In the CBMC technique a molecule is grown bead by bead, in such a way that for each bead a set of k trial orientations is generated according to the internal energy U^{int} (usually the bonded interactions) The external energy $U_i^{ext}(j)$ is used to bias the growth of the chain and is computed for each trial position j of each bead i. One of these trial positions is selected with a probability

$$P_i(j) = \frac{e^{-\beta U_i^{ext}(j)}}{\sum_{l=1}^{k} e^{-\beta U_i^{ext}(j)}} = \frac{e^{-\beta U_i^{ext}(j)}}{\omega_i} \tag{1.7}$$

where $\beta = 1/(k_B T)$, with k_B the Boltzmann constant and T the temperature. The selected trial orientation is added to the chain and the procedure is repeated until the entire molecule has been grown. The rules for acceptance or rejection of a grown molecule are chosen in a way that they exactly remove the bias caused by this growing scheme.

The Rosenbluth factor[38] for the new molecule can be computed as

$$W = \prod_i \omega(i) \tag{1.8}$$

and the Rosenbluth factor of the new configuration is related to the free energy F

$$F = \frac{1}{\beta} \ln \frac{\langle W \rangle}{\langle W^{id} \rangle} \tag{1.9}$$

where $<W^{id}>$ is the Rosenbluth factor of an ideal molecule that has only internal interactions. The Rosenbluth factor is also related to the Henry coefficient K_H

$$K_H = \beta \frac{\langle W \rangle}{\langle W^{id} \rangle} \tag{1.10}$$

MC simulations are divided in cycles. In each cycle, on average each molecule is randomly selected and one of the following moves is applied:

- Translation: A random translation is applied to the selected molecule.
- Rotation: The selected molecule is randomly rotated around its center of mass. This move has sense only if two or more atoms compose the molecule.
- Regrowth: The selected molecule is partially or entirely regrown in another position.
- Insertion: A molecule is randomly placed inside the simulation box.
- Deletion: The selected molecule is removed from the simulation box.
- Identity change: When dealing with mixtures, a molecule of one type of gas is selected and its identity is changed to another.

The last four moves are only available when performing simulations in "open" ensembles where the number of particles can vary. Depending on the property that we want to compute, MC simulations are performed in different ensembles. In this work we have used three ensembles:

- Canonical ensemble (NVT): In this ensemble the number of molecules, volume, and temperature are fixed. It is used when computing adsorption energies and entropies and Henry coefficients. It is also used in MD simulations for computing diffusion coefficients.
- Grand Canonical ensemble (μVT): In this ensemble we keep constant volume and temperature. The number of molecules can vary but the chemical potential is fixed. We use this ensemble when we want to compute adsorption of gases in confined systems.
- Gibss ensemble: In this ensemble the simulations are performed in two macroscopic regions: the vapor and the liquid phase. The thermodynamic requirements for phase coexistence are that each region should be in internal equilibrium, and that the temperature, pressure, and chemical potentials should be the same in both regions. The temperature, total number of particles, and total volume are kept fixed. This ensemble is used for computing Vapor Liquid Equilibrium (VLE) curves.

In order to take into account the periodic nature of the systems, we replicate a unit cell in the three directions of space, employing periodic boundary conditions. Due to computational limitations, only systems containing a few thousand atoms can be modeled. As a result the cell length of the systems we study is typically around 20-40 Å. In both MC and MD calculations the first stage of the simulations consists on the equilibration of the systems. The data obtained during equilibration are discarded, and only data obtained during the second stage (production) are employed to compute the properties of the system.

2.1.1. Henry Coefficients

Henry coefficients are directly related to the excess free energy (or excess chemical potential) of the adsorbed molecules (eq. 1.9 and eq 1.10). However, the absolute free energy of a molecule cannot be directly computed using Monte Carlo or Molecular Dynamics simulations techniques. At low to intermediate loading special simulation techniques such as the Widom test particle method can be applied. This method uses a probe particle that is inserted at random positions to measure the energy required for the insertion of one particle in the system. A “ghost particle” is used as the measuring probe and it receives this name because the other particles in the system do not feel its presence. The Widom test particle method can be applied at low to moderate densities around the critical point, but it fails at high densities around liquid-solid coexistence, because the probability to insert the “ghost” molecule at a given position becomes very low. Details on this and other available techniques used to compute free energies can be found in literature[36].

2.1.2. Energies and entropies of adsorption

The heat of adsorption in the infinite dilution limit can be obtained directly from the simulation average energies[39]

$$Q_{st} = \langle U_{Mg} \rangle - \langle U_M \rangle - \langle U_g \rangle - \langle k_B T \rangle \qquad 1.11$$

where $<U_{Mg}>$ and $<U_g>$ are the ensemble averages of the potential energy of the MOF-guest system and the energy of an isolated ideal molecule, respectively, and $<U_M>$ is the average MOF energy that is zero for a rigid structure. All average energies involved in the system are usually computed using MC in the canonical ensemble, where the number of molecules (N), the volume (V), and the temperature (T) are kept fixed. Two independent simulations are required: A very fast simulation to provide the energy of the ideal molecule and a much longer simulation to obtain the energy of the same molecule in the structure.

2.1.3. Adsorption isotherms

The most widely used simulation method to predict adsorption equilibria is grand canonical Monte Carlo (GCMC) simulation. In this ensemble the volume *(V),* temperature *(T)*, and chemical potential *(μ)* are fixed and the number of particles fluctuates during the simulation. In GCMC simulations particles are exchanged with a reservoir, which is held at the same chemical potential. The equilibrium conditions are equal temperatures and equal chemical potentials of the gas inside and outside the MOF. The fugacity of a gas *(f)* is its effective thermodynamic pressure and is defined so that the chemical potential of the gas is given by the expression

$$\mu = \mu^0 + RT \ln\left(\frac{f}{p^0}\right) \qquad 1.12$$

where p^0 is the standard pressure and μ^0 is the standard chemical potential, respectively. Fugacities and pressures are related through the expression: $f=\phi p$, where ϕ is the fugacity coefficient. At relatively high temperatures and low pressures is acceptable to simply replace the fugacities by pressures ($\phi=1$). However, when the pressure in the reservoir is too high for the ideal gas law to hold the fugacity coefficient must be taken into account. This coefficient can be obtained through an (experimental or theoretical) equation of state[36].

The adsorption isotherm can be simulated by running a series of simulations at increasing pressure (for desorption the series runs backwards starting from the final loading). Each MC simulation consists of millions of random translations, rotations, insertions, and deletions that are accepted or rejected according to criteria based on a Boltzmann-type weighting. The simulation results are averaged over the run of the simulation. Detailed descriptions of the simulation methods as well as sample programs can be found, among others, in the book by Frenkel and Smit[36].

The simulations provide "absolute" adsorption values, which can be compared with experimental isotherms if it is corrected for "excess" adsorption. The excess adsorption is the average number of molecules in the pores in excess above the number of molecules that would occupy the free pore volume at bulk-gas conditions[40-43]. The excess (n_{ex}) and the absolute adsorption (n_{abs}) are related by the equation:

$$n_{ex} = n_{abs} - V^g \rho^g \qquad 1.13$$

where V^g is the pore volume and ρ^g is the gas-phase density. The pore volume is obtained experimentaly through helium adsorption measurements that can also be computed by simulation[43].

2.2. Molecular Dynamics

Molecular Dynamics simulations are based on a very simple idea: the trajectories of the particles are given by Newton's laws. The movement is governed by the forces between particles, which in turn are a function of the positions. Starting from an initial configuration, for which the positions and velocities of all particles are known, we calculate the forces. Based on these forces, we compute the new velocities of the particles. With these velocities, kept fixed for one time step, we obtain the new positions for every particle. Repeating this cycle we obtain the trajectories of the particles in the system.

In this work, the previous scheme is implemented using the velocity-Verlet algorithm:

$$r(t + \Delta t) = r(t) + v(t)\Delta t + \frac{f(t)}{2m}\Delta^2 t \qquad 1.14$$

$$v(t+\Delta t) = v(t) + \frac{f(t) + f(t+\Delta t)}{2m}\Delta t \qquad 1.15$$

Where $\boldsymbol{r}(t)$, $\boldsymbol{v}(t)$, and $\boldsymbol{f}(t)$ are the position, velocity, and force vectors at time t, respectively, Δt is the time step used, and m is the mass of the particle.

We can compute diffusion coefficients based on the motion of the particles in the system. For the self-diffusion in one direction, we can use:

$$D_{\mathrm{S}}^{\alpha} = \frac{1}{2N}\lim_{\mathrm{t}\to\infty}\frac{d}{dt}\left\langle\sum_{i=1}^{N}\left(r_{i\alpha}(t) - r_{i\alpha}(t_0)\right)^2\right\rangle \qquad 1.16$$

Where N is the number of molecules, t is the time, and $r_{i\alpha}$ is the α-component of the position of molecule i, with α=x,y,z.

The directionally averaged diffusion coefficient can then be obtained calculating

$$D_S = \frac{D_{\mathrm{S}}^{\mathrm{x}} + D_{\mathrm{S}}^{\mathrm{y}} + D_{\mathrm{S}}^{\mathrm{z}}}{3} \qquad 1.17$$

When we perform MD simulations we first perform a short MC simulation to obtain a sensible starting configuration. Then a MD simulation in the NVT ensemble is performed to equilibrate the system. After this phase we can start collecting data from the simulation.

2.3. Transition State Theory (TST)

When studying diffusion with MD is not possible, usually for computing time limitations, TST is a viable alternative method. It can be used to study very slow diffusion processes. TST is based on considering the diffusion as a hopping process. We can do that if we assume that: a) the diffusion can be described as hopping in a lattice, and b) the free-energy barriers between two lattice points are high enough to make the hop a rare event and therefore there is no correlation between subsequent hops. Knowing the hopping rate between points we can compute the self-diffusion using:

$$D_S = \frac{1}{2d} k\lambda^2 = k_{AB}\lambda^2 \qquad 1.18$$

where D_s is the self-diffusion coefficient, d the dimensionality of the system, k the hopping rate from a lattice site to any adjacent lattice site, λ the distance between two lattice points, and k_{AB} the hopping rate from a given lattice point A to a specific lattice point B. This equation, which comes from Random Walk Theory, is exact, and transfers the difficulty of computing the hopping to the calculation of k_{AB}. As is described in ref [44], the hopping rate is given by

$$k_{AB} = \sqrt{\frac{k_B T}{2\pi m}} \frac{e^{-\beta F(q^*)}}{\int_{cageA} e^{-\beta F(q)} dq} \qquad 1.19$$

where $\beta=1/k_B$ is the Boltzmann constant, T the temperature, m the mass involved in the reaction coordinate, $F(q)$ the free energy as a function of the reaction coordinate q, and q^* the value of the reaction coordinate at the barrier position.

This method fails when particles not only cross the barrier from A to B but also from B to A. In these cases a dynamical correction is added to eq 1.20

$$D_S = \kappa k_{AB}\lambda^2 \qquad 1.20$$

where κ is the transmission coefficient.

2.4. Quantum calculations

In some cases, the description that classical force fields provide of the systems is not enough for our purposes. For instance, if we want to investigate the optical or electronic properties of a material we need to perform quantum calculations, which provide information about the electronic structure of the systems. If we want to model a system for which no force fields are available then quantum calculations would be the method of choice. The basis of electronic structure calculations is Schrödinger's equation: $H\Psi = E\Psi$. The problem is that solving Schrödinger's equation is an extremely complex and time consuming task. There are several

methods with which to obtain an approximate solution of that equation, such as semi-empirical and Hartree-Fock methods. There are also other techniques that provide more accurate solutions of the equation, albeit at higher computational costs, which makes them unsuitable to study large systems. The most popular method to study crystalline materials is Density Functional Theory (DFT), since it allows an accurate study of large systems at a reasonable computational cost. DFT is based on the assumption (proven by Hohenberg and Kohn in the 1960's) that the external potential, the total number of electrons, and the Hamiltonian are uniquely determined by the electronic density, $\rho(r)$, of the ground state of the system, i.e. these magnitudes can be calculated as a functional of the electron density. It is therefore possible to calculate all the properties of a system if $\rho(r)$ is known. But the main difficulty of DFT lies therefore in the calculation of $\rho(r)$, since we do know the exact form of these functionals. We know that they exist but we do not know how to calculate them. There are several functionals proposed, and there has been a steady increase in their quality over the years. At the moment the most accurate ones are the so-called hybrid functionals, in which Pauli's exclusion principle is taken into account by including into the total exchange energy a component calculated with Hartree-Fock theory.

2.5. Ideal Adsorption Solution Theory

The Ideal Adsorbed Solution Theory (IAST) of Myers and Prausnitz[45] was developed to predict the properties of adsorbed mixtures avoiding direct simulation of the isotherms. This is a rather simple model in which two or more pure component isotherms can be used to predict the adsorbed mixture composition for any gas mixture composition. The main advantage of this model is that it does not require any mixture data and it is independent of the actual model of physical adsorption. IAST calculations are accurate enough for mixtures of light gases in MOFs[46-49], but they fail when the studied mixture differs strongly in chemical characteristics[50].

IAST is analogous to Raoult's law for vapor-liquid equilibrium, i.e:

$$P_i = P_i^0(\pi_i)x_i \qquad 1.21$$

Where x_i and π_i are the molar fraction and spreading pressure of component i in the adsorbed phase, respectively. At the adsorption equilibrium, the reduced spreading pressures must be the same for each component and the mixture:

$$\pi_i^* = \frac{\pi_i}{RT} = \int_0^{P_i^0} \frac{n_i^0(P)}{P}\, dP \qquad 1.22$$

with $i = 1, 2, 3, \ldots, N$ *and* $\pi_1^* = \pi_2^* = \ldots = \pi_N^* = \pi^*$

The function $n_i^0(P)$ is the pure component equilibrium capacity and P_i^0 is the pure component hypothetical pressure which yields the same spreading pressure as that of the mixture.

By assuming ideal mixing at constant π and T, the total amount adsorbed, n_t, is:

$$\frac{1}{n_t} = \sum_{i=1}^{N} \left[\frac{x_i}{n_i^0(P_i^0)} \right] \qquad 1.23$$

with the constraint:

$$\sum_{i=1}^{N} x_i = 1 \qquad 1.24$$

Since the equations are nonlinear and the integrals of π_t^* cannot be solved analytically for most of the pure component isotherm equations, the classical IAST needs iterative integration processes.

In this work we have used the isotherm equation proposed by Jensen and Seaton for type I adsorptions[51]:

$$n(P) = KP\left[1 + \left(\frac{KP}{a(1+\kappa P)}\right)^c\right]^{-1/c} \qquad 1.25$$

First we fit the four parameters of the equation (K, a, κ, *and* c) to the pure components adsorption isotherms and then we apply IAST to obtain the mixture adsorption isotherms.

3. Force fields and Models

In this section we describe the general strategy followed to model the frameworks and adsorbates studied in this work.

3.1. Force fields

A force field is a set of functions and parameters needed to define the interactions in a molecular system. There are many generic force fields available in the literature, like the Universal Force Field (UFF)[52], Discover (CFF)[53], Dreiding[54], SHARP[55], VALBON[56], AMBER[57], CHARMM[58], OPLS[59], Tripos[60], ECEPP/2[61], GROMOS[62], MMFF[63], Burchar[64], as well as specific force fields developed for particular systems. Most popular force fields are designed to be generic, providing a broad coverage of the periodic table, including inorganic compounds, metals, and transition metals. In this section we describe the usual functional form of the force fields employed in this work. The specific values of the parameters are included in the corresponding chapter where each force field is used.

The total energy of a system U^{total} is split into two parts, the interaction between bonded atoms U^{bonded} and the interactions between non-bonded atoms $U^{non\text{-}bonded}$:

$$U^{total} = U^{bonded} + U^{non-bended} \tag{1.26}$$

In the bonded interactions part we consider the different interactions between two, three, and four consecutive atoms. This means that we take into account the bonding energy between pairs of atoms U^{bond}, the bending energy between three linked atoms U^{bend}, and the torsion energy defined between four consecutive atoms $U^{torsion}$. Therefore the bonded energy can be separated as:

$$U^{bonded} = U^{bond} + U^{bend} + U^{torsion} \tag{1.27}$$

The bonding energy can be described with many different potentials such as Quartic potential, CFF quartic potential, MM3 potential, or Restrained harmonic potential. In this work we consider the bonding energy as a function of the interatomic distances using a harmonic potential

$$U^{bond}(r_{ij}) = \frac{1}{2} k(r_{ij} - r_{eq})^2 \tag{1.28}$$

where the distance is defined as $r_{ij}=r_j-r_i$, r^{eq} is the equilibrium distance, and k is the harmonic constant.

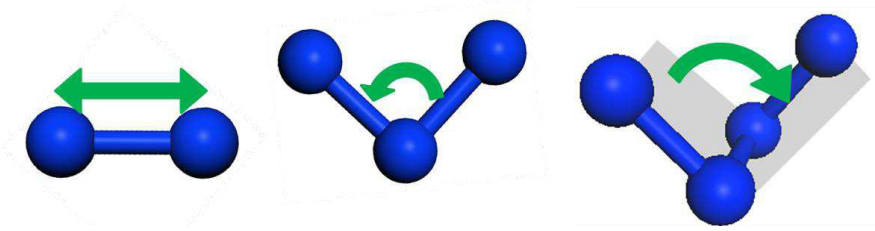

***Figure 5**. Definition of bond distance, bend angle and dihedral angle between atoms of a molecule.*

Several potentials are also available to describe the bending energy U^{bend} between three atoms. Some examples are, the cosine bend potential, Quartic bend potential, or CFF quartic Bend potential. In this work we used the harmonic potential that can be expressed as follows:

$$U^{bend}(\theta_{jik}) = \frac{1}{2}k(\theta_{jik} - \theta_{eq})^2 \qquad 1.29$$

with k the harmonic bend constant, θ_{eq} the equilibrium angle, and θ_{jik} the angle between the atoms i, j, and k:

$$\theta_{jik} = \cos^{-1}\left(\frac{r_{ij}\cdot r_{ik}}{r_{ij}r_{ik}}\right) \qquad 1.30$$

Finally the torsions are included in our description of the system with the torsion energy $U^{torsion}$. This energy is expressed as a function of the dihedral angle (see Figure 5). Again, there are many potentials available to model this interaction. We use the TraPPE dihedral potential:

$$U^{torsion} = p_0 + p_1\left[1+\cos(\varphi_{ijkl})\right] + p_2\left[1-\cos(2\varphi_{ijkl})\right] + p_3\left[1+\cos(3\varphi_{ijkl})\right] \qquad 1.31$$

where φ_{ijkl} is the dihedral angle and p_0, p_1, p_2, and p_3 fitted parameters. It is worth noting that improper torsions, which are mostly used to keep certain atoms in a plane, are not considered in this work.

The non-bonded part of the eq 1.26 corresponds to the interactions between atoms from different molecules, or between atoms of the same molecules, which are separated for three or more atoms. In this work we consider two types of non-bonded interactions Van der Waals (VdW) interactions U^{VDW} and electrostatic interactions $U^{electrostatic}$:

$$U^{non-bonded} = U^{VDW} + U^{electrostatic} \tag{1.32}$$

Van der Waals interactions are described using a Lennard-Jones pair potential while electrostatic interactions are modeled with coulombic potentials. A generic form of the Lenard-Jones potentials is:

$$U^{VDW}(r_{ij}) = 4\varepsilon_{ij}\left[\left(\frac{\sigma_{ij}}{r_{ij}}\right)^{12} - \left(\frac{\sigma_{ij}}{r_{ij}}\right)^{6}\right] \tag{1.33}$$

where the σ parameter represents the distance between the interacting atoms at which the attraction and repulsion are balanced so that the total interaction energy equals zero; the ε parameter corresponds to the depth of the energy minimum, and r_{ij} is the distance between particles i and j. Usually, the parameters σ and ε are defined for the interaction of a certain atom with another atom of the same type. In general, the cross terms describing the interaction between different atom types α and β are obtained following the Lorentz-Berthelot mixing rules:

$$\begin{aligned} \sigma_{\alpha\beta} &= \frac{\sigma_{\alpha\alpha} + \sigma_{\beta\beta}}{2} \\ \varepsilon_{\alpha\beta} &= \sqrt{\varepsilon_{\alpha\alpha} \cdot \varepsilon_{\beta\beta}} \end{aligned} \tag{1.34}$$

Electrostatic interactions are described using coulombic potentials:

$$U^{electrostatic}(r_{ij}) = \frac{1}{4\pi\varepsilon_0}\frac{q_i q_j}{r_{ij}} \qquad 1.35$$

where the ε_0 is the electric constant of vacuum, q_i and q_j the atom charges, and r_{ij} the distance between atoms.

The long-range nature of VdW and electrostatic interactions creates convergence problems and makes it unfeasible to compute a direct sum of the pair energies to compute the total energies. These problems are avoided by using a cut-off radius of 12 Å and subsequent introduction of tail corrections for VdW interactions, and the use of the Ewald summation method to compute the electrostatic energy.

3.2. Zeolites

A wide variety of general force fields avalaible in the literature can be applied to zeolites. Due to the generality of parameterization, we expect that these force fields are suitable to reproduce experimental results with a reasonable accuracy. However, when we try to increase the accuracy in predicting molecular properties while maintaining a fair broad coverage of the periodic table, the force fields require complicated functional forms[53,63,65].

The results obtained using these general force fields are not good enough for specialized systems such as adsorption and diffusion in zeolites. For this reason new force fields have been optimized for pure silica zeolites[66-68] as well as for those with nonframework cations[69-72]. These new force fields have shown improved predictions for adsorption and molecular transport in these systems[66-74]. Most molecular simulation studies in zeolites are performed using the Kiselev-type potentials, where the zeolite atoms are held rigid at the crystallographic positions[75]. However, some authors have also investigated the effect of flexibility, using a variety of potentials for the framework atoms[76-78] and testing the accuracy and viability by comparing the computed adsorption[79-80], diffusion[78,81-82], IR spectra[76-77], or structural parameters[83-84] with experimental data. In this work we have followed both strategies using rigid models as well as flexible models.

The framework of pure silica zeolites is built from silicon and oxygen. In our simulations we take the crystallographic positions of the dehydrated structures from experimental data. When using rigid frameworks, the atoms are kept fixed at their atomic positions. Therefore we do not need to include interactions between framework atoms. When using flexible models, bonded interactions (bonding, bending, and torsions energies) described in the previous section are considered. In

both cases (rigid and flexible models) the nonbonded interactions are taken into account, but for rigid structures only framework-molecule (and not framework-framework).

As all silicon atoms are surrounded by oxygen atoms we assume that the dispersive interactions between guest molecules and the framework are only due to the oxygen. Therefore we define specific Lennard-Jonnes interactions between the adsorbates and the oxygen atoms and we do not use mixing rules. Regarding the electrostatic interactions, we place point charges on both type of atoms.

3.3. MOFs and ZIFs

The metal-linker bonds present in MOFs are weaker than those of the Si-O bonds in zeolites. This leads to an intrinsic flexibility of the frameworks. Under proper conditions, this inherent flexibility can cause large structural changes in the framework. Several studies point out that certain adsorbates can induce these changes in MOFs[85-87]. Other works attribute the structural change to other factors, such as temperature[88] or pressure[89].

In order to take into account the flexibility of the frameworks, there are some models that predict realistically the motion of the framework atoms. However, the higher complexity of these models increases their computational cost, which can make them extremely time consuming. These force fields are not transferable and have to be developed for each structure. The results obtained with flexible models in most cases are similar to those obtained with rigid models[90]. For these reasons currently most simulations of MOFs and ZIFs are performed using rigids models.

In this work we consider the structures as rigid frameworks with the atoms fixed in their atomic positions. In contrast to zeolites, all framework atoms are considered as Lennard-Jonnes interaction centers and point charges are added to every atom. The interactions with guest molecules are calculated using Lorentz-Berthelot mixing rules.

3.4. Adsorbates

We can divide the models uses for the adsorbates into two types:

- Full atom models: These models consider each atom of the molecule as a single interaction center.
- United atom models: In these models a set of atoms is considered as single interaction center. These sets are named *pseudoatoms.*

In both cases these interactions centers take into account the dispersive interactions and (in some cases) the electrostatic interactions. The former are considered with specific values of the σ and ε parameters of the Lennard-Jones potential and the latter are considered by adding point charges. Besides the non-bonded energy in the cases of flexible models the bonded energies are also considered, according to the potentials defined in the force field section.

We study a wide variety of gases with varions in sizes, shapes, and polarities. We have classified them in five sets:

Air and pollutants (N_2, O_2, Ar, H_2S): The three air components and hydrogen sulfide are modeled using rigid full atom models. Therefore we consider one interaction center for each atom. Nitrogen and oxygen molecules have quadropolar moments, and in order to reproduce them, we follow the works of Murthy *et al*[91] and Stogryn[92] . We placed negative point charges on the atoms and a third positive charge in the center of mass of the molecules. To model argon we do not need to use point charges and the model only has one dispersive interaction center. Finally for hydrogen sulfide we use several available models containing three, four or five interaction centers. In all cases, Lennard-Jones interaction centers are included in each of the three atoms. In order to reproduce the dipole of the hydrogen sulfide molecule, each model uses a different number of partial charges. The three-sites model placed a charge in each atom, the four-sites model place a fourth one in the rotation axis of the molecule. Finally the five-sites model uses two point charges placed in a tetrahedral arrangement above and below the molecular plane.

Details about geometry, Lennard-Jones parameters and partial charges of the models for nitrogen, oxygen, argon, and hydrogen sulfide used in this work can be found in chapters 7 (N_2, O_2, and Ar) and 4 (H_2S).

Greenhouse gases (CO_2 – methane): Carbon dioxide is a linear molecule with a quadrupole moment. For this molecule we use the model proposed by Harris *et al.*[93] with three Lennard-Jonnes interaction centers and three partial charges, one on each atom. Lennard-Jonnes parameters and charges are taken from the work of García-Sanchez *et al.*[94].

Although there are full atom models available for methane, in this work we use a united atom model with a single interaction center to model the methane molecule. The Lennard-Jones parameters are taken from the work of Dubbeldam *et al.*[95] who adjusted the parameters to reproduce the VLE curve.

Hydrocarbons: Due to the flexibility that hydrocarbon molecules present, we model them using flexible models. Similarly to methane model, the longer chains are also described using united atoms. We define a interaction center with its own effective potential for each CH_x group [95-96]. We do not consider partial charges for alkanes. In the case of propylene, we add point charges to the $CH_2(sp^2)$ and $CH(sp^2)$ groups. In

addition to this, one more point charge is placed between them in order to reproduce the dipole of the alkene. More details can be found in chapters 2 and 7.

Alcohols: Alcohol molecules are also modeled using flexible models. In this work we use the parameters of the TraPPE[97] force field. We consider one Lennard-Jones interaction center per CH_x group and one more for the oxygen atoms. There is no dispersion center associated to the hydrogen atom bonded to the oxygen, but it carries a point charge. We placed additional point charges in the oxygen atom and in the CH_x group bonded to the oxygen. Detailed information about Lennard-Jones parameters and charges can be found in chapters 7 and 8.

Water: Water is one of the more complex molecules to deal with. There are a lot of models available but none of them is able to reproduce all the singularities of water. Each model is developed to reproduce some specific behavior of the molecule. Most models can be classified as three-sites models, four-sites models and five-sites model. In this work we use the Tip5pEw model[98], which is a five-site model.

4. Context, scope, and structure of the thesis

There are around two hundred zeolites reported in the international Zeolite Database. More than ten thousand MOFs have been synthesized up to date, and an more than a hundred ZIFs have been synthesized. Despite these astonishing numbers, most of these new materials have no industrial applications yet. A lot of research is needed to analyze those materials and their properties. In this study we aim to provide new research methods and tools that will allow to increase significantly the knowledge of these materials. We also aim to study the possible use of crystalline nanoporus materials to tackle current industrial challenges. Furthermore our last goal would be to design hypothetical structures suitable for solving some specific problems.

The scope of this thesis is therefore three-fold:

- To develop new force fields and sets of charges that allows a more accurate modeling of nanoporous materials.
- To study the potential uses of different types of nanoporous materials in processe of industrial interest.
- To design new materials with specific properties, for technological applications.

To achieve these objectives we perform molecular simulations using the methods, force fields, and models explained in previous sections.

Development of new force fields and sets of charges that allow the modeling of nanoporous materials. (Chapters 2, 3, 4, and 5)

In chapter 2 we study the propylene models available in the literature and we propose new ones. The new models are developed by fitting to experimental adsorption isotherms in zeolites. The Lennard-Jones parameters are adjusted to reproduce the VLE curve of the gas. We have also developed a specific force field able to predict diffusion and adsorption of propylene in zeolites with very narrow channels.

In chapter 3 we study the effect of the substitution of silicon atoms by germanium atoms in a zeolite framework. We focus on the deformation of the 4-, 6-, and 8-rings of the structure. We also compute the surface area as well as the pore volume of the pure silica zeolite and germanium modified zeolite, and we compare them with experimental results. In addition, we compute diffusion coefficients for methane and propene using both rigid and non-rigid frameworks.

In chapter 4 previous available models of hydrogen sulfide are discussed and three new models are proposed. We compare their accuracy reproducing VLE and vapor-pressure curves, and the liquid density. Our results show a good agreement between the models. We also compute the adsorption isotherms, heats of adsorption, and Henry coefficients of hydrogen sulfide in three MOFs.

In chapter 5 we developed a transferable and scalable set of point charges for ZIFs. This set can be used in previously synthesized ZIFs as well as in theoretical ZIFs. We validate the viability of the set of charges by comparing experimental heats of adsorption with simulation data obtained using our set of charges.

Study of different types of nanoporous materials for applications of enviromental and industrial interest. (Chapters 2, 4, 6, and 7)

In chapter 2, we use the developed models and force fields to study the adsorption and diffusion properties of propane and propylene in the ITQ-12 zeolite. Our models accurately reproduce the experimental adsorption isotherms. Using TST we compute the diffusion coefficients in order to explain the differences obtained experimentally.

In chapter 4, we study the adsorption of hydrogen sulfide in three MOFs with different topologies, namely IRMOF-1, MIL-47, and Cu-BTC. We compute heats of adsorption, Henry coefficients, and adsorption isotherms to have a better understanding of the behavior of this air pollutant inside MOFs.

In chapters 6 and 7 we perform an extensive study of the metal organic framework Cu-BTC. We study the adsorption of greenhouse gases such as carbon dioxide and methane in the structure. We compute adsorption isotherms of the pure gases as well as of equimolar mixtures. Our results match with previous simulation and experimental data. We expand the study to all feed compositions by using molecular simulations and also by using the Ideal Adsorption Solution Theory (IAST). We compute diffusion coefficients by using MD and we determine the adsorption selectivity, diffusion selectivity, and mixture selectivity.

We also identify the preferential adsorption sites in Cu-BTC and then carry out a systematic study to analyze the preferential adsorption sites of hydrocarbons, greenhouse gases, alcohols, water, and the main components of air. We focus on the molecular mechanisms governing the adsorption process of these molecules. We perform MC simulations in the canonical ensemble varying the number of molecules. Then we analyze the distribution of the molecules inside the cage system of the framework. Finally we explore the possibility of enhancing the adsorption of certain gases by adding ionic liquids to the structure.

Design of new materials with specific characteristics (Chapter 8)

In chapter 8 we develop the idea of tailoring Cu-BTC in order to favor the adsorption of some gases and prevent the adsorption of other gases. Based on the

findings of chapter 7 we focus on the alcohol-water separation. We compute adsorption isotherms of equimolar mixtures in gas and liquid phase as well as adsorption energies, entropies, and Henry coefficients. We follow two strategies to improve the separation: Blocking cages and poisoning metal centers of the framework. We test our strategies and we propose realistic alternatives. We also found a modification of the Cu-BTC framework that could lead to an increase of its water stability.

Bibliography

(1) *Zeolites and Clay Minerals as Sorbents and Molecular Sieves*; Barrer, R. M., Ed.; Academic Press: London, 1978.

(2) Barthomeuf, D. In *Progress in Zeolite and Microporous Materials, Pts a-C*; Chon, H., Ihm, S. K., Uh, Y. S., Eds. 1997; Vol. 105, p 1677.

(3) Wang, S.; Peng, Y. *Chemical Engineering Journal* **2010**, *156*, 11.

(4) Bekkum, H. v.; Flaningen, E. M.; Jansen, J. C. *Introduction to Zeolite Science and Practice*; Elsevier: Amsterdam, 1991.

(5) Ruthven, D. M. *Principles of Adsorption and Adsorption Processes*; John Wiley: New York, 1984.

(6) Davis, M. E. *Nature* **2002**, *417*, 813.

(7) Hampel, I.; Jacobi, U. *Monatshefte Fur Veterinarmedizin* **1986**, *41*, 238.

(8) Hedstrom, A. *Journal of Environmental Engineering-Asce* **2001**, *127*, 673.

(9) Corma, A. *Journal of Catalysis* **2003**, *216*, 298.

(10) Corma, A.; Martinez, A. *Advanced Materials* **1995**, *7*, 137.

(11) Martinez, C.; Corma, A. *Coordination Chemistry Reviews* **2011**, *255*, 1558.

(12) Li, H.; Eddaoudi, M.; O'Keeffe, M.; Yaghi, O. M. *Nature* **1999**, *402*, 276.

(13) Keskin, S.; Liu, J.; Rankin, R. B.; Johnson, J. K.; Sholl, D. S. *Industrial & Engineering Chemistry Research* **2009**, *48*, 2355.

(14) Meek, S. T.; Greathouse, J. A.; Allendorf, M. D. *Advanced Materials* **2011**, *23*, 249.

(15) Sumida, K.; Rogow, D. L.; Mason, J. A.; McDonald, T. M.; Bloch, E. D.; Herm, Z. R.; Bae, T.-H.; Long, J. R. *Chemical Reviews* **2012**, *112*, 724.

(16) Millward, A. R.; Yaghi, O. M. *Journal of the American Chemical Society* **2005**, *127*, 17998.

(17) Rowsell, J. L. C.; Yaghi, O. M. *Angewandte Chemie-International Edition* **2005**, *44*, 4670.

(18) Lee, J.; Farha, O. K.; Roberts, J.; Scheidt, K. A.; Nguyen, S. T.; Hupp, J. T. *Chemical Society Reviews* **2009**, *38*, 1450.

(19) Yang, Q. Y.; Zhong, C. L.; Chen, J. F. *Journal of Physical Chemistry C* **2008**, *112*, 1562.

(20) Ma, L.; Abney, C.; Lin, W. *Chemical Society Reviews* **2009**, *38*, 1248.

(21) Duren, T.; Snurr, R. Q. *Journal of Physical Chemistry B* **2004**, *108*, 15703.

(22) Keskin, S.; Sholl, D. S. *Journal of Physical Chemistry C* **2007**, *111*, 14055.

(23) Horcajada, P.; Serre, C.; Maurin, G.; Ramsahye, N. A.; Balas, F.; Vallet-Regí, M.; Sebban, M.; Taulelle, F.; Férey, G. *Journal of the American Chemical Society* **2008**, *130*, 6774.

(24) Bourrelly, S.; Moulin, B.; Rivera, A.; Maurin, G.; Devautour-Vino, S.; Serre, C.; Devic, T.; Horcajada, P.; Vimont, A.; Clet, G.; Daturi, M.; Lavalley, J. C.; Loera-Serna, S.; Denoyel, R.; Llewellyn, P. L.; Ferey, G. *Journal of the American Chemical Society* **2010**, *132*, 9488.

(25) Lee, J. Y.; Olson, D. H.; Pan, L.; Emge, T. J.; Li, J. *Advanced Functional Materials* **2007**, *17*, 1255.
(26) Phan, A.; Doonan, C. J.; Uribe-Romo, F. J.; Knobler, C. B.; O'Keefe, M.; Yaghi, O. M. *Acc. Chem. Res.* **2010**, *43*, 58.
(27) Tian, Y.-Q.; Cai, C.-X.; Ji, Y.; You, X.-Z.; Peng, S.-M.; Lee, G.-H. *Angew. Chem. Int. Ed.* **2002**, *41*, 1384.
(28) Park, K. S.; Ni, Z.; Cote, A. P.; Choi, J. Y.; Huang, R. D.; Uribe-Romo, F. J.; Chae, H. K.; O'Keeffe, M.; Yaghi, O. M. *Proc. Natl. Acad. Sci. USA* **2006**, *103*, 10186.
(29) Banerjee, R.; Phan, A.; Wang, B.; Knobler, C.; Furukawa, H.; O'Keeffe, M.; Yaghi, O. M. *Science* **2008**, *319*, 939.
(30) Huang, X. C.; Lin, Y. Y.; Zhang, J. P.; Chen, X. M. *Angew. Chem. Int. Ed.* **2006**, *45*, 1557.
(31) Tian, Y. Q.; Cai, C. X.; Ren, X. M.; Duan, C. Y.; Xu, Y.; Gao, S.; You, X. Z. *Chem. Eur. J.* **2003**, *9*, 5673.
(32) Hao, G. P.; Li, W. C.; Lu, A. H. *J. Mat. Chem.* **2011**, *21*, 6447.
(33) Farrusseng, D.; Aguado, S.; Pinel, C. *Angew. Chem. Int. Ed.* **2009**, *48*, 7502.
(34) Metropolis, N.; Rosenbluth, A. W.; Rosenbluth, M. N.; Teller, A. N.; Teller, E. *J. Chem. Phys.* **1953**, *21*, 1087.
(35) Frenkel, D. *Proceedings of the National Academy of Sciences of the United States of America* **2004**, *101*, 17571.
(36) Frenkel, D.; Smit, B. *Understanding Molecular Simulation From Algorithms to Applications*; second edition ed.; Academic Press: San Diego. C.A., 2002.
(37) Smit, B.; Siepmann, J. I. *Journal of Physical Chemistry* **1994**, *98*, 8442.
(38) Rosenbluth, M.; Rosenbluth, A. J. *Chemical Physics* **1955**, *23*, 356.
(39) Vlugt, T. J. H.; Krishna, R.; Smit, B. *Journal of Physical Chemistry B* **1999**, *103*, 1102.
(40) Macedonia, M. D.; Moore, D. D.; Maginn, E. J. *Langmuir* **2000**, *16*, 3823.
(41) Myers, A. L.; Monson, P. A. *Langmuir* **2002**, *18*, 10261.
(42) Myers, A. L. *Aiche Journal* **2002**, *48*, 145.
(43) Talu, O.; Myers, A. L. *Aiche Journal* **2001**, *47*, 1160.
(44) Dubbeldam, D.; Beerdsen, E.; Vlugt, T. J. H.; Smit, B. *J. Chem. Phys.* **2005**, *122*, 224712.
(45) Myers, A. L.; Prausnitz, J. M. *Aiche Journal* **1965**, *11*, 121.
(46) Keskin, S.; Liu, J. C.; Johnson, J. K.; Sholl, D. S. *Langmuir* **2008**, *24*, 8254.
(47) Yang, Q. Y.; Zhong, C. L. *Journal of Physical Chemistry B* **2006**, *110*, 17776.
(48) Liu, D. H.; Zhong, C. L. *Journal of Materials Chemistry* **2010**, *20*, 10308.
(49) Babarao, R.; Hu, Z. Q.; Jiang, J. W.; Chempath, S.; Sandler, S. I. *Langmuir* **2007**, *23*, 659.
(50) Chen, H. B.; Sholl, D. S. *Langmuir* **2007**, *23*, 6431.
(51) Jensen, C. R. C.; Seaton, N. A. *Langmuir* **1996**, *12*, 2866.
(52) Rappe, A. K.; Casewit, C. J.; Colwell, K. S.; Goddard, W. A.; Skiff, W. M. *J. Am. Chem. Soc.* **1992**, *114*, 10024.
(53) Hagler, A. T.; Ewig, C. S. *Computer Physics Communications* **1994**, *84*, 131.

(54) Mayo, S. L.; Olafson, B. D.; Goddard, W. A. *Journal of Physical Chemistry* **1990**, *94*, 8897.
(55) Allured, V. S.; Kelly, C. M.; Landis, C. R. *Journal of the American Chemical Society* **1991**, *113*, 1.
(56) Root, D. M.; Landis, C. R.; Cleveland, T. *Journal of the American Chemical Society* **1993**, *115*, 4201.
(57) Weiner, S. J.; Kollman, P. A.; Case, D. A.; Singh, U. C.; Ghio, C.; Alagona, G.; Profeta, S.; Weiner, P. *Journal of the American Chemical Society* **1984**, *106*, 765.
(58) Brooks, B. R.; Bruccoleri, R. E.; Olafson, B. D.; States, D. J.; Swaminathan, S.; Karplus, M. *Journal of Computational Chemistry* **1983**, *4*, 187.
(59) Jorgensen, W. L.; Tiradorives, J. *Journal of the American Chemical Society* **1988**, *110*, 1657.
(60) Clark, M.; Cramer, R. D.; Vanopdenbosch, N. *Journal of Computational Chemistry* **1989**, *10*, 982.
(61) Momany, F. A.; McGuire, R. F.; Burgess, A. W.; Scheraga, H. A. *Journal of Physical Chemistry* **1975**, *79*, 2361.
(62) Hermans, J.; Berendsen, H. J. C.; Vangunsteren, W. F.; Postma, J. P. M. *Biopolymers* **1984**, *23*, 1513.
(63) Halgren, T. A. *Journal of the American Chemical Society* **1992**, *114*, 7827.
(64) Burchart, E. D.; Jansen, J. C.; Vanbekkum, H. *Zeolites* **1989**, *9*, 432.
(65) Allinger, N. L.; Yuh, Y. H.; Lii, J. H. *Journal of the American Chemical Society* **1989**, *111*, 8551.
(66) Dubbeldam, D.; Calero, S.; Vlugt, T. J. H.; Krishna, R.; Maesen, T. L. M.; Smit, B. *J. Phys. Chem. B,* **2004**, *108*, 12301.
(67) Dubbeldam, D.; Calero, S.; Vlugt, T. J. H.; Krishna, R.; Maesen, T. L. M.; Beerdsen, E.; Smit, B. *Phys. Rev. Lett.* **2004**, *93(8), 88302*.
(68) Liu, B.; Smit, B.; Rey, F.; Valencia, S.; Calero, S. *Journal of Physical Chemistry C* **2008**, *112*, 2492.
(69) Calero, S.; Lobato, M. D.; Garcia-Perez, E.; Mejias, J. A.; Lago, S.; Vlugt, T. J. H.; Maesen, T. L. M.; Smit, B.; Dubbeldam, D. *Journal of Physical Chemistry B* **2006**, *110*, 5838.
(70) Calero, S.; Dubbeldam, D.; Krishna, R.; Smit, B.; Vlugt, T. J. H.; Denayer, J. F. M.; Martens, J. A.; Maesen, T. L. M. *Journal of the American Chemical Society* **2004**, *126*, 11377.
(71) Garcia-Perez, E.; Dubbeldam, D.; Maesen, T. L. M.; Calero, S. *Journal of Physical Chemistry B* **2006**, *110*, 23968.
(72) Garcia-Sanchez, A.; Ania, C. O.; Parra, J. B.; Dubbeldam, D.; Vlugt, T. J. H.; Krishna, R.; Calero, S. *J. Phys. Chem. C* **2009**, *113*, 8814.
(73) Castillo, J. M.; Dubbeldam, D.; Vlugt, T. J. H.; Smit, B.; Calero, S. *Molecular Simulation* **2009**, *35*, 1067.
(74) Garcia-Sanchez, A.; Garcia-Perez, E.; Dubbeldam, D.; Krishna, R.; Calero, S. *Adsorption Science & Technology* **2007**, *25*, 417.

(75) Bezus, A. G.; Kiselev, A. V.; Lopatkin, A. A.; Du, P. Q. *Journal of the Chemical Society-Faraday Transactions II* **1978**, *74*, 367.
(76) Demontis, P.; Suffritti, G. B.; Quartieri, S.; Fois, E. S.; Gamba, A. *Journal of Physical Chemistry* **1988**, *92*, 867.
(77) Nicholas, J. B.; Hopfinger, A. J.; Trouw, F. R.; Iton, L. E. *Journal of the American Chemical Society* **1991**, *113*, 4792.
(78) Leroy, F.; Rousseau, B.; Fuchs, A. H. *Physical Chemistry Chemical Physics* **2004**, *6*, 775.
(79) Vlugt, T. J. H.; Schenk, M. *Journal of Physical Chemistry B* **2002**, *106*, 12757.
(80) Garcia-Perez, E.; Parra, J. B.; Ania, C. O.; Dubbeldam, D.; Vlugt, T. J. H.; Castillo, J. M.; Merkling, P. J.; Calero, S. *Journal of Physical Chemistry C* **2008**, *112*, 9976.
(81) Zimmermann, N. E. R.; Jakobtorweihen, S.; Beerdsen, E.; Smit, B.; Keil, F. J. *Journal of Physical Chemistry C* **2007**, *111*, 17370.
(82) Bouyermaouen, A.; Bellemans, A. *Journal of Chemical Physics* **1998**, *108*, 2170.
(83) Hill, J. R.; Sauer, J. *Journal of Physical Chemistry* **1994**, *98*, 1238.
(84) Hill, J. R.; Sauer, J. *Journal of Physical Chemistry* **1995**, *99*, 9536.
(85) Serre, C.; Millange, F.; Thouvenot, C.; Nogues, M.; Marsolier, G.; Louer, D.; Ferey, G. *Journal of the American Chemical Society* **2002**, *124*, 13519.
(86) Cussen, E. J.; Claridge, J. B.; Rosseinsky, M. J.; Kepert, C. J. *Journal of the American Chemical Society* **2002**, *124*, 9574.
(87) Devautour-Vinot, S.; Maurin, G.; Henn, F.; Serre, C.; Devic, T.; Ferey, G. *Chemical Communications* **2009**, *19*, 2733-2735.
(88) Liu, Y.; Her, J.-H.; Dailly, A.; Ramirez-Cuesta, A. J.; Neumann, D. A.; Brown, C. M. *Journal of the American Chemical Society* **2008**, *130*, 11813.
(89) Beurroies, I.; Boulhout, M.; Llewellyn, P. L.; Kuchta, B.; Ferey, G.; Serre, C.; Denoyel, R. *Angewandte Chemie-International Edition* **2010**, *49*, 7526.
(90) Greathouse, J. A.; Kinnibrugh, T. L.; Allendorf, M. D. *Industrial & Engineering Chemistry Research* **2009**, *48*, 3425.
(91) Murthy, C. S.; Singer, K.; Klein, M. L.; McDonald, I. R. *Molecular Physics* **1980**, *41*, 1387.
(92) Stogryn, D. E.; Stogryn, A. P. *Molecular Physics* **1966**, *11(4), 371.*
(93) Harris, J. G.; Yung, K. H. *Journal of Physical Chemistry* **1995**, *99*, 12021.
(94) Garcia-Sanchez, A.; Ania, C. O.; Parra, J. B.; Dubbeldam, D.; Vlugt, T. J. H.; Krishna, R.; Calero, S. *Journal of Physical Chemistry C* **2009**, *113*, 8814.
(95) Dubbeldam, D.; Calero, S.; Vlugt, T. J. H.; Krishna, R.; Maesen, T. L. M.; Smit, B. *Journal of Physical Chemistry B* **2004**, *108*, 12301.
(96) Ryckaert, J. P.; Bellemans, A. *Faraday Discussions* **1978**, *66*, 95.
(97) Chen, B.; Potoff, J. J.; Siepmann, J. I. *Journal of Physical Chemistry B* **2001**, *105*, 3093.
(98) Rick, S. *Journal of Chemical Physics* **2004**, *120*, 6085.

We present a combined computational and experimental approach to evaluate the suitability of the ITQ-12 nanoporous material (ITW) as a propane/propylene separation device. For this, we have computed adsorption and diffusion of propane and propylene in the ITQ-12 zeolite. The propane isotherm is reproduced well, but the available propylene models in literature are unable to describe the propylene isotherm. Newly developed force field parameters for propylene were obtained by fitting to our own experimental adsorption isotherms and validated with previous data taken from the literature. To obtain self diffusion of propane and propylene in the zeolite we combined the Configurational Bias Monte Carlo method with rare-event molecular simulation techniques. Our results support experimental observations that point out ITQ-12 as a suitable structure for propane/propylene separation. The selectivity originates mainly from a difference in adsorption, possibly enhanced by a difference in diffusion.

Juan José Gutiérrez-Sevillano, David Dubbeldam, Fernando Rey, Susana Valencia, Miguel Palomino, Ana Martín-Calvo, and Sofía Calero

2

Analysis of the ITQ-12 Zeolite Performance in Propane/Propylene Separations Using a Combination of Experiments and Molecular Simulations

Introduction

The separation of propane–propylene mixtures is one of the most important as well as most expensive separations in the petrochemical industry. These mixtures are usually obtained from the thermal or catalytic cracking of hydrocarbons. Once separated, propylene can be used for polypropylene production whereas the propane fraction can be used as liquefied petroleum gas for household heating. Cryogenic distillation has been used for propane/propylene separations over the last 60 years[1]. However, this is a difficult and high energy consuming process and a number of alternate technologies based on adsorption processes are being investigated[2-5]. These technologies require selective adsorbents to be able to obtain high purity with efficiency. This can be achieved by employing adsorbents which have pore sizes very close to the size of these gases in order to discriminate between molecules with very similar sizes[3-4,6-9]. A second

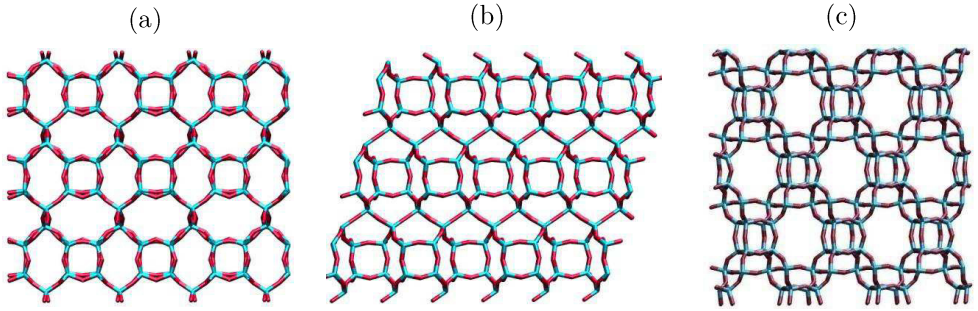

Figure 1. *ITQ-12 zeolite along axis a, axis b, and axis c.*

important issue in selecting the most appropriated adsorbent is its lifetime. This is so because oligomerization of propylene easily takes place on residual acid sites, leading to pore blocking of the adsorbent[10]. Therefore it is necessary to use materials with non acidity and high selectivity for light hydrocarbons.

The inherent molecular sieves properties of pure silica zeolites make of these materials an interesting option to be used as adsorbents based on differences in adsorption, kinetics and size exclusion separations[5,11-12]. Recent studies have shown that pure silica zeolites with 8 member ring pores provide surprisingly high kinetic selectivity for mixtures of hydrocarbons of small size[10,13-17]. This implies that a kinetically controlled adsorption separation process may be feasible and could yield a high purity olefin product with very good recovery[2-4,7,13,17-19]. To our knowledge, the best propylene/propane separation performance has been obtained using ITQ-12 as selective adsorbent. The reason could be attributed to characteristic size and shape of the pores of this zeolite, which makes it a very good candidate to be used for this separation[13,18-19].

ITQ-12 (ITW) is a two-dimensional small 8-membered ring pore zeolite that was solved in the monoclinic C1m1 symmetry with unit cell parameters of a=10.4364 Å, b=15.0183 Å and c= 8.8553 Å, α=90°, β=105.74°, and γ=90°, and cell volume V = 1326.76 Å^3. The pore aperture of ITQ-12 along the [001] direction is 3.9 x 4.2 Å and 2.4 x 5.4 Å along [100] direction. Then, the pore along [100] has no influence for adsorption since its aperture is not large enough to allow the entrance of any hydrocarbon. Consequently, from the point of view of its adsorption properties, ITQ-12 can be envisaged as a one-dimensional small pore zeolite. Importantly, the 8-membered pores running along [001] give entrance to a slit-shaped cages of 3.9 Å x 9.6 Å x 8.5 Å dimensions. A view of the zeolite along the three axes is shown in Figure 1.

In this work, we study the feasibility of using ITQ-12 for propane/propylene separations based on both, kinetic and adsorption equilibria. The adsorption isotherms were computed using molecular simulations and compared with those obtained experimentally. The diffusion coefficients were computed using molecular simulations. In addi-

tion, the advantages and disadvantages of using available or new developed models and force fields for propane and propylene are analyzed in this work.

Experimental Section

Pure silica ITQ-12 zeolite was synthesized following the reported example 2 of reference[20], consisting in hydrolyzing the appropriated amount of tetraethylorthosilicate (TEOS) in an aqueous solution of the structure directing agent 1,3,5-trimethyl-imidazolium hydroxide (SDAOH). The resulting mixture was continuously stirring at ambient temperature until the ethanol produced during hydrolysis of TEOS and the required amount of water was evaporated. Then, an aqueous solution of HF was added to the above reaction gel, and the final mixture was manually homogenized. The final gel composition was:

1 SiO_2 : 0.56 SDAOH : 0.56 HF : 7 H_2O

The resulting gel was heated at the autogenous pressure of the system in stainless steel autoclaves at 448 K for 14 days. The ITQ-12 zeolite was recovered by filtration and was exhaustively washed with distilled water and acetone, and finally was dried at 373 K for 12 hours. The occluded 1,3,5-trimethylimidazolium organic cations were removed by calcination at 973 K leading to a highly crystalline pure silica ITQ-12 zeolite, as was confirmed by means of the X-Ray diffraction technique (Figure A1.1. in Appendix 1). The adsorption capacity and pore aperture was determined by applying the Horvath-Kawazoe method to the high-resolution Ar isotherm measured at 83 K. The micropore volume was 0.154 $cm^3 \cdot g^{-1}$ and the averaged pore aperture was 0.49 nm (Figure A1.2. in Appendix 1), which is in excellent good agreement with the crystallographic structure of ITQ-12, confirming that micropore volume can be accessed through the 8-membered ring along the [001] axis.

Propane and propylene adsorption isotherms and kinetic measurements were performed in an IGA-3 gravimetric analyzer (Hiden Isochema). Approximately, 50 mg of the calcined sample were placed in the balance. Before each adsorption experiment, the sample was outgassed at 673 K under a final pressure of 10^{-5} Pa during four hours to fully remove any adsorbates from its pore volume. No weight modification was observed at the end of this pretreatment. The temperature of the sample was subsequently reduced under high vacuum until the target temperature (298 K) was reached. Adsorption measurements were performed by introducing gas to build up the desired pressures. Typically, 26 equilibrium data points up to 91.2 kPa were recorded for each gas, whereas the kinetic experiments were performed at pressures of 30.4 kPa. The equilibrium conditions were fixed at the 98 % of the calculated uptake using the Avrami's model[21] or a maximum equilibration time of 120 minutes for each point of the isotherms, while the kinetic measurements were lasted up to 12 hours.

Simulation Section

Simulations were performed in all-silica ITQ-12 zeolite. The positions of the atoms were taken from ref [22]. Following the work of Bezus *et al.*[23] we modeled the zeolite as a rigid network of oxygen and silicon atoms. This is a very common approximation for small alkanes in all-silica zeolites[24-25]. We used a simulation box of 3 x 2 x 3 unit cells. Tests on larger systems did not show any significant finite-size effects. The charge distribution on the oxygen atoms of the framework was considered static: i.e, polarization of oxygen was neglected[7,26-29]. We used point charges for the silicon and the oxygen atoms of q_{Si} = 2.05 e^- and q_O = -1.025 e^-, respectively[7].

The adsorption isotherms were computed using Configurational Bias Grand Canonical MC simulation methods. Although our models for propane and propylene contain a maximum of four beads, the Configurational Bias method speeds up the equilibration and therefore it is worthwhile to use it. In order to compare with available data most of our computed isotherms are given in excess loading *versus* pressure. The excess loading was obtained using the method of Duren *et al.*[30]. Pressures were obtained from the Peng Robinson equation with parameters Tc=369.825 K, Pc=4247660 Pa, ω=0.1524, and Tc=365.57 K, Pc=4664600 Pa, ω=0.1408, for propane and propylene, respectively.

One of the difficulties encountered when studying diffusion behavior in zeolites using simulation is that many processes occur outside the time scale accessible to Molecular Dynamics (MD), which is currently typically limited to diffusion rates in the order of 10^{-12} m^2/s. We compute zero-loading diffusion coefficients of propane and propylene in ITQ-12 by applying the Transition State Theory dynamically corrected method. This method has the potential to be orders of magnitude more efficient while still retaining full atomistic detail[31-34].

The propane and propylene molecules were described with united atom models, in which $CH_3(sp^3)$, $CH_2(sp^3)$, $CH_2(sp^2)$, and $CH(sp^2)$ groups are considered as single interaction centres[35]. The beads in the chain are connected by harmonic bonding potentials[36]. A harmonic cosine bending potential models the bond bending between three neighbouring beads. The interactions between the adsorbates as well as between the adsorbates and the zeolite are described by Lennard-Jones potentials truncated at a cutoff of 12 Å and shifted so that the energy tends smoothly to zero at the cutoff. The effective Lennard-Jones interaction parameters for propane [$CH_2(sp^3)$-$CH_2(sp^3)$ ε/k_B =56.0 K, σ=3.96 Å; $CH_3(sp^3)$-$CH_3(sp^3)$ ε/k_B =108.0 K, σ=3.76 Å] were taken from Dubbeldam *et al.*[37-38] The additional parameters for propylene [$CH(sp^2)$-$CH(sp^2)$ ε/k_B = 53.0 K, σ = 3.74 Å; $CH_2(sp^2)$-$CH_2(sp^2)$ ε/k_B=93.0 K, σ = 3.685 Å], were taken from and Liu *et al.*[39] All these values were fitted to accurately reproduce the experimental vapor-liquid coexistence curves. Lorentz-Berthelot mixing rules were

used for all mixed adsorbent-adsorbent interactions.

To keep the consistency of all interaction parameters used in this work we used the Lennard-Jones parameters proposed by Dubbeldam *et al.*[37] for describing the interactions between $CH_i(sp^3)$ and the oxygen atoms for the zeolite framework and Liu *et al.*[39] for the interactions $CH_i(sp^2)$ and the oxygen atoms for the zeolite. Theses parameters, listed in Table 1, faithfully reproduces the experimentally determined isotherms in pure silica MFI-type zeolites and has been successfully extended to other types of pure silica zeolites[38,40-41]. The model described by Liu *et al.* for propylene in zeolited is labelled in this work as (NP-Lgg-Lzg) i.e. Non-Polar model (NP) with Lennard Jones parameters taken from Liu *et al.*[39] for the guest-guest (propylene-propylene) denoted by Lgg and the guest-zeolite (zeolite-propylene) denoted by Lgz interaction. As we will see later on, this model fails to reproduce experimental adsorption of propylene in ITQ-12. Therefore new developments were needed. Besides the non polar united atom model for propylene (NP), we described here a point charge model (PC). The guest-guest Lennard-Jones parameters for these polar models were taken from Liu et al. [39] (Lgg) or developed in this work to reproduce the vapor-liquid equilibrium (VLE) curve according to our new Gutiérrez-Sevillano *et al.* model (GSgg). The Lennard-Jones propylene-zeolite interactions for the polar model were also taken from Liu *et al.* [39] (Lgz) or developed in this work from the fitting to experimental adsorption data (GSgz).

Changing propylene-zeolite Lennard-Jones interactions (GSgz). Our first approach to reproduce experimental adsorption was to refit de $CH_2(sp^2)$-Oz and $CH(sp^2)$-Oz Lennard-Jones parameters. Following a similar strategy employed in previous works[7,37-38,42], simulations were performed firstly for ethylene to determine the effective Lennard-Jones interaction parameters for the $CH_2(sp^2)$ with the oxygen atoms of the zeolite framework (Oz), and secondly propylene to obtain the $CH(sp^2)$-Oz interaction. Available experimental data for ethylene[18] and our own experimental isotherms for propylene in ITQ-12 were used as calibration sets (Figures A1.3 and A1.4 in Appendix 1).

Implementing molecular dipoles for propylene: Point charged (PC) model. As mentioned above, the available model for propylene was a non-polar model (NP). We will show in the next section that this approximation is able to reproduce experimental adsorption in most zeolites[39], but not in ITQ-12. When the zeolite-guest interactions are modified to describe the propylene in ITQ-12 isotherm properly, we find that it fails to reproduce diffusion providing extremely high free energy barriers. This finding forced us to develop a new model containing electrostatic interactions. A common choice is to use point charges on atoms to represent molecular electrostatics[43-45]. We have implemented this model in our code and in next section we analyze the way it performs when computing

Table 1. *Lennard-Jones parameters for the adsorbate-adsorbate interactions.*

	$CH(sp^2)$-Oz		$CH_2(sp^2)$-Oz		$CH_2(sp^3)$-Oz		$CH_3(sp^3)$-Oz	
	ε/k_B (K)	σ(Å)	ε/k_B (K)	σ(Å)	ε/k_B (K)	σ(Å)	ε/k_B (K)	σ(Å)
Propane	-	-	-	-	60.50	3.58	93.00	3.48
Lgz	55.215	3.502	82.05	3.53	-	-	93.00	3.48
GSgz	246.215	3.992	92.38	3.53	-	-	93.00	3.48

adsorption and diffusion properties in ITQ-12 zeolite.

The Point charged model (PC) was defined using two positive charges of (q = 0.87 e^-) located in the $CH_2(sp^2)$ and $CH(sp^2)$ beads and a third negative charge of (q =-1.74 e^-) located in a dummy atom. The dummy-$CH_2(sp^2)$ bond length (0.704 Å) was chosen in such a way that it reproduces the experimental dipole moment. We use Ewald summations[46] to compute the point charge interactions. Detailed information on these models is compiled in Figure 2 and the adsorbent-adsorbate Lennard-Jones parameters used from previous available models of propane and propylene[39] (Lgz) as well as those developed in this work (GSgz) are summarized in Table 1.

Results

In this section we firstly analyze the obtained results using previous available models[38-39] (united atom non polar models for propane and propylene). Secondly, we study the effect of variations on the Lennard-Jones parameters and the effect of adding point charges to the propylene model in order to correctly reproduce the experimental dipole. Finally the need of

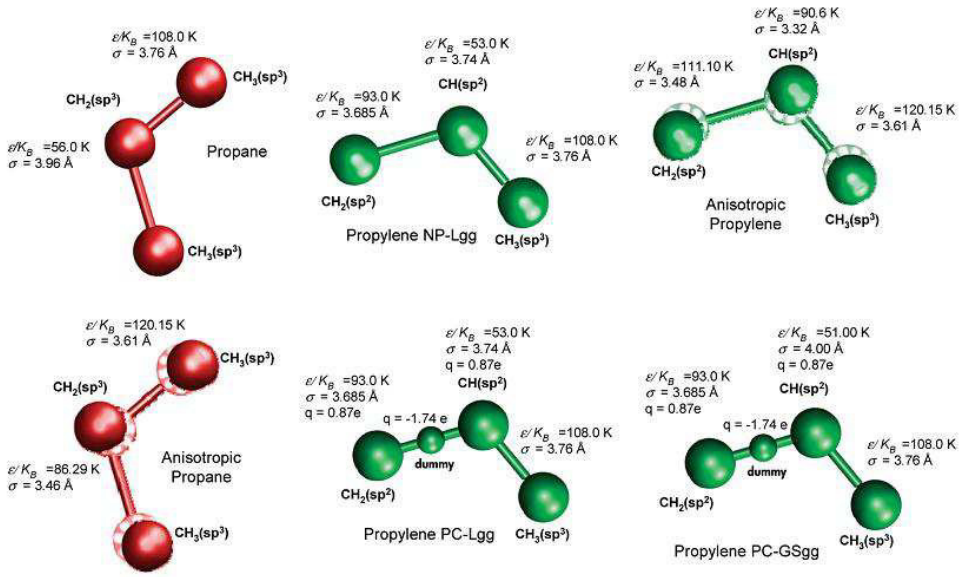

Figure 2. *Propane and propylene models used in this work.*

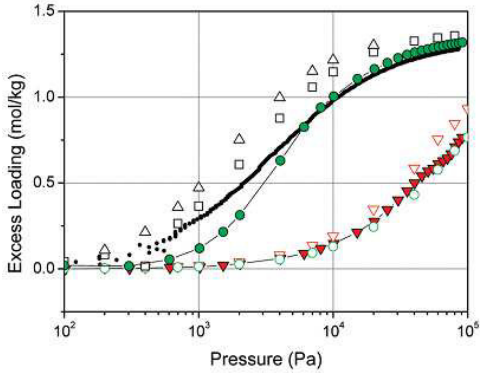

Figure 3. *Computed adsorption of propane in ITQ-12 at 300 K using previously available models -Dubbeldam et al.[39] (open down triangles), anisotropic model[48] (open triangles)- and of propylene using the NP-Lgg-Lgz model[40] (open circles), and anisotropic model[48] (open squares). Experimental data of propylene provided by Olson et al.[18](dots) and propane (solid down triangles) and propylene (solid circles) obtained in this work are included for comparison.*

a model able to accurately reproduce the VLE curve is discussed.

A. Adsorption using available models. The excess adsorption isotherms for propane and propylene at 303 K in the zeolite ITQ-12 are shown in Figure 3. At this temperature the saturation pressure of the gases is 1.08 MPa for propane and 1.31 MPa for propylene. Our experimental and simulation results are compared with previous experimental data by Olson *et al.*[18]. Simulations were performed using the model and force field parameters for propane of Dubbeldam *et al.*[38] and the (NP-Lgg-Lgz) model for propylene. The pressure range spans from 10^2 Pa to 10^5 Pa. Higher pressures involve adsorption in the liquid phase. Experimental data of the adsorption of propane in ITQ-12 zeolite were accurately reproduced using the model of Dubbeldam *et al.* This model is transferable to many other siliceous zeolites. Alkanes are modeled very successfully in zeolites. Therefore, any deviation between experimental and simulated isotherm would indicate a problem with the sample (pore-blocking, imperfections) or point to ITQ-12 being a "special" structure. Since this is not the case, we can focus on propylene. The newly obtained experimental isotherm for propylene is in very good agreement with the data of Olson *et al.*

We started with the existing models of Liu *et al.* and the anisotropic models[47] for propane and propylene. Both models fail to reproduce the difference in adsorption between propane and propylene. The model of Liu *et al.* gives similar adsorption of propane and propylene and its magnitude corresponds to the experimental isotherm of propane (it fails for propylene). The anisotropic model is also unable to signal a difference in adsorption of propane and propylene; it gives results that correspond to the experimental propylene isotherm (it fails for propane). Note that both models work in other structures, e.g. MFI, for propane[48] and propylene[49].

There are two options to explain the discrepancies: (a) the experimental adsorption isotherm for propane is not equilibrated and would eventually reach the experimental propylene isotherm, (b) the experimental isotherms are correct: there is a large difference in

adsorption of propane and propylene in ITQ-12. The experimental uptake curves after 700 minutes show a *plateau* for uptake of propane. If not equilibrated properly, then true equilibration is very, very slow. This is a discussion of theoretical nature, since in practice one can only use a finite amount of time. Option (b) implies that the Liu *et al.* model and the anisotropic model are unable to describe the adsorption difference of propane/propylene in ITQ-12. The simulation results for propylene are shifted one order of magnitude in pressure and almost overlap with the computed isotherm for propane. Similar behavior was observed at 400 K, 500 K, and 600 K (Appendix 1, Figure A1.5). The similar computed adsorption obtained for propane and propylene can be attributed to the high similarity of the models used for these molecules. In both cases, we are using a non polar united atom model. The models used do not have charges or dipole so propane and propylene molecules only differ in the adsorbent-adsorbate Lennard-Jones parameters. Similar adsorption using these models is an expected result because both molecules are similar in size and shape.

Next we study one of these models, the Liu *et al.* model, for difference in diffusion of propane/propylene. Self-diffusion has been computed using the dynamically corrected Transition State Theory (dcTST). This method requires a separated study of the free energy profile on each axis of the structure. Although previous studies about ITQ-12 reveal that the channel system of the zeolite is only accessible from one of the axis[19,22,50], we study the free energy profile for the three axes. To compute dcTST diffusion we first obtain the free energy profiles along the reaction coordinate (In this work the cell axes are used as reaction coordinate).

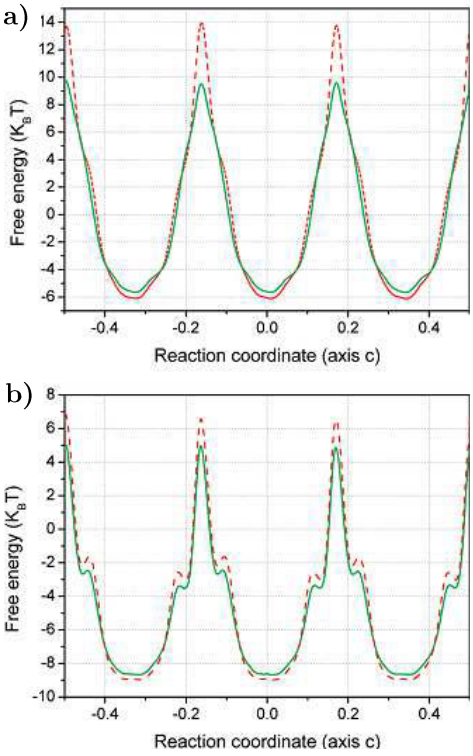

Figure 4. *Free energy profiles of (a) propane (dashed line) and propylene NP-Lgg-Lgz model (solid line) and (b) anisotropic propane (dashed line) and anisotropic propylene (solid line), computed along axis c at 300 K.*

Secondly we integrate these profiles in order to calculate the hopping rate and the diffusion TST coefficient. After that we sample the starting configurations of the beads in the top of the barriers and using these starting configurations and a short MD simulation we calculate the

transmission coefficient κ. Finally using the κ obtained we compute the dynamically corrected Diffusion TST. The computed energy profiles at 303 K in the c-channels for propane and propylene are shown in Figure 4. Energy profiles in the a-, and b-channels were also computed and can be found in the Appendix 1 (Figures A1.6a and A1.6b). The free energy profiles were obtained using the same force fields and models than in Figure 3, and they show a similar qualitative behavior for propane and propylene. The barriers are extremely high along the a- and b-axes for both molecules, but they are low enough to allow diffusion along the c-axis. These results confirm previous works[13,18] allowing the movement of both molecules along the c-axis but not along the a- and b-axes. The equipotential energy surfaces in ITQ-12 zeolite channels along x-, y-, z-directions are shown in Figure 5. According to the free energy barriers obtained we focus the diffusion study on the c-axis, computing the free energy profiles for propane and propylene at different temperatures (Appendix 1). Though the free energy profiles are similar from a qualitative point of view, the free energy barriers are lower for propylene than for propane at the same temperature. Since diffusion can be considered a hopping process from minima to minima, one can expect much lower diffusion for the higher barrier. Figure 4 compares the free energy profiles for propane and propylene at 300 K. A detailed analysis of these free energy profiles indicates that the propane free energy barriers are about 5 k_BT higher than the ones of propylene. Differences imply that propane and propylene diffusion coefficients are susceptible to be different. The obtained TST diffusion coefficient (not corrected yet) is two orders of magnitude higher for propylene (1.5×10^{-13} m^2s^{-1}) than for propane (1.2×10^{-15} m^2s^{-1}). The transmission coefficients for both molecules were 0.15 for propylene and 0.17 for propane, leading to a final dcTST diffusion coefficient of 2.4×10^{-14} m^2s^{-1} and 2.1×10^{-16} m^2s^{-1} for propylene

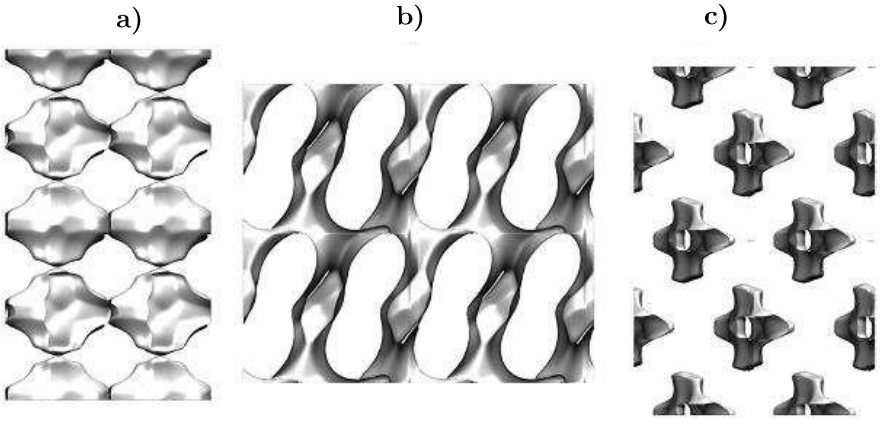

Figure 5. *Equipotential energy surfaces in ITQ-12 zeolite channels along the (a) x-, (b) y-, and (c) z- axes.*

and propane respectively. This gives a propylene to propane diffusion ratio of 114. Differences on diffusion can be attributed to the type of channels of zeolite ITQ-12.

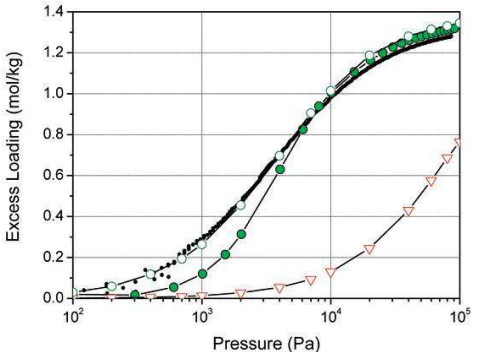

Figure 6. *Adsorption isotherms of propylene in ITQ-12 at 300 K. The computed isotherm (open circles) of propylene was obtained using the NP-Lgg-GSgz model. The experimental values obtained in this work (solid circles) are compared with previous experimental data[18](dots). The computed adsorption isotherm of propane is also included for comparison (open down triangles).*

We can conclude that NP-Lgg-Lgz model provides values for diffusion which are higher for propylene than for propane in ITQ-12 and it has been successfully tested for adsorption in zeolites with large and medium size channels[39]. However, this model fails to reproduce the experimental adsorption of propylene in zeolites with narrow channels such as ITQ-12. In order to reproduce the experimental adsorption of propylene we have followed several approaches based firstly on the variation of the Lennard-Jones parameters and secondly on the use of a polar model.

B. Variations on the Lennard-*Jones parameters.* The adsorption isotherm of propylene computed at 300 K for the NP-Lgg-GSgz model is shown in Figure 6. The agreement between the simulation and our experimental data as well as the data of Olson *et al.*[18] is now excellent. This agreement was obtained by varying the adsorbate-zeolite Lennard-Jones parameters, proving that in principle this variation is enough to reproduce experimental adsorption values. However this model is not suitable for diffusion. Figure 7 compares

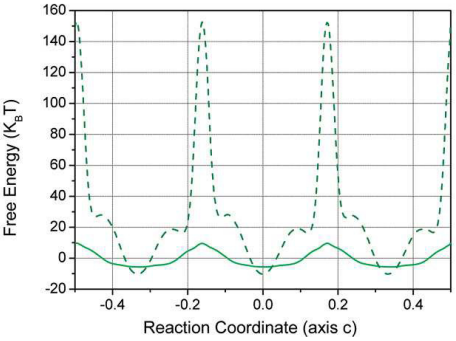

Figure 7. *Free energy profiles computed for propylene at 300 K using the NP-Lgg-Lgz model (solid line) and the NP-Lgg-GSgz model (dashed line).*

the free energy profiles for propylene along the c axis at 300 K using both, the previous model (NP-Lgg-Lgz) and the new model (NP-Lgg-GSgz). The severe increase of the energy barrier with the latter is attributed to the fact that the small narrow channels are extremely sensitive to the molecule-zeolite interaction. To reproduce the experimental adsorption it was necessary to increase the adsorbate-zeolite and $CH_2(sp^2)$–Oz Lennard-

Jones parameters. The increase in ε leads to higher zeolite-molecule attraction; the increase in σ leads to higher free energy barriers and impeded diffusion. Therefore, the NP-Lgg-GSgz model can be successfully used for adsorption but further refinements are necessary in order to obtain the reliable values for diffusion.

C. Development of polar models. We use a point charged dummy atom located on top of the $CH_2(sp^2)$-$CH(sp^2)$ bond. The negative net charge (–1.74 e^-) is compensated by adding equivalent net positive charges to the $CH_2(sp^2)$ and the $CH(sp^2)$ atoms (0.87 e^-). The position of the dummy atom was chosen such that it reproduces the experimental dipole (0.36 D) of the molecule. Figure 8 shows the adsorption isotherm of propylene obtained using this model (PC-Lgg-Lgz) and compared with available experimental data. As shown in the figure, the PC-Lgg-Lgz model leads to an excellent agreement between simulated and available experimental data. The transmission coefficient computed for propylene along the c-axis at 300 K for the point charged model provides a final dcTST diffusion one order lower to the one obtained for propane (Table 2). This model is therefore suitable to compute adsorption of propylene in ITQ-12 zeolite. However it does not reproduce the experimental vapor-liquid equilibrium curve (VLE) of propylene. In a final improvement we fitted the Lennard-Jones adsorbent-

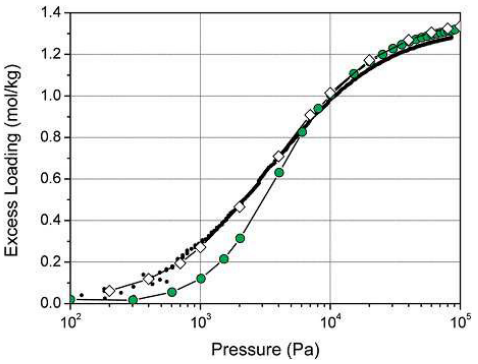

Figure 8. *Adsorption isotherms of propylene in ITQ-12 at 300 K. The computed isotherms were obtained using the PC-Lgg-Lgz model (open rhombus). The experimental values obtained in this work (solid circles) are compared with previous experimental data[18](dots).*

Table 1. *Diffusion coefficients obtained for propane and propylene at 300 K.*

		Diffusion TST (m^2s^{-1})	***Transmission Coefficient***	***Diffusion dcTST*** (m^2s^{-1})
Propane	***Dubbeldam***	1.2×10^{-15}	0.17	2.1×10^{-16}
	Anisotropic	8.6×10^{-14}	-	-
Propylene	***Anisotropic***	5.8×10^{-13}	-	-
	NP-Lgg-Lgz	1.5×10^{-13}	0.15	2.4×10^{-14}
	NP-Lgg-GSgz	-	0.07	-
	PC-Lgg-Lgz	1.1×10^{-15}	0.02	2.3×10^{-17}
	PC-GSgg-Lgz	7.1×10^{-16}	0.02	1.2×10^{-17}

adsorbent parameters to reproduce the experimental VLE curve for propylene (PC-GSgg-Lgz model) as shown in Figure 9. Since differences between PC-Lgg-Lgz and PC-GSgg-Lgz models only involve propylene-propylene interactions. The free energy profiles, the free energy barriers, the diffusion and the transmission coefficients obtained at infinite dilution using these two models are exactly the same. This model could only influence those properties that are loading-dependent i.e. the VLE curve and the adsorption properties. In particular VLE curve differences are only significant in the liquid branch of the curve (Figure 9). Since the excess

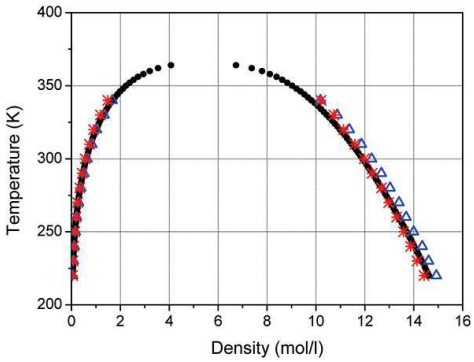

Figure 9. *Computed vapor-liquid equilibria curves for propylene using the PC-Lgg model (open triangles) and the PC-GSgg model (asterisks).Experimental data is included for comparison[18](solid circles).*

adsorption is computed in the gas phase, the PC-GSgg-Lgz model reproduces the experimental adsorption without any further refinement. To test the applicability of the model to the adsorption properties we compare in Figure 10 the propylene adsorption isotherm obtained using PC-GSgg-Lgz model with the one obtained using PC-Lgg-Lgz model. These isotherms are in perfect agreement with available experimental data. At 300 K and atmospheric pressure the computed excess adsorption is more than twice higher for propylene than for propane.

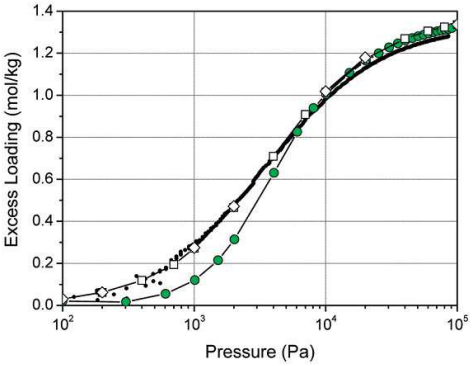

Figure 10. *Adsorption isotherms of propylene in ITQ-12 at 300 K. The computed isotherms were obtained using the PC-Lgg-Lgz model (open rhombuses) and the PC-GSgg-Lgz model (open squares). The experimental values obtained in this work (solid circles) are compared with previous experimental data[18](dots).*

D. Polar model for propylene in other zeolites. The polar model reproduces the isotherms of propylene in ITQ-12 in contrast to the Liu *et al.* model. In Figures 11a and 11b we show how well the model performs for adsorption of propylene in MFI and CHA. We note that the model performs just as well, or perhaps even slightly better than the Liu model. It appears that the ITQ-12 zeolite is more sensitive

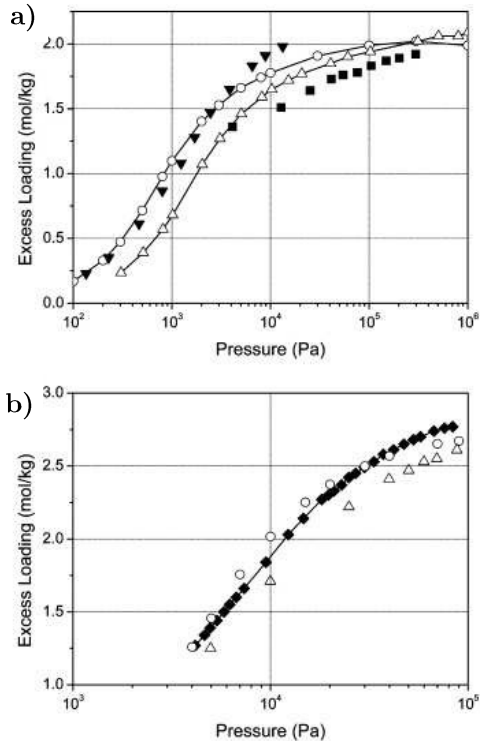

Figure 11. *Adsorption isotherms of propylene (a) in MFI at 298 K and (b) in CHA at 303 K. The computed isotherms were obtained using the PC-GSgg-Lgz model (open circles) and the Liu model (open triangles). The experimental values were from previous experimental data[40] for (a) MFI at 297 K (solid down triangles) and 298 K (solid squares) and for (b) CHA at 303 K (solid rhombuses).*

for small changes in model parameters. This is mainly due to the tight confinement of propane/propylene in ITQ-12.

Discussion

The Dubbeldam model is able to accurately describe adsorption of propane in ITQ-12 (and other zeolites) and the polar model is able to describe adsorption of propylene in ITQ-12 (and other zeolites), in contrast to previous models. However, the polar model leads to high diffusivities for propane compared to propylene, while the previous models indicate a faster diffusivity of propylene compared to propane. An interesting question is: whether the propane/propylene selectivity is due to adsorption or diffusion (or both)? In the Appendix 1 we have shown uptake curves for propane and propylene in ITQ-12. At first sight it appears that uptake of propylene is much faster than propane. This would be a correct conclusion if both species have similar isotherms, which they have not. Therefore the uptake is influenced by the difference in adsorption and it remains unclear how much of this is due to difference in adsorption. Furthermore, these uptake experiments can give Fickian (transport) diffusivities, which can be orders of magnitude higher than self-diffusivities (albeit that they are equal in the limit of infinite dilution). We hope that experimental measurements using methods like NMR or QENS that can probe self-diffusivities will shed further light on this. If this new data shows that diffusion of propylene is much faster than propane, we will have to choose a more sophisticated simulation model for propylene (e.g. all-atom including polarization).

From a modeling point of view we have established that electrostatic interactions are needed for propylene in ITQ-12. However, this leads to the undesirable situation that propane is modeled without and propylene with

charge interactions. Adsorption sites are usually located inside the larger cages while diffusion is largely controlled by the size and shape of the windows separating the cages. We speculate that here, flexibility of the windows might influence diffusion. Charge interactions inside the cages are screened to a higher degree inside the cages compared to a propylene molecule in the window. As a consequence, polarization-effects also could play an important role, because the dynamic charge re-distribution might be very different in the 8-ring window compared to in the cage environment. Therefore, our work is intended to show that there is a need for further experimental and modeling studies on propane/propylene diffusion in tight confinement.

Conclusions

The feasibility of ITQ-12 zeolite for propane/propylene separations based on both, kinetic and adsorption equilibria has been studied. The steric effect that is based on the molecular sieving properties of zeolites, explains that only small or properly shaped molecules such as propylene can diffuse into ITQ-12. Larger molecules such as propane are excluded from entering the internal pore of this zeolite. We have computed adsorption and diffusion properties in zeolite ITQ-12 using four models for propylene as well as the available models for propane. Our results show that previous available models and forcefields for propylene (NP-Lgg-Lgz) are not able to reproduce the experimental adsorption in ITQ-12. This can be solved 1) by fitting the Lennard-Jones interaction parameters (NP-Lgg-GSgz) to accurately reproduce the experimental isotherm, or 2) by adding point charges to the molecule (PC-Lgg-Lgz) in order to reproduce the experimental dipole. However, the former approximation fails to reproduce diffusion while the latter does not reproduce the vapor-liquid equilibria curve of propylene. Based on these findings we developed a new model (PC-GSgg-Lgz) that provides reasonable though low values for diffusion (one order lower than those obtained for propane) but it also can be used to successfully reproduce the experimental values for the molecular dipole, the VLE curve, and the adsorption isotherm in ITQ-12. Molecular separation of mixtures on zeolites is based not only on the adsorption selectivity but also on the differences between the diffusivities of the components of the mixture. With the PC-GSgg-Lgz model we are able to corroborate previous experimental findings pointing out ITQ-12 as a suitable structure for propane/propylene separations.

Bibliography

(1) Manley, D. B.; Swift, G. W. *Journal of Chemical and Engineering Data* **1971**, *16*, 301.

(2) Krishna, R.; Calero, S.; Smit, B. *Chemical Engineering Journal* **2002**, *88*, 81.

(3) Krishna, R.; Smit, B.; Calero, S. *Chemical Society Reviews* **2002**, *31*, 185.

(4) Maesen, T. L. M.; Krishna, R.; van Baten, J. M.; Smit, B.; Calero, S.; Sanchez, J. M. C. *Journal of Catalysis* **2008**, *256*, 95.

(5) Calero, S. In *Zeolites and Catalysis. Reactions and applications*; Ed. Wiley-VCH: 2010; Vol. 1, p 335.

(6) Calero, S.; Smit, B.; Krishna, R. *Physical Chemistry Chemical Physics* **2001**, *3*, 4390.

(7) Calero, S.; Dubbeldam, D.; Krishna, R.; Smit, B.; Vlugt, T. J. H.; Denayer, J. F. M.; Martens, J. A.; Maesen, T. L. M. *Journal of the American Chemical Society* **2004**, *126*, 11377.

(8) Schenk, M.; Calero, S.; Maesen, T. L. M.; van Benthem, L. L.; Verbeek, M. G.; Smit, B. *Angewandte Chemie-International Edition* **2002**, *41*, 2500.

(9) Schenk, M.; Calero, S.; Maesen, T. L. M.; Vlugt, T. J. H.; van Benthem, L. L.; Verbeek, M. G.; Schnell, B.; Smit, B. *Journal of Catalysis* **2003**, *214*, 88.

(10) Olson, D. H.; Camblor, M. A.; Villaescusa, L. A.; Kuehl, G. H. *Microporous and Mesoporous Materials* **2004**, *67*, 27.

(11) Grande, C. A.; Rodrigues, A. E. *Industrial & Engineering Chemistry Research* **2004**, *43*, 8057.

(12) Grande, C. A.; Rodrigues, A. E. *Industrial & Engineering Chemistry Research* **2005**, *44*, 8815.

(13) Barrett, P. A.; Boix, T.; Puche, M.; Olson, D. H.; Jordan, E.; Koller, H.; Camblor, M. A. *Chemical Communications* **2003**, 2114.

(14) Cheng, L. S.; Wilson, S. T.; U.S., Ed. 2001.

(15) Olson, D. H.; U.S., Ed. 2002.

(16) Padin, J.; Rege, S. U.; Yang, R. T.; Cheng, L. S. *Chemical Engineering Science* **2000**, *55*, 4525.

(17) Zhu, W.; Kapteijn, F.; Moulijn, J. A.; den Exter, M. C.; Jansen, J. C. *Langmuir* **2000**, *16*, 3322.

(18) Olson, D. H.; Yang, X. B.; Camblor, M. A. *Journal of Physical Chemistry B* **2004**, *108*, 11044.

(19) Yang, X. B.; Toby, B. H.; Camblor, M. A.; Lee, Y.; Olson, D. H. *Journal of Physical Chemistry B* **2005**, *109*, 7894.

(20) Boix, T. P., M.; Camblor, M. A., Corma, A. US, 2002; Vol. 6,471,939 B1

(21) Dokl, B. V. E. e. a. C. R. *Acad. Sci.* **1946**, *32*.

(22) Yang, X. B.; Camblor, M. A.; Lee, Y.; Liu, H. M.; Olson, D. H. *Journal of the American Chemical Society* **2004**, *126*, 10403.

(23) Bezus, A. G.; Kiselev, A. V.; Lopatkin, A. A.; Du, P. Q. *Journal of the Chemical Society-Faraday Transactions Ii* **1978**, *74*, 367.

(24) Leroy, F.; Rousseau, B.; Fuchs, A. H. *Physical Chemistry Chemical Physics* **2004**, *6*, 775.

(25) Vlugt, T. J. H.; Schenk, M. *Journal of Physical Chemistry B* **2002**, *106*, 12757.

(26) Beerdsen, E.; Dubbeldam, D.; Smit, B.; Vlugt, T. J. H.; Calero, S. *Journal of Physical Chemistry B* **2003**, *107*, 12088.

(27) Beerdsen, E.; Smit, B.; Calero, S. *Journal of Physical Chemistry B* **2002**, *106*, 10659.

(28) Garcia-Sanchez, A.; Ania, C. O.; Parra, J. B.; Dubbeldam, D.; Vlugt, T. J. H.; Krishna, R.; Calero, S. *J. Phys. Chem. C* **2009**, *113*, 8814.

(29) Castillo, J. M.; Vlugt, T. J. H.; Calero, S. *Journal of Physical Chemistry C* **2009**, *113*, 20869.

(30) Duren, T.; Snurr, R. Q. *Journal of Physical Chemistry B* **2004**, *108*, 15703.

(31) Dubbeldam, D.; Beerdsen, E.; Calero, S.; Smit, B. *Proceedings of the National Academy of Sciences of the United States of America* **2005**, *102*, 12317.

(32) Dubbeldam, D.; Beerdsen, E.; Calero, S.; Smit, B. *Journal of Physical Chemistry B* **2006**, *110*, 3164.
(33) Dubbeldam, D.; Calero, S.; Maesen, T. L. M.; Smit, B. *Phys Rev Lett* **2003**, *90*, 245901.
(34) Dubbeldam, D.; Calero, S.; Maesen, T. L. M.; Smit, B. *Angewandte Chemie-International Edition* **2003**, *42*, 3624.
(35) Ryckaert, J. P.; Bellemans, A. *Faraday Discussions* **1978**, *66*, 95.
(36) Wick, C. D.; Martin, M. G.; Siepmann, J. I. *Journal of Physical Chemistry B* **2000**, *104*, 8008.
(37) Dubbeldam, D.; Calero, S.; Vlugt, T. J. H.; Krishna, R.; Maesen, T. L. M.; Beerdsen, E.; Smit, B. *Physical Review Letters* **2004**, *93*.
(38) Dubbeldam, D.; Calero, S.; Vlugt, T. J. H.; Krishna, R.; Maesen, T. L. M.; Smit, B. *Journal of Physical Chemistry B* **2004**, *108*, 12301.
(39) Liu, B.; Smit, B.; Rey, F.; Valencia, S.; Calero, S. *Journal of Physical Chemistry C* **2008**, *112*, 2492.
(40) Chong, S. S.; Jobic, H.; Plazanet, M.; Sholl, D. S. *Chemical Physics Letters* **2005**, *408*, 157.
(41) Liu, B.; Smit, B.; Calero, S. *Journal of Physical Chemistry B* **2006**, *110*, 20166.
(42) Garcia-Perez, E.; Dubbeldam, D.; Maesen, T. L. M.; Calero, S. *Journal of Physical Chemistry B* **2006**, *110*, 23968.
(43) Allinger, N. L. *Journal of the American Chemical Society* **1977**, *99*, 8127.
(44) Allinger, N. L.; Yuh, Y. H.; Lii, J. H. *Journal of the American Chemical Society* **1989**, *111*, 8551.
(45) Williams, D. E. *Journal of Computational Chemistry* **1988**, *9*, 745.
(46) Frenkel, D.; Smit, B. *Understanding molecular simulation 2nd edition*; Academic Press: London, UK, 2002.
(47) Bourasseau, E.; Haboudou, M.; Boutin, A.; Fuchs, A. H. *Journal of Physics* **2003**, *118(7)*, 3020-3034.
(48) Pascual, P.; Ungerer, P.; Tavitian, B.; Pernot, P.; Boutin, A. *Physical Chemistry Chemical Physics* **2003**, *5*, 3684.
(49) Pascual, P.; Ungerer, P.; Tavitian, B.; Boutin, A. *Journal of Physical Chemistry B* **2004**, *108*, 393.
(50) Zicovich-Wilson, C. M.; San-Roman, M. L.; Camblor, M. A.; Pascale, F.; Durand-Niconoff, J. S. *Journal of the American Chemical Society* **2007**, *129*, 11512.

Ge-containing ITQ-29 shows a much higher molecular diffusivity than the isomorphous Si-ITQ-29. Is not possible to rationalize this behavior analyzing static structural features. A novel explanation is provided, based on the unexpected high framework flexibility arising from the presence of Ge atoms.

Juan José Gutiérrez-Sevillano, Sofía Calero, Said Hamad, Salvador Rodríguez Gómez Balestra, Ricardo Grau-Crespo, Fernando Rey, Susana Valencia, Miguel Palomino, and Ángel Rabdel Ruíz-Salvador

3 Enhanced Dynamic Flexibility in Ge Containing Zeolites: Impact on Diffusion

Introduction

Zeolites are nanoporous framework inorganic solids widely used in industry as catalysts, ion exchangers, adsorbents and molecular sieves.[1-3] Since the performance of these solids in industrial applications is closely related to their framework properties, during the last two decades, most attention has been focused on the discovery of new large pore frameworks.[4] Many efforts have also been devoted to the preparation of zeolites, both new and with known topologies, having only tetravalent atoms in the frameworks, due to their potential good performance in separation processes, such as those relevant in petrochemical and related industries.[5] It is worth noting that the inclusion of germanium in tetrahedral sites helps to achieve both goals.[6-8] According to the predictions of Brunner and Maier,[9] its role in the synthesis of large pore zeolites is related to the ability of the Ge atoms to promote the formation of small rings, particularly 3- and 4-member rings.[7,10-11] Indeed, both experimental and theoretical works have shown that Ge atoms preferentially locate in these small units, which has been interpreted as a consequence of the flexibility of the Ge atoms, which allows the stress to be released in these small units.[12-13] We must point out that the flexibility associated to the Ge atoms has been always linked to a static picture; i.e. the formation of otherwise strained bonds.

In this chapter, we show that the flexibility associated to the Ge atoms in zeolites also has a dynamic nature and that this feature accounts for the enhanced molecular diffusion observed in Ge-containing frameworks. Our study combines experimental and theoretical methods to provide not only experimental evidences, but also a rationalization based on an atomistic view of diffusion processes.

To address to this issue, we have selected isomorphous ITQ-29 zeolites, both pure silica and silicogermanate frameworks.[14]

Methods

The geometry relaxation of the structures were carried out with the Vienna Ab Initio Simulation Program (VASP).[17] We employed the Perdew-Burke-Ernzerhof (PBE) exchange-correlation functional.[20] For the *ab initio* Molecular Dynamics, VASP was also employed, using a time step of 0.5 fs and a simulation time of 5 ps. The adsorption isotherms and classical molecular dynamics simulations were modeled in full atomistic detail using calibrated classical force fields. Periodic boundary conditions are used to extrapolate the finite system results to macroscopic bulk values.

Results and Discussion

The aim of studying Ge-containing ITQ-29 zeolites (Ge-ITQ-29) was to improve the selectivity for the industrially relevant separation of propylene and propane. Since the crystallographic data indicate that the pore size of Ge-ITQ-29 is slightly smaller than that of the pure silica ITQ-29 (Si-ITQ-29), it was expected that if a diffusional restriction for propane to enter into the Ge-containing zeolite increases, a better separation factor for propane/propylene would be obtained.

The smaller pore size of Ge-ITQ-29 was confirmed by performing high-resolution Ar adsorption experiments for assessing the diameter of the micropore. This very small narrowing of the pore entrance by Ge incorporation in zeolite ITQ-29 was clearly evidenced by the small shift towards low pressure of the capillary condensation uptake in the Ar isotherm, compared to that of the pure silica material. This shift in the Ar adsorption uptake quotes for a reduction of 0.013 Å of the averaged micropore diameter in Ge-ITQ-29 compared to that of the pure silica. The pore reduction observed by Ar adsorption completely agrees with the corresponding refined structures obtaind with X-Ray diffraction patterns.

Surprisingly, the observed reduction of the pore entrance in Ge-ITQ-29 does not reduce the propane diffusion, quite the contrary, Ge-ITQ-29 shows a much faster propane uptake than Si-ITQ-29, while propylene diffusion rates remain nearly the same for both materials. Of course, the diffusion rate of propane strongly depends on the crystal size. We prepared two different Si-ITQ-29 frameworks, differing in the crystal size and both samples show a much slower diffusion of propane and nearly the same diffusion coefficient for propylene. While Ge-ITQ-29 has nearly the same diffusion parameters for propane and propylene, regardless of the crystal size. It could therefore be concluded that Ge-ITQ-29 allows a much faster entrance of propane than Si-ITQ-29 despite having a smaller crystallographic pore opening, which goes against to is normally observed.

Since ITQ-29 zeolites have only one tetrahedral site in the asymmetric unit

cell, it should not be expected a high degree of ordering upon Ge incorporation into the framework, as has been observed during heteroatoms incorporation in other zeolites with multiple tetrahedral atoms [15-16]. In order to select appropriate structural models with which to perform simulations of molecular adsorption and diffusion, we randomly selected 100 different Si-Ge configurations with a 2:1 ratio, and a wide range of Ge-Ge distances, including those having multiple Ge atoms condensed in the same double-4-member rings (D4R). The as-built structures were subject to full energy and cell relaxations by means of electronic structure calculations performed with the Viena Ab initio Software Package (VASP) [17]. In order to allow direct comparison with the simulated Ge-ITQ-29 zeolites, the Si-ITQ-29 framework was also subjected to the same structural relaxation procedure.

Upon energy minimization, the cell parameters of the relaxed configurations do not show significant differences among the different structures, which can be understood as an evidence of static flexibility of Ge atoms in adopting a range of local environments at low energetic cost, despite the fact that its inclusion distorts the T-O distances by about 10% (from ca. 1.605 Å to ca. 1.74 Å). In line with this, we selected five representative configurations of the whole range of structures, i.e. we order all configurations as a function of energy and chose the most stable one, and four more, with placed in positions 25, 50, 75 and 100 respectively.

Table 1. *Cell volume (Å^3), average T-O distances (Å), pore volume (Å^3) and surface area (Å^2) in modeled and experimental ITQ-29 zeolites.*

[a]	S0	S1	S2	S3	S4	S5
C. V.	1723	1783	1789	1781	1807	1803
T-O	1.62	1.67	1.67	1.67	1.67	1.67
P. V.	697.1	669.4	677.3	669.7	701.9	692.3
S. A.	212.1	215.6	216.4	218.5	219.7	216.2

	Exp.Si-ITQ-29	Exp.Ge-ITQ-29 (Si/Ge=2)
C.V	1668	1734
T-O	1.60	1.62
P.V	765	801
S.A	158	171

[a] C.V. cell volume, T-O mean T-O distances, P.V pore volume and S.A. surface area are given by unit cell. P.V and S.A in modeled zeolites are computed using He and N_2, respectively, as probe molecules.

They are labeled as S1 to S5, respectively. Analogously Si-ITQ-29 has been labeled as S0. The calculated average T-O distances of Ge-ITQ-29 are larger than those in Si-ITQ-29, in agreement with experimental results, as can be seen in Table 1. Consequently, the calculated cell volumes of Ge-ITQ-29 structures are larger than that of Si-ITQ-29, in agreement with the experimental results (Table 1). Note that the increase of the cell volume is not proportional to the cube of the increase of the T-O distances, due to the smaller T-O-T angles in presence of Ge atoms, a fact that allows absorbing local distortions

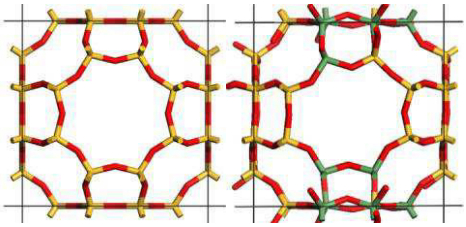

Figure 1. *Unit cell of modeled Si-ITQ-29 (left) and S1 Ge-ITQ-29 (right). Atom color labels: O red, Si yellow and Ge green.*

without larger distortions beyond the GeO_4 tetrahedra, as shown in Figure 1.

Since the pore volumes of Si- and Ge-ITQ-29 zeolites do not differ significantly, and the replacement of Si by Ge does not generate charge unbalance, being the O atoms those having the larger polarizability in both cases, it is expected that small molecules will be adsorbed with similar strength regardless of the presence or not of Ge atoms. This is what calculated and experimental adsorption heats reflect (see Table 2 for data related to propane). Taking into account exclusively a static picture, this adsorption behavior of isomorphous zeolites would suggest that the diffusion coefficient of these molecules in ITQ-29 materials would very similar. Moreover, as the pore volumes of modeled Ge-ITQ-29 are in most cases smaller than Si-ITQ-29, the confinement in the former zeolites is higher, and the geometric hindrance towards diffusion will be higher too, one would expect that the molecules diffuse slower in these solids comparing with their pure silica counterparts. However, the experimental results, as will be discussed below, point out to a noticeable enhanced diffusion in Ge-ITQ-29.

The above analysis based on static structures fails to predict the observed enhanced diffusion in Ge-ITQ-29. We will therefore focus on the dynamic features of the solids. First, we compare the intrinsic dynamics of the frameworks, i.e. without adsorbate molecules. For this end, we have chosen *ab initio* Molecular Dynamics simulations (AIMD), as implemented in VASP, which although computationally very expense, are able to provide a reliable image of the dynamical behavior at an atomic level, with an accurate description of framework deformations. Indeed, the movie obtained with the succesive configurations of the simulation of the Si-ITQ-29 structure reveals the typical behavior of most solids, with Si and O atoms vibrating within localized regions around their equilibrium positions. However, the behavior is starkly different in Ge-ITQ-29, since there are much larger deformations of the pores, exhibiting a breathing-like behavior. The movies created with the snapshots allow a simple visual comparison of the deformations of the different zeolites.

Table 2. *Adsorption heats (kJ/mol) of propane in modeled and experimental ITQ-29 zeolites*

[a]	S0	S1	S2	S3	S4	S5
A.H	22.1	20.9	20.7	20.9	20.8	20.9
	Exp.Si-ITQ-29			Exp.Ge-ITQ-29 (Si/Ge=2)		
A.H	21.2			27.4		

[a] A.H. adsorption heats.

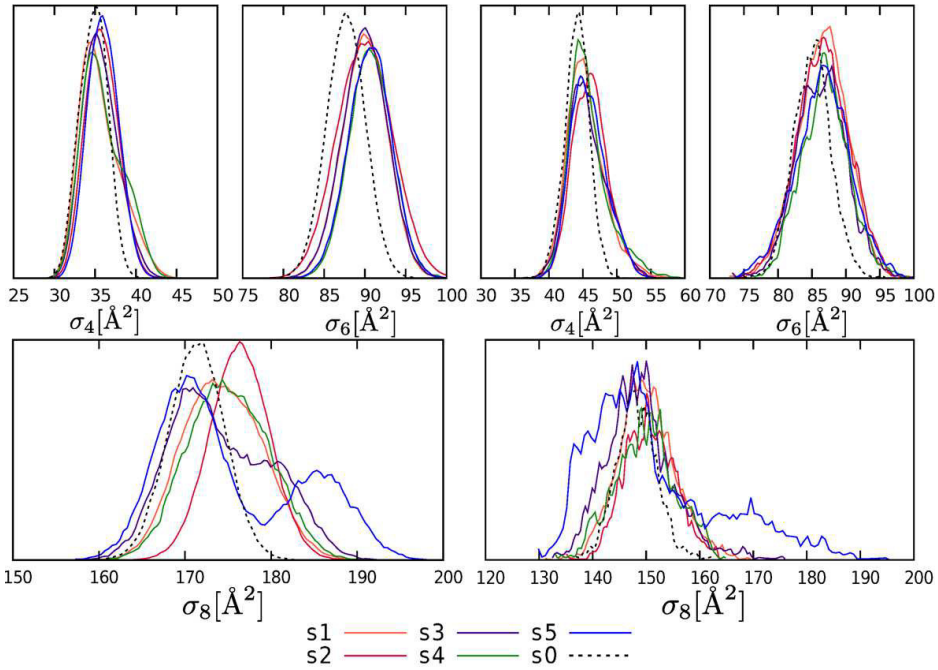

Figure 2. Distribution of the a*rea of the zeolites 4-, 6-, and 8-MR computed by CMD (left) and AIMD (rigth).*

In order to quantify the degree of flexibility we considered the 8-member rings (8MR) as ellipsoids and then computed for each time step the two ellipsoid diameters[18]. The most illustrative description in two dimensions of the dynamic flexibility of the zeolite rings is shown in Figure 2, where the distributions of areas of the 4-, 6- and 8-MR for the 6 structures (S0-S5) are shown. It is observed that the average values, as well as the width of the distribution, in Si-ITQ-29 are smaller than those corresponding to the Ge-containing structures. This is a clear evidence, directly obtained at an atomic level, that the presence of Ge atoms imposes a dynamic flexibility in the zeolite frameworks.

As to the the impact that this dynamic flexibility might exert on molecular diffusion, it is worth noting that there is a substantial amount of configurations where the pores of Ge-ITQ-29 zeolites are at least 0.2 Å wider than those in the pure silica one. This difference increases the probability for cage to cage crossings, since there is a large difference in the energy barrier for these intercage jumps. It is important to notice that this difference in diameter can act as control for a molecular sieving valve that could be relevant for separation processes.

Since the calculation of the diffusion coefficients requires large simulation times, AIMD is computationally

Table 3. *Calculated diffusion coefficient ($\cdot 10^{-8}$ m^2s^{-1}) of methane and propane in modeled ITQ-29 zeolites.*

	S0	S1	S2	S3	S4	S5
Modeled Rigid Framework[a]						
methane	0.464	0.194	0.209	0.280	0.221	0.237
propane	-	-	-	-	-	
Modeled Non-Rigid Framework[a]						
Mol.	**S0**	**S1**	**S2**	**S3**	**S4**	**S5**
methane	0.644	0.731	0.731	0.726	0.724	0.711
propane	0.042	0.047	0.054	0.058	0.096	0.043

[a] *modeled at 500 K.*

unaffordable and therefore we use classical molecular dynamics (CMD) to model methane, ethane and propane diffusion. Firstly, in order to ensure that the most important framework flexibility features are captured by the CMD, we conducted simulations with the empty frameworks, which allow us to compare the results with those obtained with the AIMD (Figure 2). We see that the main features are well reproduced by CMD.

It is known that computing the diffusion coefficient in pure silica zeolites using rigid framework models gives values that are much lower than those obtained for the same zeolite, but using framework models where framework atoms are allowed to move. In the case of the pure silica LTA zeolite, the diffusion coefficient is enlarged by 33 % when non-rigid frameworks are considered[19]. Besides simulations with non-rigid frameworks, we also performed simulations with rigid framework models, in order to assess how much the diffusion coefficients in Ge-ITQ-29 zeolites is improved, compared with the pure siliceous material.

The theoretically computed diffusion coefficients of small hydrocarbon molecules in ITQ-29 zeolites are presented in Table 3. In contrast to the experimental results showing higher diffusivity in Ge bearing ITQ-29, the modeled values using a static approach (rigid framework) do not show significant differences between the 6 structures, which confirms the failure of the framework static picture. On the other hand, the simulations carry out using non-rigid framework are in agreement with the experimental results, most notably for propane, which ratifies the role of Ge in imprinting dynamic flexibility to the framework.

Conclusions

We have shown, by combining experimental and theoretical tools, that the presence of Ge atoms in zeolite frameworks not only favours the formation of small rings, as it is well known, but also incorporates dynamic flexibility to the framework, which results in a breathing-like motion of the zeolites. This previously non-described finding has a direct impact on molecular diffusion, and in the case of the zeolite framework type LTA we observe a large enhancement of the diffusion, with an increase of the diffusion coefficient of at least by a factor of two. It is expected that this will open new avenues where the accelerated diffusion synergistically improves other properties of practical interest, like catalysis and adsorption. We also consider that this dynamic flexibility can be exploited for the

development on zeolites that act as molecular valves for selective separation of molecules of very similar structure. A further joint computational and experimental study will be carried out along these directions.

Bibliography

(1) *Introduction to zeolite science and pratice 3 Revised edition*; Cejka, J.; van Beekkum, H.; Corma, A.; Schuth, F., Eds.; Elsevier: Amsterdam, 2007; Vol. 168.

(2) Martinez, C.; Corma, A. *Coord. Chem. Rev.* **2011**, *255*, 1558.

(3) Corma, A. *J. Catal.* **2003**, *216*, 298.

(4) Jiang, J.; Yu, J.; Corma, A. *Angew. Chem. Int. Ed.* **2010**, *49*, 3120.

(5) Palomino, M.; Cantin, A.; Corma, A.; Leiva, S.; Rey, F.; Valencia, S. *Chem. Comm* **2007**, *12*, 1233.

(6) Corma, A.; Diaz-Cabanas, M. J.; Martinez-Triguero, J.; Rey, F.; Rius, J. *Nature* **2002**, *418*, 514.

(7) Corma, A.; Diaz-Cabanas, M. J.; Jorda, J. L.; Martinez, C.; Moliner, M. *Nature* **2006**, *443*, 842.

(8) Hernandez-Rodriguez, M.; Jordá , J. L.; Rey, F.; Corma, A. *J. Am. Chem. Soc.* **2012**, *134*, 13232.

(9) Brunner, G. O.; Meier, W. M. *Nature* **1989**, *337*, 146

(10) Jiang, J.; Jorda, J. L.; Diaz-Cabanas, M. J.; Yu, J.; Corma, A. *Angew. Chem. Int. Ed.* **2010**, *49*, 4986.

(11) Corma, A.; Navarro, M. T.; Rey, F.; Rius, J.; Valencia, S. *Angew. Chem. Int. Ed.* **2001**, *40*, 2277.

(12) Sastre, G.; Pulido, A.; Corma, A. *Microporous Mesoporous Mater.* **2005**, *82*, 159.

(13) Sastre, G.; Corma, A. *J. Phys. Chem. C* **2010**, *114*, 1667.

(14) Corma, A.; Rey, F.; Rius, J.; Sabater, M. J.; Valencia, S. *Nature* **2004**, *431*, 287.

(15) Han, O. H.; Kim, C. S.; Hong, S. B. *Angew. Chem.-Int. Edit.* **2002**, *41*, 469.

(16) Ruiz-Salvador, A. R.; Almora-Barrios, N.; Gomez, A.; Lewis, D. W. *Phys. Chem. Chem. Phys.* **2007**, *9*, 521.

(17) Kresse, G.; Furthmuller, J. *Phys. Rev. B* **1996**, *54*, 11169

(18) Parise, J. B.; Prince, E. *Mater. Res. Bull.* **1983**, *18*, 841

(19) Garcia-Sanchez, A.; Dubbeldam, D.; Calero, S. *J. Phys. Chem. C* **2010**, *114*, 15068.

(20) Perdew, J.; Burke, K.; Ernzerhof, M. *Phys. Rev. Lett.* **1996**, *77*, 3865.

Three new sets of interatomic potentials to model hydrogen sulphide (H_2S) have been fitted. One of them is a 3-sites potential (which we named 3S) and the other two are 5-sites potentials (which we named 5S and 5Sd). The molecular dipole of the 3S and 5S potentials is 1.43 D, which is the value usually employed for H_2S potentials, while the dipole of the 5Sd is the dipole measured experimentally for the H_2S molecule, circa 0.974 D. The interatomic potentials parameters were obtained by fitting the experimental vapor-liquid equilibrium, vapor pressure and liquid density curves. The potential parameters fitted so far for H_2S have been obtained applying long-range corrections to the Lennard-Jones energy. For that reason, when a cut and shift of the Lennard-Jones potentials is applied they do not yield the correct results. We employed a cut and shift of the Lennard-Jones potentials in the fitting procedure, which facilitates the use of the new potentials to model H_2S adsorption on systems such as Metal-Organic Frameworks (MOFs). We have employed the newly developed potentials to study the adsorption of H_2S on Cu-BTC, MIL-47 and IRMOF-1 and the results agree with the available electronic structures calculations. All calculations (both quantum and interatomic potential-based) predict that H_2S does not bind to the Cu atoms in Cu-BTC.

Juan José Gutiérrez-Sevillano, Ana Martín-Calvo, David Dubbeldam, Sofía Calero, and Said Hamad

4

Adsorption of Hydrogen Sulphide on Metal-Organics Frameworks

Introduction

Hydrogen sulphide (H_2S) is a gas with harmful effects on human health. The main anthropogenic sources of emissions of H_2S are chemical industries, biogas production plants, and water treatment plants. Even when present in small concentrations, H_2S can be detected by humans, so there are many efforts being made towards achieving methods of reducing as much as possible the amount of H_2S present in the gases that are emitted by water treatment plants. Currently the two most used methods for reducing the amounts of H_2S emitted are biological treatments and chemical scrubbing[1]. But there is an increasing body of research[3-11] devoted to investigate the ability of different

materials to adsorb H_2S. One set of studied materials is formed by Metal-Organic Frameworks[13-14] (MOFs), which have a wide range of properties in terms of adsorption, since they are structures with a variety of metal centres (Cu, Zn, Ti, etc), of pore sizes (large, medium or small) or even of framework flexibility [16-18]. In this study we will focus on the study of H_2S adsorption on three well known MOFs, namely Cu-BTC, MIL-47, and IRMOF-1[19-23] . The main problem when trying to model H_2S adsorption is that the choice of the interatomic potential parameters is of key importance. Despite the availability of a number of force field parameters[2,12,15,24-28], they are often quite complex and their performance in modeling adsorption has not been tested extensively so far.

One problem in which we are particularly interested is the adsorption of H_2S on Cu-BTC. There have been a number of experimental studies[9,29] which suggest that H_2S molecules adsorb preferentially on the metallic centres and subsequently induce the decomposition of the framework. Although it has also been observed that the presence of water is crucial to the adsorption of H_2S,[30] simulation studies employing any of the existing force fields predict a different pattern of adsorption when H_2S/H_2O mixtures are adsorbed in Cu-BTC. In a DFT study, Watanabe and Sholl[31] observed that the adsorption of H_2O molecules on the metal centres of Cu-BTC is energetically favored over the adsorption of H_2S molecules. Employing Monte Carlo simulations to study the adsorption of various molecules in Cu-BTC, Castillo *et al.*[32] found that water has a surprisingly large affinity for the metal centre compared to other that for molecules like carbon dioxide, nitrogen, oxygen or hydrocarbons. In a set of preliminary calculations that we performed, employing the Kristoff and Liszi[23] force field, we found that indeed water molecules bind preferentially on the Cu atoms, while H_2S molecules stay at the centre of the small cages of the structure. All these results obtained from simulation studies are in apparent contradiction with the experimental observations, or with the way in which the experimental data are interpreted We therefore set up to develop a new set of force field parameters in order to check whether a model that provides a dipole moment closer to the experimental one could predict an adsorption behavior more similar to the experimentally described. We have also studied the influence of the number of sites on the adsorption properties of H_2S, not only on Cu-BTC, but also on MIL-47 and IRMOF-1.

Achieving a realistic modeling of H_2S is a challenging task, which has been undertaken in several studies. In Table 1 we present all the sets of interatomic potentials parameters (or simply 'force field') which have been published so far, to the best of our knowledge. Each force field has been fitted to model a particular aspect of the behavior of H_2S. The first force field is that of Jorgensen[28], who introduced some changes into the OPLS[21] force field (Optimized Potentials for Liquid Simulations) to model a range of liquid sulphur compounds, H_2S among them. The force field is based upon a 3-site

model of the H_2S molecule, such as that shown in Figure 1a. Its main finding regarding H_2S is that there are no strong interactions between H_2S molecules. The dimerisation energy pair distribution has a broad peak centred roughly around -1.0 kcal/mol, so that if the dimerisation energy cut-off employed to define a hydrogen bond is a reasonable value such as -2.25 kcal/mol, 92 % of the molecules are monomers and the percentage of hydrogen bonded

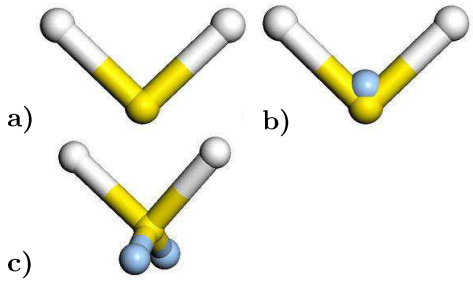

Figure 1. *The three types of models which are commonly used for H_2S: a) three-site (3S), b) four-site (4S), c) five-site (5S). Yellow and white balls represent sulphur and hydrogen atoms respectively. Blue balls represent dummy sites where charges can be included.*

molecules is only 8 % in the liquid phase. Jorgensen also calculated the radial distribution functions (RDFs) S-S and S-H, although at the time there were no experimental data for comparison.

As mentioned above, Jorgensen[28] employed a simple 3S model to describe the H_2S molecule, with a negative charge at the S atom and positive charge at the H atoms. A better description of the electrostatic potential around H_2S molecule could be achieved by increasing the complexity of the model, as it is usually done to simulate water molecules[32-33]. For instance, an additional charge can be placed on the C_2 axis of the molecule, at a distance δ from the sulphur atom, towards the hydrogen atoms, so that a 4S model is generated (see Figure 1b). Similarly to H_2O molecules, H_2S molecules have two pairs of non-bonding electrons in non-occupied sp^3 orbitals of the S atom, thus the S atom is surrounded by four pairs of electrons arranged in a tetrahedral manner. In order to model this charge distribution a 5S model (see Figure 1c) is often employed, which includes charges on the three atoms as well as in two additional sites placed above and below the C_2 axis, at a distance δ' from the sulphur atom.

Forester *et al.*[22] studied the three types of force fields for H_2S. The first one is the 3S force field developed by Jorgensen[28] with a slight change to the geometrical parameters. The second and third force fields are newly developed ones, with 4 and 5 sites respectively. All the parameters are shown in Table 1. They found that the 3S force field developed by Jorgensen[28] provide a poor description of H_2S dimers. The force field that best agreed with the experimental data was the one employing a 4S model of the molecule. They validated their force fields by comparing the simulated RDFs with the experimental RDFs obtained by Andriani *et al.*[34], who performed XRD measurements of liquid H_2S. The three force fields predicted the first peak of the S-S RDF to be shifted inwards, while the second peak is correctly positioned. They also compared their

simulation results with a range of dynamical properties of the liquid and high-temperature solid phases and found that the 4S force field was the one that yielded a better agreement with the experiments.

An important experimental set of data which was not included by Forester *et al.*[22] in the fitting of their interatomic potential parameters is the vapor-liquid equilibrium (VLE) curve of H_2S[35]. In a later study Kristoff and Liszi[23] employed a newly developed NpH Gibbs ensemble Monte Carlo simulation method[36] to carry out simulations of the coexistence of the liquid and vapor phases of H_2S with which to parameterize a new force field. They studied three different force fields. The first one is the 3S force field developed by Jorgensen[28]. The second one is 4S force field developed by Forester *et al.*[22] (although with small differences in the intramolecular geometry). The third one is a re-parameterization of the latter, with the aim of providing a better agreement between the simulated and experimental VLE curves. Their new 4S force field achieved this goal and it also increased the agreement between the simulated and experimental S-S RDFs. Since we

Table 1. *Interatomic potential parameters and most relevant geometric information of all the sets of potentials parameters developed scpecifically for H_2S. a) The Lennard-Jones centre is not the S atom, but a dummy site placed along the C_2 axis (which is the only rotation axis of the molecule) at a distance of 0.1254 Å from the S atoms towards the H atoms. δ is the distance, along the C_2 axis, between the sulphur atom and the additional charge. δ´ is the distance between the sulphur atom and the two additional charges, placed in a tetrahedral arrangement above and below the molecular plane.*

	sites	**ε/k_B (K) S**	**σ (Å) S**	**q_S (e^-)**	**q_H (e^-)**	**q_A (e^-)**	**δ' (Å)**	**δ (Å)**	**$d_{S\text{-}H}$ (Å)**	**H-S-H angle (º)**
Jorgersen *et al.*[28]	3	125	3.7	-0.47	0.235				1.34	92
Forester *et al.*[22]	3	125	3.7	-0.47	0.235				1.3322	92.1
	4	269	3.69	0.661	0.278	-1.217	0.1933		1.3322	92.1
	5	163	3.69	0.614	0.145	-0.452	-0.0377	0.719	1.3322	92.1
Kristoff and Liszi[23]	4	269	3.69	0.661	0.278	-1.217	0.1933		1.34	92
	4	250	3.73	0.4	0.25	-0.9	0.1862		1.34	92
Kamath *et al.*[26]	3	278	3.71	-0.252	0.126				1.34	92.5
	3	252	3.72	-0.338	0.169				1.34	92.5
	3	232	3.72	-0.380	0.19				1.34	92.5
	3	219	3.72	-0.4	0.2				1.34	92.5
Delhommelle *et al.*[24]	5	230[a]	3.74[a]	1.393	0.323	-2.039	0.1933			

will refer often to the later 4S force field we will call it KL force field.

The force fields described so far include the polarizability of the H_2S molecule implicitly, through the presence of a permanent dipole due to the point charges distribution. There have been efforts to develop H_2S models which take into account the polarizability, for example by using isotropic multipolar models[37] or Stockmayer potential models[25]. But these models perform marginally better, if at all, than simpler models, and their higher complexity limits their applicability, since these models are not implemented in all molecular simulation codes, are somewhat difficult to implement and introduce new problems regarding the combination rules. With the aim of including an explicit description of the polarizability of the H_2S molecule, Delhommelle *et al.*[10] developed a new 5S force field, in which the atomic centres beared no Lennard-Jones interactions. A large negative charge was placed at an additional site a small distance from the S atom along the C_2 axis. The Lennard-Jones centre was placed at an additional polarizable, chargeless site located at a small distance along that axis. However, this additional complexity of the model does not bring a significant increase of the accuracy of the simulations of pure H_2S phases, since the VLE curves are already well reproduced by the simpler force field developed by Kristoff and Liszi.[23] They found that it is important to consider explicitly the polarizability of H_2S in order to obtain the correct mixing behavior of mixtures of species with very different dipoles, such as H_2S/n-pentane. But this was refuted by Kamath *et al.*[26], who developed four simpler 3S force fields to model H_2S/n-pentane mixtures. They studied the influence of the atomic charges on the liquid phase behavior of H_2S, by studying four different charges for the S atom, namely -0.252 e^-, -0.338 e^-, -0.380 e^- and -0.400 e^-. The Lennard-Jones parameters were accordingly refitted to obtain a good description of the VLE curves. The RDFs and the liquid phase properties are well described by all parameters sets, although H_2S/n-pentane mixtures are better described by the two models with higher charges (charges of -0.380 e^- and -0.400 e^- for the S atoms). They stated that it is therefore possible to reproduce the phase behavior of complex mixtures including polar and non-polar components without recurring to use very complex models for the molecules; a careful fitting of the charges and Lennard-Jones potential parameters is enough in the case of H_2S/n-pentane mixtures. In a recent article Hellman *et al.*[27] developed a new force field, by fitting the interatomic potential parameters in order to reproduce a six-dimensional potential energy hypersurface for two rigid H_2S molecules calculated with high level CCSD(T)/aug-cc-pV(Q+d)Z calculations. The force field provides very good predictions of the second pressure virial coefficient, shear viscosity and thermal conductivity, with results that are within the experimental error bars. This force field, however, is also a very complex one, since the functional form of the energy includes two damping functions and it makes use of 11 sites per molecule, with a total number of

site-site interaction parameters of 140. It is therefore very complex to use this force field to study the interaction of H_2S with other molecules.

Although all the force fields mentioned above provide an accurate description of liquid and gas phases of H_2S, they predict a weak interaction between H_2S molecules and Cu atoms of the Cu-BTC framework, which contradicts previous experimental observations. We therefore set to develop three new force fields with different number of interaction sites and dipole moments, in order to check whether they still predict the same adsorption patterns. In the present article we have studied the influence of the number of sites on the adsorption properties of H_2S in Metal-Organic Frameworks, and we have developed new simple force fields able to provide a good description of the VLE curves. We also study the performance of these new force fields when describing the adsorption in the Metal-Organic Frameworks Cu-BTC, MIL-47, and IRMOF-1.

Computational Details

The adsorption isotherms were computed using Monte Carlo (MC) simulations in the μVT ensemble, where the chemical potential, volume and temperature were kept fixed. The MC moves were performed in cycles and in each cycle one of the following trial moves was selected at random for a given molecule: translation, rotation, reinsertion at a random position, insertion and deletion. Coulombic interactions were computed using the Ewald summation.

We studied the adsorption of H_2S in Cu-BTC, IRMOF-1, and MIL-47 frameworks. The structures were modeled as rigid networks and the positions of the atoms were taken from Chui *et al.*[17](Cu-BTC), Eddaoudi *et al.*[38](IRMOF-1) and Barthelet *et al.*[20](MIL-47). The Lennard-Jones parameters for the structures were taken from the DREIDING[39] force field except those for Cu, V, and Cr, which were taken from the UFF[40] force field. We used Lorentz-Berthelot mixing rules to calculate mixed Lennard-Jones parameters. Atomic charges were taken from Frost and Snurr[41] and Dubbeldam *et al.*[42] for IRMOF-1, Castillo *et al.*[32] for Cu-BTC and from Bueno-Perez *et al.*[43] for MIL-47. Detailed information about the materials can be found elsewhere[43-47].

The vapor-liquid equilibrium and vapor pressure curves are calculated by means of Monte Carlo simulations in the Gibbs ensemble[48]. Gibbs ensemble simulations are performed in two microscopic regions within the bulk phases, away from the interface. Each region is simulated within standard periodic boundary with a unit cell of 30x30x30 $Å^3$. The thermodynamic requirements for phase coexistence are that each region should be in internal equilibrium, and that the temperature, pressure, and chemical potentials of all components should be the same in the two regions. In order to achieve that we performed three types of Monte Carlo "moves", displacements of particles within each region (to satisfy internal equilibrium), fluctuations in the volume of the two regions (to satisfy equality of pressures) and transfers of particles between regions (to satisfy the equality of

chemical potentials of all components). These moves were performed in cycles selecting one random move for each molecule in each cycle. The temperature, total number of particles, and total volume employed in the MC simulations were specified in advance and kept constant during the simulations. The simulations consisted on 10^5 production cycles and $5 \cdot 10^4$ equilibration cycles. 166 H_2S molecules were placed initially in each box to reproduce the experimental critical density of H_2S.

Classical MC simulations in the μVT and Gibbs ensembles were performed using the RASPA code[49]. This code developed by D. Dubbeldam, S. Calero, D. E. Ellis and R.Q. Snurr has been employed in several studies of gas adsorption[50-52].

The electronic structure calculations were performed at DFT level, using the Gaussian09 code[53]. In order to take into account the presence of open metal centres and non covalent interactions at a reasonable computational cost we made use of Density Functional Theory calculations, with the hybrid meta exchange-correlation functional M06-2X, developed by Zhao and Truhlar.[54] which has been proven to provide reliable results for this type of systems at a reasonable computational cost.[55-56] The metal atoms were modeled with the Stuttgart/Dresden effective core potentials[57] and basis set, with 10 core electrons, while the 6-31++G** basis set for the rest of the atoms. The counterpoise method[58] was employed to reduce the basis set superposition error. In order to keep the cluster models as realistic models of the systems, we carried out the energy optimizations allowing the adsorbate molecules to relax, but keeping the atoms of the framework fixed at their experimental positions.

Results and discussion

A. Fitting of the new parameters to model experimental data. We have employed the experimental[59] data

Table 2. *Interatomic potential parameters and values of the most relevant geometric information of the three H_2S force fields developed in this study, as well as the other two existing force fields also employed. a) This force field has been fitted to model correctly the 0.974 D dipole of the H_2S molecule. b) This force field is the 4S force field developed by Kristoff and Liszi[23]. c) This force field is the flexible 3S force field developed by Kamath et al.[26]*

	sites	ε/k_B (K) S	σ (Å) S	q_S (e^-)	q_H (e^-)	q_A (e^-)	δ (Å)	$d_{S\text{-}H}$ (Å)	H-S-H angle (º)
3S	3	275	3.7	-0.32	0.16			1.34	92
5S	5	295	3.75	0.0	0.152	-0.152	0.3	1.34	92
5Sd[a]	5	310	3.71	0.0	0.1027	-0.1027	0.3	1.34	92
KL[b]	4	250	3.73	0.4	0.25	-0.9	0.1862	1.34	92
Kamath[c]	3	232	3.72	-0.38	0.19			1.34	92.5

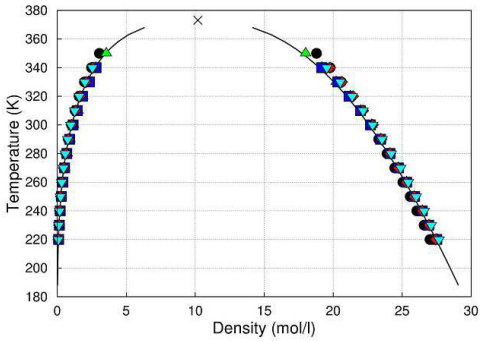

Figure 2. *Comparison between the VLE experimental[59] curve (line) and those obtained with the three newly developed force fields, 3S (upwards pointing triangles), 5S (squares) and 5Sd (circles), and the force fields developed by Kristoff and Liszi[23](diamonds) and Kamath et al[26](downwards pointing triangles). The cross represents the critical point predicted from the experimental data.*

of the VLE curve to fit the interatomic potential parameters of the three new force fields. The first one is a 3-site force field, which we name as 3S. The second one is a 5-site force field which we name as 5S. Since one of the aims of this article is to study the influence of the number of sites on the adsorption properties, we kept the same dipole of the H_2S molecule in these two force fields. In order to compare with the force field developed by Kristoff and Liszi[23] (which we will refer to as KL), we have chosen the point charges in such a way that the dipole in the two new force fields is the same dipole than that of the KL force field, namely 1.43 D. This value is higher than the experimental value, which is 0.974 D[60-61]. The third force field we have developed is a 5-site potential with the correct value of the dipole moment. We will name this force field as 5Sd. For the sake of comparison, we have also calculated the VLE curve employing the Kamath *et al.*[26] force field (which we will refer to as Kamath). All parameters are listed in Table 2.

The VLE curves obtained with the 3S, 5S and 5Sd force fields are shown in Figure 2 where the experimental curve and those predicted by the KL and Kamath force fields are also shown.

The three new force fields give an excellent agreement with the experimental curve, as is also the case of the previous ones, the KL and Kamath force fields. It is important to note that the newly developed force fields do not employ long-range corrections[62], while they are employed in the previous ones. It has been suggested that simulations in which the Lennard-Jones potentials are cut and shifted could provide better results when modeling adsorption on crystalline confined systems than simulations in which conventional long-range corrections[63] are applied. Although long-range corrections can indeed be employed to model accurately adsorption on crystalline confined systems[64]. All the force fields to model H_2S that have been published so far employ long-range corrections to the Lennard-Jones interaction. In order to provide the possibility to choose, we developed the new force fields employing a cut and shift of the Lennard-Jones potentials from 12 Å.

We obtained the parameters at the critical point, employing the density scaling law (1) and the law of rectilinear diameters[65-68] (2):

$$\rho_{liq} - \rho_{vap} = B \cdot (T - T_C)^{\beta} \quad (1)$$

$$(\rho_{liq} + \rho_{vap}) / 2 = \rho_C + A \cdot (T - T_C) \quad (2)$$

Due to the nature of these equations, the values of the critical temperature, density and pressure are very sensitive to the value of the β parameter employed. In Table 3 we show the critical parameters obtained with different values of the β parameter, 0.325 (the value employed by Kamath *et al.*[26]), 0.315 (the value employed by Kristóf and Liszi[23]) and the value obtained by letting the β parameter vary in the fitting procedure. Given the large errors involved in this type of calculations, all force fields predict the critical parameters with a reasonable degree of accuracy.

Table 3. *Critical parameters obtained with experiment as with the KL, Kamath, 3S, 5S, and 5Sd force fields. The parameters were predicted using the density scaling law and the law of rectilinear diameters.*

	Temp. (K)	Density (mol/l)	Press. (MPa)	Beta
Exp.	373.10	10.19	9.00	
KL	378.07	10.279	8.794	0.325
	375.42	10.337	8.624	0.315
	374.91	10.348	8.557	0.313
Kamath	375.78	10.169	8.858	0.325
	373.24	10.229	8.503	0.315
	371.2	10.278	8.227	0.307
3S	381.62	10.242	9.347	0.325
	379.13	10.293	9.017	0.315
	376.14	10.354	8.632	0.303
5S	371.6	10.285	8.919	0.325
	369.45	10.333	8.63	0.315
	367.2	10.387	8.319	0.304
5Sd	371.83	10.829	9.601	0.325
	369.42	10.344	9.237	0.315
	366.33	10.415	8.783	0.302

We can get a further insight into the performance of the different force fields by analyzing the vapor pressure curve. Employing the interatomic parameters developed from the fitting of the VLE curve (which are shown in Table 1) we obtain the correct dependence of the vapor pressure *versus* temperature for all force fields studied, as can be seen in Figure 3a. The deviation from the experimental data at low temperatures could also be analyzed by examining the plot of log P *versus* 1/T (see Figure 3b).

The best results at lower temperatures are obtained with the KL force field, while the Kamath force field is the one that provides results further away from the experimental data. But the differences between all the force fields are not significant. In order to get a deeper insight into how each of the force fields performs in the whole range of temperature we also plot, in Figure 3c, the absolute error between the calculated and experimental values of adsorption. We can see that the smaller error is obtained with the 3S and 5S force fields, followed by 5Sd and KL, which are very close to each other, while the Kamath force field provides the largest errors. But again, the errors are all relatively small (typically less than 10%), so the comparison between the

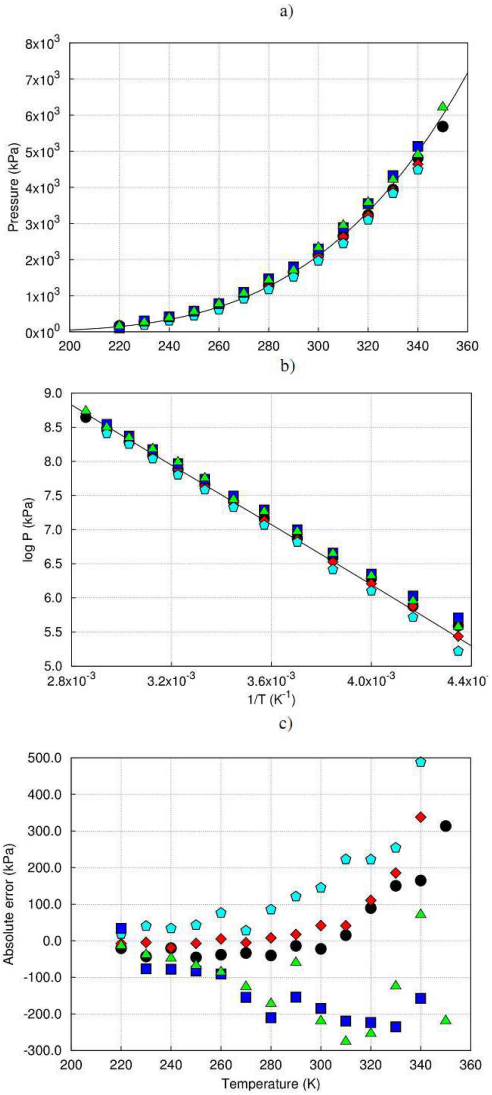

different force fields and the experimental data shown in the previous figures cannot be employed to assess which of them can model the system in a more realistic manner.

Further information about the performance of the different force fields can be obtained from the analysis of the heats of vaporization (see Table 4). The experimental[69] heats of vaporization at 212.77 K and 760 mmHg is 18.67 kJ/mol. The force fields that best reproduce this value are 3S and Kamath, followed closely by 5S. Lower values are predicted by the KL force field (17.33 kJ/mol), while the 5Sd force field predicts a much lower value, around 15.95 kJ/mol). The fact that the 5Sd force field predicts a lower value of heat of vaporization than the rest of the force fields is not surprising, since its dipole moment is almost 50 % lower, which decreases significantly the intermolecular interactions. This is in line with what it is observed in other polar molecules, such as water, for which the models usually have dipoles higher than the experimental ones in order to model both gas and liquid properties.

Figure 3. *a) Experimental[59] vapor pressure curve of H_2S versus temperature (line), compared with the simulated curves obtained with the three newly developed force fields, 3S (upwards pointing triangles), 5S (squares) and 5Sd (circles), and the force fields developed by Kristoff and Liszi[23] (diamonds) and Kamath et al[26] (pentagons). The same symbols are employed in b) and c). Error bars are not shown, because they would lie within the symbols used to represent the data. b) Logarithm of the vapor pressure versus 1/T for the experiment and for the same force fields shown in a). c) Absolute error (respect to the experimental values) of the vapor pressure versus temperature, for the same force fields shown in a). The absolute error is defined as the experimental pressure minus the calculated pressure.*

Table 4. *Heats of vaporization of H_2S, at 212.77 K and 760 mmHg, calculated with the 3S, KL,[23] Kamath,[26] 5S, and 5Sd force fields. The experimental value is also shown.[69]*

	Heat of vaporization (kJ/mol)
Experiment	18.67
3S	18.68
KL	17.33
Kamath	18.58
5S	18.99
5Sd	15.93

Another property that can help assessing how the force fields perform is the variation of the liquid density with the temperature. We therefore calculated the liquid density that each of them predicts for different temperatures (see Figure 4), and we find that the 5S and 5Sd force fields are the ones that show the best agreement with the experimental data, followed by the KL and Kamath force fields, and finally the 3S.

We see that none of the force fields outperforms the rest consistently; i. e. the force field that best models some property can also predict another property with the largest error.

In order to investigate the ability of the potentials to model the interaction between H_2S molecules, we can make use of a set of very precise and time consuming *ab initio* calculations of H_2S dimers carried out by Hellman *et al.*[27] They calculated the dimerisation energy using 16 different dimer structures, the most stable of which is a dimer structure similar to that of most stable

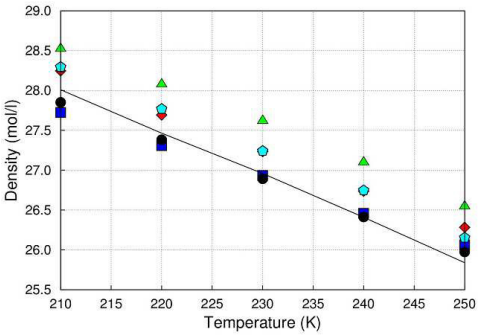

Figure 4. *Variation of the liquid densities of H_2S (at 0.5 MPa) as a function of temperature. The experimental data[59] (line) are compared with the liquid densities obtained with the three newly developed force fields, 3S (upwards pointing triangles), 5S (squares) and 5Sd (circles), and the force field developed by Kristoff and Liszi[23] (diamonds) and Kamath et al[26] (pentagons).*

water dimer. Its dimerisation energy is -6.6 kJ/mol, which is higher than the value of -2.97 kJ/mol obtained in previous[70] *ab initio* studies. It is worth noting that the potential energy surface has a very shallow minimum, which suggests that it is quite easy for the H_2S molecules of the dimer to stay far from the minimum, i.e. there will not be a significant energy penalty to separate the molecules from the equilibrium distance. If we take into account the fact that the thermal energy at room temperature is of the order of 2.5 kJ/mol, the electronic structure calculations suggest that H_2S has a very low tendency to form clusters. The S-S distance at which the dimer energy is found is circa 4.1 Å, thus the S-S radial distribution function (RDF) of any simulation of H_2S molecules should present a broad first peak around that

distance. And that is indeed what the interatomic potential-based simulations show. In Figure 5 we report the calculated S-S and S-H RDFs. There are no experimental data to compare the S-S RDF, so in Figure 5 we can only show the comparison between the S-S RDF (at 212.9 K and 1 bar) calculated by Kamath *et al.*[26] and the one calculated with the 5Sd force field.

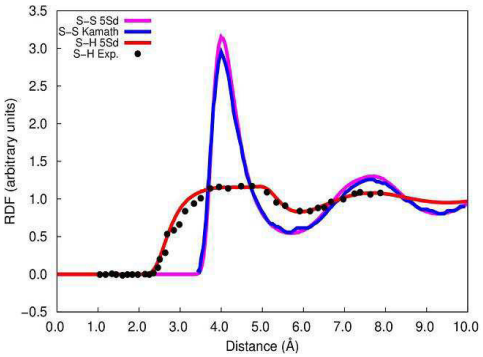

Figure 5. *S-S and S-H radial distribution functions, at 212.9 K and 1 bar. Experimental values are taken from Andreani et al.[71] The values denoted as Kamath are taken from Kamath et al.[26]*

Despite being developed with different number of interaction sites, both force fields predict very similar RDFs, which suggests that the VLE curves of H_2S can only be predicted accurately if the S-S interatomic distances vary around 4.1 Å. Regarding S-H distances, since there is no formation of H-bond, there should not be a narrow peak. In fact, this feature can be seen in the experimental S-H RDF (at 212.9 K and 1 bar) shown in Figure 5, in which there is a broad peak around between radial distances of 3 Å and 5 Å. The Kamath force field was shown[26] to reproduce very well the experimental S-H RDF and that is also the case of the three newly developed force fields. For clarity reasons only the 5Sd S-H RDF is shown in Figure 5, although those of 3S and 5S are very close, they would lie within the symbols employed to represent them. There is a very good agreement between simulated (with both the Kamath and 5Sd force fields) and experimental S-H RDFs, which suggests that the underlying physics of the intermolecular interactions are described correctly by the force fields employed.

B. Modeling of the adsorption properties of H_2S on three materials. The potential parameters which we have developed allow us to calculate the adsorption energies of H_2S on any porous materials for which we already know the Lennard-Jones parameters that best model them. To calculate the potential parameters for the guest-host interactions we make use of the Lorentz-Berthelot mixing rules. To investigate the influence of the H_2S potential parameters on the adsorption properties we studied the adsorption of H_2S on Cu-BTC, MIL-47, and IRMOF-1. Figure 6 shows the isosteric heats of adsorption obtained with the four sets of potential parameters.

For all materials, the 4S potential predicts slightly lower heats of adsorption than the 3S potential, while the 5S potential predicts consistently higher values of heats of adsorption. The material for which the heat of adsorption is higher is Cu-BTC, since the molecule confines better in the tetrahedral-shaped pockets of this structure than in the wider pores of MIL-47 and IRMOF-1. The three potentials predict heats of adsorption

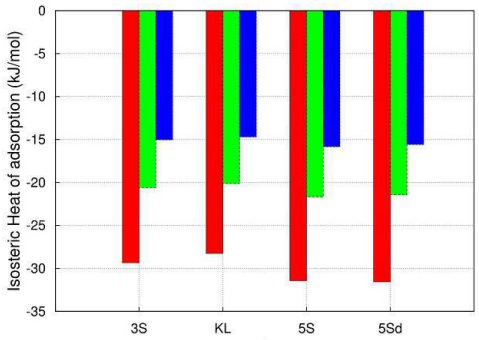

Figure 6. *Isosteric heats of adsorption of H_2S adsorbed on three different MOFs, employing the three potential parameters fitted in our study, as well as the KL force field. Red: Cu-BTC. Green: MIL-47. Blue: IRMOF-1.*

ranging from -25 kJ/mol to -32 kJ/mol. In the case of MIL-47 the values range between -18 kJ/mol and -19 kJ/mol. And the lowest heats of adsorption correspond to IRMOF-1, for which the predicted values vary from -13 kJ/mol to -14 kJ/mol. This behavior can be readily understood by considering the respective values of the interaction parameters shown in Table 2. The values of the σ parameters are almost the same in the four force fields, but the values of the ε do vary significantly, following the order KL < 3S < 5S < 5Sd. And this is indeed the ordering that we observe for the values of the heats of adsorption. There is only a slight change in this trend for 5S and 5Sd, since the former has a smaller value of the ε parameter but it predicts a larger value of the heat of adsorption than 5Sd. This difference of the ε parameter is compensated by the difference of molecular dipole, which is 50 % larger for 5S than for 5Sd.

Table 5. *Energies of adsorption of H_2S and H_2O on the three cluster models of Cu-BTC, MIL-47 and IRMOF-1 shown in Figure 7. The energies are BSSE-corrected and they are calculated with DFT, using the M06-2X exchange-correlation functional.*[54]

	Adsorption energy (kJ/mol)	
	H_2S	**H_2O**
Cu-BTC	-43.4	-46.7
MIL-47	-33.9	-41.0
IRMOF-1	-16.7	-22.5

There is no experimental data available for comparison, but, since the three potentials predict similar values of heats of adsorption, it would not be possible to rule out the capability of any of them to model the system correctly, based only on this property. Due to this lack of experimental data, we carried out electronic structure calculations, which provide independent information with which we could compare the heats of adsorption of H_2S. Watanabe and Scholl carried out a periodic DFT study[31] (using the PW91 exchange-correlation functional[71] with an energy cutoff of 500 eV) of H_2O and H_2S adsorption on Cu-BTC. They found that the adsorption energy of a H_2O molecule is -41.0 kJ/mol, while that of a H_2S molecule is -31.2 kJ/mol. We have carried out DFT calculations on the cluster models of the systems shown in Figure 7, employing the M06-2X functional mentioned in the compu-tational details. The BSSE-corrected energies of adsorption of H_2S and H_2O on the three materials are shown in Table 5. We have obtained values of adsorption energies for

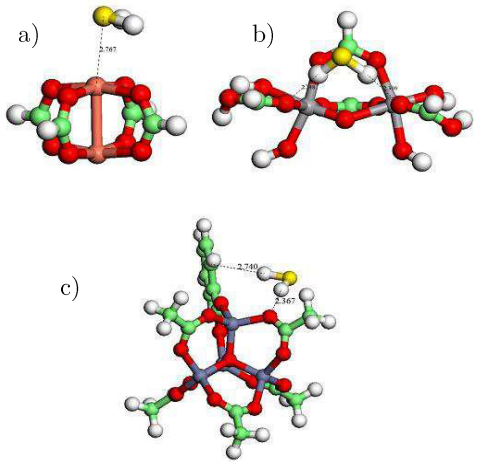

Figure 7. *Minimum energy configurations of H_2S adsorbed on three clusters models of (a) Cu-BTC, (b) MIL-47, and (c) IRMOF-1. The energy minimizations were carried out with DFT calculations, employing the M06-2X exchange correlation functional. The cluster models of the surfaces are kept fixed during the minimizations.*

H_2O and H_2S of -46.7 kJ/mol and -43.4 kJ/mol respecttively, which are higher than the energies obtained by Watanabe and Scholl[31]. This is not surprising, since the PW91 functional was not developed to include accurately the non covalent interactions that are important in this system.

Grajciar *et al.*[72] employed very accurate CCSD(T)/CBS calculations (on the same cluster model we have studied) and obtained an energy of adsorption of -52 kJ/mol for H_2O molecules on Cu-BTC. This value of adsorption energy is close to that predicted by our calculations, -46.7 kJ/mol, suggesting that the M06-2X calculations accurate enough to provide reliable predictions of adsorption energies, at a fraction of the cost of CCSD(T)/CBS calculations. The adsorption energy predicted by the DFT calculations for the H_2S molecule is -43.4 kJ/mol, which is higher than values of heats of adsorption obtained from the Monte Carlo simulations (between -25 kJ/mol and -32 kJ/mol). This suggest that the force fields 5S and 5Sd give the best description of the adsorption energy in Cu-BTC, followed by 3S, with KL giving the lower adsorption energy.

For IRMOF-1 all the force fields predict similar values of isosteric heat of adsorption, around -15 kJ/mol, which is very close to the adsorption energy of -16.7 kJ/mol obtained with the DFT calculations. Something similar occurs in the case of the adsorption in MIL-47, for which there are experimental data to compare with. Hamon *et al.*[15] found experimental values of adsorption energy for MIL-47 from -27 kJ/mol to -29 kJ/mol. But all the force fields studied predict this energy to be between -20 kJ/mol (for KL) and -22 kJ/mol (for 5S). Our DFT calculations predict an adsorption energy of -33.9 kJ/mol, which is slightly closer to the experimental values. It is puzzling to find that all the force fields predict similar values of adsorption energy for each of the three materials studied, independently of how their parameters where fitted. At first sight it would be easy to assign the origin of this fact to the only common value in all the force fields, which is the σ parameter (it has a value that only varies from 3.70 Å to 3.75 Å among all the force fields). But this assumption does not hold true, since we performed a study of the variation of the adsorption energy of

H_2S in IRMOF-1 when the σ parameter was changed 8 % and when the ε parameter was changed also 8 %, and the results suggest that both parameters are equally important, causing a change of the adsorption energy of circa 5 % and 8 % for the ε and σ parameters respectively.

We could therefore conclude that out of the three potential parameters we have developed for H_2S, 3S, 5S, and 5Sd (which predict higher adsorption energies) are the ones that predict values of the adsorption energies in closer agreement with the DFT data, although the energy differences are so small that it is not possible to rule out the validity of any of the force fields.

As to the distance at which the H_2S molecule is predicted to stay from the framework, the DFT calculations do have a minimum energy configuration when the S atom of the H_2S molecule is at 2.6 Å from the Cu atom of the Cu-BTC framework. Since the DFT calculations do not include neither thermal effects nor the effects of H_2S-H_2S interactions, the S-Cu distance predicted with them is expected to be shorter than that predicted with Monte Carlo simulations, which is around 3.1 Å, as can be seen in Figure 8a, where for clarity reasons only the results for KL and 5Sd are shown, although the other force fields predict similar RDFs.

It was previously observed[15] that the presence of the MIL-47 framework influences the interatomic interactions, so that the S-H RDF of liquid H_2S is very different to that obtained when H_2S is adsorbed. Figure 8b shows

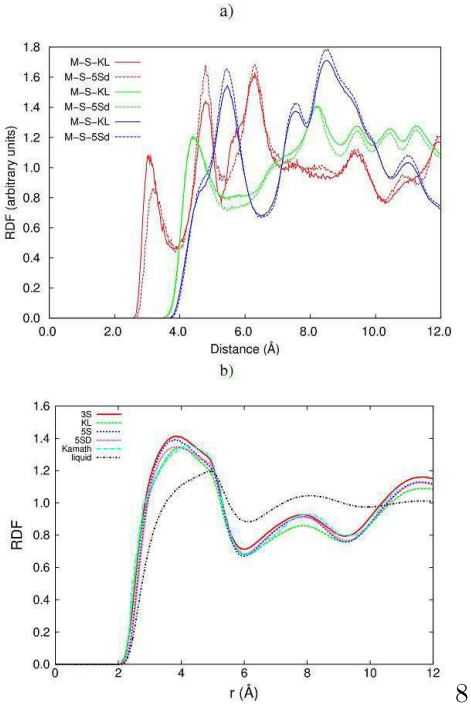

8

Figure 8. *a) Calculated M-S radial distribution functions at 303 K, where M is the metal atom of the framework: Cu in Cu-BTC (red), Zn in IRMOF-1 (green), and V in MIL-47 (blue). b) H(H_2S)-S(H_2S) RDFs of H_2S adsorbed in MIL-47, calculated with the 3S, 5S, 5Sd, KL, and Kamath force fields, at 1 bar and 303 K. The results for the Kamath force field are taken from Hamon et al.[15] The RDF in the liquid phase is also shown here for comparison.*

that is also observed when the new force fields are employed. The confinement makes the first S-H peak to grow and displace towards a shorter distance.

Another factor that provides valuable information regarding the adsorption behavior is the Henry coefficient, which is defined as $k_H=C/P$, where P is the pressure of the system and C is the H_2S

loading. The values of the Henry coefficients obtained from our simulations are shown in the top panel of Figure 9. As in the case of the heats of adsorption, the 5S and 5Sd potentials predict higher values of the Henry coefficients than the other force fields, for the same reason that mentioned when discussing the heats of adsorption. As to the dependence of the Henry coefficients with the type of material, it can be explained by analyzing the different sites in which the H_2S molecules are adsorbed for each material. Cu-BTC adsorbs H_2S molecules preferentially confining them inside small cages (see the bottom panel of Figure 9), which increases the value of k_H. MIL-47 has some kinks in the structure, where H_2S molecules are adsorbed, while IRMOF-1 has large cages where the H_2S molecules are adsorbed, thus inducing lower values of k_H than the other two structures.

There is only one experimental value of k_H for any of the three materials studied, which was obtained by Hamon *et al.*[15] for MIL-47. They obtained two values of k_H, one corresponding to a linear region at pressures below 25 kPa ($0.47 \cdot 10^{-4}$ mol $\cdot$ kg^{-1} $\cdot$ Pa^{-1}), and another one corresponding to a linear region at pressures between 25 and 30 kPa ($0.81 \cdot 10^{-4}$ mol $\cdot$ kg^{-1} $\cdot$ Pa^{-1}). The KL force field predicts a value of k_H ($0.49 \cdot 10^{-4}$ mol $\cdot$ kg^{-1} $\cdot$ Pa^{-1}) which is very close to the experimental one at low pressures. The value predicted by the 3S force fields is slightly higher ($0.60 \cdot 10^{-4}$ mol $\cdot$ kg^{-1} $\cdot$ Pa^{-1}), while those predicted by the two five-sites force fields are much higher (around $0.90 \cdot 10^{-4}$ mol $\cdot$ kg^{-1} $\cdot$ Pa^{-1}).

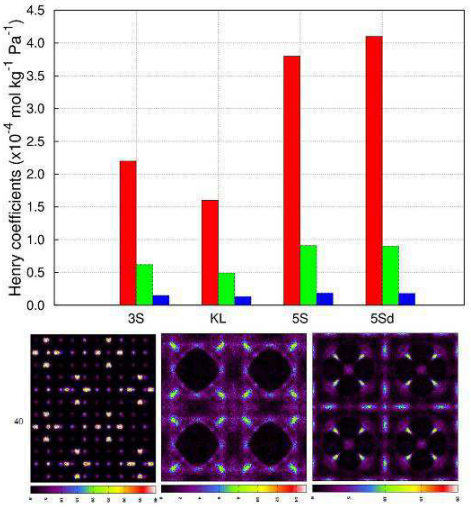

Figure 9. *Top panel: Henry coefficients of H_2S for three different materials at 298 K, employing the KL, 3S, 5S and 5Sd potential parameters. Red: Cu-BTC. Green: MIL-47. Blue: IRMOF-1. Bottom panel: Average occupation profiles of the H_2S centre of mass (at 100 kPa) on Cu-BTC, IRMOF-1, and MIL-47, using the 5Sd force field.*

The analysis of the Henry coefficients seems to suggest that the KL force field could provide a better description of the adsorption of H_2S in MIL-47. But given the usually large errors involved both in the experimental measurements of the Henry coefficients and in their theoretical calculation, we could not conclude that the KL is definitely better suited than any of the others to model H_2S adsorbed in MIL-47.

The adsorption isotherms of H_2S on Cu-BTC, IRMOF-1, and MIL-47, calculated with the three potentials developed in this study, are shown in Figure 10. The most remarkable feature observed in the adsorption isotherms is that the 5S potential predicts similar values of

adsorption for low and high pressures than the rest of the potentials, but in the transition regions it predicts higher adsorption for the three materials than the other potentials. This implies that the adsorbed molecules pack in a slightly different way depending on the potential used. Another remarkable feature is the fact that the KL force field consistently predict lower adsorption values than the rest of the force fields. There are not enough experimental values to test which of the models provides a better agreement with experiment. The only experimental isotherm that of MIL-47, which is shown in Figure 10c. The best agreement is found for the KL force field, followed closely by the 3S and Kamath force fields. Although, due to the large variation of the experimental adsorption isotherms, it is necessary to compare with more than one isotherm, once a reasonable consensus is found as to what the adsorption isotherm is.[50,73-76]

With the results obtained so far we can shed some light into the interpretations of the experimental data regarding H_2S adsorption in Cu-BTC. In an experimental study Petit *et al.*[9] found that Cu-BTC is degraded upon adsorption of H_2S. They proposed a mechanism for the Cu-BTC crystal degradation, which is based on the assumption that H_2S does bind strongly to the Cu atoms and is able to replace water molecules present at those sites. Nevertheless, our simulations (both classical and Quantum-based simulations) do not agree with that view, i.e. water is predicted to bind more strongly

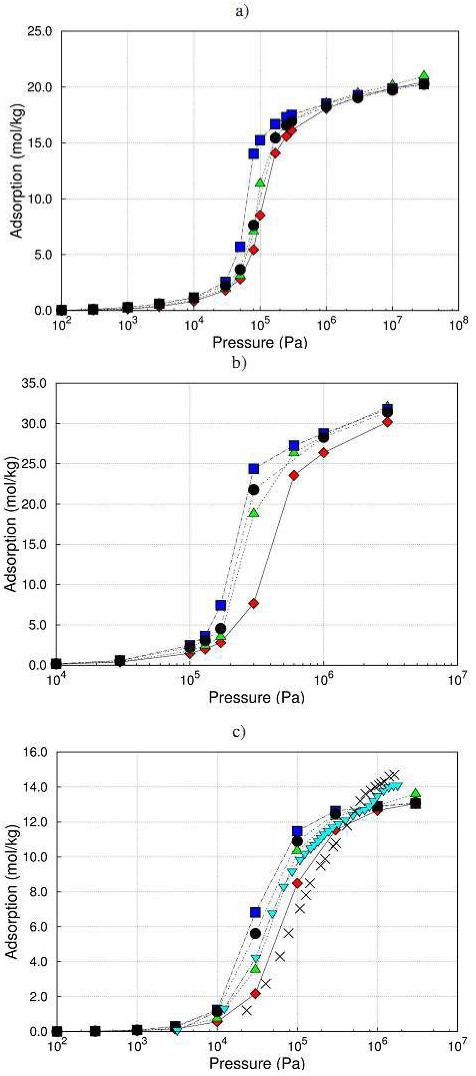

Figure 10. *Adsorption isotherms (at 300 K) of H_2S adsorbed in Cu-BTC (a), IRMOF-1 (b), and MIL-47 (c), using the three potentials developed in this study, 3S (upwards pointing triangles), 5S (squares), 5Sd (circles), as well as the force field developed by Kristoff and Liszi[23] (diamonds). Previous experimental data[15] (crosses) of adsorption on MIL-47 (at 303 K) are included for comparison. For this material we also show (downwards pointing triangles) the adsorption isotherm calculated by Hamon et al.[15] employing with the Kamath force field.*

to Cu-BTC than H_2S. This is observed for every force field studied and confirmed not only by our hybrid DFT calculations of the cluster model of the system, but also by a previous study,[31] which employs a different kind of calculation, namely periodical plane waves DFT. We carried out a study of the dipole moment that H_2S molecules would need to have in order to replace the water molecules. We found that, for a temperature of 300 K and a pressure of 10 kPa, as the dipole increases from 0.95 D to 1.95 D there is a small, gradual increase of adsorption, from 1.2 mol/kg to 2 mol/kg (see Appendix 2). But when the dipole has the unphysical value of 2.1 D the adsorption abruptly increases to values higher than 15 mol/kg. But this sudden increase of adsorption is not due to a stronger interaction with the Cu atoms, but to stronger intermolecular interactions, i. e. the higher dipole causes the H_2S molecules to nucleate and form clusters, away from the Cu atoms (see Appendix 2).

In an attempt to test whether the mechanism proposed by Petit *et al*[9]. is confirmed by DFT simulation, we tried to calculate the difference in Gibbs Free energy between the H_2S molecule adsorbed on the cluster shown in Figure 7a and different reaction states, such as 1) the S atom bonded to the Cu atom with the two H atoms desorbed, forming a H_2 molecule; 2) the S atom bonded to the Cu atom and to one H atom, with the remaining H atom either desorbed or bonded to an O atom that has broken its bond to the Cu atom. Unfortunately, all these structures are so unstable that in none of them could the SCF cycles achieve convergence.

In order to get a further insight into the interaction between the Cu-BTC structure and H_2S and H_2O molecules we carried out *ab initio* molecular dynamics of the molecules adsorbed on the model cluster shown in Figure 7 employing the Atom-Centered Density Matrix Propagation molecular dynamics method[77-78], as implemented in Gaussian 09. In this method the nuclear degrees of freedom are treated with quantum mechanics, while the electronic degrees of freedom are propagated adiabatically, employing an extended Lagrangian approach. The level of theory used is HF/LanL2MB[79]. The calculations were 3 ps long, with a time step was 0.1 fs, and the temperature was 300 K. The simulations show that there is a large difference of adsorption between the two molecules, since the H_2O molecule stays close to the cluster, at an average distance from the Cu atom of circa 2.7 Å, while the H_2S molecule is desorbed and leaves the cluster, reaching distances of circa 5.3 Å. Snapshots of these simulations are shown in the Appendix 2. This new piece of information is in line with the other theoretical results, so it is then clear that all types of simulations agree on the prediction that the interaction between H_2S and Cu-BTC is much weaker than that of H_2O. There seems to be an apparent discrepancy between experimental and theoretical results. But we would like to note that there is not really a contradiction, since it would be possible that another mechanism not yet presented could explain the reasons why H_2S degrades the crystalline

structure, even in the presence of water molecules, which interact more strongly with the Cu atoms. This is an interesting problem that deserves further studies.

Conclusions

We have developed three new force fields that model the liquid and gas phases of H_2S correctly. All previous force fields include long-range corrections to the Lennard-Jones energy, so in order to check whether other force fields with different fitting procedures to the previously published ones would yield different description of the adsorption properties in microporous materials (particularly in Metal-Organic Frameworks), we applied a cut and shift of the Lennard-Jones energy. Moreover we employed various values of the molecular dipole moment and different number of interaction sites. Two of the force fields have a molecular dipole (1.43 D) higher than the one obtained experimentally (0.974 D), and one has the experimental dipole. The fitting of the parameters was carried employing Gibbs ensemble Monte Carlo simulations, with which we obtained three set of interatomic potentials that model the experimental properties of liquid and gaseous H_2S. Comparing the results of the interatomic potential-based adsorption simulations on Cu-BTC, MIL-47, and IRMOF-1 with those obtained with DFT calculations, we have found that the newly developed potentials do provide reliable results and could therefore be employed in further studies of H_2S adsorption. But the improvement of the description of the electrostatic potential around the molecule achieved by the models with a larger number of point charges (5S and 5Sd models) does not necessarily imply that the interaction between the H_2S molecules and the framework is better modelled with those force fields.

Our study also sheds some light into the mechanisms by which Cu-BTC degrades when H_2S is adsorbed. Experimental studies suggest that the interaction between H_2S and the Cu atom in Cu-BTC is strong, with H_2S molecules being able to displace H_2O molecules. But the results of the simulations, performed both with the new force fields and with the previous ones, suggest otherwise, H_2O does interact with the Cu atoms more strongly than H_2S, which stays in the cages of the framework. DFT calculations predict similar results than classical simulations. Our simulation study therefore suggests that there must be something missing in the mechanisms proposed so far to explain the degradation observed in Cu-BTC upon adsorption of H_2S.

Bibliography

(1) Groenestijn, J. W. v.; Kraakman, N. J. R. *Chemical Engineering Journal* **2005**, *113*, 85.

(2) Cal, M. P.; Strickler, B. W.; Lizzio, A. A.; Gangwal, S. K. *Carbon* **2000**, *38*, 1767.

(3) Polychronopoulou, K.; Fierro, J. L. G.; Efstathiou, A. M. *Applied Catalysis B: Environmental* **2005**, *57*, 125.

(4) Xiao, Y.; Wang, S.; Wu, D.; Yuan, Q. *Journal of Hazardous Materials* **2008**, *153*, 1193.

(5) Kim, K.; Park, N. *Journal of Industrial and Engineering Chemistry* **2010**, *16*, 967.

(6) Godini, H. R.; Mowla, D. *Chem. Eng. Res. Des.* **2008**, *86*, 401.

(7) Marzouk, S. A. M.; Al-Marzouqi, M. H.; Abdullatif, N.; Ismail, Z. M. *J. Membr. Sci.* **2010**, *360*, 436.

(8) Novochinskii, I.; Song, C. S.; Ma, X. L.; Liu, X. S.; Shore, L.; Lampert, J.; Farrauto, R. J. *Energy Fuels* **2004**, *18*, 576.

(9) Petit, C.; Mendoza, B.; Bandosz, T. J. *ChemPhysChem* **2010**, *11*, 3678

(10) Farha, O. K.; Yazaydin, A. Ö.; Eryazici, I.; Malliakas, C. D.; Hauser, B. G.; Kanatzidis, M. G.; Nguyen, S. T.; Snurr, R. Q.; Hupp, J. T. *Nat Chem* **2010**, *2*, 944.

(11) Li, H.; Eddaoudi, M.; O'Keeffe, M.; Yaghi, O. M. *Nature* **1999**, *402*, 276.

(12) Zhou, H. C.; Long, J. R.; Yaghi, O. M. *Chemical Reviews* **2012**, *112*, 673.

(13) Trung, T. K.; Trens, P.; Tanchoux, N.; Bourrelly, S.; Llewellyn, P. L.; Loera-Serna, S.; Serre, C.; Loiseau, T.; Fajula, F. o.; FeÌ rey, G. r. *Journal of the American Chemical Society* **2008**, *130*, 16926.

(14) Horcajada, P.; Serre, C.; Maurin, G.; Ramsahye, N. A.; Balas, F.; Vallet-Regí, M.; Sebban, M.; Taulelle, F.; Férey, G. *Journal of the American Chemical Society* **2008**, *130*, 6774.

(15) Hamon, L.; Leclerc, H.; Ghoufi, A.; Oliviero, L.; Travert, A.; Lavalley, J.-C.; Devic, T.; Serre, C.; Férey, G.; De Weireld, G.; Vimont, A.; Maurin, G. *The Journal of Physical Chemistry C* **2011**, *115*, 2047.

(16) Rowsell, J. L. C.; Yaghi, O. M. *Microporous and Mesoporous Materials* **2004**, *73*, 3.

(17) Chui, S. S. Y.; Lo, S. M. F.; Charmant, J. P. H.; Orpen, A. G.; Williams, I. D. *Science* **1999**, *283*, 1148.

(18) Li, J. R.; Kuppler, R. J.; Zhou, H. C. *Chemical Society Reviews* **2009**, *38*, 1477.

(19) Czaja, A. U.; Trukhan, N.; Muller, U. *Chemical Society Reviews* **2009**, *38*, 1284.

(20) Barthelet, K.; Marrot, J.; Riou, D.; Ferey, G. *Angewandte Chemie-International Edition* **2001**, *41*, 281.

(21) Jorgensen, W. L.; Madura, J. D.; Swenson, C. J. *Journal of the American Chemical Society* **1984**, *106*, 6638.

(22) Forester, T. R.; McDonald, I. R.; Klein, M. L. *Chemical Physics* **1989**, *129*, 225.

(23) Kristóf, T.; Liszi, J. *Journal of Physical Chemistry B* **1997**, *101*, 5480.

(24) Delhommelle, J.; Millié, P.; Fuchs, A. H. *Molecular Physics* **2002**, *98*, 1895.

(25) Lin, W.; Yang, Q.; Zhong, C. *Fluid Phase Equilibria* **2004**, *220*, 1.

(26) Kamath, G.; Lubna, N.; Potoff, J. J. *The Journal of Chemical Physics* **2005**, *123*, 124505.

(27) Hellmann, R.; Bich, E.; Vogel, E.; Vesovic, V. *Physical Chemistry Chemical Physics* **2011**, *13*, 13749.

(28) Jorgensen, W. L. *The Journal of Physical Chemistry* **1986**, *90*, 6379.

(29) Bandosz, T. J.; Petit, C. *Dalton Transactions* **2012**, *41*, 4027.

(30) Bandosz, T. *Activated Carbon Surfaces in Environmental Remediation*; Academic Press: Oxford, UK, 2006.

(31) Watanabe, T.; Sholl, D. S. *Journal of Chemical Physics* **2010**, *133(9)*, 094509.

(32) Castillo, J. M.; Vlugt, T. J. H.; Calero, S. *Journal of Physical Chemistry C* **2008**, *112*, 15934.

(33) Sorenson, J. M.; Hura, G.; Glaeser, R. M.; Head-Gordon, T. *J. Chem. Phys.* **2000**, *113*, 9149.

(34) Andreani, C.; Merlo, V.; Ricci, M. A.; Ruocco, G.; Soper, A. K. *Europhysics Letters* **1989**, *8*, 441.

(35) Goodwin, R., 1983.

(36) Kristóf, T.; Liszi, J. *Mol. Phys.* **1997**, *90(6),* 1031.

(37) Galliero, G.; Nieto-Draghi, C.; Boned, C.; Avalos, J. B.; Mackie, A. D.; Baylaucq, A.; Montel, F. *Industrial & Engineering Chemistry Research* **2007**, *46*, 5238.

(38) Eddaoudi, M.; Kim, J.; Rosi, N.; Vodak, D.; Wachter, J.; O'Keeffe, M.; Yaghi, O. M. *Science* **2002**, *295*, 469.

(39) Mayo, S. L.; Olafson, B. D.; Goddard, W. A. *Journal of Physical Chemistry* **1990**, *94*, 8897.

(40) Rappe, A. K.; Casewit, C. J.; Colwell, K. S.; Goddard, W. A.; Skiff, W. M. *Journal of the American Chemical Society* **1992**, *114*, 10024.

(41) Frost, H.; Snurr, R. Q. *Journal of Physical Chemistry C* **2007**, *111*, 18794.

(42) Dubbeldam, D.; Walton, K. S.; Ellis, D. E.; Snurr, R. Q. *Angewandte Chemie-International Edition* **2007**, *46*, 4496.

(43) Bueno-Perez, R.; Garcia-Perez, E.; Jose Gutierrez-Sevillano, J.; Merkling, P. J.; Calero, S. *Adsorption Science & Technology* **2010**, *28*, 823.

(44) Getzschmann, J.; Senkovska, I.; Wallacher, D.; Tovar, M.; Fairen-Jimenez, D.; Duren, T.; van Baten, J. M.; Krishna, R.; Kaskel, S. *Microporous and Mesoporous Materials* **2010**, *136*, 50.

(45) Martin-Calvo, A.; Garcia-Perez, E.; Castillo, J. M.; Calero, S. *Physical Chemistry Chemical Physics* **2008**, *10*, 7085.

(46) Castillo, J. M.; Vlugt, T. J. H.; Calero, S. *Journal of Physical Chemistry C* **2009**, *113*, 20869.

(47) Dubbeldam, D.; Frost, H.; Walton, K. S.; Snurr, R. Q. *Fluid Phase Equilibria* **2007**, *261*, 152.

(48) Frenkel, D.; Smit, B. *Understanding Molecular Simulation From Algorithms to Applications*; second edition ed.; Academic Press: San Diego. C.A., 2002.

(49) Dubbeldam, D.; Calero, S.; Ellis, D. E.; Snurr, R. Q. 2008.

(50) Garcia-Sanchez, A.; Ania, C. O.; Parra, J. B.; Dubbeldam, D.; Vlugt, T. J. H.; Krishna, R.; Calero, S. *The Journal of Physical Chemistry C* **2009**, *113*, 8814.

(51) Vlugt, T. J. H.; Garcia-Perez, E.; Dubbeldam, D.; Ban, S.; Calero, S. *Journal of Chemical Theory and Computation* **2008**, *4*, 1107.

(52) Martín-Calvo, A.; García-Pérez, E.; Castillo, J. M.; Calero, S. *Physical Chemistry Chemical Physics* **2008**, *10*, 7085.

(53) Frisch, M. J.; Trucks, G. W.; Schlegel, H. B.; Scuseria, G. E.; Robb, M. A.; Cheeseman, J. R.; Scalmani, G.; Barone, V.; Mennucci, B.; Petersson, G. A.; Nakatsuji, H.; Caricato, M.; Li, X.; Hratchian, H. P.; Izmaylov, A. F.; Bloino, J.; Zheng, G.; Sonnenberg, J. L.; Hada, M.; Ehara, M.; Toyota, K.; Fukuda, R.; Hasegawa, J.; Ishida, M.; Nakajima, T.; Honda, Y.; Kitao, O.; Nakai, H.; Vreven, T.; J. A. Montgomery, J.; Peralta, J. E.; Ogliaro, F.; Bearpark, M.; Heyd, J. J.; Brothers, E.; Kudin, K. N.; Staroverov, V. N.; Kobayashi, R.; Normand, J.; Raghavachari, K.; Rendell, A.; Burant, J. C.; Iyengar, S. S.; Tomasi, J.; Cossi, M.; Rega, N.; Millam, J. M.; Klene, M.; Knox, J. E.; Cross, J. B.; Bakken, V.; Adamo, C.; Jaramillo, J.; Gomperts, R.; Stratmann, R. E.; Yazyev, O.; Austin, A. J.; Cammi, R.; Pomelli, C.; Ochterski, J. W.; Martin, R. L.; Morokuma, K.; Zakrzewski, V. G.; Voth, G. A.; Salvador, P.; Dannenberg, J. J.; Dapprich, S.; Daniels, A. D.; Farkas, Ö.; Foresman, J. B.; Ortiz, J. V.;

Cioslowski, J.; Fox, D. J.; Gaussian, Inc.: Wallingford CT, 2009, p Gaussian 09.

(54) Zhao, Y.; Truhlar, D. G. *Theor. Chem. Acc.* **2008**, *120*, 215.

(55) Tzeli, D.; Petsalakis, I. D.; Theodorakopoulos, G.; Ajami, D.; Rebek, J. *Int. J. Quantum Chem.* **2013**, *113*, 734.

(56) Tzeli, D.; Petsalakis, I. D.; Theodorakopoulos, G. *The Journal of Physical Chemistry A* **2011**, *115*, 11749.

(57) Fuentealba, P.; Preuss, H.; Stoll, H.; Szentpaly, L. v. *Chem. Phys. Lett.* **1982**, *89*, 418.

(58) Simon, S.; Duran, M.; Dannenberg, J. J. *Journal of Chemical Physics* **1996**, *105*, 11024.

(59) http://webbook.nist.gov/chemistry/.

(60) Huiszoon, C.; Dymanus, A. *Physica (Amsterdam)* **1965**, *31*, 1049.

(61) Weast, R. C. *Handbook of Chemistry and Physics*; 67 ed.; Boca Raton: CRC Press, 1986.

(62) Allen, M. P.; Tildesley, D. J. *Computer Simulation of Liquids* Oxford University Press, USA, 1989.

(63) Macedonia, M. D.; Maginn, E. J. *Molecular Physics* **1999**, *96*, 1375.

(64) Siperstein, F.; Myers, A. L.; Talu, O. *Molecular Physics* **2002**, *100*, 2025.

(65) Atkins, P. W. *Physical Chemistry*; Oxford Higher Education: New York, 1990.

(66) Martin, M. G.; Siepmann, J. I. *Journal of Physical Chemistry B* **1998**, *102*, 2569.

(67) Rowlinson, J. S.; Swinton, F. L. *Liquids and Liquid Mixtures*; 3rd ed.; Butterworth: London, 1982.

(68) Rowlinson, J. S.; Widom, B. *Molecular Theory of Capillarity*; Oxford University Press: New York, 1989.

(69) Giauque, W. F.; Blue, R. W. *Journal of the American Chemical Society* **1936**, *58*, 831.

(70) Sabin, J. R. *Journal of the American Chemical Society* **1971**, *93(15)*, 3613.

(71) Perdew, J. P.; Wang, Y. *Phys. Rev. B* **1992**, *45(23)*, 13244.

(72) Grajciar, L.; Bludský, O.; Nachtigall, P. *The Journal of Physical Chemistry Letters* **2010**, *1*, 3354.

(73) Chowdhury, P.; Bikkina, C.; Meister, D.; Dreisbach, F.; Gumma, S. *Microporous and Mesoporous Materials* **2009**, *117*, 406.

(74) Figini-Albisetti, A.; Velasco, L. F.; Parra, J. B.; Ania, C. O. *Applied Surface Science* **2010**, *256*, 5182.

(75) Dubbeldam, D.; Calero, S.; Vlugt, T. J. H.; Krishna, R.; Maesen, T. L. M.; Smit, B. *Journal of Physical Chemistry B* **2004**, *108*, 12301.

(76) Calero, S.; Dubbeldam, D.; Krishna, R.; Smit, B.; Vlugt, T. J. H.; Denayer, J. F. M.; Martens, J. A.; Maesen, T. L. M. *Journal of the American Chemical Society* **2004**, *126*, 11377.

(77) Schlegel, H. B.; Iyengar, S. S.; Li, X.; Millam, J. M.; Voth, G. A.; Scuseria, G. E.; Frisch, M. J. *Journal of Chemical Physics* **2002**, *117*, 8694.

(78) Iyengar, S. S.; Schlegel, H. B.; Millam, J. M.; Voth, G. A.; Scuseria, G. E.; Frisch, M. J. *J. Chem. Phys.* **2001**, *115*, 10291.

(79) Hay, P. J.; Wadt, W. R. *Journal of Chemical Physics* **1985**, *82*, 299.

In a combined experimental and theoretical study, the first transferable set of charges of imidazolate linkers has been derived specifically to model Zeolitic Imidazolate Frameworks (ZIFs). The validity of the charges is demonstrated by comparing experimental and computed results of CH_4 and CO_2 adsorption on ZIF-7, ZIF-8, ZIF-69, and ZIF-71. The sets of charges obtained with this method provide values of isosteric heats of adsorption and adsorption isotherms of similar accuracy as those obtained using specific sets of charges derived for each individual structure, with the great advantage of being readily transferable to a wide range of ZIFs.

5

Juan José Gutiérrez-Sevillano, Sofía Calero, Conchi O. Ania, José B. Parra, Freek Kapteijn, Jorge Gascón, and Said Hamad

Towards a Transferable Set of Charges to Model Zeolitic Imidazolate Frameworks: A Combined Experimental-Theoretical Research

Introduction

Zeolitic imidazolate frameworks (ZIFs) are porous crystalline structures formed by the repetition of tetrahedral Structural Building Units[1] (SBU). ZIFs were first synthesized[2-6] in the early 2000s, since then the number of studies on these materials has grown exponentially.[8-10] ZIFs present higher thermal and chemical stabilities[3] than many Metal Organic Frameworks (MOFs), increasing their range of possible applications.[1,12-13] The main feature that differentiates these structures from other MOFs is that the metal nodes (typically Zn or Co) are tetrahedrically coordinated to imidazolates (im) or functionalized imidazolate ligands (such as those shown in Figure 1), which are shared between two adjacent SBUs. This connectivity is very similar to that found in zeolites, where the centers of the tetrahedra are occupied by Si atoms and the vertices by O atoms. Due to the topological similarity between zeolites and ZIFs, several structures in which the disposition of the tetrahedra is the same are found for both types of materials. On the other hand, the greater flexibility of the metal-imidazolate bonds allows the synthesis of a larger number of ZIF structures.

An increasing number of studies on ZIFs concerns simulation techniques. Molecular simulations are becoming a very important tool for researchers in the field of materials science, since they have proven to accurately predict important properties of structured porous materials, such as adsorption isotherms and diffusivities. When

applying interatomic potential-based simulation techniques to study neutral, non-polar molecules (such as CH_4 or H_2) there is no need to include the charge of the framework in the simulations, but when dealing with polar molecules (either dipolar or quadrupolar), framework charges play a key role in the description of guest-host interactions. Regrettably, no method to uniquely determine the values of the atomic partial charges is available, since they are not associated to a quantum observable. Just useful approximations are employed, which allow modeling a system by means of empirically calculated interatomic potentials.

Several methods are commonly used to calculate atomic charges. The most popular are those based on the fitting of charges to mimic the electrostatic potential around the molecule (such as the CHelpG[14] and Merz-Singh-Kollman[15-16] schemes). Another type of method used is the Natural Population Analysis (NPA)[17-18], based on the analysis of the Natural Bond Orbitals[17,19] (NBO). The NPA charge of an atom is calculated by removing from the nuclear charge the electron density associated with its orbitals.

Employing *ab initio* calculations to fit the charges that will allow modeling ZIFs is a time-consuming process. It requires knowledge and expertise that is not available to most of the groups working on interatomic potentials simulations. Thus, an important factor

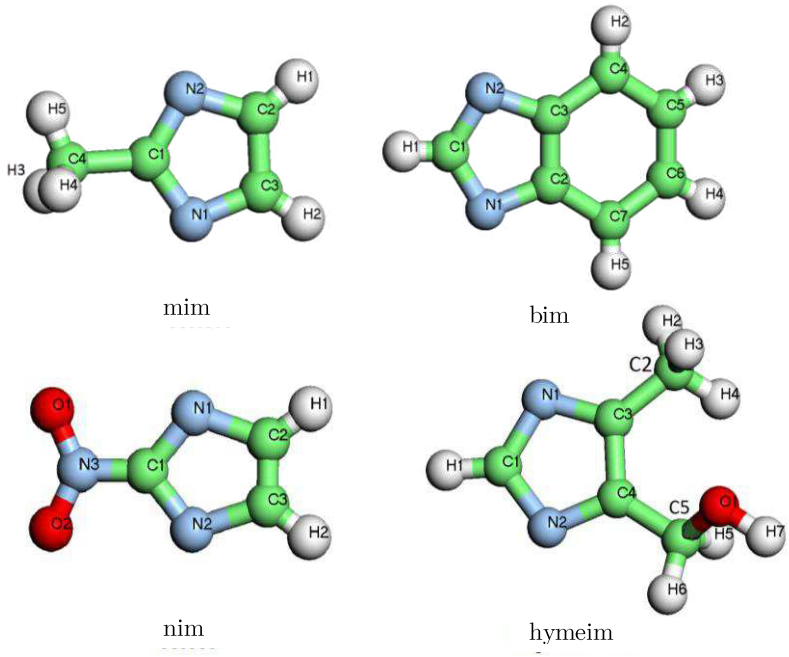

Figure 1. *Atom types of the imidazolates linkers that form ZIF-8 (mim), ZIF-68 (bim and nim) and ZIF-96 (hymeim). The atom charges for these imidazolates are shown in Table 1. The charges and structures of the rest of the imidazolates studied are presented in the Appendix 3.*

that precludes the widespread use of atomic charges to model ZIFs is the lack of an uniform, general set of charges that could be used directly without the need of further fitting from the end user. In the case of ZIFs, to the best of our knowledge, the only available set of charges has been reported by Xu and Zhong.[20] This model has, however, two main drawbacks: i) it was fitted to model MOFs in general, not ZIFs in particular and ii) the unit cells have a net charge, so that the user needs to introduce further changes to the charges in order to achieve neutrality. For example, if this set is used to assign the charges of the imidazolate molecules, the total charges vary from -0.991 e^- to 0.805 e^- (as shown in the Appendix 3). Since the charge assigned to the Zn atoms is 0.787 e^-, the unit cells employed to model the ZIFs are not neutral. The adjustment needed to use this set of charges in simulation studies is a delicate task, and results only in a limited validity. Recently, a new method for estimating partial atomic charges for every atom in the periodic table has been published.[21] It employs all of the measured ionization energies to perform an analysis similar in nature to the charge equilibration (Qeq) method.[22-23], so it has been named EQeq. EQeq charges can be obtained for any material, and it has proved that they predict correct results for various MOFs.[21] But we are interested in obtaining an uniform set of charges specifically designed to model ZIFs, for which we have made use *ab initio* calculations. We have checked the validity of the obtained charges by comparing the predicted isosteric heats of adsorption and adsorption isotherms with those obtained experimentally.

Computational Details

Methane was modeled using a pseudo atom model[24] where the molecule is considered as a single Lennard- Jones site with ε/k_B = 158.5 K and σ = 3.27 Å. No charges are considered. For carbon dioxide a full atom model[25-26] is used. This model has three Lennard-Jones sites centered at each atom. The parameters for carbon atoms are ε/k_B = 29.93 K and σ = 2.745 Å, and those for oxygen are ε/k_B = 85.67 K and σ = 3.017 Å. Point charges are placed at each site in order to model the quadrupole moment (q_C= 0.6512 e^- and q_O= -0.3256 e^-). Carbon-Oxygen distance is kept fixed (d= 1.149 Å). Details about the use of this type of models in MOFs and related porous materials can be extensively found in literature[27-31].

Adsorption isotherms were computed using GCMC simulations, where the temperature, the volume, and the chemical potential were kept fixed. The MC moves were performed in cycles, allowing one of the following trial moves in each cycle: regrowth, rotation, translation, insertion and deletion. More details on this simulation technique can be found elsewhere[28].

Simulations were performed using the RASPA code developed by D. Dubbeldam, S. Calero, D. E. Ellis, and R.Q. Snurr. This code has been extensively tested and validated with a large number of experimental and simulation data.[26,32-38]

Experimental details

ZIF-8 was purchased from Sigma-Aldrich. High resolution experimental adsorption isotherms of the selected gases (CH_4 and CO_2) were performed in a volumetric analyzer (Tristar 3020, Micromeritics) in the pressure range from 10^{-2} up to 120 kPa; the instrument was equipped with one pressure transducer (0-133 kPa, uncertainty within 0.15% of each reading), that guarantees an excellent sensitivity for gas adsorption in the low pressure range, which is especially useful in adsorption studies on highly microporous materials.

Each adsorption isotherm in ZIF-8 was measured along 24 h, allowing for over 70 equilibrium points to be registered. The saturation pressures of each gas were measured every 2 hours by means of a pressure transducer. The temperature of the isotherms was controlled using a thermostatic circulating oil bath. All the gases were supplied by Air Products with an ultrahigh purity (i.e., 99.995%). Prior to the adsorption measurements, the samples were in-situ outgassed under vacuum (ca. 10^{-3} kPa) at 393 K overnight to remove any adsorbed impurities. All the isotherms were done in triplicate and the data is reproducible with an error below 0.1 %. The isosteric heat of adsorption for the studied gases was determined from the set of equilibrium isotherms at 258, 278 and 298 K, using the Clausius–Clapeyron equation.

The ZIF-7 sample was synthesized according to the procedure given elsewhere. A solid mixture of $Zn(NO_3)_2.6H_2O$ (0.803 g) and benzimidazole (0.235 g) is dissolved in 75 ml of dimethylformamide (DMF). The solution is poured into the teflon liners and synthesis is carried out at 400 K for 48 hours, after heating at a rate of 5 K/min. The polycrystalline product had an average particle size of 4 microns. A Micromeritics ASAP 2010 gas adsorption analyzer (stainless-steel version) was used to measure the adsorption isotherms of carbon dioxide, in the pressure range from 0.002 to 120 kPa. The instrument is equipped with a turbo molecular vacuum pump and three different pressure transducers (0.13, 1.33, and 133 kPa) to enhance the sensitivity in different pressure ranges. The static-volumetric technique was used to determine the volume of the gas adsorbed at different partial pressures.

Prior to the adsorption measurements the adsorbent particles were outgassed *in situ* under vacuum at 448 K for 16 h to remove any adsorbed impurities. The obtained dry sample weight was used in the calculation of isotherm data. Adsorption measurements were done at 298, 338 and 373 K. The 195 K isotherms were measured using solid carbon dioxide in isopropylalcohol as coolant. The isosteric heat of CO_2 adsorption was determined from the set of equilibrium isotherms using the Clausius-Clapeyron equation.

Results and discussion

With the sets of charges obtained in this study the unit cells are neutral for all ZIFs, allowing its use in conjunction with a general force field such as UFF[7] to model any of the ZIFs based on Zn and the most common imidazolate molecules. The topological properties of crystalline ZIFs structures were used to obtain this set. ZIFs are built up of a network of Zn (or Co) cations tetrahedrally coordinated to four imidazolates like the ones shown in Figure 1. Since each imidazolate is shared by two cations, the unit cell might be regarded as just one cation and two imidazolates. Therefore, assigning a negative charge of -1 e^- to the imidazolates and +2 e^- to the cations, we ensure charge neutrality of the system. The natural charges of each atom of these imidazolate molecules were calculated by performing a Natural Population Analysis[18,39] of the MP2/aug-cc-pVTZ electron density obtained with the Gaussian09 code.[40] Although the most popular methods to obtain atomic charges useful in interatomic potential-based simulations are ESP methods such as CHelpG,[14] (in which a set of point charges centered on the atomic nuclei are fitted to reproduce the *ab initio*-calculated electrostatic potential around the molecule as best as possible), we found that the charges fitted for several H atoms were negative. The REPEAT method is more complex and it predicts negative charges even for Zn atoms in some cases.[41] In contrast,

Table 1. *Atomic charges for the imidazolate linkers mim, bim, hymeim, and nim (see* Figure 1*, where the atom types are defined). The total charge of each imidazolate linker is -1* e^-.

mim		bim		hymeim		nim	
Atom	**Charge**	**Atom**	**Charge**	**Atom**	**Charge**	**Atom**	**Charge**
N1	-0.590	**N1**	-0.569	**N1**	-0.567	**N1**	-0.529
N2	-0.590	**N2**	-0.569	**N2**	-0.566	**N2**	-0.529
C1	0.250	**C1**	0.141	**C1**	0.007	**N3**	0.457
C2	-0.150	**C2**	0.039	**C2**	-0.716	**C1**	0.229
C3	-0.150	**C3**	0.039	**C3**	0.043	**C2**	-0.102
C4	-0.570	**C4**	-0.153	**C4**	0.010	**C3**	-0.102
H1	0.130	**C5**	-0.244	**C5**	-0.109	**H1**	0.154
H2	0.130	**C6**	-0.244	**H1**	0.194	**H2**	0.154
H3	0.180	**C7**	-0.153	**H2**	0.221	**O1**	-0.366
H4	0.180	**H1**	0.121	**H3**	0.220	**O2**	-0.366
H5	0.180	**H2**	0.149	**H4**	0.205		
		H3	0.147	**H5**	0.167		
		H4	0.147	**H6**	0.200		
		H5	0.149	**H7**	0.465		
				O1	-0.774		

NPA usually provides atomic charges which are physically sound and it gives a reasonable description of the variation of the charges with changes on the atomic composition. Furthermore, the charges obtained with NPA tend to be less dependent on the basis set and molecular geometry[42-43] employed than ESP methods.[44-49] NPA charges correlate well with experimental and computed NMR chemical shifts,[50] and provides reliable information to predict pKa values of organic molecules.[51] In particular, Pacios *et al.*[52] found that NPA charges provide a better description of imidazole-acetate complexes than the ESP based MK charges, and recommend the use of NPA in molecular mechanics simulations. We therefore employed NPA to obtain a transferable set of charges, capable of modeling a wide range of ZIFs.

Charges obtained directly from *ab initio* calculations could be employed in the simulations, although their use would imply that the system behaves as a purely ionic material, in which the charges of the Zn cations are equal to their formal charges, i.e. +2 e^-. Since this is not the case, in order to take into account the covalent nature of the chemical bonds in these materials, we employed charges smaller than the formal ones. A similar approach is used when modeling zeolites, where the charges employed for Si atoms are not the formal +4, but charges in the range between +0.5 e^- and +2 e^-. It is worth noting that this reduction of the charges is already being employed[20,41,53-56] in other MOF and ZIF simulation studies, where the charges of the cations vary

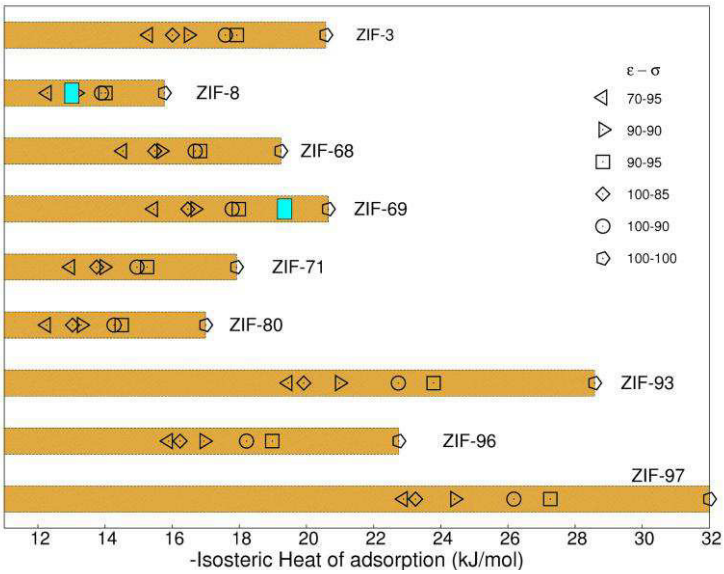

Figure 2. *Comparison between the experimental and simulated isosteric heats of adsorption of methane. The different percentages of the original UFF [7] ε and σ Lennard Jones parameters are indicated. Orange bars are a guide for the eye. Experimental data are shown as cyan squares: ZIF-8 (obtained in this work); ZIF-69 (reference 11).*

typically between +0.3 e^- and +1.7 e^-. We studied Zn charges of values +0.7 e^-, +1.0 e^-, and +1.3 e^-, so that all the charges of the atoms belonging to the imidazolates were scaled to obtain total imidazolate charges of -0.35 e^-, -0.5 e^-, and -0.65 e^-. An example of the charges obtained for four representative imidazolate linkers is shown in Table 1. The numbering employed to assign the charges is shown in Figure 1. Although the values reported in Table 1 add up to -1 e^-, employing the mentioned charges of -0.35 e^-, -0.5 e^-, and -0.65 e^- can be easily achieved by multiplying each atomic charge by the corresponding factor (0.35, 0.5, and 0.65 when the values for Zn are set to +0.7 e^-, +1.0 e^-, and +1.3 e^- respectively).

The adsorption of CH_4, a non-polar molecule, was used to optimize the interatomic potential parameters, without the need to include framework charges. Figure 2 shows that the predicted values of isosteric heat of adsorption for methane agree with the experiments when the UFF potential parameters are reduced in the order of 10 % (see Appendix 3).

UFF parameters were obtained by minimizing the differences between the experimental and predicted geometries (bond distances and angles) of a large set of molecules. Although UFF has been very successful in describing

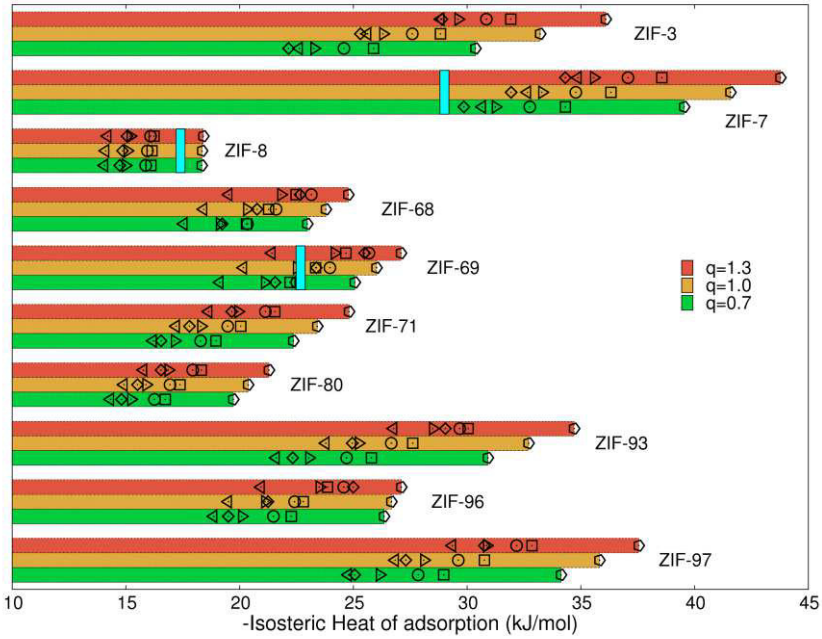

Figure 3. *Comparison between the experimental and simulated isosteric heats of adsorption of carbon dioxide. The simulations employed the newly developed set of charges and scaled UFF [7] parameters. The key is the same as in* Figure 2. *Figures with green, orange, and red backgrounds correspond to calculations employing Zn charges of 0.7 e^-, 1.0 e^-, and 1.3 e^- respectively. Experimental data are shown as cyan bars: ZIF-7 (this work), ZIF-8 (this work), ZIF-69 (reference [11]).*

several systems and processes, it is not always the case that the results obtained with it will be in agreement with the experiment.[57-62] The same deficiency applies to any other general force field. For example, UFF is known to predict systematically higher values of adsorption[63] in ZIFs than DREIDING and none of them is expected to provide the correct results for every system.

Adsorption of methane is mainly controlled by van der Waals interactions, since the molecule neither possesses a dipole nor a quadrupole moment. In order to assess the influence of the point charges, the adsorption of CO_2 was studied. Figure 3 shows that the predicted values of isosteric heat of adsorption are close to the experimental ones.

Although the isosteric heats of adsorption vary with the scaling applied to the original UFF parameters, we obtain good agreement between predicted and experimental results when the parameters are scaled down by less than 10 %, which is smaller than the circa 30% needed in previous studies.[55-56,64]

It has to be stressed that isosteric heats of adsorption at low coverage are not easy to calculate experimentally from equilibrium adsorption data, especially on samples with heterogeneous adsorption sites, as is the case for ZIFs. This might often result in deviations from computed values at low coverage, as it has been frequently reported in the literature[65].

Employing the new set of charges we can now calculate the adsorption isotherms of every ZIF composed of Zn and any combination of the imidazolate linkers for which we have obtained their charges (presented in the Appendix 3). For instance, the adsorption isotherms of CO_2 at 298 K in three of the most studied ZIFs, namely ZIF-8, ZIF-71, and ZIF-69 are shown in Figure 4.

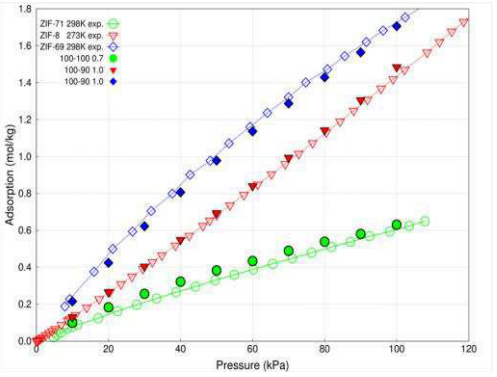

Figure 4. *Comparison between the experimental (solid) and simulated (open symbols) adsorption isotherms of CO_2 in several ZIFs. Simulations were performed using the newly developed set of charges and scaled UFF[7] parameters. Experimental data for ZIF-69 and ZIF-71 are taken from references [4], and [11] respectively, while data for ZIF-8 are obtained in this work.*

Using the new set of charges in combination with conveniently scaled UFF parameters, we are now able to obtain an excellent agreement with the experimental isotherms, with a level of accuracy similar to that obtained when more sophisticated and time consuming methods are employed to obtain the sets of charges and force field parameters.[20,41,54-55] As to the prediction of gas separation properties, we found that

there is a qualitative agreement between the adsorption selectivities computed with these charges and those obtained experimentally. For instance, the experimental[11] values of CO_2/CH_4, CO_2/N_2, and CO_2/O_2 adsorption selectivities at 298 K in ZIF-69 are 5.1, 19.9, and 18.1 respectively, while the values predicted by our calculations are 3.4, 13.1 and 11.1. It is worth noting that this qualitative agreement is found with simulations that only take a few minutes to be completed, highlighting the great potential to screen a large number of materials with little computational cost.

Conclusions

We provide new sets of charges that can be applied to model any ZIF composed of Zn and any of the 20 imidazolate linkers studied. Employing these charges and scaled UFF force field parameters we can successfully predict the isosteric heats of adsorption and the adsorption isotherms of CH_4 and CO_2 in ZIF-7, ZIF-8, and ZIF-69. These charges will be very valuable to predict the adsorption and separation properties of ZIFs, since they will allow the study of several systems without needing to perform complex and time consuming, *ab initio*-based, calculations of atomic charges.

Bibliography

(1) Phan, A.; Doonan, C. J.; Uribe-Romo, F. J.; Knobler, C. B.; O'Keefe, M.; Yaghi, O. M. *Acc. Chem. Res.* **2010**, *43*, 58.

(2) Tian, Y.-Q.; Cai, C.-X.; Ji, Y.; You, X.-Z.; Peng, S.-M.; Lee, G.-H. *Angew. Chem. Int. Ed.* **2002**, *41*, 1384.

(3) Park, K. S.; Ni, Z.; Cote, A. P.; Choi, J. Y.; Huang, R. D.; Uribe-Romo, F. J.; Chae, H. K.; O'Keeffe, M.; Yaghi, O. M. *Proc. Natl. Acad. Sci. USA* **2006**, *103*, 10186.

(4) Banerjee, R.; Phan, A.; Wang, B.; Knobler, C.; Furukawa, H.; O'Keeffe, M.; Yaghi, O. M. *Science* **2008**, *319*, 939.

(5) Huang, X. C.; Lin, Y. Y.; Zhang, J. P.; Chen, X. M. *Angew. Chem. Int. Ed.* **2006**, *45*, 1557.

(6) Tian, Y. Q.; Cai, C. X.; Ren, X. M.; Duan, C. Y.; Xu, Y.; Gao, S.; You, X. Z. *Chem. Eur. J.* **2003**, *9*, 5673.

(7) Rappe, A. K.; Casewit, C. J.; Colwell, K. S.; Goddard, W. A.; Skiff, W. M. *J. Am. Chem. Soc.* **1992**, *114*, 10024.

(8) Sumida, K.; Rogow, D. L.; Mason, J. A.; McDonald, T. M.; Bloch, E. D.; Herm, Z. R.; Bae, T.-H.; Long, J. R. *Chem. Rev.* **2012**, *112*, 724.

(9) Gucuyener, C.; van den Bergh, J.; Gascon, J.; Kapteijn, F. *J. Am. Chem. Soc.* **2010**, *132(50),* 17704.

(10) van den Bergh, J.; Gücüyener, C.; Pidko, E. A.; Hensen, E. J. M.; Gascon, J.; Kapteijn, F. *Chem. Eur. J.* **2011**, *17(32),* 8832.

(11) Banerjee, R.; Furukawa, H.; Britt, D.; Knobler, C.; O'Keeffe, M.; Yaghi, O. M. *J. Am. Chem. Soc.* **2009**, *131*, 3875.

(12) Hao, G. P.; Li, W. C.; Lu, A. H. *J. Mat. Chem.* **2011**, *21*, 6447.

(13) Farrusseng, D.; Aguado, S.; Pinel, C. *Angew. Chem. Int. Ed.* **2009**, *48*, 7502.

(14) Breneman, C. M.; Wiberg, K. B. *J. Comp. Chem.* **1990**, *11*, 361.

(15) Singh, U. C.; Kollman, P. A. *J. Comp. Chem.* **1984**, *5*, 129.

(16) Besler, B. H.; Merz Jr., K. M.; Kollman, P. A. *J. Comp. Chem.* **1990**, *11*, 431.

(17) Reed, A. E.; Curtiss, L. A.; Weinhold, F. *Chem. Rev.* **1988**, *88* 899.

(18) Weinhold, F.; Carpenter, J. E.; Naaman, E. R., Vager, Z., Eds.; Plenum: 1988, p 227.

(19) Foster, J. P.; Weinhold, F. *J. Am. Chem. Soc.* **1980**, *102*, 7211.

(20) Xu, Q.; Zhong, C. *J. Phys. Chem. C* **2010**, *114*, 5035.

(21) Wilmer, C. E.; Kim, K. C.; Snurr, R. Q. *J. Phys. Chem. C* **2012**, *3*, 2506.

(22) Rappé, A. K.; Goddard, W. A., III. *J. Phys. Chem.* **1991**, *95*, 3358.

(23) Ramachandran, S.; Lenz, T. G.; Skiff, W. M.; Rappé, A. K. *J. Phys. Chem.* **1996**, *100*, 5898.

(24) Ryckaert, J. P.; Bellemans, A. *Faraday Discussions* **1978**, *66*, 95.

(25) Harris, J. G.; Yung, K. H. *J. Phys. Chem.* **1995**, *99*, 12021.

(26) Garcia-Sanchez, A.; Ania, C. O.; Parra, J. B.; Dubbeldam, D.; Vlugt, T. J. H.; Krishna, R.; Calero, S. *J. Phys. Chem. C* **2009**, *113*, 8814.

(27) Dubbeldam, D.; Calero, S.; Vlugt, T. J. H.; Krishna, R.; Maesen, T. L. M.; Beerdsen, E.; Smit, B. *Phys. Rev. Lett.* **2004**, *93(8),* 088302.

(28) Dubbeldam, D.; Calero, S.; Vlugt, T. J. H.; Krishna, R.; Maesen, T. L. M.; Smit, B. *J. Phys. Chem. B* **2004**, *108*, 12301.

(29) Walton, K. S.; Millward, A. R.; Dubbeldam, D.; Frost, H.; Low, J. J.; Yaghi, O. M.; Snurr, R. Q. *J. Am. Chem. Soc.* **2008**, *130*, 406.

(30) Vlugt, T. J. H.; Zhu, W.; Kapteijn, F.; Moulijn, J. A.; Smit, B.; Krishna, R. *J. Am. Chem. Soc.* **1998**, *120*, 5599.

(31) Dubbeldam, D.; Galvin, C. J.; Walton, K. S.; Ellis, D. E.; Snurr, R. Q. *J. Am. Chem. Soc.* **2008**, *130*, 10884.

(32) Castillo, J. M.; Vlugt, T. J. H.; Calero, S. *J. Phys. Chem. C* **2008**, *112*, 15934.

(33) Calero, S.; Martin-Calvo, A.; Hamad, S.; Garcia-Perez, E. *Chem. Commun.* **2011**, *47*, 508.

(34) Garcia-Perez, E.; Gascon, J.; Morales-Florez, V.; Castillo, J. M.; Kapteijn, F.; Calero, S. *Langmuir* **2009**, *25*, 1725.

(35) Garcia-Sanchez, A.; Dubbeldam, D.; Calero, S. *J. Phys. Chem. C* **2010**, *114*, 15068.

(36) Kuhn, J.; Castillo-Sanchez, J. M.; Gascon, J.; Calero, S.; Dubbeldam, D.; Vlugt, T. J. H.; Kapteijn, F.; Gross, J. *J. Phys. Chem. C* **2010**, *114*, 6877.

(37) Bueno-Perez, R.; García-Perez, E.; Gutierrez-Sevillano, J. J.; Merkling, P. J.; Calero, S. *Adsorpt. Sci. Technol.* **2010**, *28*, 823.

(38) Castillo, J. M.; Vlugt, T. J. H.; Calero, S. *J. Phys. Chem. C* **2009**, *113*, 20869.

(39) Reed, A. E.; Weinstock, R. B.; Weinhold, F. *J. Chem. Phys.* **1985**, *83*, 735.

(40) Frisch, M. J.; Trucks, G. W.; Schlegel, H. B.; Scuseria, G. E.; Robb, M. A.; Cheeseman, J. R.; Scalmani, G.; Barone, V.; Mennucci, B.; Petersson, G. A.; Gaussian, Inc.: Wallingford CT, 2009, p Gaussian 09.

(41) Morris, W.; Leung, B.; Furukawa, H.; Yaghi, O. K.; He, N.; Hayashi, H.; Houndonougbo, Y.; Asta, M.; Laird, B. B.; Yaghi, O. M. *J. Am. Chem. Soc.* **2010**, *132*, 11006.

(42) Pacios, L. F.; Gómez, P. C. *J. Mol. Struc. THEOCHEM* **2001**, *544*, 237.

(43) Jaeger, R.; Vancso, G. J. *Macromol. Theor. Simul.* **1996**, *5*, 673.

(44) Yerushalmi, R.; Scherz, A.; Baldridge, K. K. *J. Am. Chem. Soc.* **2004**, *126*, 5897.

(45) Nolan, E. M.; Linck, R. G. *J. Am. Chem. Soc.* **2000**, *122*, 11497.

(46) Carey, F. A.; Sundberg, R. J. *Advanced Organic Chemistry: Structure and mechanisms*; Springer: New York, 2007.

(47) Liu, T.; Zhu, W.; Gu, J.; Shen, J.; Luo, X.; Chen, G.; Puah, C. M.; Silman, I.; Chen, K.; Sussman, J. L.; Jiang, H. *J. Phys. Chem. A* **2004**, *108*, 9400.

(48) Ruzsinszky, A.; Alsenoy, C. V.; Csonka, G. I. *J. Phys. Chem. A* **2002**, *106*, 12139.

(49) Monev, V.; Spassova, M.; Champagne, B. *Int. J. Quantum Chem.* **2005**, *104*, 354.

(50) Levy, J. B. *Struct. Chem.* **1999**, *10*, 121.

(51) Gross, K. C.; Seybold, P. G.; Hadad, C. M. *Int. J. Quantum Chem.* **2002**, *90*, 445.

(52) Pacios, L. F.; Gómez, P. C.; Gálvez, O. *J. Comp. Chem.* **2006**, *27*, 1650.

(53) Tafipolsky, M.; Schmid, R. *J. Phys. Chem. B* **2009**, *113*, 1341.

(54) McDaniel, J. G.; Yu, K.; Schmidt, J. R. *J. Phys. Chem. C* **2012**, *116*, 1892.

(55) Amrouche, H.; Aguado, S.; Pérez-Pellitero, J.; Chizallet, C.; Siperstein, F.; Farrusseng, D.; Bats, N.; Nieto-Draghi, C. *J. Phys. Chem. C* **2011**, *115*, 16425.

(56) Fairen-Jimenez, D.; Seaton, N. A.; Duren, T. *Langmuir* **2010**, *26*, 14694.

(57) Tafipolsky, M.; Amirjalayer, S.; Schmid, R. *Micropor. Mesopor. Mat.* **2010**, *129*, 304.

(58) McDaniel, J. G.; Yu, K.; Schmidt, J. R. *J. Phys. Chem. C* **2012**, *116*, 1892.

(59) Sillar, K.; Sauer, J. *J. Am. Chem. Soc.* **2012**, *134*, 18354.

(60) Fischer, M.; Gomes, J. R. B.; Fröba, M.; Jorge, M. *Langmuir* **2012**, *28(22),* 8537.

(61) Chen, L.; Grajciar, L.; Nachtigall, P.; Düren, T. *J. Phys. Chem. C* **2011**, *115*, 23074.

(62) Chen, L.; Morrison, C. A.; Düren, T. *J. Phys. Chem. C* **2012**, *116*, 18899.

(63) Rankin, R. B.; Liu, J.; Kulkarni, A. D.; Johnson, J. K. *J. Phys. Chem. C* **2009**, *113*, 16906.

(64) Fairen-Jimenez, D.; Moggach, S. A.; Wharmby, M. T.; Wright, P. A.; Parsons, S.; Düren, T. *J. Am. Chem. Soc.* **2011**, *133*, 8900.

(65) Shen, D.; Bulow, M.; Siperstein, F.; Engelhard, M.; Myers, A. L. *Adsorpt. Sci. Technol.* **2000**, *6*, 275.

We report a molecular simulation study for Cu-BTC metal organic frameworks as carbon dioxide-methane separation devices. For this study we have computed adsorption and diffusion of methane and carbon dioxide in the structure, both as pure components and mixtures over the full range of bulk gas compositions. From the single component isotherms, mixture adsorption is predicted using the ideal adsorbed solution theory. These predictions are in very good agreement with our computed mixture isotherms and with previous reported data. Adsorption and diffusion selectivities and preferential sitings are also discussed with the aim to provide new molecular level information for all studied systems.

Juan José Gutiérrez-Sevillano, Alejandro Caro-Pérez, David Dubbeldam, and Sofía Calero

6

Performance of Cu-BTC Metal Organic Frameworks for Carbon Dioxide-Methane Separations

Introduction

The separation of carbon dioxide from mixtures containing methane is an important process from a scientific and industrial point of view. It is for this reason that a broad range of technologies and materials are being explored and developed on a daily basis. However, the commercialization of novel technologies and materials still faces important challenges, not only on the part that involves the technological and processes aspects, but also on the separation capabilities of the materials. This is one of the reasons why the search of adsorbents with tailored structures and tunable surface properties remains an imperative target.

Metal organic frameworks (MOFs) constitute an important group of porous crystalline adsorbents with tailorable cavities and surface areas[1-6]. They are nanoporous, molecule-based, hybrid materials built from metal-organic points and bridging ligands[3]. Up to date, there are thousands of MOFs catalogued in the Cambridge Crystallographic Data Center[7] but only a small percentage of them are porous and stable upon solvent removal.

The adsorption of mixtures is probably one of the most interesting potential applications of MOFs in industry. However, only a few MOFs have been assessed for their adsorptive separation performance, since experimental adsorption of mixtures is difficult and expensive[8-10]. Among them, Cu-BTC is

probably one of the most promising materials to be applied in technological applications[11-16]. Cu-BTC, also known as HKUST-1, is composed of benzene-1,3,5-tricarboxylate (BTC) ligands coordinating copper ions, forming large cavities and small octahedral cages that are accessible to small molecules through small windows[17]. The large and small cages are about 9 and 5 Å in diameter, respectively and the triangular window that connects the two types of cages is about 3.5 Å in diameter. The isocontour picture of the energy landscape of Cu-BTC is shown in Figure 1.

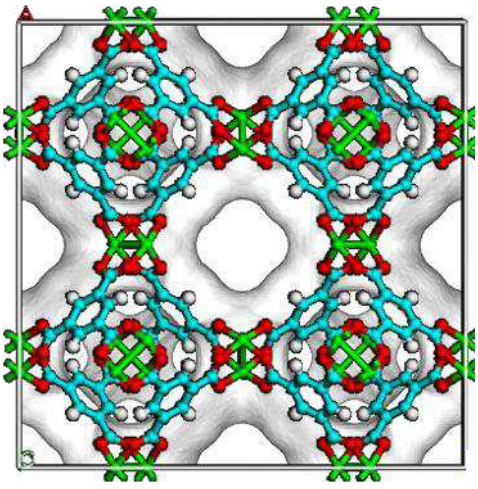

Figure 1. *Isocontour picture of energy landscape of Cu-BTC showing the big central cages (about 9 Å diameter) and the small octahedral cages (about 5 Å diameter) that are connected by windows of ~ 3.5 Å in diameter. The atomic structure is superimposed.*

When experimental data are unavailable molecular simulation becomes an indispensable tool to predict adsorption and shed light on the separation mechanisms that take place inside the pores[16,18-22]. The main advantages of using computational approaches are that simulations provide unique microscopic insight and perfect control on the conditions. In addition, simulations are cheap, allow the study of hypothetical structures, can be used as a prediction tool, and are an excellent complement to the experimental work. One of the first computational studies of carbon dioxide and methane separation in Cu-BTC were performed by Yang and Zhong[23-25]. Their simulations were carried out for an equimolar mixture, showing that the strength of electrostatic interactions between the open metal sites and the carbon dioxide as well as the geometry and pore size of the structure were responsible for the separation performance. In 2010 Jiang *et al.* showed by molecular simulations that small quantities of water in the structure (0.1% of water in the mixture) have a negligible effect on the separation of carbon dioxide and methane in Cu-BTC[26]. Interestingly, in an experimental and simulation study the addition of water in Cu-BTC does have a large effect on the pure component CO_2 isotherms[27].

In 2009 Keskin *et al.* used atomistic simulations and continuum modeling to compare the adsorption and diffusion selectivity of CO_2/methane. Based on these comparisons they proved that the overall performance of Cu-BTC for this mixture was dominated by the selectivity of adsorption[22]. In a recent publication we provided molecular simulation isotherms for a 10:90 mixture of carbon dioxide and methane[16], and to

the best of our knowledge these are to date, the only reported adsorption isotherms of non-equimolar mixtures of carbon dioxide-methane in Cu-BTC. The aim of this work is to cover the gap with a detailed simulation study which provides (1) full loading range adsorption and diffusion of methane and carbon dioxide Cu-BTC, both as pure components and mixtures, (2) prediction of mixture adsorption from the pure component isotherms using the ideal adsorbed solution theory, (3) comparison of our results with previous reported data, (4) adsorption and diffusion selectivities for the studied systems, and (5) providing molecular level information for all the systems obtained from the preferential siting of the molecules.

Methods and models

We use Monte Carlo (MC) and Molecular Dynamics (MD) simulations to study adsorption and diffusion of carbon dioxide and methane molecules as pure components and mixtures in Cu-BTC. The adsorption and diffusion selectivity values, and the mixture selectivity for carbon dioxide are analyzed. The bulk partial pressure ratios of CO_2 : CH_4 were (1 - 0.1 n) : (0.1 n), where n spans from 0, to 10. Simulations were performed at room temperature using a single unit cell (a = b = c = 26.343 Å, α=β=γ=90°) of Cu-BTC. The unit cell contains 624 atoms of which 48 are copper, 192 oxygen, 96 hydrogen and 288 carbon. The carbon atoms are classified in three groups depending on the neighbouring atoms, C*a*: next to two atoms of oxygen, C*b*: between three atoms of carbon, and C*c*: linked to one atom of hydrogen. The different environment of the neighbouring atoms lead to different charges for each carbon atom and are listed in Table 1. Detailed information about the crystallographically different atoms used in this work can be found elsewhere[14,16,19].

Table 1. *Lennard-Jones parameters and point charges used for Cu-BTC framework and adsobed molecules*[15,28-30 39-40].

Atom types	ε/k_B (K)	σ (Å)	Charge (e^-)
Cu-BTC			
MOF-Cu	2.518	3.114	1.248
MOF-Ob	48.19	3.03	-0.624
MOF-Ca	47.86	3,47	0.494
MOF-Cb	47.86	3.47	0.13
MOF-Cc	47.86	3.47	-0.156
MOF-H	7.65	2.85	0.156
Adsorbates			
C_CO_2	29.933	2.745	0.651
O_CO_2	85.671	3.017	-0.326
CH_4	158.5	3.72	-

The model that we use for carbon dioxide consists of three Lennard-Jones sites with charges centered at each atom. The carbon-oxygen bonds are rigid and the Lennard-Jones parameters have been fitted by Harris and Yung using Gibbs ensemble Monte Carlo simulations to reproduce the vapor-liquid coexistence curve[28-29]. For methane we use a united atom model[30] that considers the CH_4 group as single interaction centers with their own effective potentials. Details about the use of this type of models in MOFs and

related porous materials can be extensively found in literature[31-34].

The Cu-BTC framework is considered rigid. The use of rigid frameworks has been proven to be accurate enough when studying the adsorption of small molecules in this structure at room temperature[14-16,19-20,35]. Note that the development of reliable flexible models for MOFs is still extremely complex and that diffusion results when flexibility is included tend to depend on the used model. Moreover, in general, the flexibility is usually effectively included in the parametrization of rigid models. Therefore, if there are no large structural changes of the framework it is often desirable to use a rigid framework instead of a flexible model[36-38].

To model the interactions between the adsorbates and the framework we use van der Waals interactions. For carbon dioxide Coulombic interactions are also taken into account. The Lennard-Jones parameters are taken from the DREIDING[39] force field except those for Cu, that were taken from the UFF[40] force field. Lorentz-Berthelot mixing rules were used to calculate mixed Lennard-Jones parameters and the atomic charges for the MOF were taken from Castillo *et al.*[15]. The Lennard-Jones potential is truncated and shifted to zero at 12 Å. We obtained a helium void fraction of 0.76 for Cu-BTC. The crystal structure of Chui *et al.* includes axial oxygen atoms weakly bonded to the Cu atoms that correspond to water ligands. Our simulations have been performed on the dry Cu-BTC with these oxygen atoms removed. The complete set of parameters and charges used in this work for adsorbates and adsorbents is listed in (Table 1).

Monte Carlo and molecular dynamics calculations were performed using the RASPA code developed by D. Dubbeldam, S. Calero, D. E. Ellis, and R.Q. Snurr as basis. This code has been extensively tested and validated with a large number of experimental and simulation data[14-15,19,29,35,38,41-44].

The self-diffusion coefficients were obtained by calculating the slope of the mean-squared displacement at long times[45]. In these simulations the velocity-Verlet algorithm was used to integrate Newton's Law of motion. We performed MD simulations of 10^7 cycles in the NVT ensemble (Nose-Hoover chain thermostat) at 298K using a time step of 0.5 fs and keeping the atoms of the framework fixed. We used 10^4 equilibration cycles and we took the initial positions of the molecules from previous MC simulations.

The adsorption isotherms were computed using Grand Canonical Monte Carlo (GCMC) simulations at 298 K. Pressure was converted into fugacity using the Peng-Robinson equation of state. The MC moves were performed in cycles and in each cycle one of the following trial moves was selected at random for a given molecule: translation, rotation, reinsertion at a random position, insertion, deletion, and identity change. We used at least 10^9 Monte Carlo moves. Coulombic interactions were computed using the

Ewald summation with a relative precision of 10^{-6}.

The Ideal Adsorbed Solution Theory (IAST) of Myers and Prausnitz[46] was developed to predict the properties of adsorbed mixtures using single component isotherms as input. The main advantage of this model is that it does not require any mixture data and it is independent of the actual model of physical adsorption. IAST calculations are accurate enough for mixtures of light gases in MOFs[24,47-49], but they fail when the studied mixture differs strongly in chemical characteristics[50].

In this work we applied the isotherm equation proposed by Jensen and Seaton for type I adsorptions[51]:

$$n(P) = KP\left[1 + \left(\frac{KP}{a(1+\kappa P)}\right)^{c}\right]^{-1/c}$$

where we first fitted the four parameters of the equation (K, c, a, and κ) to the pure components excess adsorption isotherms and then we applied IAST to obtain the mixture adsorption isotherms.

Results and discussion

Figure 2 shows the agreement between the computed and experimental adsorption isotherms for carbon dioxide and methane in Cu-BTC at 298 K[16,23,52-61]. The adsorption isotherms are obtained as a function of the pressure and they are given in mol of adsorbed molecule per gram of structure and also in molecules adsorbed in a given unit cell. Our simulations provide absolute adsorption, which can be compared with experimental isotherms if it is corrected for excess adsorption. The excess adsorption is the average number of molecules in the pores minus the number of molecules that would occupy the free pore volume at bulk-gas conditions[62-63]. The excess (n_{ex}) and the absolute adsorption (n_{abs}) are related by the expression ($n_{ex} = n_{abs} - V^g\rho^g$), where V^g is the pore volume and ρ^g is the gas-phase density. The pore volume was computed from Monte Carlo simulations[64]. The obtained value is 0.848 cm^3/g, in very good agreement with the experimental value of 0.828 cm^3/g reported by Liu *et al.*[65]

Figure 2 shows some discrepancies on adsorption between different groups. These discrepancies have been attributed to the differences between simulation and experimental surface areas and pore volumes and therefore implicitly to the quality of the MOF samples. The adsorption isotherms obtained using simulations tend to overpredict the experimental amount adsorbed. This is expected since simulations use perfect, infinite crystalline structures, whereas the quality of the experimental sample depends on the synthesis and the activation processes that can result in partial framework collapse, contamination with catenations, or pore blockage by solvent and unreacted molecules.

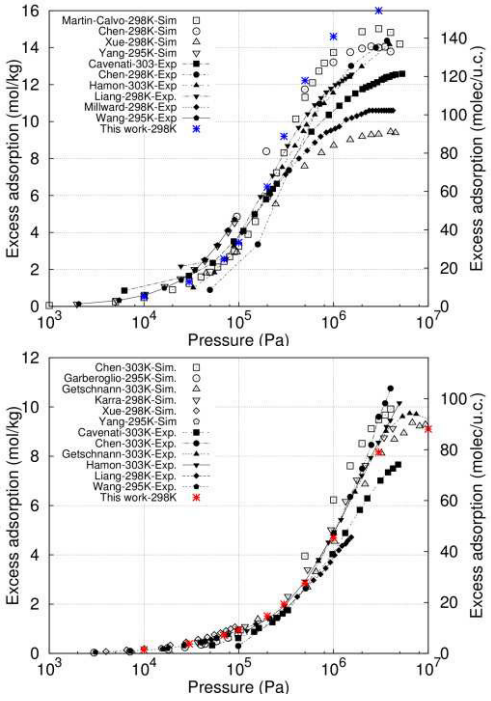

Figure 2. *Excess adsorption isotherms of (top) carbon dioxide and (bottom) methane in Cu-BTC at 298 K. The values obtained in this work are compared with previous experimental and simulation data*[16,23,52-60,70].

Previous works reported that the adsorption of polar molecules such as water is very sensitive to the set of charges used for the structure[15,66-67]. In this work methane has been modeled as a non-charged molecule, and therefore its adsorption is not affected by the set of point charges used for Cu-BTC. However, the adsorption of carbon dioxide can be affected by the selection of the point charges, since this molecule is modeled with point charges to reproduce its quadrupole moment. To analyze the sensitivity of the adsorption of carbon dioxide to the set of charges selected for the structure we additionally compare our computed values –obtained with the set of charges reported in reference 15– with previous simulation data obtained with different sets of charges[16,21,23,52-58]. The comparison shows that the adsorption is not very sensitive to the set of charges used for the structure at this temperature. This was observed for the adsorption isotherms of carbon dioxide obtained in both, pure component simulations (Figure 2 top) and equimolar mixtures (Figure 3).

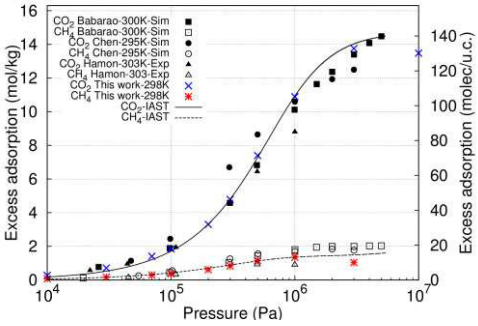

Figure 3. *Excess adsorption isotherms for the equimolar mixture obtained from GCMC (symbols) and from IAST (curves) at 298 K in Cu-BTC. The values obtained in this work are compared with previous experimental and simulation data*[21,52,55]

Figure 3 shows the computed adsorption isotherms for an equimolar mixture of carbon dioxide and methane in Cu-BTC at 298 K. The agreement between the IAST and the calculated mixture isotherms was found to be good for the equimolar mixture in Cu-BTC[24]. We have performed IAST calculations not only to check the agreement with our computed equimolar mixture (Figure 3),

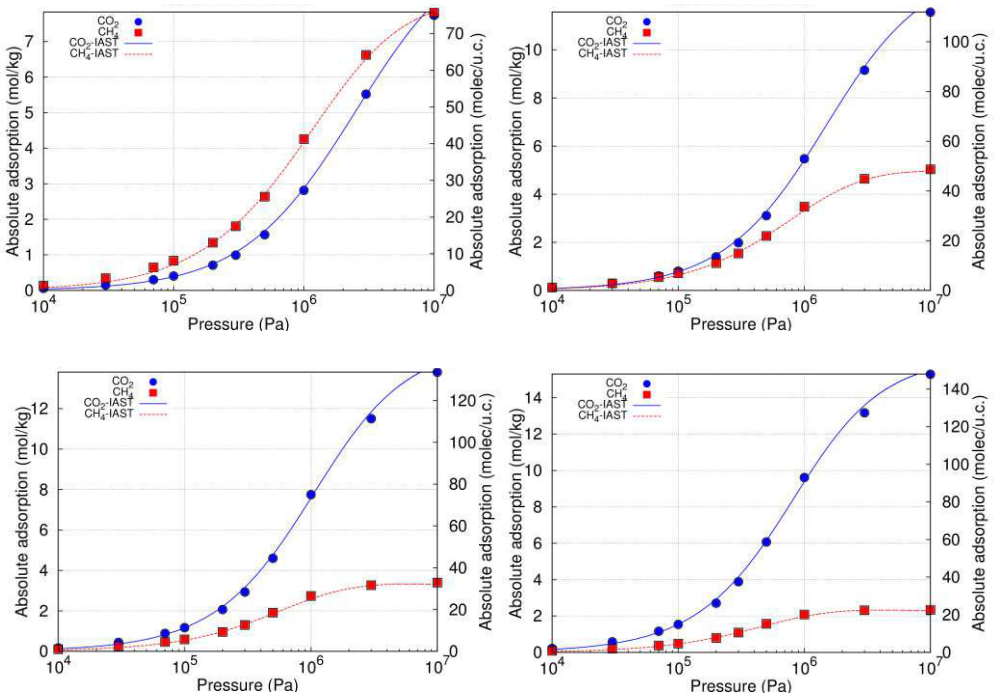

Figure 4. *Absolute adsorption isotherms obtained from GCMC (symbols) and from IAST (curves) for the mixtures with bulk partial pressure ratios of CO_2:CH_4 were (1 - 0.1 n) : (0.1 n), where n spans from 9, to 6 (from left to right and top to bottom) in Cu-BTC at 298 K.*

but also to verify that similar agreement can be obtained for mixtures with other bulk compositions (Figures 4 and 5). The adsorption isotherms show the expected trends, i.e. except for the 0.1:0.9 CO_2:CH_4 mixture, the adsorption of carbon dioxide is always higher than the adsorption of methane, and it becomes larger as the carbon dioxide composition in the bulk increases. Detailed isotherms showing this trend can be found in the Appendix 4 (Figures A4.1a and A4.1b).

According to our simulation results for all mixtures of methane and carbon dioxide, the latter molecule preferentially adsorbs in Cu-BTC. This is due to the stronger interactions between this molecule and the structure. The adsorption sites of carbon dioxide and methane in Cu-BTC obtained from our simulations are in agreement with those reported in the literature[15-16,21]. At low pressures these molecules are preferentially adsorbed in the interior of the octahedral cages and only a few molecules adsorb in the neighbourhood of the metal of the framework. The octahedral cages are first saturated with carbon dioxide molecules, followed by adsorption around the exposed metal sites and organic linkers. At the highest pressures the large central cages become filled with both types of molecules. The siting of methane and carbon dioxide

molecules during adsorption of the equimolar mixture follows similar trend that when they are computed as pure component[16]. The octahedral cages and the region that separates these cages from the large ones are the preferential adsorption sites. At higher pressures and once the octahedral cages are full, the large central cages become preferential adsorption site. Figure 6 depicts the average occupation profiles obtained for the single components and for the equimolar mixture at a total pressure of 3000 kPa. Similar average profiles were obtained for the mixtures at bulk composition other than 50:50. These profiles were obtained from the average values (averaged over all configurations) of the projections of the centre of mass coordinates over the x-y plane. Due to the symmetry of the system, the profile over the x-y plane is the same as the profiles obtained projecting the coordinates over the x-z or y-z planes.

The adsorption selectivity for CO_2 relative to CH_4 is defined as $(x_{CO2}/y_{CO2})/(x_{CH4}/y_{CH4})$, where x_{CO2} and x_{CH4} are the molar fractions in the adsorbed phase and y_{CO2} and y_{CH4} are the molar fractions in the bulk phase. Selectivities were computed for the 50:50 (Figure 7) and for all CO_2/CH_4 bulk compositions considered in this work (Figure A4.2 in the Appendix 4). In all cases the

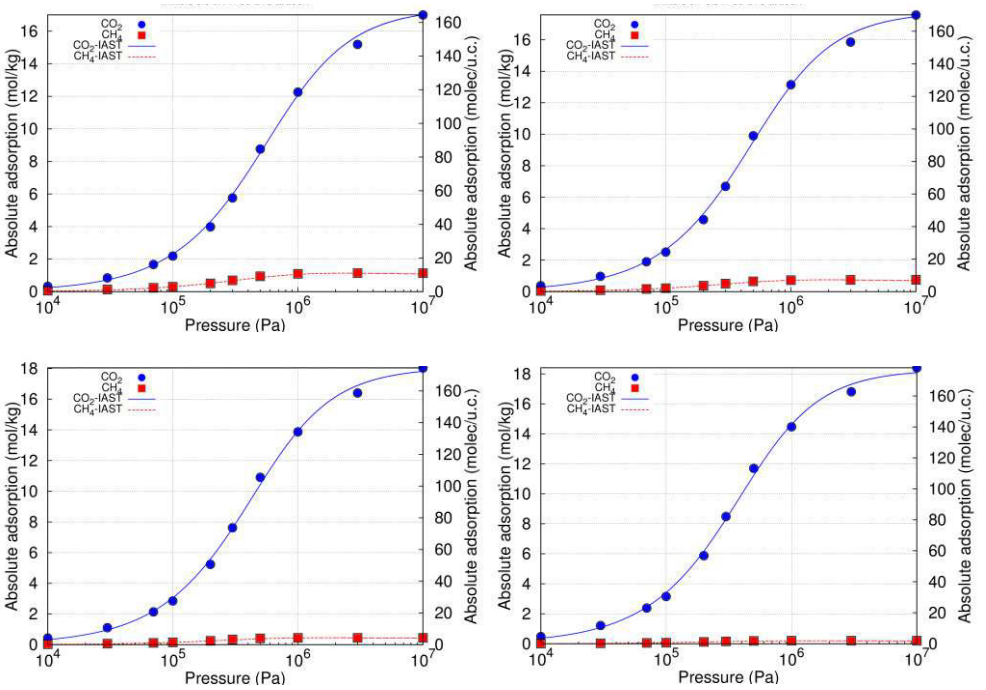

Figure 5. *Absolute adsorption isotherms obtained from GCMC (symbols) and from IAST (curves) for the mixtures with bulk partial pressure ratios of CO_2:CH_4 were (1 - 0.1 n) : (0.1 n), where n spans from 4, to 1 (from left to right and top to bottom) in Cu-BTC at 298 K.*

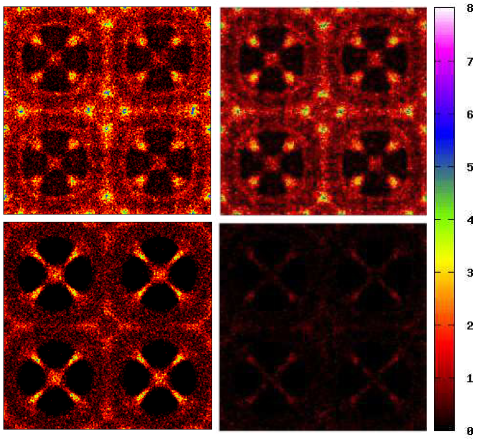

Figure 6. *Average occupation profiles of carbon dioxide (top) and methane (bottom) in Cu-BTC at 298 K and 10^3 kPa. The profiles were obtained from the molecular simulations of pure components (left) and equimolar mixtures (right). The same color gradation (from dark to light) is employed in all figures, although the total number of molecules present in the unit cell is different for each calculation.*

adsorption of carbon dioxide is higher than the adsorption of methane due to the stronger interactions between the carbon dioxide molecules and the adsorption surfaces. Previously reported data[21-23,52-53,55,68] –only available for the 50:50 equimolar mixture– were added for comparison, showing a reasonable agreement if we consider the scattering in data reported by the different groups. It is also important to note that very small deviation in the number of adsorbed molecules may result in a larger deviation in the adsorption selectivity. The high selectivity in favor of carbon dioxide increases with increasing pressure due to

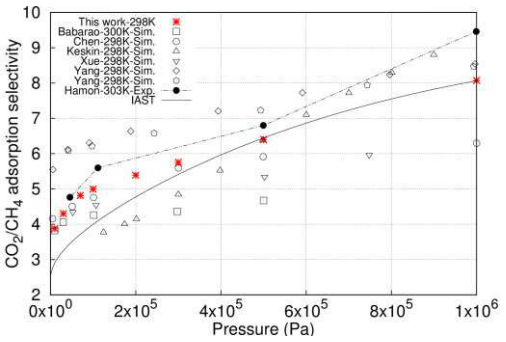

Figure 7. *Adsorption selectivity for the equimolar mixture of carbon dioxide and methane obtained from GCMC (asterisks) and from IAST (curves). Available experimental and simulation data are included for comparison*[21-24,52-53,55].

the combination of two effects: the electrostatic interactions between carbon dioxide and the framework, and the strong confinement effects in the octahedral cages of Cu-BTC[16].

Figure 8 shows the adsorbed fractional content of both, methane and carbon dioxide, against the same fraction in the external gas phase computed at room conditions (298 K and 1 atmosphere of pressure). The curves indicate that the ratio carbon dioxide/methane in the adsorbed phase is higher than in the gas phase. At these conditions, an adsorbed fractional content of 0.5 is reached for mole fractions of methane and carbon dioxide in the external gas of 0.816 and 0.184, respectively. The methane mole fraction increases slightly with the increase of pressure and it varies from 0.786 at 10^4 Pa to 0.9 at 10^7 Pa (Figure 9). These values were taken from the adsorbed

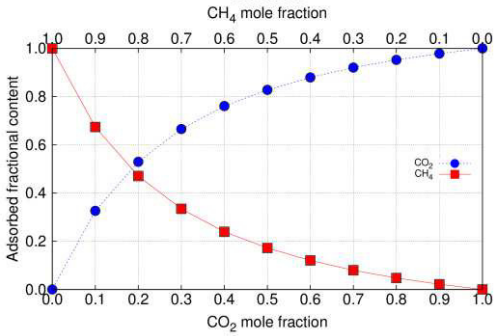

Figure 8. *Adsorbed fractional content of molecule plotted as a function of the fraction in the external gas phase computed at ambient conditions.*

fractional content against the same fraction in the external gas phase computed for the whole range of pressures, and the obtained figures are collected in the Appendix 4 (Figures A4.3-A4.5).

The computed self-diffusivities values for the equimolar and non-equimolar mixtures as a function of pressure are shown in Figure 10 and Figure A4.6 of the Appendix 4, respectively. Self diffusivity values for

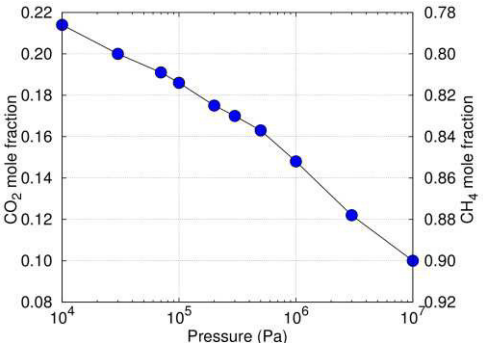

Figure 9. *Mole fractions of methane and carbon dioxide in the external gas corresponding to an adsorbed fractional content of 0.5 at 298 K.*

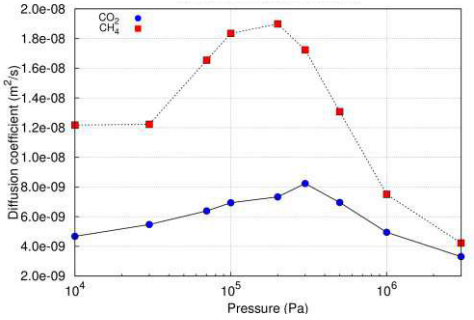

Figure 10. *Self diffusion coefficients computed as a function of pressure at 298 K in Cu-BTC for the equimolar mixture of carbon dioxide and methane.*

methane-carbon dioxide mixtures with a total loading of 60 and 110 molecules per unit cell are also depicted in Figure 11. In all cases the diffusion coefficients obtained for methane are higher than those obtained for carbon dioxide. However, in the systems with a fixed number of adsorbed molecules, the diffusion of methane decreases when increases the methane mole fraction while the diffusion of carbon dioxide remains almost constant with loading. To quantify mixture diffusion we calculated diffusion selectivity as the ratio of the diagonal Fickian diffusivities computed by the SSK method[69]. The diffusion selectivity is shown in Figure 11, where we have also added for comparison the value reported by Keskin *et al.* at the same simulation conditions[22]. As shown in the figure, the diffusion selectivity values are almost constant for the systems with 60 molecules (around 2.25), whereas for the systems with 110 molecules they decrease from 2 (for the system with 96 molecules of methane and 14 molecules of carbon dioxide) to 1.5 (for the system

with 14 molecules of methane and 96 molecules of carbon dioxide). Hence, at high loadings, the molecules adsorbed in the structure reduce the diffusivity of the more mobile component in an adsorbed mixture. Additional comparison of our simulation data and previous simulation results reported by Keskin *et al.* for the situation where the feed gas is an equimolar mixture is included in the Appendix 4 (Figure A4.7).

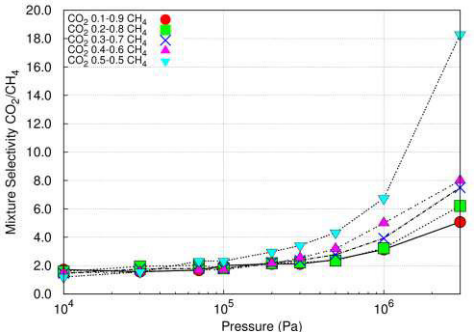

Figure 12. *Mixture selectivity of mixtures containing carbon dioxide and methane in Cu-BTC at 298 K*

Figure 12 indicates the contribution of the adsorption and the diffusion of the overall selectivity of the structure. The mixture selectivities were obtained from the product of the adsorption and the diffusion selectivity for all feed gas mixture compositions. According to our results, the mixture adsorption is always in favor of carbon dioxide, though it remains almost constant for a wide pressure range. This is attributed to the fact that adsorption selectivity favors carbon dioxide over methane, whereas

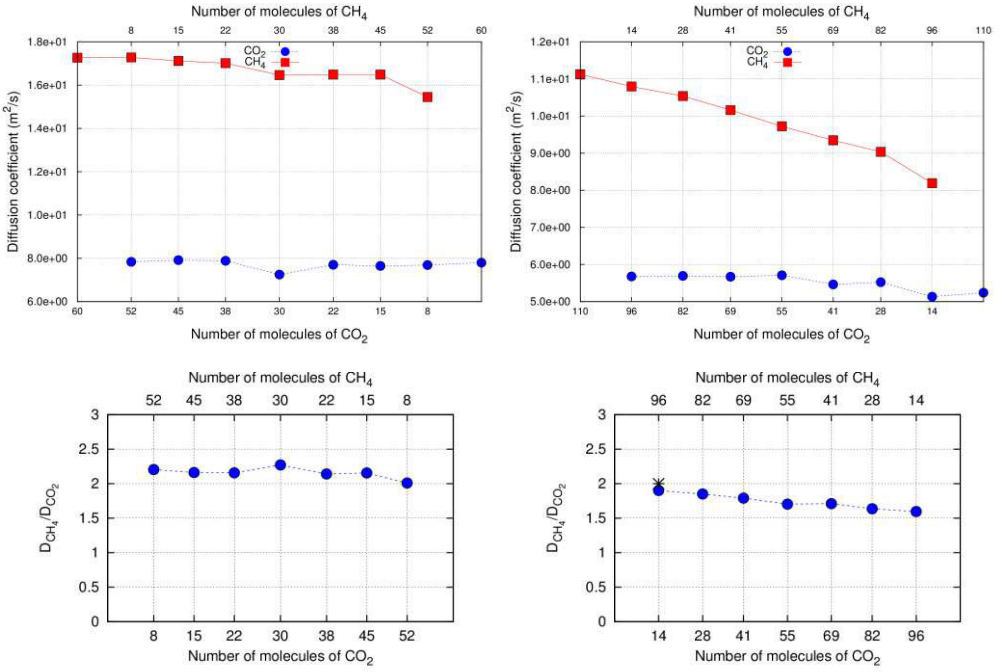

Figure 11. *Diffusion coefficients (top) and diffusion coefficient selectivity (bottom) as a function of the number of carbon dioxide and methane molecules adsorbed in Cu-BTC for a total loading of (a) 60 molecules per unit cell and (b) 110 molecules per unit cell.*

diffusion selectivity follows the opposite trend. At the highest pressures, carbon dioxide adsorbs strongly in the structure, reducing the diffusion rate of methane and leading to an increase of the mixture selectivity in favor of the less mobile specie.

Conclusions

We have used molecular simulations and Ideal Adsorbed Solution Theory to study the separation behavior of carbon dioxide and methane mixtures in Cu-BTC. This behavior is directly related to the differences in polarizability of each molecule. The diffusion selectivity is in favor of methane, while the adsorption strongly favors carbon dioxide over methane. The comparison of the diffusion and adsorption selectivities indicates that the overall performance of this MOF for separation of carbon dioxide from the carbon dioxide/methane mixtures is dominated by the adsorption.

Bibliography

(1) Eddaoudi, M.; Kim, J.; Rosi, N.; Vodak, D.; Wachter, J.; O'Keefe, M.; Yaghi, O. M. *Science* **2002**, *295*, 469.

(2) James, S. L. *Chemical Society Reviews* **2003**, *32*, 276.

(3) Yaghi, O. M.; O'Keeffe, M.; Ockwig, N. W.; Chae, H. K.; Eddaoudi, M.; Kim, J. *Nature* **2003**, *423*, 705.

(4) Kitagawa, S.; Kitaura, R.; Noro, S. *Angewandte Chemie-International Edition* **2004**, *43*, 2334.

(5) Ferey, G. *Chemical Society Reviews* **2008**, *37*, 191.

(6) Bourrelly, S.; Llewellyn, P. L.; Serre, C.; Millange, F.; Loiseau, T.; Ferey, G. *Journal of the American Chemical Society* **2005**, *127*, 13519.

(7) database, C. In *The Cambridge Crystallographic Data Centre via* www.ccdc.cam.ac.uk/data_request/cif.

(8) Czaja, A. U.; Trukhan, N.; Muller, U. *Chemical Society Reviews* **2009**, *38*, 1284.

(9) Li, J. R.; Ma, Y.; McCarthy, M. C.; Sculley, J.; Yu, J.; Jeong, H. K.; Balbuena, P. B.; Zhou, H. C. *Coordination Chemistry Reviews* **2011**, *255(15-16)*, 1791

(10) Kuppler, R. J.; Timmons, D. J.; Fang, Q. R.; Li, J. R.; Makal, T. A.; Young, M. D.; Yuan, D. Q.; Zhao, D.; Zhuang, W. J.; Zhou, H. C. *Coordination Chemistry Reviews* **2009**, *253*, 3042.

(11) Li, J. R.; Kuppler, R. J.; Zhou, H. C. *Chemical Society Reviews* **2009**, *38*, 1477.

(12) Keskin, S.; van Heest, T. M.; Sholl, D. S. *Chemsuschem* **2010**, *3*, 879.

(13) Duren, T.; Bae, Y. S.; Snurr, R. Q. *Chemical Society Reviews* **2009**, *38*, 1237.

(14) Calero, S.; Martin-Calvo, A.; Hamad, S.; Garcia-Perez, E. *Chemical Communications* **2011**, *47*, 508.

(15) Castillo, J. M.; Vlugt, T. J. H.; Calero, S. *Journal of Physical Chemistry C* **2008**, *112*, 15934.

(16) Martin-Calvo, A.; Garcia-Perez, E.; Castillo, J. M.; Calero, S. *Physical Chemistry Chemical Physics* **2008**, *10*, 7085.

(17) Chui, S. S. Y.; Lo, S. M. F.; Charmant, J. P. H.; Orpen, A. G.; Williams, I. D. *Science* **1999**, *283*, 1148.

(18) Krishna, R.; van Baten, J. A. *Langmuir* **2010**, *26*, 3981.

(19) Garcia-Perez, E.; Gascon, J.; Morales-Florez, V.; Castillo, J. M.; Kapteijn, F.; Calero, S. *Langmuir* **2009**, *25*, 1725.

(20) Babarao, R.; Jiang, J. W. *Langmuir* **2008**, *24*, 5474.

(21) Babarao, R.; Jiang, J. W.; Sandler, S. I. *Langmuir* **2009**, *25*, 5239.

(22) Keskin, S.; Liu, J. C.; Johnson, J. K.; Sholl, D. S. *Microporous and Mesoporous Materials* **2009**, *125*, 101.

(23) Yang, Q. Y.; Zhong, C. L. *Chemphyschem* **2006**, *7*, 1417.

(24) Yang, Q. Y.; Zhong, C. L. *Journal of Physical Chemistry B* **2006**, *110*, 17776.

(25) Banerjee, R.; Phan, A.; Wang, B.; Knobler, C.; Furukawa, H.; O'Keeffe, M.; Yaghi, O. M. *Science* **2008**, *319*, 939.

(26) Nalaparaju, A.; Zhao, X. S.; Jiang, J. W. *Journal of Physical Chemistry C* **2010**, *114*, 11542.

(27) Yazaydin, A. O.; Benin, A. I.; Faheem, S. A.; Jakubczak, P.; Low, J. J.; Willis, R. R.; Snurr, R. Q. *Chemistry of Materials* **2009**, *21*, 1425.

(28) Harris, J. G.; Yung, K. H. *Journal of Physical Chemistry* **1995**, *99*, 12021.

(29) Garcia-Sanchez, A.; Ania, C. O.; Parra, J. B.; Dubbeldam, D.; Vlugt, T. J. H.; Krishna, R.; Calero, S. *Journal of Physical Chemistry C* **2009**, *113(20),* 8814.

(30) Ryckaert, J. P.; Bellemans, A. *Faraday Discussions* **1978**, *66*, 95.

(31) Dubbeldam, D.; Calero, S.; Vlugt, T. J. H.; Krishna, R.; Maesen, T. L. M.; Beerdsen, E.; Smit, B. *Physical Review Letters 93(8), 88302.*.

(32) Dubbeldam, D.; Calero, S.; Vlugt, T. J. H.; Krishna, R.; Maesen, T. L. M.; Smit, B. *Journal of Physical Chemistry B* **2004**, *108*, 12301.

(33) Dubbeldam, D.; Galvin, C. J.; Walton, K. S.; Ellis, D. E.; Snurr, R. Q. *Journal of the American Chemical Society* **2008**, *130*, 10884.

(34) Vlugt, T. J. H.; Zhu, W.; Kapteijn, F.; Moulijn, J. A.; Smit, B.; Krishna, R. *J. Am. Chem. Soc.* **1998**, *120*, 5599.

(35) Martin-Calvo, A.; Garcia-Perez, E.; Garcia-Sanchez, A.; Hamad-Gomez, S.; Calero, S. *Physical Chemistry Chemical Physic* **2011,** 13(23)**,** 11165.

(36) Dubbeldam, D.; Walton, K. S.; Ellis, D. E.; Snurr, R. Q. *Angewandte Chemie-International Edition* **2007**, *46*, 4496.

(37) Rosenbach, N.; Ghoufi, A.; Deroche, I.; Llewellyn, P. L.; Devic, T.; Bourrelly, S.; Serre, C.; Ferey, G.; Maurin, G. *Physical Chemistry Chemical Physics* **2010**, *12*, 6428.

(38) Garcia-Sanchez, A.; Dubbeldam, D.; Calero, S. *Journal of Physical Chemistry C* **2010**, *114*, 15068.

(39) Mayo, S. L.; Olafson, B. D.; Goddard, W. A. *Journal of Physical Chemistry* **1990**, *94*, 8897.

(40) Rappe, A. K.; Casewit, C. J.; Colwell, K. S.; Goddard, W. A.; Skiff, W. M. *Journal of the American Chemical Society* **1992**, *114*, 10024.

(41) Kuhn, J.; Castillo-Sanchez, J. M.; Gascon, J.; Calero, S.; Dubbeldam, D.; Vlugt, T. J. H.; Kapteijn, F.; Gross, J. *Journal of Physical Chemistry C* **2010**, *114*, 6877.

(42) Bueno-Perez, R.; García-Perez, E.; Gutierrez-Sevillano, J. J.; Merkling, P. J.; Calero, S. *Adsorpt. Sci. Technol.* **2010**, *28*, 823.

(43) Castillo, J. M.; Vlugt, T. J. H.; Calero, S. *Journal of Physical Chemistry C* **2009**, *113*, 20869.

(44) Garcia-Perez, E.; Parra, J. B.; Ania, C. O.; Dubbeldam, D.; Vlugt, T. J. H.; Castillo, J. M.; Merkling, P. J.; Calero, S. *Journal of Physical Chemistry C* **2008**, *112*, 9976.

(45) Dubbeldam, D.; Ford, D. C.; Ellis, D. E.; Snurr, R. Q. *Molecular Simulation* **2009**, *35*, 1084.

(46) Myers, A. L.; Prausnitz, J. M. *Aiche Journal* **1965**, *11*, 121.

(47) Keskin, S.; Liu, J. C.; Johnson, J. K.; Sholl, D. S. *Langmuir* **2008**, *24*, 8254.

(48) Liu, D. H.; Zhong, C. L. *Journal of Materials Chemistry* **2010**, *20*, 10308.

(49) Babarao, R.; Hu, Z. Q.; Jiang, J. W.; Chempath, S.; Sandler, S. I. *Langmuir* **2007**, *23*, 659.

(50) Chen, H. B.; Sholl, D. S. *Langmuir* **2007**, *23*, 6431.

(51) Jensen, C. R. C.; Seaton, N. A. *Langmuir* **1996**, *12*, 2866.

(52) Chen, Y. F.; Lee, J. Y.; Babarao, R.; Li, J.; Jiang, J. W. *Journal of Physical Chemistry C* **2010**, *114*, 6602.

(53) Xue, C. Y.; Yang, Q. Y.; Zhong, C. L. *Molecular Simulation* **2009**, *35*, 1249.

(54) Cavenati, S.; Grande, C. A.; Rodrigues, A. E. *Industrial & Engineering Chemistry Research* **2008**, *47*, 6333.

(55) Hamon, L.; Jolimaitre, E.; Pirngruber, G. D. *Industrial & Engineering Chemistry Research* **2010**, *49*, 7497.

(56) Liang, Z. J.; Marshall, M.; Chaffee, A. L. *Greenhouse Gas Control Technologies 9* **2009**, *1*, 1265.

(57) Millward, A. R.; Yaghi, O. M. *Journal of the American Chemical Society* **2005**, *127*, 17998.

(58) Wang, Q. M.; Shen, D. M.; Bulow, M.; Lau, M. L.; Deng, S. G.; Fitch, F. R.; Lemcoff, N. O.; Semanscin, J. *Microporous and Mesoporous Materials* **2002**, *55*, 217.

(59) Garberoglio, G.; Skoulidas, A. I.; Johnson, J. K. *Journal of Physical Chemistry B* **2005**, *109*, 13094.

(60) Getzschmann, J.; Senkovska, I.; Wallacher, D.; Tovar, M.; Fairen-Jimenez, D.; Duren, T.; van Baten, J. M.; Krishna, R.; Kaskel, S. *Microporous and Mesoporous Materials* **2010**, *136*, 50.

(61) Karra, J. R.; Walton, K. S. *Journal of Physical Chemistry C* **2010**, *114*, 15735.

(62) Macedonia, M. D.; Moore, D. D.; Maginn, E. J. *Langmuir* **2000**, *16*, 3823.

(63) Myers, A. L.; Monson, P. A. *Langmuir* **2002**, *18*, 10261.

(64) Walton, K. S.; Snurr, R. Q. *Journal of the American Chemical Society* **2007**, *129*, 8552.

(65) Liu, J. C.; Culp, J. T.; Natesakhawat, S.; Bockrath, B. C.; Zande, B.; Sankar, S. G.; Garberoglio, G.; Johnson, J. K. *Journal of Physical Chemistry C* **2007**, *111*, 9305.

(66) Chen, Y. F.; Babarao, R.; Sandler, S. I.; Jiang, J. W. *Langmuir* **2010**, *26*, 8743.

(67) Babarao, R.; Jiang, J. W. *Journal of Physical Chemistry C* **2009**, *113*, 18287.

(68) Yang, Q. Y.; Zhong, C. L. *Journal of Physical Chemistry B* **2006**, *110*, 655.

(69) Skoulidas, A. I.; Sholl, D. S.; Krishna, R. *Langmuir* **2003**, *19*, 7977.

We use molecular simulations to analyze the preferential adsorption sites of molecules that differ in size, shape, and polarity in Cu-BTC Metal Organic Framework. The cage system of the framework can be exploited to enhance adsorption of small gases. We find that non polar molecules adsorb preferentially in the small tetrahedral cages while alcohols and water molecules adsorb close to the copper atoms in one of the big cages. Blocking potentially enhances selective adsorption and separation and we therefore investigate how to block these cages in a practical manner. We propose to use ionic liquids for it and we find that the addition of these components reduces the adsorption of polar molecules near the open metal centers. For this reason the presence of ionic liquids reduces the attack of the molecules of water to the metallic centers improving the framework stability.

7

Juan José Gutiérrez-Sevillano, José Manuel Vicent-Luna, David Dubbeldam, and Sofía Calero

On the Molecular Mechanisms for Adsorption in Cu-BTC Metal Organic Framework

Introduction

Metal organic frameworks (MOFs) are hybrid materials where atoms or small clusters of metal sites are linked by multi-functional organic linkers forming one-, two-, or three-dimensional structures. The combination of inorganic metals and organic synthetic linkers results in a large diversity of MOFs. In many cases it is possible to remove solvent molecules from internal voids, leaving open microstructures with high porosities and surface areas. Such porous materials have large potential as new adsorbents and catalysts, since -in principle- it should be possible to use conventional organic procedures to introduce a variety of functional groups, and thus tailor the affinity towards reactants and host molecules.

Among MOFs, Cu-BTC is a reference material widely studied both experimentally[1-5] and theoretically[6-12]. This structure, also known as HKUST-1, was firstly synthesized by Chui *et al.*[13] It has paddle-wheel type metal corners connected by benzene-1,3,5-tricarboxylate (BTC) linkers. Each metal corner contains two copper atoms that are bonded to the oxygen atoms of four BTC linkers forming four-connected square-planar vertexes. The advantage of this system is that it can be synthesized quite easily. The remaining axial coordination sites, usually referred to as open metal sites[14-

[25] are stable after exposure to liquid water[4,7,26-29] and can be particularly suitable for the adsorption and separation of gasses[29-30] and for catalysis[31]. In addition, the partial positive charges on the copper metal sites in Cu-BTC have the potential to enhance adsorption properties, offering extra binding sites to the guest gas molecules. This is particularly important for the adsorption of small molecules such as hydrogen[16,32-33] and to improve adsorption selectivities for separating mixtures with molecules of different polarities, especially at low pressures[25,34-36].

A schematic representation of Cu-BTC is shown in Figure 1. This structure is formed by two types of large central cavities of 9 Å in diameter (L_2 and L_3) surrounded by small cavities (T_1) of 5 Å in diameter. In addition we define two more sites that correspond to the triangular shaped apertures that connect T_1 and L_3 (T_w) and the windows connecting the large cavities L_2 and L_3 (L_w)[37]. The accessibility of these sites has been proven both experimentally[38-39] and with molecular simulations[40].

The cavities L_2 and L_3 are similar in size and shape but only L_3 has open copper sites pointing into the pore. This characteristic implies that the adsorption properties of Cu-BTC could be given by both, unspecific van der Waals interactions that play a relevant role at high coverage, and specific interactions due to the copper atoms that might offer extra binding sites to the adsorbed molecules at low coverages[35-36,41].

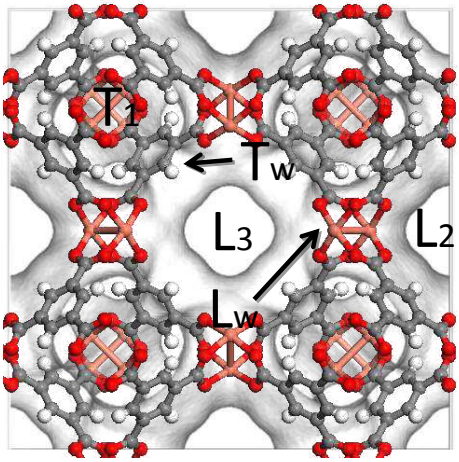

Figure 1. *Energy landscape and atomic structure showing the preferential adsorption sites of Cu-BTC.*

The combined presence of sites overlooking the cages and a framework topology characterized by cages of different sizes seems to be the key point to show very promising adsorption properties on a large variety of adsorbates. The interest in this area is broad, ranging from industrial applications on gas separation to environmental applications on gas capture[42]. For this reason great efforts are being made to improve the synthesis and activation of Cu-BTC experimentally[43-44] and from molecular simulations[45-46]. In spite of these efforts, the role played by the open metal sites during adsorption is not fully understood and more research is needed to address details of the adsorbate-adsorbent interactions at the low, medium and high coverage regime. In this regard we report a theoretical analysis of the preferential adsorption sites of Cu-BTC for molecules that

differ in size, shape, and polarity. Our theoretical approach elucidates the adsorption mechanisms that take place in this particular MOF for a wide variety of gases and leads to practical strategies for control of pore, windows sizes, and structural tuning.

Methods and Models

We used Monte Carlo (MC) simulations in the NVT ensemble and in the Grand Canonical (GC) Ensemble. Simulations were performed at 295 K. The volume of the structure is 18280.2 $Å^3$ that corresponds to a simulation cell of a = b = c = 26.343 Å, with computed helium void fraction 0.76. The pore volume and the surface area obtained for this system are 0.8482 cm^3/g and 2344.4 m^2/g respectively, in good agreement with experimental values given by Liu *et al.*[47]. Simulations were carried out for methane, ethane, propane, butane, propene, argon, nitrogen, oxygen, carbon dioxide, methanol, ethanol, propanol, and water. For each type of molecules we performed 29 NVT MC simulations by fixing the number of molecules with values that span from 4 to 192 molecules per unit cell. Monte Carlo simulations consists on at least of $2 \cdot 10^5$ equilibration cycles and $2 \cdot 10^6$ production cycles. In each cycle one of the following trial moves is randomly selected: regrow, rotation, and translation. Additionally, in the Grand Canonical ensemble moves of insertion and deletion are performed. We used Lennard-Jones and electrostatic cutoffs of 12.0 Å. Coulombic interactions were computed using the Ewald summation technique with a relative precision of 10^{-6}.

Additional MC simulations in the Grand Canonical ensemble were performed to obtain the saturation value for all the systems. MC simulations with ionic liquids were performed in the NVT keeping ionic liquids confined in L_3 cages.

The framework was modeled based on the crystal structure of Chui *et al.*[13]. Cu-BTC shows five preferential sites of adsorption (Figure 1): small tetrahedral cages that we define as spheres with 9.5 Å in diameter (T_1); large cages defined as spheres of 12 Å in diameter centered at the pore with inner surface conformed by the benzene rings (L_2), or located at the pores with the copper atoms of BTC pointing into the center of the pore (L_3); windows that communicate cages T_1 and L_3, as a crown surrounding sites T_1 with radius of 1.8 Å larger than T_1 (T_w). The rest of molecules would be considered as located at the windows that communicate the big cages (L_w).

For methane, ethane, propane, butane, propene, methanol, ethanol, and propanol we used united atom models that consider the CH_4, CH_3, $CH_2(sp^3)$, $CH_2(sp^2)$, and $CH(sp^2)$ as single interaction centers with their own effective potentials[48-50]. To reproduce the dipole moment of propene we use a point charge model with two positive charges located in the $CH_2(sp^2)$ and $CH(sp^2)$ and a third negative charge located in a dummy atom. Following the work of Chen *et al.*[51] for methanol, ethanol, and propanol we also considered the oxygen atom as

additional single interaction center and we placed point charges on the atoms of oxygen and hydrogen of the OH groups.

For carbon dioxide, oxygen, nitrogen, and argon we use full atom models. To reproduce the molecular quadrupole moment of carbon dioxide we placed charges centered at each atom[52-53]. The quadrupole moments of nitrogen and oxygen were reproduced by placing negative point charges in the atoms, and a positive point charge in the center of mass of the molecules[54-55]. For water we used the Tip5pEw model that was parameterized for use with the Ewald summation method[34,56]. Details about these models can be found in the Appendix 5 (Table A5.1).

We have used full atom models for the ionic liquids (Figure 2). The cation is composed by a rigid ring attached to flexible ethyl and methyl groups. In the imidazole ring the atomic positions are fixed and the intramolecular interactions in the ethyl and methyl groups are given by harmonic potential for bonds and bends. We used dihedral potentials for torsions. The anion of the ionic liquid is fully flexible, and the interactions were defined with the same potential for bond, bend, and torsions that the cation:

defined with van der Waals and

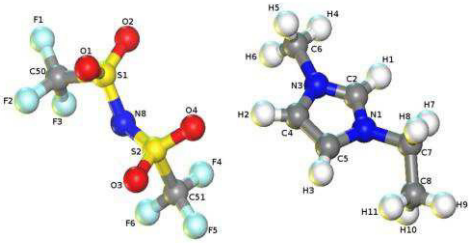

Figure 2. *Schematic representation oj [Tf_2N^-] bis[(trifluoromethyl)sulfonyl]imide anion (left) and [$EMIM^+$] 1-ethyl-3-methylimidazolium cation (right).*

Coulombic interactions. The Cu-BTC framework is considered rigid with Lennard-Jones parameters taken from the DREIDING[58] force field except those for Cu, that were taken from the UFF[59] force field. Lorentz-Berthelot mixing rules were used to calculate mixed Lennard-Jones parameters and the atomic charges for the MOF were taken from Castillo *et al.*[34]. The Lennard-Jones potential is truncated and shifted to zero at 12 Å. Simulations were carried out for dry Cu-BTC. We used the crystallographic structure reported by Chui *et al.*[13] removing the axial oxygen atoms weakly bonded to the Cu atoms that correspond to water ligands. The complete set of Lennard-Jones parameters and charges used in this work for adsorbates, ionic liquids,

$$\Phi \text{int} = \sum_{bonds} k_b (r - r_0)^2 + \sum_{angles} k_\theta (\theta - \theta_0)^2 + \sum_{dihedrals} k_\chi [1 + \cos(n\chi - \delta)]$$

The forcefield parameters for the ionic liquid were adopted from Kelkar and Maggin[57].

The interactions between adsorbates, ionic liquids, and framework were

and adsorbents can be found in Table A5.1 of the Appendix 5.

Simulations were performed using the RASPA code developed by D. Dubbeldam, S. Calero, D. E. Ellis, and

R.Q. Snurr. The code and most of the forcefields and models used in this work have been extensively tested and validated with a large number of experimental and simulation data[34,39,46,60-63].

Results and discussion

We analyze the preferential adsorption sites of the Cu-BTC metal organic framework for molecules that differ in size, shape, and polarity. Our simulations identify T_1 as preferential adsorption site for argon, carbon dioxide, nitrogen, and oxygen. For all loadings studied the percentage of site filled by these four non-polar molecules is higher for T_1 than for the other four preferential sites. Besides, the percentage of molecules adsorbed in this site increases for the lowest values of molecular loading. Considering that site T_1 is located at the smallest cages and that argon, carbon dioxide, nitrogen, and oxygen lack of dipole moment, it is the combination of both, quadrupole moment and molecular size that induces these molecules to adsorb in the small tetrahedral cages. Altogether, carbon dioxide shows the higher percentages of site T_1 occupation, followed by nitrogen and finally by argon and oxygen. This trend can be explained from the quadrupole moments and kinetic diameters. The quadrupole moment hierarchy for these gases is $CO_2 > N_2 > O_2$ with values of $-4.3 \cdot 10^{-26}$, $-1.4 \cdot 10^{-26}$, and $-0.4 \cdot 10^{-26}$ esu, respectively[64]. The kinetic diameters follow the trend $CO_2 < O_2 < N_2 < Ar$ with values of 3.30, 3.46, 3.64, and 3.70 Å, respectively[65-67]. As

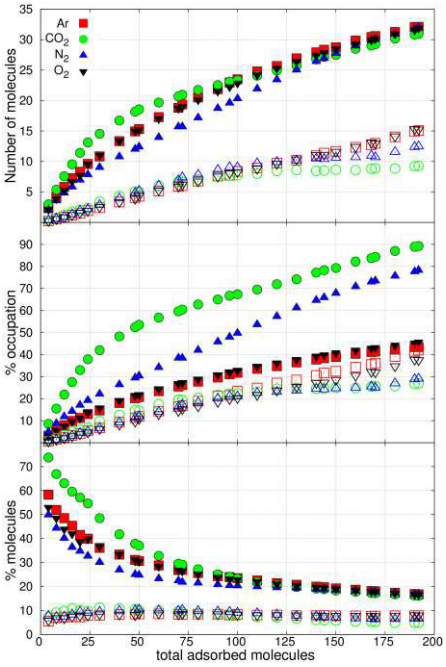

Figure 3. *Adsorption of argon (squares), carbon dioxide (circles), nitrogen (triangles), and oxygen (down triangles). Top: number of molecules adsorbed as a function of loading on sites T_1 (full symbols) and T_w (empty symbols). Center: ratio of occupation for each site. Bottom: fraction of the total adsorbed molecules in the structure.*

shown in Figure 3, the larger the quadrupole moment the higher is the adsorption in site T_1, except for oxygen and argon, where the effect on the adsorption due to the small quadrupole moment of oxygen seems to be compensated by the lager kinetic diameter of argon.

In all sites but T_1, the adsorption of argon and oxygen exhibits linear trend when increasing the total number of adsorbed molecules in the structure. We

use the slope of the adsorbate percentage occupation data curve to deduce the preferential adsorption sites of a given molecule at different loadings. Based on this slope, carbon dioxide adsorbs preferentially on the T_1 sites up to ~ 40 molecules per unit cell. The fact that at higher loadings the percentage occupation on T_1 increases on par with other sites implies that the molecules adsorb indistinctly on the big cages and on the remaining free space of the tetrahedral cages. It is interesting to observe that the maximum occupation percentage for T_w is ~ 25% for carbon dioxide and ~ 30% for nitrogen (Figure 3). This is about 10-12 molecules of nitrogen and 8-10 molecules of carbon dioxide adsorbed in the windows. The maximum amount of molecules that can be adsorbed in the tetrahedral cages (T_1) and their windows (T_w) is ~ 32-40, i.e. ~4-5 molecules per tetrahedral.

At high values of total loading we observe that the number of molecules of argon, nitrogen, and oxygen adsorbed in the cage L_2 is almost equal. For example, independently of the type of gas, when the simulations were performed at a total loading of 192 molecules per unit cell we found that the 33% was adsorbed on L_2 sites (Figure 4). This corresponds to 16 molecules adsorbed in each cage L_2. The percentage of occupation of the site varies with the type of gas as the molecules with lower quadrupole moment pack more efficiently in the cavity. Since the interaction of non-polar molecules with the open metal centers is weak[68], the adsorption of carbon dioxide, nitrogen, oxygen, and

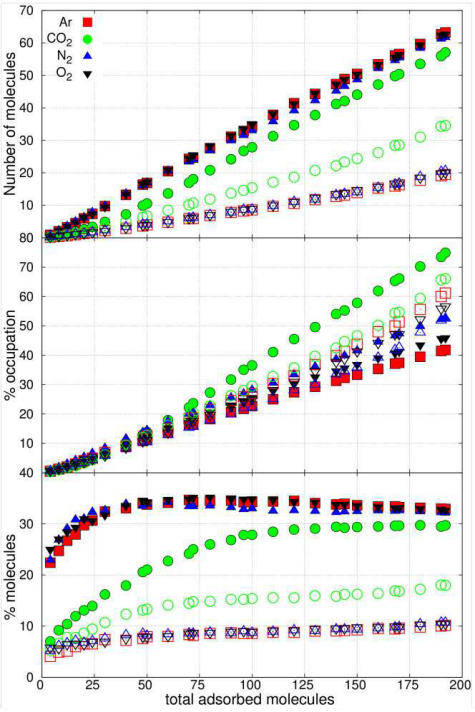

Figure 4. *Adsorption of argon (squares), carbon dioxide (circles), nitrogen (triangles), and oxygen (down triangles). Top: number of molecules adsorbed as a function of loading on sites L_2 (full symbols) and L_w (empty symbols). Center: ratio of occupation for each site. Bottom: fraction of the total adsorbed molecules in the structure.*

argon is similar in L_2 and L_3 cages (Figure A5.1).

Simulations performed for lower total loading (up to 80 molecules per unit cell) show similar variations on the percentage of occupation of site L_2 but differences in the preference of the non-polar gases for this site. Figure 4 shows, for example, that for a total loading of 24 molecules per unit cell sites L_2 are occupied by 5% that

corresponds to around 30% the molecules of oxygen, nitrogen or argon, but less than 15% of the molecules of carbon dioxide. The percentage of occupation for site L_3 at low loadings is similar than for L_2, although the number of molecules of oxygen, nitrogen, and argon adsorbed in the former are slightly lower than in the latter. This, and the fact that carbon dioxide - the molecule with the smallest kinetic diameter- adsorbs better in the L_w windows point to subtle size entropy effects.

Size entropy effects play a more important role in the adsorption of larger non-polar molecules, such as methane, ethane, propane, and butane. Methane, with kinetic diameter of 3.8 Å, adsorbs in a similar way than nitrogen. However, the larger alkanes exhibit different behavior. Up to 24 molecules per unit cell T_1 is the preferential adsorption site for ethane, propane, and butane. This corresponds to one molecule per tetrahedral cage. At higher loadings, the occupation percentage of T_1 remains constant, but the number of molecules adsorbed in the T_w windows increases up to four molecules per tetrahedron (one molecule in T_1 and three molecules in T_w). Hence, in the simulations performed with eight molecules per unit cell for the larger alkanes we find one molecule on each one of the eight sites T_1 of the unit cell (Figure 5). Once the sites T_1 are full the molecules populate the windows T_w and the big cages L_2 and L_3 as shown in Figure 5 and Figures A5.2-A5.4 in the Appendix 5. It is interesting to highlight that the percentage in occupation of site T_1 remains constant for propane and

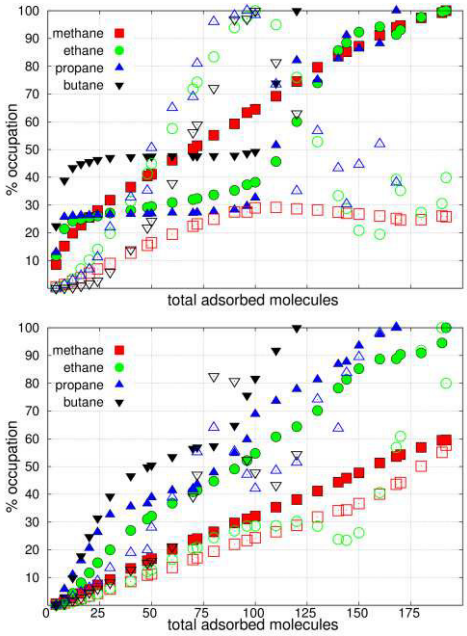

Figure 5. *Adsorption of methane (squares), ethane (circles), propane (triangles), and butane (down triangles) on the sites of Cu-BTC as a function of loading: (a) sites T_1 (full symbols) and T_w (empty symbols); (b) sites L_2 (full symbols) and L_w (empty symbols).*

butane up to the total loading of 100 molecules per unit cell. The molecule of ethane is shorter and more linear than the molecules of propane and butane. These differences in shape and size lead to the slight increase of molecules of ethane. The preferential adsorption sites for the hydrocarbons change from the tetrahedral cages and windows to the big cage L_2 for total loadings higher than 32 molecules per unit cell (Figure 5). Simulations performed for more than 100 molecules per unit cell show a clear decrease on the occupation of the T_w windows. This is due to the rapid increase on the number of molecules in L_3, exerting pressure over the molecules

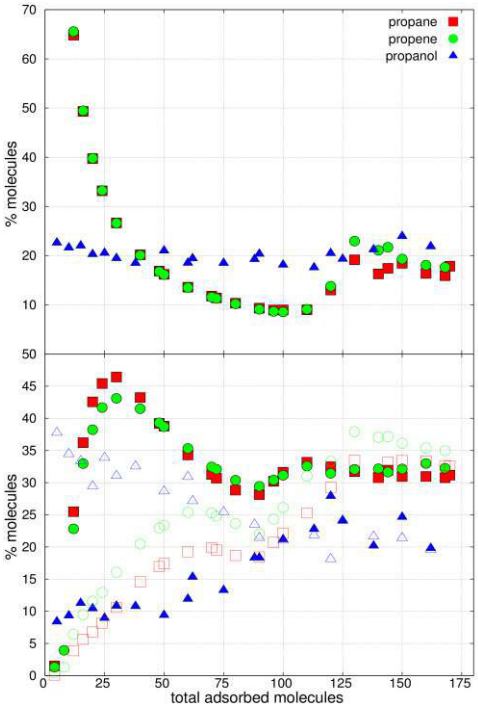

Figure 6. *Fraction of adsorbed molecules of propane (squares), propene (circles), and propanol (triangles) on sites T_1 (top), L_2 (bottom full symbols), and L_3 (bottom empty symbols) as a function of loading.*

originally located at T_w and displacing these molecules to the tetrahedral cages. The percentage of molecules entering L_w is low and quite similar for the four alkanes (Figures A5.3 and A5.4).

Figure 6 shows the percentage of molecules of propane, propene, and propanol adsorbed in sites T_1, L_2, and L_3. The adsorption trend observed for propene is very similar to this observed for propane, i.e., the preferential adsorption is in T_1 and once the tetrahedral cages are full the molecules adsorb preferentially in L_2 and finally in L_3. This trend indicates that the adsorption is mainly dominated by the size and shape of these two molecules, and that the effect of small dipole moment of propane (0.366 D) on the adsorption is only observed on the slightly higher adsorption of this molecule in L_3. However, molecules similar in shape and size but with a higher dipole moment such as propanol (1.68 D) are affected by the copper paddle-wheel configuration in such a way that the tetrahedral cages are no longer considered as preferential adsorption sites for them. The dipole moment of propanol favors the adsorption close to the copper atoms on the biggest cages L_3 inhibiting molecular confinement in the tetrahedral cages. As shown in Figure 6, only the 20% of the adsorbed molecules can be found in the tetrahedral cages independently of the total loading. The percentage of occupation in the L_3 is around 35% for total loadings lower than 60 molecules and it is around 10% in L_2. For higher loadings the percentages of occupation in L_2 increases and the one in L_3 decreases. This percentage tends to converge to 20% in T_1. (Figures A5.5-A5.7).

The analysis of the adsorption sites for methanol, ethanol, and propanol in Cu-BTC evidences competition between entropic and dipole effects (Figure 7). The size entropic effect that favors adsorption in T_1 increases for the longer molecules while the dipole effect that favors adsorption in L_3 decreases for them. This competition also implies that the big cage in which the copper atoms are not accessible (L_2) remains empty at low and medium loadings. The initial attemps for filling this cage require mo-

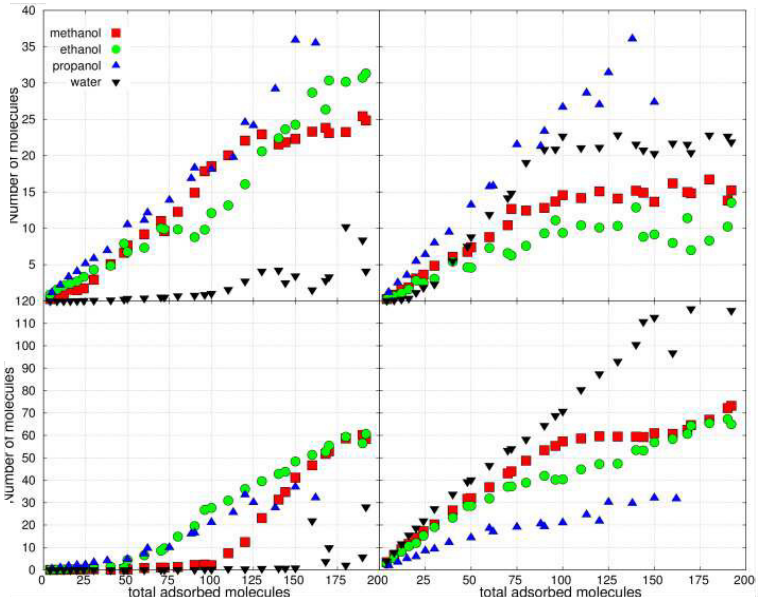

Figure 7. *Adsorption of methanol (squares), ethanol (circles), propanol (triangles), and water (down triangles) on sites T_1 (top left), T_w (top right), L_2 (bottom left), and L_3 (bottom right) as a function of loading.*

re than 50 molecules of ethanol and propanol, and more than 100 molecules of methanol adsorbed per unit cell of Cu-BTC. The effect that dipole moment exerts on the adsorption near the copper paddle-wheel unit is particularly remarkable for water that combines low molecular weights with large dipole moments (Figure 7). Besides L_3, the other preferred sites for the adsorption of water are the windows that communicate L_3 and T_1 (T_w). This can be attributed to the combination of an adequate size of the windows (that favors water confinement in them) and the effect created by the presence of other molecules of water near the copper atoms in L_3. In contrast to the high adsorption of water in T_w, the adsorption in the windows that communicate cages L_2 and L_3 (site L_w) is negligible. Additional information on the percentages of occupation can be found in Figures A5.8-A5.10.

We carried out an additional study to identify not only which cage a gas may adsorb first but also the relative strength of the adsorbate-adsorbent interactions. In particular, we performed NVT Monte Carlo simulations at 295 K to compute isosteric heats of adsorption, Henry coefficients, Gibbs and Helmholtz free energies, Internal energies, and entropies of adsorption. These values were computed for all the adsorbates in Cu-BTC and in T_1, L_2, L_3, and windows. All the values are listed in Tables A5.2-A5.7 in the Appendix 5. The computed Henry coefficients show that the hierarchy of adsorption is propanol >butane > propene > propane

> ethanol > water > methanol > ethane > carbon dioxide > methane > oxygen > argon > nitrogen. As shown in Figure A5.12, alcohols and water compete for site L_3, whereas the competition of the rest of the adsorbates is for site T_1. On the other hand, the isosteric heats of adsorption of the studied alcohols and water in Cu-BTC are quite similar (Figure A5.13). However, the similarity is broken when we analyze these values for the different sites. The heat of adsorption of water is much higher in L_3 than in the other cages. Methanol also exhibits the highest values for L_3 but the difference with the value obtained for T_1 decreases. For the longer alcohols this difference is almost negligible due to steric effects. This is corroborated by the high values of entropy obtained for these molecules (as well as for the hydrocarbons) in the tetrahedral cages (Table A5.7).

In recent works we have reported theoretical methods to enhance the adsorption selectivity of a given mixture by blocking the tetrahedral cages[45-46] . Based on this idea and with the aim to analyze water distribution when the site L_3 is partially blocked or shielded, we have performed additional simulations adding ionic liquids to the Cu-BTC cages. Composites of ionic liquids supported on IRMOF-1, with formula Zn_4O(1,4,-benzenedicarboxylate)$_3$, have been recently reported by Jiang *et al.* as a method to enhance carbon dioxide capture using this metal-organic framework[69-70].

The ionic liquids (ILs) considered in this

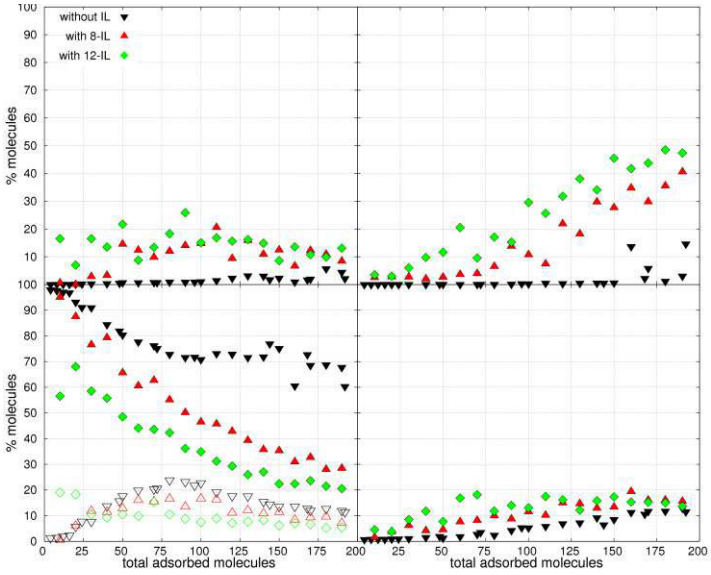

Figure 8. *Fraction of adsorbed molecules of water on sites T_1 (top left), L_2 (top right), L_3 (bottom left with full symbols), T_w (bottom left with empty symbols), and L_w (bottom right) as a function of loading. Adsorption without ILs in Cu-BTC pores (down triangles), with 8 (triangles) and 12 (diamonds) molecules of IL per unit cell respectively.*

work are formed by the cation 1-ethyl-3-methylimidazolium, and by the anion bis[(trifluoromethyl)sulfonyl]imide. Due to their high polarity L_3 is the preferred site for these molecules. On the other hand, the size and molecular weight of the ionic liquids limit the number to two or three per cage L_3, i.e. 8 and 12 ion pairs per unit cell of Cu-BTC. These molecules partially block the L_3 cages while screening some of the copper metal centers. The effect exerted by the presence of ionic liquids on L_3 is shown in Figure 8. Though L_3 remains as prefe-
rred adsorption site for water, the presence of bulkier polar molecules reduces the adsorption of water on this site and forces the molecules of water to move to the other two cages (sites T_1 and L_2) and also to the windows that communicate these cages with L_3. This finding leads to explore the potential use of ILs to enhance the water resistance of the Cu-BTC structure. Previous works pointed out that water molecules attack the copper atoms of the framework collapsing the structure. As the copper atoms are accessible only from L_3 cages the blockage of these cages might improve the stability of the MOF by preventing the water adsorption on these sites. The average occupation profiles obtained for 100 molecules of water in the bare Cu-BTC and adding 8 and 12 ILs per unit cell - that corresponds to 2 and 3 ILs per L_3 cages, respectively- are shown in Figure 9. The effect of the ILs in the structure is twofold: the ILs (1) favor the dispersion of the molecules of water in L_3 and (2) reduce the number of molecules of water adsorbed near the metallic center from 4 molecules per copper (bare structure) to 1 molecule of water per copper (structure with 12

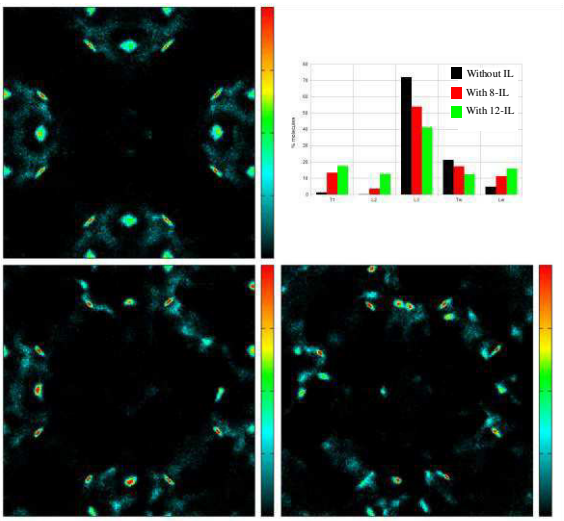

Figure 9. *Average occupation profiles obtained for 100 molecules of water in the bare Cu-BTC (top left), in the structure with 2ILs (bottom left) and 3 ILs per L_3 cage (bottom right). The figure shows the average values of the projections of the center of mass coordinates over the x–y plane (cubic symmetry). The relation between colour and occupation (from black to red) is shown in the bar situated on the right side of the figure. The percentage of molecules of water per site is also depicted (top right).*

ILs). This behavior is also observed for the computed adsorption isotherms of water in the three structures (Figure A5.11). The adsorption of water on sites L_2, T_1, L_w, and T_w is unaffected by the presence of ILs in L_3. However, these molecules increase the total loading of water in the structure at low and medium pressure and decrease this loading at the highest values of pressure due to the partial blockage that they exert in L_3.

Conclusions

The preferred adsorption site of a given molecule in Cu-BTC depends on the size, the shape, and the dipole moment of the molecule. Hence T_1 will be the preferred site for non-polar molecules with size and shape able to confine in the tetrahedral cages. Larger non-polar molecules that are unable to enter the tetrahedral cages adsorb in the cages L_2 and L_3. The adsorption in cages with the copper atoms pointing into the pore (L_3) is mainly determined by the dipole moment of the molecule, and it is the competition between confinement and polarity that favor adsorption in T_1 (when confinement dominates dipole moment) or in L_3 (when dipole moment dominates confinement). This work reinforces the idea that Cu-BTC is a good material to separate molecules differing in size, shape, or polarity and suggests that selective blockage using ionic liquids might enhance its resistance to water and its performance in separation processes.

Bibliography

(1) Liang, Z. J.; Marshall, M.; Chaffee, A. L. *Greenhouse Gas Control Technologies 9* **2009**, *1*, 1265.

(2) Kusgens, P.; Rose, M.; Senkovska, I.; Frode, H.; Henschel, A.; Siegle, S.; Kaskel, S. *Microporous and Mesoporous Materials* **2009**, *120*, 325.

(3) Li, Y. W.; Yang, R. T. *Journal of the American Chemical Society* **2006**, *128*, 8136.

(4) Prestipino, C.; Regli, L.; Vitillo, J. G.; Bonino, F.; Damin, A.; Lamberti, C.; Zecchina, A.; Solari, P. L.; Kongshaug, K. O.; Bordiga, S. *Chemistry of Materials* **2006**, *18*, 1337.

(5) Bordiga, S.; Regli, L.; Bonino, F.; Groppo, E.; Lamberti, C.; Xiao, B.; Wheatley, P. S.; Morris, R. E.; Zecchina, A. *Physical Chemistry Chemical Physics* **2007**, *9*, 2676.

(6) Fischer, M.; Hoffmann, F.; Froeba, M. *Chemphyschem* **2010**, *11*, 2220.

(7) Grajciar, L.; Bludsky, O.; Nachtigall, P. *Journal of Physical Chemistry Letters* **2010**, *1*, 3354.

(8) Zhou, C.; Cao, L.; Wei, S.; Zhang, Q.; Chen, L. *Computational and Theoretical Chemistry* **2011**, *976*, 153.

(9) Wang, S. Y.; Yang, Q. Y.; Zhong, C. L. *Separation and Purification Technology* **2008**, *60*, 30.

(10) Greathouse, J. A.; Ockwig, N. W.; Criscenti, L. J.; Guilinger, T. R.; Pohl, P.; Allendorf, M. D. *Physical Chemistry Chemical Physics* **2010**, *12*, 12621.

(11) Amirjalayer, S.; Tafipolsky, M.; Schmid, R. *Journal of Physical Chemistry C* **2011**, *115*, 15133.

(12) Krishna, R.; van Baten, J. M. *Physical Chemistry Chemical Physics* **2011**, *13*, 10593.

(13) Chui, S. S. Y.; Lo, S. M. F.; Charmant, J. P. H.; Orpen, A. G.; Williams, I. D. *Science* **1999**, *283*, 1148.

(14) Chen, B. L.; Ockwig, N. W.; Millward, A. R.; Contreras, D. S.; Yaghi, O. M.

Angewandte Chemie-International Edition **2005**, *44*, 4745.

(15) Yang, Q. Y.; Zhong, C. L. *Journal of Physical Chemistry B* **2006**, *110*, 655.

(16) Karra, J. R.; Walton, K. S. *Langmuir* **2008**, *24*, 8620.

(17) Xiang, S. C.; Zhou, W.; Gallegos, J. M.; Liu, Y.; Chen, B. L. *Journal of the American Chemical Society* **2009**, *131*, 12415.

(18) Jorge, M.; Lamia, N.; Rodrigues, A. E. *Colloids and Surfaces a-Physicochemical and Engineering Aspects* **2010**, *357*, 27.

(19) Mu, B.; Schoenecker, P. M.; Walton, K. S. *Journal of Physical Chemistry C* **2010**, *114*, 6464.

(20) Wu, H.; Simmons, J. M.; Liu, Y.; Brown, C. M.; Wang, X. S.; Ma, S.; Peterson, V. K.; Southon, P. D.; Kepert, C. J.; Zhou, H. C.; Yildirim, T.; Zhou, W. *Chemistry-a European Journal* **2010**, *16*, 5205.

(21) Chowdhury, P.; Mekala, S.; Dreisbach, F.; Gumma, S. *Microporous and Mesoporous Materials* **2012**, *152*, 246.

(22) Zhang, Q.; Cao, L.; Li, B.; Chen, L. *Chemical Science* **2012**, *3*, 2708.

(23) Getzschmann, J.; Senkovska, I.; Wallacher, D.; Tovar, M.; Fairen-Jimenez, D.; Duren, T.; van Baten, J. M.; Krishna, R.; Kaskel, S. *Microporous and Mesoporous Materials* **2010**, *136*, 50.

(24) Karra, J. R.; Walton, K. S. *Journal of Physical Chemistry C* **2010**, *114*, 15735.

(25) Yazaydin, A. O.; Benin, A. I.; Faheem, S. A.; Jakubczak, P.; Low, J. J.; Willis, R. R.; Snurr, R. Q. *Chemistry of Materials* **2009**, *21*, 1425.

(26) Low, J. J.; Benin, A. I.; Jakubczak, P.; Abrahamian, J. F.; Faheem, S. A.; Willis, R. R. *Journal of the American Chemical Society* **2009**, *131*, 15834.

(27) Martin-Calvo, A.; Garcia-Perez, E.; Garcia-Sanchez, A.; Bueno-Perez, R.; Hamad, S.; Calero, S. *Physical Chemistry Chemical Physics* **2011**, *13*, 11165.

(28) Li, Y.; Yang, R. T. *Aiche Journal* **2008**, *54*, 269.

(29) Henninger, S. K.; Schmidt, F. P.; Henning, H. M. *Applied Thermal Engineering* **2010**, *30*, 1692.

(30) Liu, J.; Wang, Y.; Benin, A. I.; Jakubczak, P.; Willis, R. R.; LeVan, M. D. *Langmuir* **2010**, *26*, 14301.

(31) Marx, S.; Kleist, W.; Baiker, A. *Journal of Catalysis* **2011**, *281*, 76.

(32) Rosseinsky, M. J. *Microporous and Mesoporous Materials* **2004**, *73*, 15.

(33) Rowsell, J. L. C.; Yaghi, O. M. *Angewandte Chemie-International Edition* **2005**, *44*, 4670.

(34) Castillo, J. M.; Vlugt, T. J. H.; Calero, S. *Journal of Physical Chemistry C* **2008**, *112*, 15934.

(35) Dietzel, P. D. C.; Morita, Y.; Blom, R.; Fjellvag, H. *Angewandte Chemie-International Edition* **2005**, *44*, 6354.

(36) Collins, D. J.; Zhou, H.-C. *Journal of Materials Chemistry* **2007**, *17*, 3154.

(37) Calero, S.; Gutiérrez-Sevillano, J. J.; García-Pérez, E. *Microporous and Mesoporous Materials* **2013**, *165*, 79.

(38) Chmelik, C.; Karger, J.; Wiebcke, M.; Caro, J.; van Baten, J. M.; Krishna, R. *Microporous and Mesoporous Materials* **2009**, *117*, 22.

(39) Garcia-Perez, E.; Gascon, J.; Morales-Florez, V.; Castillo, J. M.; Kapteijn, F.; Calero, S. *Langmuir* **2009**, *25*, 1725.

(40) Xue, C. Y.; Yang, Q. Y.; Zhong, C. L. *Molecular Simulation* **2009**, *35*, 1249.

(41) Martin-Calvo, A.; Lahoz-Martin, F. D.; Calero, S. *Journal of Physical Chemistry C* **2012**, *116*, 6655.

(42) Chen, B.; Xiang, S.; Qian, G. *Accounts of Chemical Research* **2010**, *43*, 1115.

(43) Montoro, C.; Garcia, E.; Calero, S.; Perez-Fernandez, M. A.; Lopez, A. L.;

Barea, E.; Navarro, J. A. R. *Journal of Materials Chemistry* **2012**, *22*, 10155.

(44) Cao, F.; Zhang, C.; Xiao, Y.; Huang, H.; Zhang, W.; Liu, D.; Zhong, C.; Yang, Q.; Yang, Z.; Lu, X. *Industrial & Engineering Chemistry Research* **2012**, *51*, 11274.

(45) Martin-Calvo, A.; Garcia-Perez, E.; Garcia-Sanchez, A.; Hamad-Gomez, S.; Calero, S. *Physical Chemistry Chemical Physic* **2011,** 13(23)**,** 11165.

(46) Calero, S.; Martin-Calvo, A.; Hamad, S.; Garcia-Perez, E. *Chemical Communications* **2011**, *47*, 508.

(47) Liu, J. C.; Culp, J. T.; Natesakhawat, S.; Bockrath, B. C.; Zande, B.; Sankar, S. G.; Garberoglio, G.; Johnson, J. K. *Journal of Physical Chemistry C* **2007**, *111*, 9305.

(48) Ryckaert, J. P.; Bellemans, A. *Faraday Discussions* **1978**, *66*, 95.

(49) Dubbeldam, D.; Calero, S.; Vlugt, T. J. H.; Krishna, R.; Maesen, T. L. M.; Smit, B. *Journal of Physical Chemistry B* **2004**, *108*, 12301.

(50) Gutierrez-Sevillano, J. J.; Dubbeldam, D.; Rey, F.; Valencia, S.; Palomino, M.; Martin-Calvo, A.; Calero, S. *Journal of Physical Chemistry C* **2010**, *114*, 14907.

(51) Chen, B.; Potoff, J. J.; Siepmann, J. I. *Journal of Physical Chemistry B* **2001**, *105*, 3093.

(52) Harris, J. G.; Yung, K. H. *Journal of Physical Chemistry* **1995**, *99*, 12021.

(53) Garcia-Sanchez, A.; Ania, C. O.; Parra, J. B.; Dubbeldam, D.; Vlugt, T. J. H.; Krishna, R.; Calero, S. *Journal of Physical Chemistry C* **2009**, *113*, 8814.

(54) Stogryn, D. E.; Stogryn, A. P. *Molecular Physics* **1966**, *11(4), 371.*

(55) Murthy, C. S.; Singer, K.; Klein, M. L.; McDonald, I. R. *Molecular Physics* **1980**, *41*, 1387.

(56) Rick, S. *Journal of Chemical Physics* **2004**, *120*, 6085.

(57) Kelkar, M. S.; Maginn, E. J. *Journal of Physical Chemistry B* **2007**, *111*, 4867.

(58) Mayo, S. L.; Olafson, B. D.; Goddard, W. A. *Journal of Physical Chemistry* **1990**, *94*, 8897.

(59) Rappe, A. K.; Casewit, C. J.; Colwell, K. S.; Goddard, W. A.; Skiff, W. M. *Journal of the American Chemical Society* **1992**, *114*, 10024.

(60) Martin-Calvo, A.; Garcia-Perez, E.; Castillo, J. M.; Calero, S. *Physical Chemistry Chemical Physics* **2008**, *10*, 7085.

(61) Ania, C. O.; Garcia-Perez, E.; Haro, M.; Gutierrez-Sevillano, J. J.; Valdes-Solis, T.; Parra, J. B.; Calero, S. *Journal of Physical Chemistry Letters* **2012**, *3*, 1159.

(62) Kuhn, J.; Castillo-Sanchez, J. M.; Gascon, J.; Calero, S.; Dubbeldam, D.; Vlugt, T. J. H.; Kapteijn, F.; Gross, J. *Journal of Physical Chemistry C* **2010**, *114*, 6877.

(63) Thornton, A. W.; Dubbeldam, D.; Liu, M. S.; Ladewig, B. P.; Hill, A. J.; Hill, M. R. *Energy & Environmental Science* **2012**, *5*, 7637.

(64) Buckingham, A. D.; Disch, R. L.; Dunmurl, D. A. *Journal of the American Chemical Society* **1968**, *90*, 3104.

(65) Breck, D. W. *Zeolite Molecular Sieves*; Krieger Publishing Company: Malabar, Florida, 1984.

(66) Sircar, S. *Industrial & Engineering Chemistry Research* **2006**, *45*, 5435.

(67) Kuznicki, S. M.; Bell, V. A.; Petrovic, I.; Desa, B. T. *US Patent 6068,682* **2000**.

(68) Liu, J.; Wang, Y.; Benin, A. I.; Jakubczak, P.; Willis, R. R.; LeVan, M. D. *Langmuir* **2010**, *26*, 14301.

(69) Gupta, K. M.; Chen, Y.; Hu, Z.; Jiang, J. *Physical Chemistry Chemical Physics* **2012**, *14*, 5785.

(70) Chen, Y.; Hu, Z.; Gupta, K. M.; Jiang, J. *Journal of Physical Chemistry C* **2011**, *115*, 21736.

Metal Organic Frameworks with open metal sites such as Cu-BTC have the potential to improve separations of molecules of differing polarities. In the Cu-BTC structure, molecules with high dipole moment such as water are preferentially adsorbed in the cages containing the open metal sites, while less polar molecules such as alcohols can be adsorbed in the other cages. We combine Monte Carlo simulations and *ab initio* calculations with the aim of tuning the adsorption properties of Cu-BTC (a) via selective blockage of cages or (b) poisoning the open metal centers. The simulation results propose selective blocking and screening of the active sites as the best strategies to enhance the alcohol/water selectivity in the gas and liquid phase as well as the water resistance of the structure.

Juan José Gutiérrez-Sevillano, David Dubbeldam, Luca Bellarosa, Nuria López, Xin Liu, Thijs J. H. Vlugt, and Sofía Calero

8

Strategies to Simultaneously Enhance the Hydrostability and the Alcohol-Water Separation Behavior of Cu-BTC

Introduction

The use of molecular sieves for separation of alcohol-water vapor and liquid mixtures is important from an industrial point of view[1-3]. Water is typically present at various levels in streams of bioethanol, a renewable energy vector and possible candidate to substitute fossil fuels. This biofuel can be obtained by fermentation from agricultural feedstock or by transesterification of the oils contained in algae, but to be usable as a fuel the majority of the water must be removed. Most water can be eliminated by distillation but the formation of a low-boiling water-ethanol azeotrope limits the purity of ethanol and makes the purification processes expensive and particularly challenging to implement. Whether or not there is an azeotrope, distillation is always very energy-intensive. The global demand for energy-saving technology is fostering other methods that replace distillation altogether for dehydration. Out of these methods, separations using molecular sieves hold many advantages for their low energy requirements. The process that is usually applied for a liquid feed is pervaporation[4-5]. This is a suitable process to separate organic liquid mixtures and close-boiling point mixtures, but the molecular sieves are in direct contact with the liquid mixture and they can be swollen or shrunk by it, lowering the separation performance. An

alternative is to carry out the alcohol-water separation in the vapor phase[6], where the feed solution is vaporized first and then permeated through the structure. This technique has also disadvantages such as the dependence of diffusion and separation on the feed pressure or the possibility of condensation[7].

In both pervaporation and vapor permeation processes, the separation factor is governed by the way in which the molecules adsorb and diffuse in the molecular sieve. Therefore, the key to success for such processes is to find porous materials with high permeability, selectivity, and stability. Several types of porous structures have been considered for separation of water-alcohol mixtures and, depending on the affinity of the structure for water, the separation process can enrich ethanol in either the feed (hydrophilic structure) or the adsorbed (hydrophobic structure) sides. Among porous materials, some recent works are reporting insights for the design of water stable Metal-Organic Frameworks (MOFs)[8-10] and also for the applicability of MOFs in alcohol-water separations[11-13]. In particular, the hydrophilic Na-rho-ZMOF exhibits preferential adsorption of water over ethanol and methanol whereas hydrophobic MOFs such as ZIF-71, and the paddle-wheels Zn(tbip) and $Zn(BDC)(TED)_{0.5}$ show the opposite behavior[14-17]. The latter MOFs were also found to exhibit substantial adsorption of alcohols ranging from 3 to 9 mol/kg of ethanol[12,16]. Unfortunately, there is a drawback that hinders the industrial applications of this type of MOFs. When exposed to humid conditions, the molecules of water disrupt the framework by hydrolyzing the carboxylate groups coordinated to the metallic centers[18-21]. To overcome this drawback some recent works advocate the introduction of hydrophobic groups at the most adjacent sites of the coordinating atoms of the organic ligands[22] or the substitution of zinc by other metals[20-21]. However, these initial findings also indicate that the multiple coordination spheres of Zn and their avidity for water might prevent the implementation of these zinc-containing structures.

Other MOFs such as $Cu_3(btc)_2$ (BTC=benzene tricarboxylic acid, Cu-BTC) have been prepared on the basis of unsaturated (open) metal centers that are formed after the removal of axial ligands of metal atoms by thermal activation or other methods[23-24]. The advantage of these structures is that they offer extra binding sites to the adsorbed molecules[25-26] and exhibit stability in moist air[23,27-30].

Compared with MOFs without open metal sites, Cu-BTC exhibits high selectivity for ethanol[31]. The chemical structures of water and alcohol are quite similar, i.e. the dipole moments are 1.85 and 1.69 D, respectively. Thus, the open metal sites would also have a strong affinity for water that could disrupt the structure and also reduce the adsorption capacity for the alcohol. Preventing water from entering Cu-BTC could be an approach to improve its performance in humid media, but it is difficult to fully exclude water from adsorbing in the structure for long exposure times.

Thus, instead of preventing water adsorption we suggest strategies to limit water attack to the open metal sites so that the structure remains stable even after water has entered the pores. This knowledge could be used as design criterion for a new generation of MOFs with better separation properties and higher stability to the feed mixture.

This work explores at a molecular level the influence of the open metal centers on the mechanisms governing ethanol/water separation. Our strategy consists on (1) the use of simulations to tune adsorption using simple methods and (2) to investigate how the tuning can be realized in practice. We show that the effect of the metal centers goes beyond binding positions and we provide atomistic guidelines toward the topology and composition of the structure to improve the separation factor of the alcohol while enhancing the water resistance of the structure.

Computational Details

Monte Carlo (MC) simulations were performed using a single unit cell (a = b = c = 26.343 Å, $\alpha = \beta = \gamma = 90°$) with the crystal structure of Chui *et al.*[32], removing the axial oxygen atoms weakly bonded to the Cu atoms that correspond to water ligands. Lennard-Jones parameters for guest-host interactions were taken from DREIDING[33] force field except those for Cu that were taken from the UFF[34] force field. To calculate mixed Lennard-Jones parameters we used Lorentz-Berthelot mixing rules and the atomic charges for the MOF were taken from Castillo *et al.*[35] Water was modeled using the Tip5pEw model parameterized for use with the Ewald summation[36] and ethanol using the TraPPE[37] force field. All sets of charges and Lennard-Jones parameters used in this work are compiled in the Appendix 6 (Table A6.1).

Adsorption isotherms were computed using Grand Canonical Monte Carlo (GCMC) simulations where temperature, volume, and chemical potential are kept fixed. Partial pressures are directly related with the chemical potential using the Peng Robinson equation. Configurational Bias Monte Carlo (CBMC) technique was used for the insertion and deletion of molecules in and from the system. The MC moves were performed in cycles allowing one of the following trial moves in each cycle: regrow rotation, translation, insertion and deletion. In the case of mixtures, identity change moves were also allowed. Heats of adsorption and Henry coefficients were obtained from MC simulations in the NVT ensemble. We used the Widom particle-insertion method to obtain the chemical potentials and adsorption energies. These simulations consist on at least of $2 \cdot 10^5$ equilibration cycles and $2 \cdot 10^6$ production cycles. In each cycle regrow, rotation, or translation trial moves were randomly selected. We used Lennard-Jones and electrostatic cutoffs of 12 Å. Coulombic interactions were computed using the Ewald summation technique with a relative precision of 10^{-6}. More details on these simulation techniques can be found elsewhere[38].

MC simulations were performed using our in-house code RASPA[39]. This code has been extensively tested and validated with a large number of experimental and simulation data concerning the computation of adsorption and diffusion properties of gases in confined systems[40-43].

Density functional theory (DFT) calculations were carried out to evaluate the distances of these molecules to the copper atoms and the adsorption energies of water, acetone and dimethyl ether in Cu-BTC. The Cu-BTC lattice was represented through a cluster model $Cu_2(COOH)_4$ that has been proved to be reliable to examine solvent adsorption on this MOF[30]. The geometry optimizations have been carried out with the program package Gaussian 09[44] using the B3LYP functional[45-47]. Optimizations were performed with the 6-31G(d) basis set for all the atoms[48-49], whereas the LANL2DZ pseudopotential with associated basis set was employed for the description of the copper centers[50].

Results and discussion

The adsorption isotherms for an equimolar water-ethanol mixture at 298 K, 323 K, and 373 K obtained with MC simulations are shown in Figure 1. These isotherms are important for practical application but difficult to measure experimentally. Therefore, our data act as an efficient tool in predicting the adsorption of this type of mixtures. Although water uptake into Cu-BTC is less than the ethanol uptake up to $5 \cdot 10^3$ Pa (at 298 K), 10^4 Pa (at 323 K), and 10^5 Pa (at 373 K), the

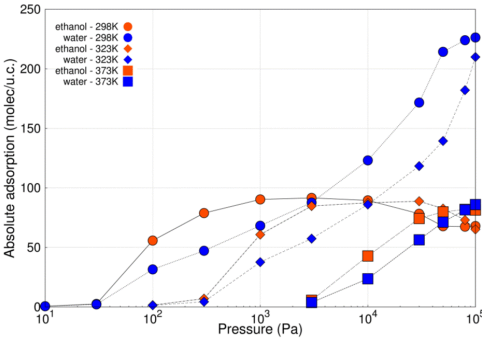

Figure 1. *Adsorption isotherms for an equimolar mixture of ethanol (orange) and water (blue) in Cu-BTC at 298 K (circles), 323 K (diamonds) and 373K (squares).*

simulations show that this material is not able to separate the two components of the mixture.

Water has a large affinity for the metal center in Cu–BTC[35] and consequently, the molecules of water preferentially adsorb in the neighborhood of the copper atoms competing with the molecules of ethanol for this adsorption site. Based on this finding, we introduce two strategies for simultaneously enhancing the alcohol selectivity and the water resistance of the structure. These approaches consist on fine-tuning the adsorption via selective blockage of the MOF cages or via selective screening of the open metal centers. To illustrate these strategies we have performed adsorption studies of mixtures containing water and ethanol in the gas and in the liquid phase.

A. Tuning adsorption via selective blockage of cages

Cu-BTC is formed by large central cavities of about 9 Å in diameter

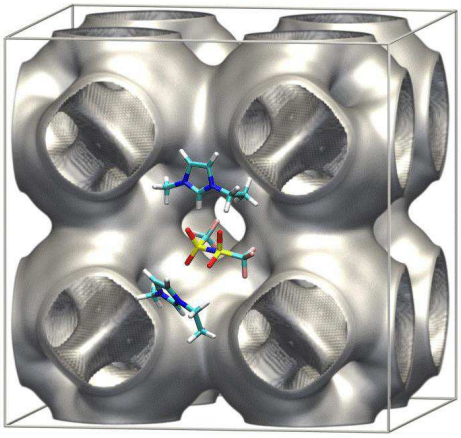

Figure 2. *Schematic picture of the cages of Cu-BTC. The big cages with inner surfaces formed by benzene rings from the BTC with their 6-fold pointing towards the center of the pore are blocked with ionic liquids formed by the cation 1-ethyl-3-methylimidazolium, and the anion bis[(trifluoromethyl) sulfo-nyl]imide.*

surrounded by small cavities of about 5 Å in diameter (Figure 2). The large cavities are similar in size and shape but only the ones that are communicated by windows with the small cavities have open copper sites pointing towards the pore[31]. In recent works we have reported strategies to improve carbon tetrachloride removal from air by blocking the small cavities of Cu-BTC[27,42]. Using a similar idea, and with the aim of reducing water uptake we generated *artificial spheres* of 12 Å in diameter centered in the cages with the copper atoms of BTC pointing to the center of the pore to block these sites. Figure 3 compares the adsorption isotherms obtained for the equimolar mixture at 323 K in both, the bare and the blocked Cu-BTC. Note that the mixture, as in Figure 1, could be a vapor or liquid phase under the pressure range. Although the blockage reduces the adsorption capacity of the MOF it also hinders water uptake up to 10^4 Pa. This enhances the water resistance of the structure up to this pressure, and at the same time provides higher adsorption selectivity for ethanol at 10^4 Pa when compared to the bare structure at $5 \cdot 10^3$ Pa.

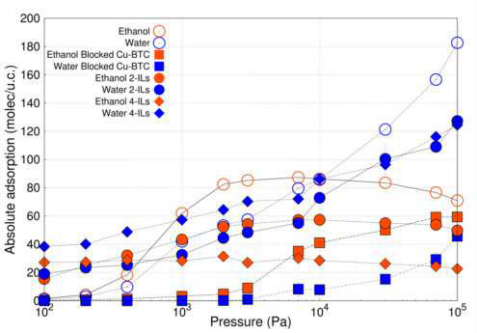

Figure 3. *Adsorption isotherms for the equimolar mixture of ethanol (orange) and water (blue) at 323 K in the bare (empty circles) and the blocked (squares) Cu-BTC, and in the structure containing 2 (filled circles) and 4 (diamonds) ionic liquids per cage.*

To realize this concept of blocking in a practical way we used ionic liquids (ILs) instead of spheres. Composites of ILs supported on the structure Zn_4O(1,4,-benzenedicarboxy-late)$_3$, have been recently reported as a method to enhance carbon dioxide capture using this metal-organic framework[51-52]. The ionic liquid selected to block the cages is formed by 1-ethyl-3-methyl-imidazolium cations and bis[(trifluoromethyl) sulfonyl]imide anions. We use all atom

models for the molecules (Figure 2). The bis[(trifluoromethyl)sulfonyl]imide anion is considered flexible and the 1-ethyl-3-methylimidazolium cation is modeled with a rigid imidazolate ring bonded to flexible ethyl and methyl groups. The bonded interactions are described by bond bending, bond stretching and torsional terms, and the non-bonded van der Waals and electrostatic interactions are described by the sum of Lennard Jones and Coulomb potentials[53]. For mixed Lennard-Jones parameters we applied Lorentz-Berthelot mixing rules. A table containing the parameters and charges used in this work can be found in the Appendix 6 (Table A6.1).

The cages of Cu-BTC with open metal centers pointing towards the center of the pore are preferred adsorption sites for the ILs, due to the high polarity of these molecules. The size and molecular weight of them limit the number to a maximum of four per cage, i.e. sixteen ion pairs per unit cell of Cu-BTC. This reduces the pore volume of the structure from 0.863 (cm^3/g) to 0.373 (cm^3/g) (Appendix 6 table A6.2).

The effect exerted on the adsorption by the presence of six units of the ionic liquid per cage is shown in Figure 3. Instead of a reduction on the water uptake we observe the opposite behavior. Detailed analysis of the average occupation profiles in Figure 4 reveals that filling the cages with ionic liquids inhibits water to enter these cages but also creates new preferential adsorption sites at the windows. These sites favor the nucleation of water inside the big cages that are not filled by the ionic liquids and also inside the small cages, leading to the increase on the water uptake observed in Figure 3.

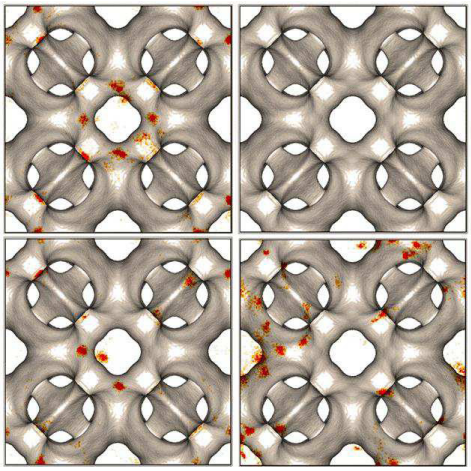

Figure 4. *Average density plots showing the adsorption of water for the equimolar feed mixture of alcohol and water at 10^8 Pa and 323 K in the bare Cu-BTC (top left), the blocked Cu-BTC (top right), Cu-BTC with 2 ILs per cage (bottom left) and with 4ILs per cage (bottom right).*

The additional adsorption sites generated by filling the cages with ILs disappear when we partially block the cages, i.e. when we reduce to 2 the number of ionic liquids per cage (Figure 4). In this case, the open metal centers remain as preferred adsorption sites for water. However, the presence of ILs favors the dispersion of the water molecules in the cage improving the hydroresistance of the structure. Although our simulations show that it could be possible to separate ethanol from water at low values of pressure via selective blockage of cages using ionic liquids, it is not a suitable route for the blockage. However, the obtained

insights may help to find other blocking molecules able to provide more effective response in this regard. In any case, further experimental and theoretical work needs to be carried out to confirm, extend, and improve this concept. As for the water stability of Cu-BTC, we have proved that it can be enhanced to some extent because the blockage hinders water adsorption. However, using the selective blocking strategy it is difficult to fully exclude water from adsorbing in the cages that contain the open metal centres.

B. Tuning adsorption poisoning the open metal centers

To screen the interaction of water with the copper atoms of the framework we use helium as a *proof-of-principle molecule* to modify Cu-BTC such that these open metal centers are poisoned inhibiting the preferential adsorption in this site. The site poisoned Cu-BTC consists on the former Cu-BTC unit cell where 48 fixed helium atoms have been added at specific positions. To define these positions we first identified the preferential adsorption sites for water in Cu-BTC. Based on these sites we obtained the average distance between the atoms of copper and the molecules of water (2.34 Å). This distance was obtained from the radial distribution function copper-oxygen computed in a NVT Monte Carlo simulation at room temperature with one water molecule per Cu atom of the framework. The figure with the radial distribution function (Figure A6.1) is provided in the Appendix 6.

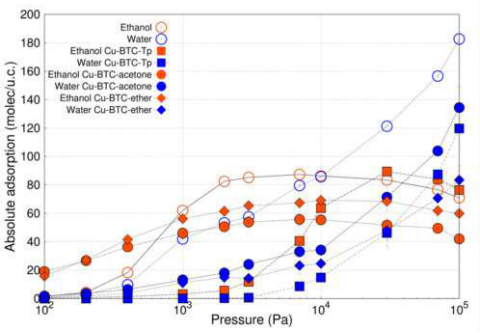

Figure 5. *Adsorption isotherms for the equimolar mixture of ethanol (orange) and water (blue) at 323 K in the bare (empty circles) and the site poisoned (squares) Cu-BTC, and in the structure containing acetone (filled circles) and dimethyl ether (diamonds).*

As shown in Figure 5, at 323 K the site poisoned Cu-BTC inhibits water adsorption up to 10^4 Pa while at this pressure the ethanol uptake is 6.4 mol/kg, i.e. 62 molecules per unit cell. In Cu-BTC the adsorbed polar molecules are not homogenously distributed within the pores but competing for the open metal centers. The poisoning of these centers displaces the preferential adsorption sites of ethanol to other cages while inhibiting the adsorption of water. The average density plots taken from the simulations of the equimolar mixtures at 10^3 Pa show that only the cavities with the open metal centers are partially filled with water while the others are almost empty. This is consistent with the copper distribution (Figure 6). In the site poisoned structure, the preferential adsorption site for water disappears and only a few molecules remain in the cages

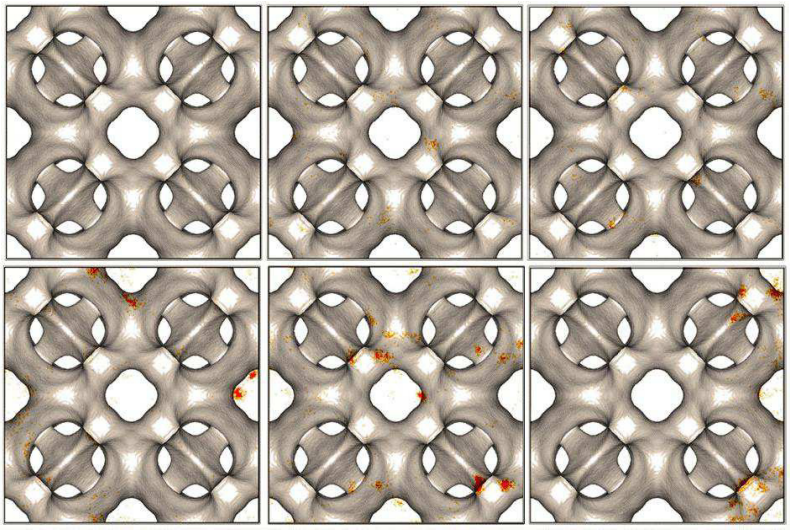

Figure 6. *Average density plots showing the adsorption of water for the equimolar feed mixture of alcohol and water at 10^3 Pa (top) and 10^4 Pa (bottom) and at 323 K in the site poisoned Cu-BTC (left), Cu-BTC with acetone (center), and Cu-BTC with dimethyl ether (right).*

The modification using atoms of helium acts as a *proof of principle*. In experiments it might be possible to tune the structure adding functional groups or to first adsorb shielding species near the metal[22]. As we did with the blockage, to opt for a more realistic approach to screen the copper atoms we are going to use acetone and dimethyl ether. We designed new structures adding 48 molecules to acetone (Cu-BTC-$CO(CH_3)_2$) or with 48 molecules of dimethyl ether (Cu-BTC-$O(CH_3)_2$) at specific positions. To analyze the specific adsorption at the Cu sites we have employed DFT on a Cu-BTC substructure modeled via a Cu_2 dimer coordinated to 4 COOH units through the oxygen atoms (Figure 7). All the structures correspond to triplet states.

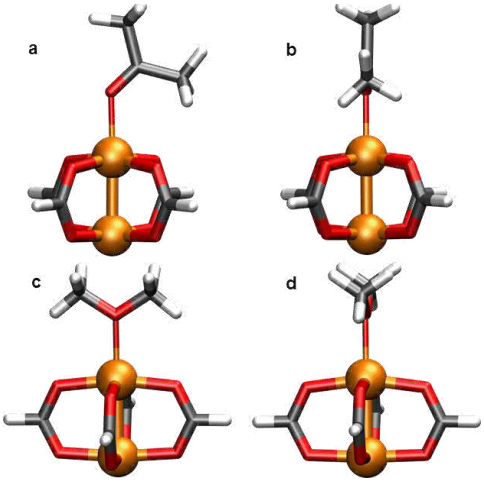

Figure 7. *Front and lateral views for the complex Cu-BTC-acetone (a, b) and Cu-BTC-dimethyl ether (c, d). The hybridization of the O atom is responsible for the reduced symmetry of Cu-BTC-acetone with respect to Cu-BTC-dimethyl ether. Color code: Cu: orange; C: gray; O: red; H: white.*

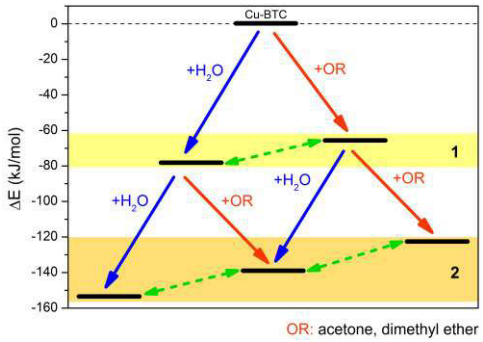

Figure 8. *Adsorption energies for water (blue arrows), acetone and dimethyl ether (red arrows) on Cu-BTC. Green dashed arrows represent the process of exchange one adsorbed molecule for another.*

Figure 8 depicts a diagram of the adsorption. The energy of the Cu-BTC cluster without any molecule adsorbed is set to be the reference. The process of adsorption is indicated through a blue arrow when it refers to water and red when it deals with either acetone or dimethyl ether, given that the energies for OR (OR=acetone and dimethyl ether) lie within 1 kJ/mol. For a more detailed description of the energies, refer to Tables A6.3 and A6.4 in the Appendix 6, where tests with larger basis sets and van der Waals contributions are also presented[54]. Dashed green arrows represent the process of displacement of one adsorbed molecule for another. Adding a water molecule to naked Cu-BTC is an exothermic process that releases about 80 kJ/mol; adding a second water molecule to the free Cu further decreases the energy of the system of 70 kJ/mol, for a total gain of 150 kJ/mol with respect to the native Cu-BTC. This implies that, even at low pressures of water, all the molecules are adsorbed on the Cu centers.

The presence of acetone/ether (OR) affects the water adsorption. In this case, the process is slightly less exothermic: the first adsorption of OR decreases the energy of about 70 kJ/mol, and the second by 50 kJ/mol, with a total gain of 120 kJ/mol with respect to the free Cu-BTC. When OR is already coordinated to the cluster, Cu-BTC-2OR, the site is blocked for the incoming water molecules as no coordination positions are available. The energy gain by the displacement Cu-BTC-2OR by H_2O is between 0 and -15 kJ/mol to be compared of the large exothermic value for Cu-BTC-2OR. In addition, the terminal groups of OR would push away water molecules and the rotation of these terminations would sweep away the incoming water molecules. Therefore, compared to Cu-BTC, Cu-BTC-2OR would not interact with water at low humidity contents and higher water pressures would be necessary to substitute the adsorbed OR.

The adsorption isotherms obtained by MC simulations for the equimolar mixture in the structures containing acetone and dimethyl-ether are shown in Figure 5. The introduction of the organic molecules at the nearest sites of each open metal center could shield these sites from the attack of incoming water molecules, and thus enhances water resistance of the structure significantly. Among the two molecules dimethyl ether shields more efficiently the copper atoms. Differences between the isotherms obtained when poisoning

with helium and this with organic molecules can be attributed to the fact that the organic molecules partially block the cages while screening some of the copper metal centers (Figure 6). On the other hand Cu-BTC-O$(CH_3)_2$ structure has better adsorption selectivity for the alcohol than the Cu-BTC-CO$(CH_3)_2$ structure since the interaction with the copper atom is stronger for dimethyl ether than for acetone. Comparison with the adsorption isotherms obtained for the original Cu-BTC shows a decrease in the surface areas due to the insufficient shielding. However, this drawback is highly compensated by the much better selectivity and the much higher stability of the new structures. A table with the pore volumes and surface areas obtained for all the structures can be found in the Appendix 6 (Table A6.2).

C. Low coverage adsorption

The feasibility of applying these structures to the purification of ethanol can be evaluated by estimating the vapor phase ethanol/water sorption selectivity. One method to obtain the ideal selectivity consists on calculating the ratio of the Henry coefficients for the two gases, that are computed from the average Rosenbluth factor of the molecule[54]. Besides the Henry coefficient and the ideal selectivity we examined the adsorption energy and entropy with the aim of gaining additional insight into why the tuned structures reduce water adsorption and favor selectivity towards ethanol (Table 1). These properties were computed in the low coverage regime.

The Henry coefficients obtained for ethanol are one order of magnitude lower in the blocked than in the site poisoned structures, and the adsorption energies decrease by 8%. On the other hand, the decrease observed for water is of three orders of magnitude in the

Table 1. *Henry coefficients (mol/(kg · Pa)), adsorption energies (kJ/mol), and adsorption entropies (J/(K · mol)) computed in Cu-BTC and in the tuned structures at 323 K.*

		K_H	K_{HE}/ K_{Hw}	-ΔU	-ΔH	-ΔG	-ΔS
Cu-BTC	E	$2.8\ 10^{-3}$	1.33	43.2	45.9	26.3	60.5
	W	$2.1\ 10^{-3}$		43.9	46.6	25.3	66.0
Blocked	E	$7.4\ 10^{-4}$	389	39.9	42.7	22.8	61.6
	W	$1.9\ 10^{-6}$		12.1	14.7	6.7	25.0
ILs(2)	E	5.6	9.8	81.0	83.7	47.3	112
	W	$5.7\ 10^{-1}$		66.2	69.0	40.9	86.8
Poisoned	E	$8.1\ 10^{-4}$	337	40.0	42.7	23.0	61.1
	W	$2.4\ 10^{-6}$		11.6	14.3	7.4	21.3
Ketone	E	$9.8\ 10^{-2}$	33.7	56.9	59.6	36.5	71.3
	W	$2.9\ 10^{-3}$		41.9	44.6	26.4	56.1
Ether	E	$3.4\ 10^{-2}$	51.5	53.3	56.0	33.6	69.3
	W	$6.6\ 10^{-4}$		35.7	38.4	22.4	49.3

Henry coefficients, and by 70% in the energies. This contrast between the behavior for water and ethanol clearly indicates the influence of the nature of the adsorbent in the adsorption conditions. The selectivity of ethanol over water is revealing in terms of the preferred interactions and shed light on the adsorption results. Compared to Cu-BTC, all the tuned versions show enhanced adsorption selectivity for ethanol. Both blocked and site poisoned Cu-BTC structures present the highest selectivity (300 times higher than for native Cu-BTC), with the most hydrophobic cage environment and similar adsorption energies. The adsorption energies obtained for the structures with acetone and dimethyl ether show different trend to the latter structures. In particular, the heats of adsorption obtained for ethanol are higher than those obtained in the original structure, implying that the organic groups are acting as preferential adsorption sites for the alcohol. On the other hand, the heats of adsorption obtained for water in the Cu-BTC-OR structures are slightly lower than the values obtained for the Cu-BTC structure as a consequence of the partial screening of the open metal centers. Therefore, the Cu-BTC-OR structures exhibit higher ideal selectivity for the alcohol than the original structure and simultaneously higher stability to water. In particular, the adsorption selectivity can be enhanced by almost a factor of 25 by screening the copper atoms with acetone and by a factor of 40 by screening the cooper atoms with dimethyl ether. As we mentioned above, selective blockage using ionic liquids does not seem a good option for ethanol purification. The strong interactions between the ionic liquids and the adsorbates lead to higher values on the Henry coefficients and heats of adsorption, and therefore to lower selectivity in favor of ethanol for the structure with two ILs per cage, and even to the inversion of the selectivity for the structure with four ILs per cage (Figure 3).

D. Liquid phase adsorption

The adsorption isotherms of a liquid feed with a given concentration can also be computed using GC Monte Carlo simulations. In a liquid mixture the partial fugacity of each component (f_i) is obtained from the expression[55]:

$$f_i = \varphi_i^{sat} p_i^{sat} \gamma_i x_i \exp\left[\frac{V_i^{mol}\left(p - p_i^{sat}\right)}{RT}\right]$$

in which p_i^{sat} is the saturated vapor pressure of pure component i and φ_i^{sat} is the fugacity coefficient of pure component i in the gas phase at the saturated vapor pressure. The value of φ_i^{sat} is obtained from the Peng-Robinson equation of state[56-57] and p_i^{sat} is obtained from the Antonie equation[58-59]. γ_l is the activity coefficient in the liquid mixture and calculated from the experimental vapor-liquid equilibrium data[60-61] and x_i is the mole fraction of component i in the mixture. V_i^{mol} is the molar volume of pure component i in the liquid phase. The factor $exp\ [V_i^{mol}\ (p\ -p_i^{sat}\ )/RT]$ is very close to 1. Comparison of the obtained fugacity coefficients with the experimental values can be found in the Appendix 6 (Figure A6.2).

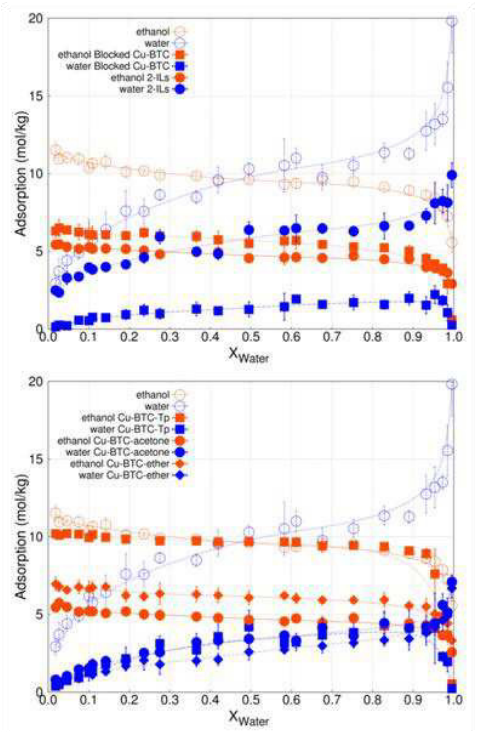

Figure 9. *Computed adsorption of ethanol (orange) and water (blue) as a function of the molar fraction of water for mixtures in the liquid phase at 323 K and 1 atm. Top: Cu-BTC (open symbols), blocked Cu-BTC (closed squares), and structure with 2 ILs per cage (closed circles). Bottom: Cu-BTC (open symbols), site poisoned Cu-BTC (filled squares), and structures with acetone (filled circles), and dimethyl ether (filled diamonds).*

As shown in Figure 9, the tuning structures also separate water and ethanol in the liquid phase for all feed compositions. As for the gas mixture, the interaction between the water molecules and the framework strongly differs in both structures and the adsorption of water in the tuning structures is inhibited in the entire feed range. An interesting aspect in these figures is that the adsorption of water when molar fraction is 1 goes to zero for the blocked and the screened structure, proving that the hydrogen-bonding of ethanol and water is needed to allow water to enter the structure. This is further demonstrated by the fact that the isosteric heats of adsorption of water is enhanced from -14.3 kJ/mol (empty structure) to -20.2 kJ/mol for the structure containing 46 molecules of ethanol per unit cell.

As in the gas phase, the structure containing ionic liquids is not suitable for ethanol-water separation (Figure 9). On the contrary, Cu-BTC-$CO(CH_3)_2$ and Cu-BTC-$O(CH_3)_2$ exhibit promising separation performance in the liquid phase. Because of the screening, the decrease in total adsorption for these structures compared to Cu-BTC is pronounced. High adsorption loadings at high concentrations are typically a function of large pore volume. However, the pore volume differences between Cu-BTC (0.863 cm^3/g) and the Cu-BTC-$CO(CH_3)_2$ (0.549 cm^3/g) and Cu-BTC-$O(CH_3)_2$ (0.589 cm^3/g) structures cannot totally account for the fact that Cu-BTC adsorbs a much greater amount of water than the tuned MOFs. Clearly, the organic functional groups are depressing the water adsorption, in spite of the presence of open metal centers. Among the organic groups, dimethyl ether performs better probably due to a more efficient coordination between the open metallic center and the oxygen of the ether.

Conclusions

This work explores at a molecular level the influence of the open metal centers on the mechanisms governing ethanol/water separation. We show that the effect of the metal centers goes beyond binding positions and we provide atomistic guidelines toward the topology and composition of the structure to improve the separation factor of the alcohol while enhancing the water resistance of the structure.

The screening of the metal-site changes the specific interactions of water and ethanol. Screening shields the metal centers from attack by water molecules while simultaneously, enhances the separation factor. This finding supports the idea that one can shield the weakest point of the structure with hydrophobic groups to enhance the water stability of the framework.

Bibliography

(1) Huang, H. J.; Ramaswamy, S.; Tschirner, U. W.; Ramarao, B. V. *Separation and Purification Technology* **2008**, *62*, 1.

(2) Huber, G. W.; Corma, A. *Angewandte Chemie-International Edition* **2007**, *46*, 7184.

(3) Vane, L. M. *Biofuels Bioproducts & Biorefining-Biofpr* **2008**, *2*, 553.

(4) Blume, I.; Wijmans, J. G.; Baker, R. W. *Journal of Membrane Science* **1990**, *49*, 253.

(5) Psaume, R.; Aptel, P.; Aurelle, Y.; Mora, J. C.; Bersillon, J. L. *Journal of Membrane Science* **1988**, *36*, 373.

(6) Uragami, T.; Takigawa, K. *Polymer* **1990**, *31*, 668.

(7) Will, B.; Lichtenthaler, R. N. *Journal of Membrane Science* **1992**, *68*, 119.

(8) N., B.; H., J.; D., D.; Walton, K. *Journal of the American Chemical Society* **2013**, *135*, 7172.

(9) H., J.; Y.-G., H.; K., W. *Langmuir* **2012**, *28*, 16874.

(10) H., J.; C., B. N.; Y-G., H.; Cai, Y.; Walton, K. S. *Langmuir* **2013**, *29*, 633.

(11) Nalaparaju, A.; Zhao, X. S.; Jiang, J. W. *Energy & Environmental Science* **2011**, *4*, 2107.

(12) Lee, J. Y.; Olson, D. H.; Pan, L.; Emge, T. J.; Li, J. *Advanced Functional Materials* **2007**, *17*, 1255.

(13) Bourrelly, S.; Moulin, B.; Rivera, A.; Maurin, G.; Devautour-Vino, S.; Serre, C.; Devic, T.; Horcajada, P.; Vimont, A.; Clet, G.; Daturi, M.; Lavalley, J. C.; Loera-Serna, S.; Denoyel, R.; Llewellyn, P. L.; Ferey, G. *Journal of the American Chemical Society* **2010**, *132*, 9488.

(14) Pan, L.; Parker, B.; Huang, X. Y.; Olson, D. H.; Lee, J.; Li, J. *Journal of the American Chemical Society* **2006**, *128*, 4180.

(15) Nalaparaju, A.; Zhao, X. S.; Jiang, J. W. *Journal of Physical Chemistry C* **2010**, *114*, 11542.

(16) Lively, R. P.; Dose, M. E.; Thompson, J. A.; McCool, B. A.; Chance, R. R.; Koros, W. J. *Chemical Communications* **2011**, *47*, 8667.

(17) Chen, Y. F.; Lee, J. Y.; Babarao, R.; Li, J.; Jiang, J. W. *Journal of Physical Chemistry C* **2010**, *114*, 6602.

(18) Greathouse, J. A.; Allendorf, M. D. *Journal of the American Chemical Society* **2006**, *128*, 10678.

(19) Kaye, S. S.; Dailly, A.; Yaghi, O. M.; Long, J. R. *Journal of the American Chemical Society* **2007**, *129*, 14176.

(20) Bellarosa, L.; Calero, S.; Lopez, N. *Physical Chemistry Chemical Physics* **2012**, *14*, 7240.

(21) Bellarosa, L.; Manuel Castillo, J.; Vlugt, T.; Calero, S.; Lopez, N. *Chemistry-a European Journal* **2012**, *18*, 12260.

(22) Ma, D.; Li, Y.; Li, Z. *Chemical Communications* **2011**, *47*, 7377.

(23) Prestipino, C.; Regli, L.; Vitillo, J. G.; Bonino, F.; Damin, A.; Lamberti, C.; Zecchina, A.; Solari, P. L.; Kongshaug, K. O.; Bordiga, S. *Chemistry of Materials* **2006**, *18*, 1337.

(24) Alaerts, L.; Seguin, E.; Poelman, H.; Thibault-Starzyk, F.; Jacobs, P. A.; De Vos, D. E. *Chemistry-a European Journal* **2006**, *12*, 7353.

(25) Collins, D. J.; Zhou, H.-C. *Journal of Materials Chemistry* **2007**, *17*, 3154.

(26) Dietzel, P. D. C.; Morita, Y.; Blom, R.; Fjellvag, H. *Angewandte Chemie-International Edition* **2005**, *44*, 6354.

(27) Martin-Calvo, A.; Garcia-Perez, E.; Garcia-Sanchez, A.; Bueno-Perez, R.; Hamad, S.; Calero, S. *Physical Chemistry Chemical Physics* **2011**, *13*, 11165.

(28) Li, Y.; Yang, R. T. *Aiche Journal* **2008**, *54*, 269.

(29) Henninger, S. K.; Schmidt, F. P.; Henning, H. M. *Applied Thermal Engineering* **2010**, *30*, 1692.

(30) Grajciar, L.; Bludsky, O.; Nachtigall, P. *Journal of Physical Chemistry Letters* **2010**, *1*, 3354.

(31) Gutierrez-Sevillano, J. J.; Vicent-Luna, J. M.; Dubbeldam, D.; Calero, S. *Journal of Physical Chemistry C* **2013**, manuscript accepted.

(32) Chui, S. S. Y.; Lo, S. M. F.; Charmant, J. P. H.; Orpen, A. G.; Williams, I. D. *Science* **1999**, *283*, 1148.

(33) Mayo, S. L.; Olafson, B. D.; Goddard, W. A. *Journal of Physical Chemistry* **1990**, *94*, 8897.

(34) Rappe, A. K.; Casewit, C. J.; Colwell, K. S.; Goddard, W. A.; Skiff, W. M. *Journal of the American Chemical Society* **1992**, *114*, 10024.

(35) Castillo, J. M.; Vlugt, T. J. H.; Calero, S. *Journal of Physical Chemistry C* **2008**, *112*, 15934.

(36) Rick, S. *Journal of Chemical Physics* **2004**, *120*, 6085.

(37) Chen, B.; Potoff, J. J.; Siepmann, J. I. *Journal of Physical Chemistry B* **2001**, *105*, 3093.

(38) Dubbeldam, D.; Calero, S.; Vlugt, T. J. H.; Krishna, R.; Maesen, T. L. M.; Smit, B. *Journal of Physical Chemistry B* **2004**, *108*, 12301.

(39) Dubbeldam, D.; Calero, S.; Ellis, D. E.; Snurr, R. Q.; 1.0 ed. Northwestern University: Evanston IL, 2008.

(40) Martin-Calvo, A.; Calero, S.; Martens, J. A.; van Erp, T. S. *Journal of Physical Chemistry C* **2013**, *117*, 1524.

(41) Dubbeldam, D.; Calero, S.; Maesen, T. L. M.; Smit, B. *Physical Review Letters* **2003**, *90*(24), 245901.

(42) Calero, S.; Martin-Calvo, A.; Hamad, S.; Garcia-Perez, E. *Chemical Communications* **2011**, *47*, 508.

(43) Gutierrez-Sevillano, J. J.; Caro-Perez, A.; Dubbeldam, D.; Calero, S. *Physical Chemistry Chemical Physics* **2011**, *13*, 20453.

(44) Frisch, M., J. et al.; Gaussian, Inc,Pittsburgh PA: 2009.

(45) Becke, A. D. *Journal of Chemical Physics* **1993**, *98*, 5648.

(46) Lee, C. T.; Yang, W. T.; Parr, R. G. *Physical Review B* **1988**, *37*, 785.

(47) Stephens, P. J.; Devlin, F. J.; Chabalowski, C. F.; Frisch, M. J. *Journal of Physical Chemistry* **1994**, *98*, 11623.

(48) Harihara.Pc; Pople, J. A. *Molecular Physics* **1974**, *27*, 209.

(49) Rassolov, V. A.; Ratner, M. A.; Pople, J. A.; Redfern, P. C.; Curtiss, L. A. *Journal of Computational Chemistry* **2001**, *22*, 976.

(50) Hay, P. J.; Wadt, W. R. *Journal of Chemical Physics* **1985**, *82*, 270.

(51) Gupta, K. M.; Chen, Y.; Hu, Z.; Jiang, J. *Physical Chemistry Chemical Physics* **2012**, *14*, 5785.

(52) Chen, Y.; Hu, Z.; Gupta, K. M.; Jiang, J. *Journal of Physical Chemistry C* **2011**, *115*, 21736.

(53) Kelkar, M. S.; Maginn, E. J. *Journal of Physical Chemistry B* **2007**, *111*, 4867.

(54) Smit, B.; Siepmann, J. I. *Journal of Physical Chemistry* **1994**, *98*, 8442.

(55) Smith, J. M.; van Ness, H. C.; Abbott, M. M. *Introduction to Chemical Engineering Thermodynamics*; McGraw-Hill: USA, 2001.

(56) Melhem, G. A.; Saini, R.; Goodwin, B. M. *Fluid Phase Equilibria* **1989**, *47*, 189.

(57) Peng, D. Y.; Robinson, D. B. *Ind. Eng. Chem. Fundamen.* **1976**, *15*, 59.

(58) Ambrose, D.; Sprake, C. H. S. *J. Chem. Thermodyn.* **1970**, *2*, 631.

(59) Bridgeman, O. C.; Aldrich, E. W. *J. Heat Transfer* **1964**, *86*, 279.

(60) Taylor, R.; Krishna, R. *Multicomponent mass transfer*; Wiley: New York, NY, 1993.

(61) Pemberton, R. C.; J., M. C. *J. Chem. Thermodyn.* **1978**, *10*, 867.

9

Conclusions

Concerning the development of force fields and sets of charges these are the main results achieved in this work:

1. Models of propylene able to reproduce the experimental dipole and the VLE curve have been proposed. A new force field with specific interactions between propylene and zeolites with narrow channels has also been developed.
2. The presence of Ge atoms in zeolite frameworks not only favors the formation of small rings but also incorporates dynamic flexibility to the framework, which induces a breathing-like motion of the zeolites. This previously non-described finding has a direct impact on molecular diffusion, and in the case of the zeolite framework type LTA it is observed an enhancing of the diffusion coefficient at least by a factor of two.
3. Three sets of interatomic potential parameters to model liquid and gas phases of H_2S correctly, based on 3-sites, and 5-sites models have been developed. Choosing among the models depends on the property to measure.
4. A complete scalable and transferable set of charges for ZIFs has been developed. The predicted heats of adsorption of CO_2 in several ZIFs, are in good agreement with experimental results.

Regarding the study of nanoporous materials for applications of enviromental and industrial interest, we have obtained the following results:

5. The steric effect explains that only small molecules or properly shaped molecules such as propylene can diffuse into ITQ-12. Larger molecules such as propane are excluded from entering the internal pore of this zeolite.

6. The combination of our diffusion and adsorption results corroborates previous experimental findings, pointing out ITQ-12 as a suitable structure for propane/propylene separations.
7. Interactions between H_2S molecules and copper atoms from the Cu-BTC framework are weaker than interactions between water molecules and copper atoms. The coordination of hydrogen sulfide molecules to the metallic centers could not be the reason of the Cu-BTC degradation upon adsorption of H_2S.
8. The separation of carbon dioxide/methane mixtures in Cu-BTC metal organic framework is governed by the adsorption process. The adsorption of carbon dioxide is higher than the adsorption of methane in Cu-BTC. On the other hand diffusion is higher for methane than for carbon dioxide.
9. The competition between size and dipole effects defines the preferred adsorption site of a given molecule in the metal organic framework Cu-BTC. Small molecules prefer to adsorb in the tetrahedral cages due to the isosteric effect. Larger nonpolar molecules prefer to adsorb in the big cages of the framework. Molecules with high dipole moment adsorb close to the copper atoms.
10. To improve the water/alcohol separation and to enhance the water stability of Cu-BTC, the interactions between water and copper atoms have to be weakened.

Related to the design of new materials with specific characteristics:

11. It is possible to block certain cages of Cu-BTC adding ionic liquids to the framework, but this addition is not enough to prevent water from entering the cages.
12. It is possible to screen the copper atoms, preventing the water attack to the metallic centers, with molecules such as dimethyl ether and acetone.

Molecular simulation can be an extremely useful tool. It not only corroborates experimental results and predicts the behavior of systems but also tackles problems from a different approach. The main finding of this thesis is that it is possible to descend to an atomic level and to study the mechanisms responsible of adsorption processes. Based on that knowledge we can design specific strategies to solve specific problems. The application of this methodology to the study of nanoporous materials leads us to identify key points of a framework. Then we can tailor the structure in order to achieve a certain goal. We can design materials and test our predictions about them. In this way we are giving guidelines to pass from theoretical structures to real materials.

Resumen y conclusiones

Existen unas doscientas zeolitas registradas en la base de datos internacional de zeolitas. Hay más de diez mil estructuras Metal-Orgánicas (MOFs) sintetizadas hasta la fecha y el número de nuevos materiales Metal-Orgánicos con estructura Zeolítica (ZIFs) que se sintetizan no deja de crecer. A pesar de estos números impresionantes, la mayoría de los materiales no tiene aún una aplicación industrial. Todavía es necesaria mucha investigación para analizar dichos materiales y sus propiedades. En este estudio se persigue proporcionar nuevos métodos y herramientas de investigación para incrementar significativamente nuestro conocimiento sobre estos materiales. También se pretende estudiar el posible uso de los materiales nanoporosos cristalinos para afrontar algunos de los desafíos actuales a los que se enfrenta la industria. Finalmente, el objetivo último es dar un paso más allá y ser capaces de diseñar estructuras hipotéticas que sean apropiadas para resolver problemas concretos.

Por tanto, el propósito de esta tesis es triple:

- Desarrollar nuevos campos de fuerza y conjuntos de cargas que permitan modelar materiales nanoporosos.
- Estudiar los potenciales usos de distintos materiales nanoporosos en diversos procesos de interés industrial.
- Diseñar nuevos materiales con propiedades específicas para aplicaciones tecnológicas.

Para alcanzar estos objetivos utilizamos la simulación molecular empleando los métodos, modelos y campos de fuerza que han sido explicados en secciones anteriores.

Desarrollo de nuevos campos de fuerza y conjuntos de cargas que permitan modelar materiales nanoporosos. (Capítulos 2, 3, 4 y 5)

En el capítulo 2 se realiza un estudio de los modelos de propileno disponibles en la literatura y se proponen nuevos modelos. Estos modelos se desarrollan a partir del ajuste de los parámetros a resultados experimentales de adsorción en zeolitas. Los parámetros Lennard-Jones se ajustan para reproducir la curva de equilibrio líquido-vapor (VLE). En este capítulo se desarrolla también un campo de fuerzas específico que es capaz de predecir la difusión y adsorción de propileno en zeolitas con canales muy estrechos.

En el capítulo 3 se estudia el efecto de la sustitución de átomos de silicio por átomos de germanio en una zeolita. El estudio se centra en la deformación que se produce en los anillos de 4, 6 y 8 miembros que forman la estructura. Se calculan el área superficial y el volumen de poro tanto de la estructura pura sílice como de las distintas estructuras modificadas con germanio. Estos valores se comparan

entre sí a la vez que con datos experimentales. Por último se calculan los coeficientes de difusión del metano y el propano en las estructuras consideradas, usando modelos rígidos para las zeolitas e incorporando flexibilidad a dichos modelos.

En el capítulo 4 se lleva a cabo una discusión de los modelos existentes de sulfuro de hidrógeno y se proponen tres nuevos modelos. Se hace una comparación entre ellos atendiendo a la precisión para reproducir la curva VLE y la densidad en fase líquida. Los resultados muestran un buen acuerdo entre modelos. En este capítulo también se calculan las isotermas de adsorción, calores de adsorción y coeficientes de Henry del sulfuro de hidrógeno en tres MOFs.

En el capítulo 5 se desarrolla un conjunto de cargas puntuales escalables y transferibles para el modelado de ZIFs. Este conjunto de cargas se puede utilizar tanto para modelar ZIFs ya sintetizados como para ZIFs hipotéticos. En el capítulo se comprueba también la viabilidad del conjunto de cargas comparando los calores de adsorción que se obtienen por simulación utilizando las cargas propuestas, con los datos experimentales.

Estudio de los potenciales usos de distintos materiales nanoporosos en diversos procesos de interés industrial. (Capítulos 2, 4, 6 y 7)

En el capítulo 2, usamos los modelos y campos de fuerza desarrollados para estudiar las propiedades de adsorción y difusión de propano y propileno en la zeolita ITQ-12. Los modelos propuestos reproducen las isotermas de adsorción experimentales. Utilizando TST se calculan los coeficientes de difusión para explicar las diferencias obtenidas experimentalmente.

En el capítulo 4, se estudia la adsorción de sulfuro de hidrógeno en tres MOFs con diferentes topologías, IRMOF-1, MIL-47 y Cu-BTC. Se calculan los calores de adsorción, los coeficientes de Henry y las isotermas de adsorción para obtener un mejor entendimiento del comportamiento del gas dentro de las estructuras.

En los capítulos 6 y 7 se realiza un extenso estudio de la estructura Cu-BTC. Se estudia la adsorción de gases de efecto invernadero, como el dióxido de carbón y el metano en dicha estructura. Se calculan las isotermas de adsorción de los gases puros y en mezclas binarias equimolares. Los resultados coinciden con los ya existentes en simulación y con los experimentales. El estudio se amplía para mezclas variando la fracción molar de cada componente utilizando tanto simulaciones moleculares como IAST. Se calculan también los coeficientes de difusión utilizando dinámica molecular y se determinan las selectividades de adsorción, difusión y de mezclas. También se identifican los sitios de adsorción en Cu-BTC. Conforme a ellos se lleva a cabo un estudio sistemático para analizar los sitios preferenciales de adsorción de hidrocarburos, gases de efecto invernadero, alcoholes, agua y los principales componentes del aire. El estudio se centra también en los mecanismos que gobiernan los procesos de adsorción de las

moléculas anteriores. Utilizando la simulación molecular en el colectivo canónico y variando el número de moléculas, analizamos la distribución de las mismas dentro del sistema de canales de la estructura. Finalmente se explora la posibilidad de mejorar la adsorción de determinados gases mediante la adición de líquidos iónicos a la estructura.

Diseño de nuevos materiales con propiedades específicas para aplicaciones tecnológicas. (Capítulo 8)

En el capítulo 8 se desarrolla la idea de modificar la estructura Cu-BTC para favorecer la adsorción de ciertos gases y evitar la adsorción de otros. Tomando como base los resultados del capítulo 6, se estudia la separación de alcoholes y agua. Se calculan isotermas de adsorción de mezclas equimolares en fase gas y fase líquida, así como energías de adsorción, entropías y coeficientes de Henry. Se siguen dos estrategias para mejora la separación: bloquear las cajas de la estructura y "envenenar" los centros metálicos de la estructura. Ambas estrategias se prueban y discuten en el capítulo y se proponen alternativas reales para llevarlas a cabo experimentalmente. Finalmente, se predice que una de las modificaciones del Cu-BTC podría incrementar su estabilidad ante la presencia de agua.

Las principales conclusiones de la tesis, agrupadas según los objetivos, son:

Respecto al desarrollo de campos de fuerza y conjuntos de cargas:

1. Se han presentado modelos de propileno que reproducen el dipolo experimental y la curva VLE. Se ha desarrollado un nuevo campo de fuerzas específico para zeolitas con canales estrechos.

2. La presencia de átomos de germanio en la estructura de zeolitas tipo LTA, no sólo promueve la formación de pequeños anillos sino que confiere flexibilidad a la estructura. Este hecho repercute directamente en la difusión. Se observa una mejora de los coeficientes de difusión para el caso del metano y el propano de al menos el doble.

3. Se han desarrollado tres conjuntos de parámetros Lennard-Jones, para modelos H_2S de 3 cuerpos y 5 cuerpos, que reproducen la coexistencia de las fases líquido-gas correctamente. La elección de uno u otro modelo depende de la propiedad que se desee medir.

4. Se ha desarrollado un conjunto de cargas escalable y transferible para ZIFs. Los calores de adsorción predichos con ellas para el CO_2 en diversos ZIFs están en buen acuerdo con los resultados experimentales.

Sobre el estudio de los potenciales usos de distintos materiales nanoporosos en diversos procesos de interés industrial:

5. El efecto estérico explica que solo las moléculas pequeñas o con la forma adecuada, como el propileno, pueden difundir en la zeolita ITQ-12. Moléculas más grandes como el propanol no pueden entrar en los poros internos de la zeolita.

6. La combinación de los resultados de difusión y adsorción en este estudio corroboran los resultados experimentales anteriores que situaban a la ITQ-12 como una estructura apropiada para separar propano y propileno.

7. Las interacciones entre las moléculas de sulfuro de hidrógeno y los átomos de cobre de la estructura Cu-BTC son más débiles que las interacciones entre las moléculas de agua y los cobres. La coordinación del sulfuro de hidrógeno a los centros metálicos puede que no sea la razón de la degradación del Cu-BTC.

8. La separación de mezclas de dióxido de carbono y metano en la estructura metal orgánica Cu-BTC está gobernada por los procesos de adsorción. La adsorción de dióxido de carbono es mayor que la de metano, mientras que en el caso de la difusión ocurre lo contrario. La difusión de metano es mayor que la de dióxido de carbono.

9. La competición entre los efectos de tamaño y los del dipolo definen los sitios preferentes de adsorción para una molécula dada en el Cu-BTC. Las moléculas pequeñas prefieren adsorberse en las cajas tetraédricas, debido a efectos estéricos. Las moléculas más grandes no polares prefieren situarse en las cajas grandes de la estructura. Aquellas moléculas con momento dipolar elevado se adsorben junto a los átomos de cobre.

10. Para mejorar la separación de agua y alcoholes y aumentar la estabilidad del Cu-BTC al agua, es necesario debilitar las interacciones entre el cobre y las moléculas de agua.

Relativo al diseño de nuevos materiales con propiedades específicas:

11. Es posible bloquear algunas de las cajas del Cu-BTC añadiendo líquidos iónicos a la estructura. No obstante esta adición de moléculas no es suficiente para evitar la entrada de agua en las cajas.

12. Se puede apantallar los átomos de cobre, evitando así que el agua los ataque, utilizando moléculas como el dimetil éter y la acetona.

En este trabajo hemos podido comprobar que la simulación molecular es una herramienta extremadamente útil. Con simulaciones moleculares no sólo podemos corroborar resultados experimentales y predecir el comportamiento de

los sistemas, sino que también se pueden abordar problemas desde una perspectiva distinta. El principal resultado de la tesis es que es posible descender a niveles atómicos y estudiar los mecanismos responsables de cada proceso. Basándonos en ese conocimiento, es posible diseñar estrategias específicas para resolver problemas concretos. La aplicación de esta metodología al estudio de materiales nanoporosos nos lleva a identificar los puntos clave de cada estructura. Una vez conocidos, podemos modificar la estructura, aprovechando esas claves, para lograr un objetivo previamente establecido. Podemos diseñar materiales y probar nuestras predicciones en ellos. De esta forma, estamos proporcionando líneas maestras para pasar de estructuras teóricas a materiales reales.

Appendix 1

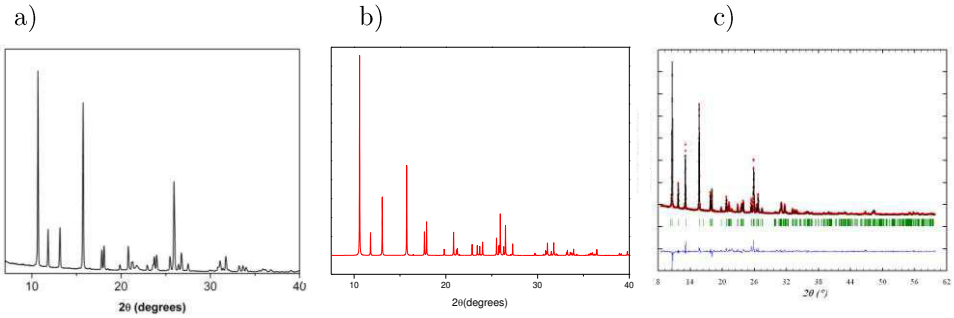

Figure A1.1. X-Ray diffraction pattern of calcined pure silica ITQ-12 zeolite: (a) experiment, (b) simulation, an (c) Rietveld analysis of the X-Ray diffraction pattern of ITQ-12 sample. X-Ray diffraction pattern were obtained on a X'Pert Pro diffractometer equipped with an Anton-Parr XRK900 high temperature reactor. The sample was dehydrated at 500 ^{o}C prior to the measurement. The intensity data were collected using Cu K-alpha 1,2 radiation (lambda 1=1.5406, lambda 2=1.5444 E) at 303 K in a Bragg Brentano geometry (tube voltage and intensity: 45 kV and 40 mA; divergence slit: fixed (1/16); scan range (2theta): 8–60^{o}; step size (2theta): 0.0178, time per step: 600 s). The structure was refined using the Rietveld method with the FullProf program. Rwp=19.6, Rexp=4.87, RB=16.4,RF=22.3.

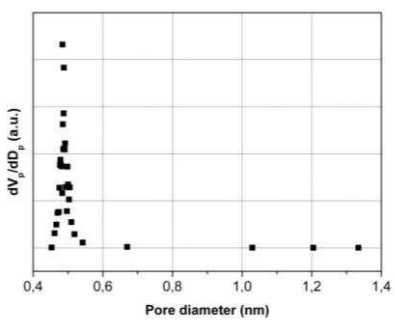

Figure A1.2. Micropore volume distribution of pure silica ITQ-12 zeolite obtained from the Ar adsorption isotherm at 83 K using the Horvath-Kawazoe method.

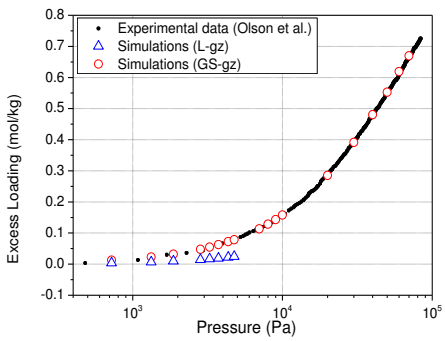

Figure A1.3. Adsorption isotherms of ethene in ITQ-12 at 300 K. Simulations were performed using previous (open triangles) and new (open circles) $CH_2(sp^2)$-$O_{zeolite}$ Lennard-Jones interacttion parameters.

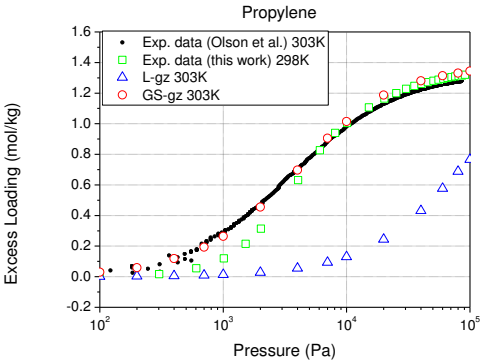

Figure A1.4. Adsorption isotherms of propylene in ITQ-12 at 300 K. Simulations were performed using previous (open triangles) and new (open circles) CH(sp^2)-$O_{zeolite}$ Lennard Jones interaction parameters. These parameters correspond to Lgz and GSgz models respectively and are listed in Table 1. Experimental data obtained in this work (open squares) and taken from the literature (dots)[1] are included for comparison.

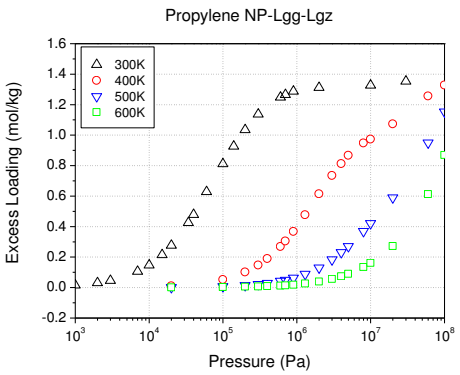

Figure A1.5. Computed adsorption isotherms for propylene at 300 K (triangles), 400 K (circles), 500 K (down triangles), and 600 K (squares) using the NP-Lgg-Lgz model.

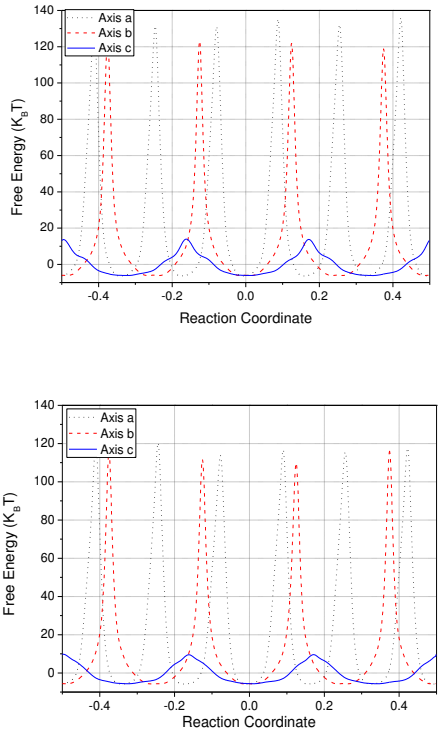

Figure A1.6. Computed free energy profiles in ITQ-12 at 300 K for (top) propane and (bottom) propylene using NP-Lgg-Lgz model. The reaction coordinate is choosen along the a-channel (dot line), b-channel (dash line) and c-channel (solid line) direction.

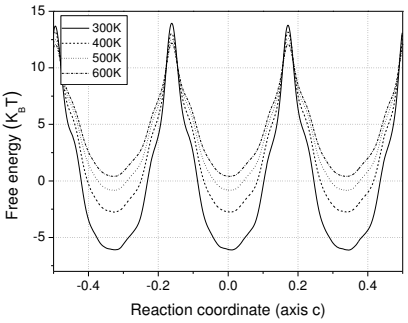

Figure A1.7. Computed free energy profiles in ITQ-12 along the c-axis for propane at 300 K (solid line), 400 K (dash line), 500 K (dot) and 600 K (dash and dot line).

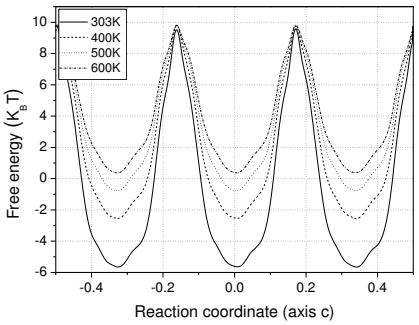

Figure A1.8. Computed free energy profiles in ITQ-12 along the c-axis for propylene (NP-Lgg-Lgz) 300 K (solid line), 400 K (dash line), 500 K (dot) and 600 K (dash and dot line).

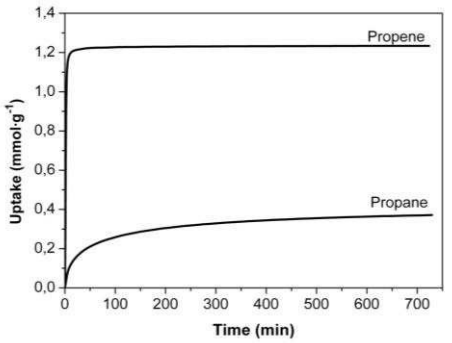

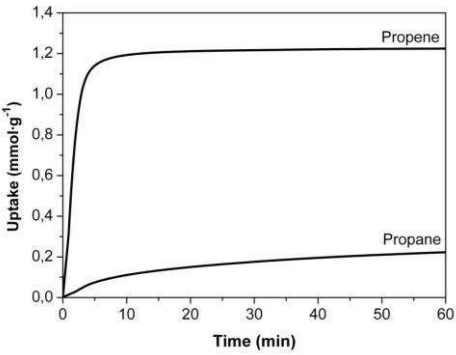

Figure A1.9. Kinetic adsorption measurements of propene and propylene at 298 K and 30.4 kPa on pure silica ITQ-12 zeolite. (Top) Long equilibration time (12 hours); (bottom) Short equilibration time (60 min).

Appendix 2

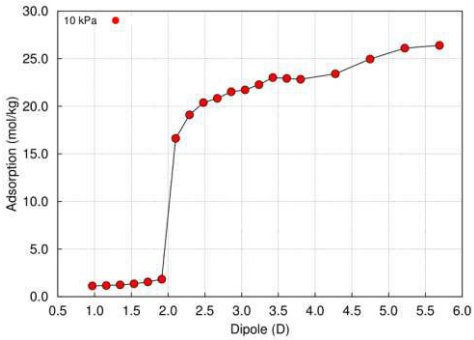

Figure A2.1. Adsorption of H_2S in Cu-BTC as a function of the dipole moment of the molecule, employing the 5S force field. The temperature is 300 K and the pressure 10 kPa.

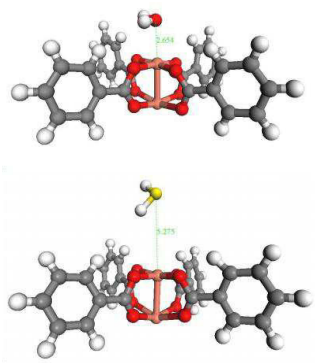

Figure A2.3. Snapshots of *ab initio* Molecular Dynamics simulations of H_2O (top) and H_2S (bottom) adsorbed on a cluster model of Cu-BTC. The simulations are carried out employing the Gaussian 09 code, with the Atom Centered Density Matrix Propagation molecular dynamics method. The level of theory used is HF/LanL2MB. The calculations were 3 ps long, with a time step 0.1 fs, and the temperature 300 K.

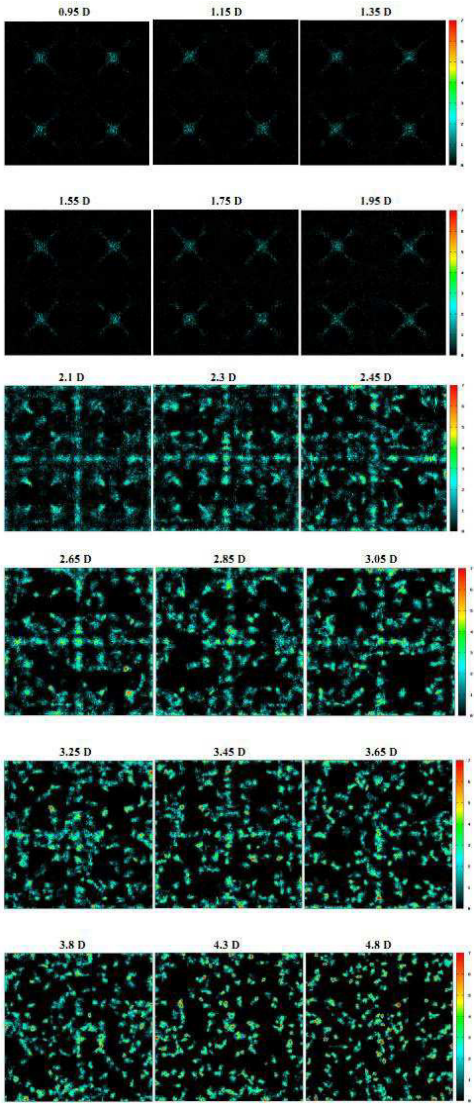

Figure A2.2. Variation of the average occupation profiles of the H_2S centers of mass (at 10 kPa and 300 K) in Cu-BTC, as the molecular dipole changes from 0.95 D to 5.7 D. The force field employed is the five-sites 5S.

Appendix 3

Figure A3.1. Atomic charges for all the imidazolates studied

im

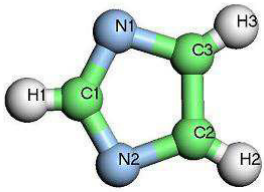

mim

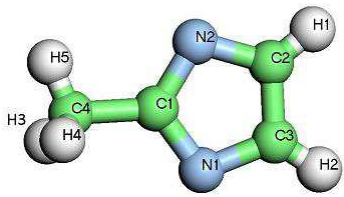

eim

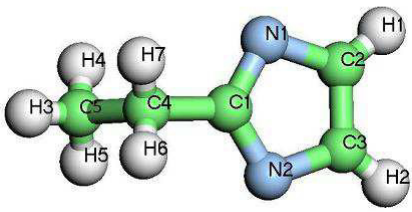

nim

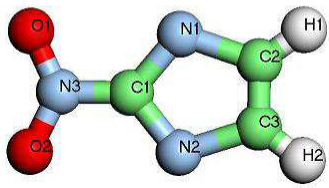

im		mim		eim		nim	
Atom	**Charge**	**Atom**	**Charge**	**Atom**	**Charge**	**Atom**	**Charge**
N1	-0.561	N1	-0.59	N1	-0.591	N1	-0.529
N2	-0.561	N2	-0.59	N2	-0.591	N2	-0.529
C1	0.081	C1	0.25	C1	0.236	N3	0.457
C2	-0.154	C2	-0.15	C2	-0.144	C1	0.229
C3	-0.154	C3	-0.15	C3	-0.144	C2	-0.102
H1	0.107	C4	-0.57	C4	-0.358	C3	-0.102
H2	0.121	H1	0.13	C5	-0.524	H1	0.154
H3	0.121	H2	0.13	H1	0.136	H2	0.154
		H3	0.18	H2	0.136	O1	-0.366
		H4	0.18	H3	0.154	O2	-0.366
		H5	0.18	H4	0.177		
				H5	0.177		
				H6	0.168		
				H7	0.168		

cnim

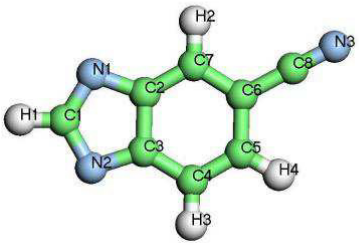

dcim

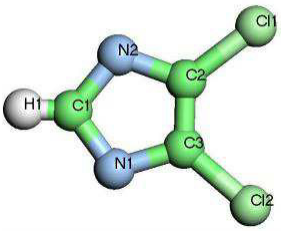

ica

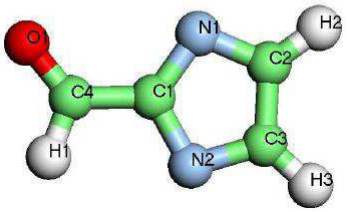

abim1

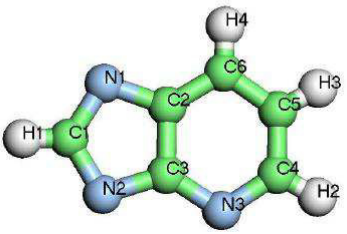

cnim		dcim		ica		abim1	
Atom	**Charge**	**Atom**	**Charge**	**Atom**	**Charge**	**Atom**	**Charge**
N1	-0.574	N1	-0.563	N1	-0.484	N1	-0.560
N2	-0.576	N2	-0.563	N2	-0.506	N2	-0.556
N3	-0.396	C1	0.106	C1	0.077	N3	-0.421
C1	0.182	C2	0.054	C2	-0.120	C1	0.158
C2	0.088	C3	0.054	C3	-0.136	C2	0.038
C3	0.077	H1	0.140	C4	0.359	C3	0.232
C4	-0.196	Cl1	-0.114	H1	0.081	C4	-0.022
C5	-0.239	Cl2	-0.114	H2	0.155	C5	-0.274
C6	-0.227			H3	0.156	C6	-0.176
C7	-0.182			O1	-0.582	H1	0.124
C8	0.309					H2	0.135
H1	0.148					H3	0.158
H2	0.201					H4	0.164
H3	0.193						
H4	0.192						

abim2

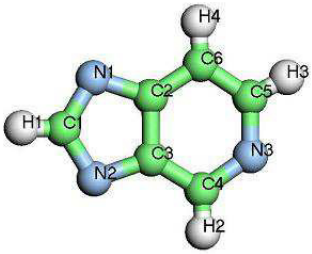

bim

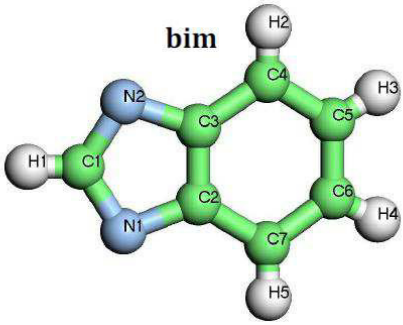

cbim

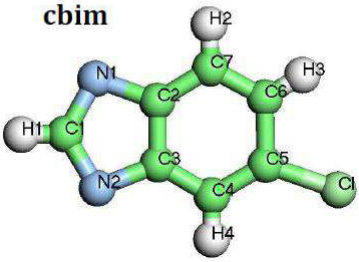

dmbim

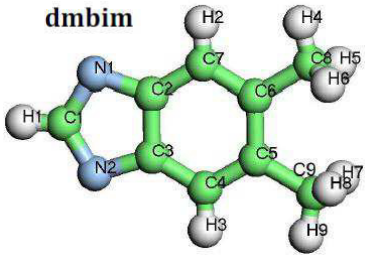

abim2		bim		cbim		dmbim	
Atom	**Charge**	**Atom**	**Charge**	**Atom**	**Charge**	**Atom**	**Charge**
N1	-0.551	N1	-0.569	N1	-0.546	N1	-0.603
N2	-0.547	N2	-0.569	N2	-0.542	N2	-0.600
N3	-0.473	C1	0.141	C1	0.157	C1	0.175
C1	0.151	C2	0.039	C2	0.035	C2	0.082
C2	0.065	C3	0.039	C3	0.055	C3	0.085
C3	0.019	C4	-0.153	C4	-0.201	C4	-0.211
C4	0.024	C5	-0.244	C5	0.093	C5	-0.056
C5	-0.027	C6	-0.244	C6	-0.386	C6	-0.055
C6	-0.233	C7	-0.153	C7	-0.127	C7	-0.208
H1	0.123	H1	0.121	H1	0.119	C8	-0.541
H2	0.147	H2	0.149	H2	0.176	C9	-0.540
H3	0.133	H3	0.147	H3	0.186	H1	0.119
H4	0.169	H4	0.147	H4	0.167	H2	0.155
		H5	0.149	Cl1	-0.186	H3	0.155
						H4	0.177
						H5	0.172
						H6	0.172
						H7	0.173
						H8	0.172
						H9	0.177

mbim

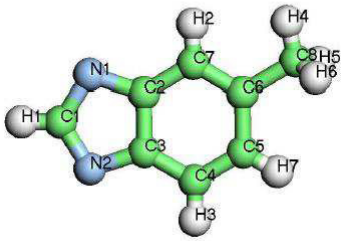

brbim

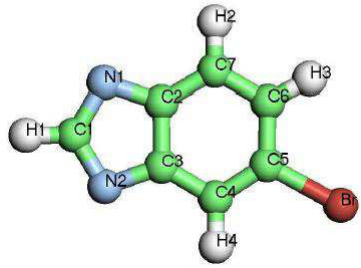

nbim

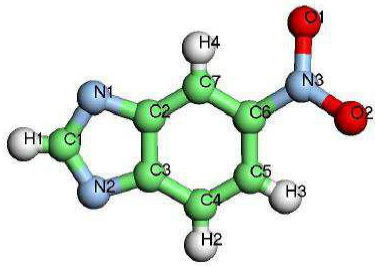

mbim		brbim		nbim	
Atom	**Charge**	**Atom**	**Charge**	**Atom**	**Charge**
N1	-0.604	N1	-0.572	N1	-0.563
N2	-0.601	N2	-0.574	N2	-0.555
C1	0.180	C1	0.164	N3	0.238
C2	0.078	C2	0.062	C1	0.207
C3	0.073	C3	0.084	C2	0.121
C4	-0.185	C4	-0.248	C3	0.077
C5	-0.246	C5	-0.142	C4	-0.133
C6	-0.051	C6	-0.293	C5	-0.245
C7	-0.212	C7	-0.192	C6	0.155
C8	-0.538	H1	0.141	C7	-0.184
H1	0.124	H2	0.187	O1	-0.391
H2	0.157	H3	0.191	O2	-0.391
H3	0.156	H4	0.200	H1	0.128
H4	0.175	Br	-0.008	H2	0.165
H5	0.172			H3	0.179
H6	0.172			H4	0.192
H7	0.150				

Appendix 4

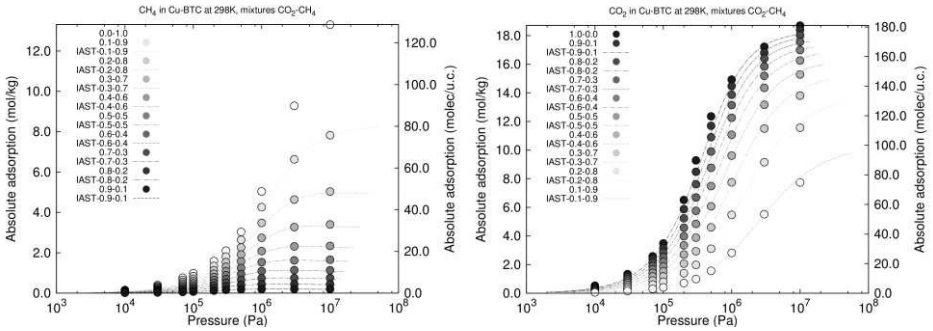

Figure A4.1. Adsorption isotherms of methane (left) and carbon dioxide (right) obtained from GCMC (symbols) and from IAST (curves) for the different mixtures.

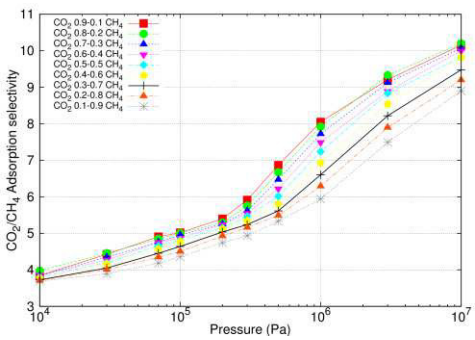

Figure A4.2. Adsorption selectivity for the different mixtures of carbon dioxide and methane obtained from GCMC (symbols) and from IAST (curves).

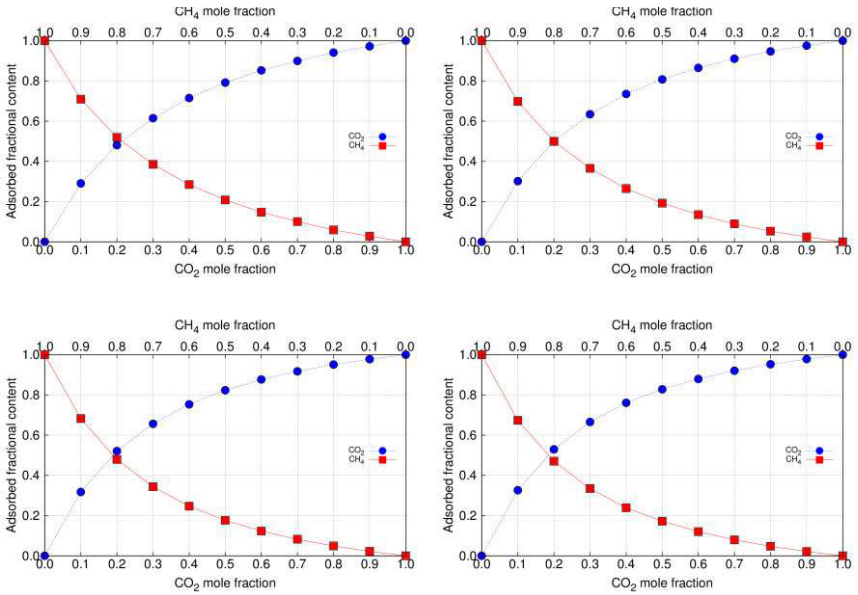

Figure A4.3. Adsorbed fractional content of molecules against the same fraction in the external gas phase computed at 298 K and 10^4 Pa (top left), $3 \cdot 10^4$ Pa (top right), $7 \cdot 10^4$ Pa (bottom left), and 10^5 Pa (bottom right).

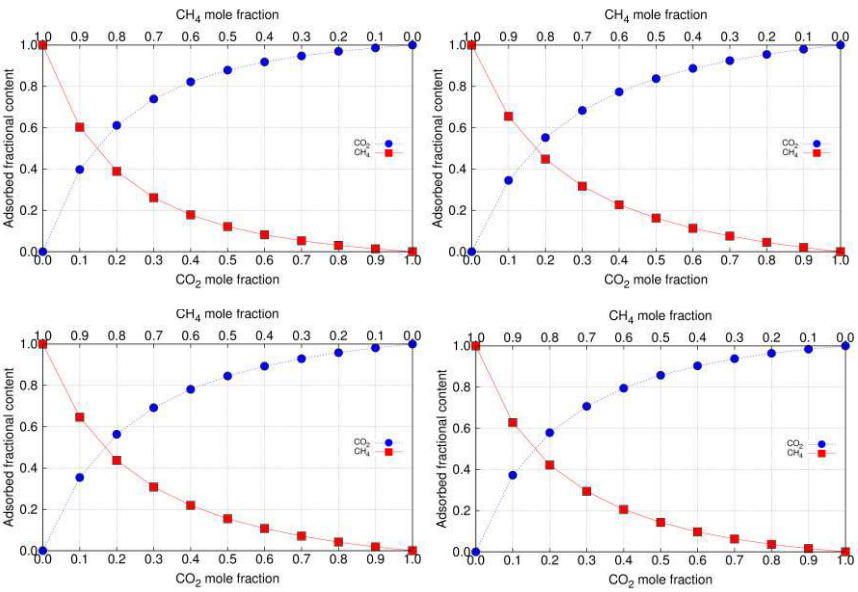

Figure A4.4. Adsorbed fractional content of molecule against the same fraction in the external gas phase computed at 298 K and $2 \cdot 10^5$ Pa (top left), $3 \cdot 10^5$ Pa (top right), $5 \cdot 10^5$ Pa (bottom left), and 10^6 Pa (bottom right).

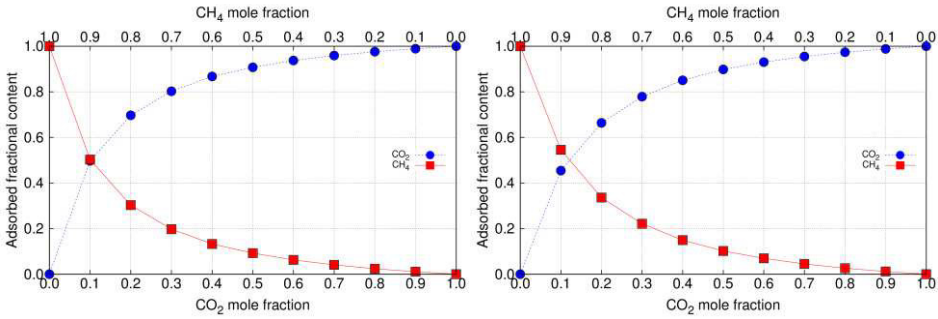

Figure A4.5. Adsorbed fractional content of molecules against the same fraction in the external gas phase computed at 298 K and $3 \cdot 10^6$ Pa (left) and 10^7 Pa (right)

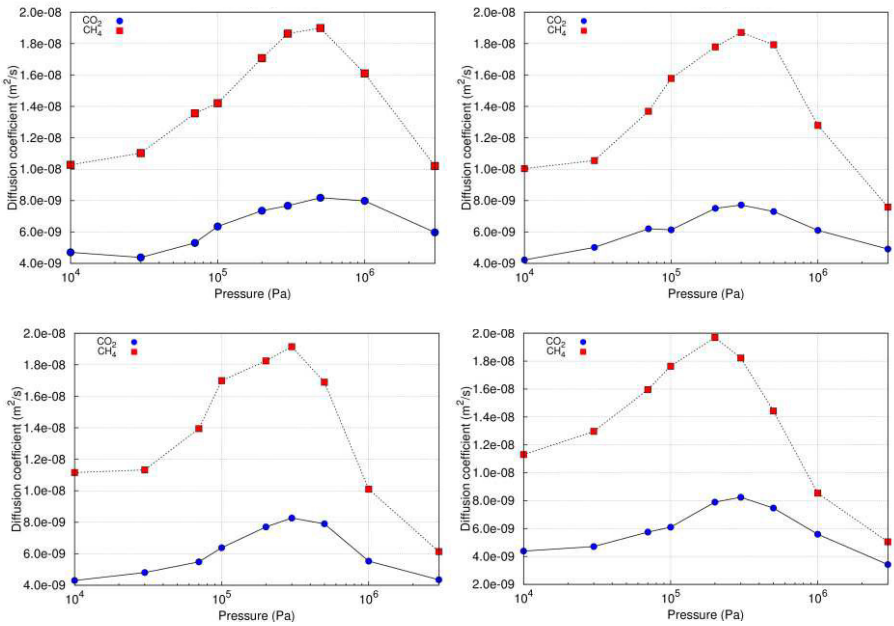

Figure A4.6 Diffusion coefficients computed as a function of pressure in Cu-BTC for the 10:90 mixture of carbon dioxide and methane (top left), 20:80 mixture of carbon dioxide and methane (top right), 30:70 mixture of carbon dioxide and methane (bottom left), and 40:60 mixture of carbon dioxide and methane (bottom right).

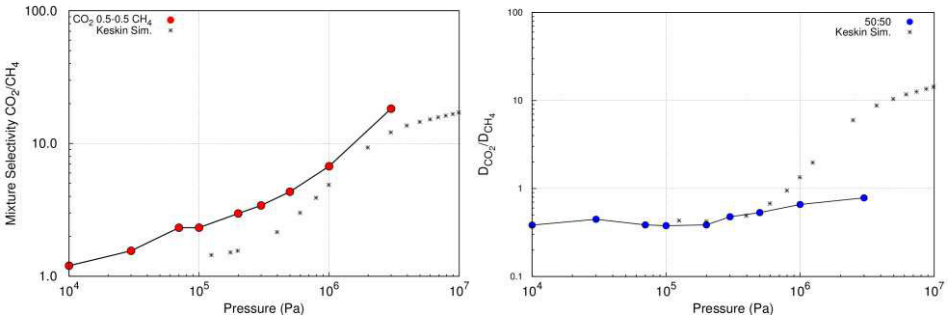

Figure A4.7. Comparison between diffusion selectivity (left) and Mixture selectivity (right) of this work and previous Keskin *et al.* results[1].

(1) Keskin, S.; Liu, J. C.; Johnson, J. K.; Sholl, D. S. *Microporous and Mesoporous Materials* **2009**, *125*, 101.

Appendix 5

Table A5.1 Lennard-Jones parameters and point charges for the adsorbent, adsorbates, and ionic liquids.

Atom types	**Epsilon/k_B (K)**	**Sigma (Å)**	**Charge (e^-)**	**Atom types**	Epsilon/k_B (K)	Sigma (Å)	Charge (e^-)
Adsorbates				**Ionic Liquid**			
C_CO_2	29.933	2.745	0.652	EMIM-C5	25.192	3.207	-0.13487
O_CO_2	85.671	3.017	-0.326	EMIM-C4	25.192	3.207	-0.14717
N_N_2	38.298	3.306	-0.40484	EMIM-C2	25.192	3.207	-0.09121
N_dummy	-	-	0.8096	EMIM-N1	100.761	3.296	0.05941
O_O_2	53.023	3.045	-0.112	EMIM-H3	3.93	2.616	0.22037
O_dummy	-	-	0.224	EMIM-H2	3.93	2.616	0.20999
Ar	124.07	3.38	-	EMIM-H1	23.175	1.604	0.21887
CH_4	158.5	3.72	-	EMIM-N3	100.761	3.296	0.19371
CH_3_sp^3	108.0	3.76	-	EMIM-C6	10.0761	4.054	-0.2508
CH_2_sp^3	56.0	3.96	-	EMIM-H4,5,6	11.084	2.352	0.14516
CH_2_sp^2	93.0	3.685	0.87	EMIM-C7	10.076	4.054	0.10394
CH_sp^2	51.0	4.0	0.87	EMIM-H7,8	11.084	2.352	0.0555
CH_sp^2_dummy	-	-	-1.74	EMIM-C8	27.709	3.875	-0.10455
CH_3_C_ol	98.0	3.75	-	EMIM-H9,10,11	11.084	2.352	0.05858
CH_3_O_ol	98.0	3.75	0.265	Tf_2N-N8	85.647	3.25	-0.66
CH_2_C_ol	46.0	3.95	-	Tf_2N-S1,2	125.951	3.55	1.02
CH_2_O_ol	46.0	3.95	0.265	Tf_2N-C50,51	33.251	3.5	0.35
O_ol	93.0	3.02	-0.7	Tf_2N-O1,2,3,4	105.799	2.96	-0.5
H_ol	-	-	0.435	Tf_2N-F1,2,3,4,5,6	26.702	2.95	-0.16
O_water	89.516	3.097	-				
H_water	-	-	0.241				
Dummy_water	-	-	-0.241				
Cu-BTC							
MOF-Cu	2.518	3.114	1.248				
MOF-O	48.19	3.03	-0.624				
MOF-C1	47.86	3,47	0.494				
MOF-C2	47.86	3.47	0.13				
MOF-C3	47.86	3.47	-0.156				
MOF-H	7.65	2.85	0.156				

Table A5.2. -ΔH (kJ · mol^{-1}) of the gases in the structure and in the sites at 295 K. The second columns indicate the statistical error.

Molecules	Cu-BTC		T1		L2		L3		Windows	
argon	14.3	0.1	16.8	0.1	10.0	0.1	8.6	0.1	10.1	0.1
N_2	14.3	0.1	17.5	0.1	10.1	0.1	8.8	0.1	9.9	0.1
CO_2	25.5	0.1	27.5	0.1	16.9	0.1	18.3	0.1	15.0	0.1
O_2	15.3	0.1	18.0	0.1	10.4	0.1	8.5	0.1	10.0	0.1
methane	20.7	0.1	22.8	0.1	12.7	0.1	11.2	0.1	13.2	0.1
ethane	35.9	0.1	36.5	0.1	17.6	0.1	15.3	0.1	16.7	0.1
propane	45.6	0.1	46.0	0.1	21.4	0.1	17.3	0.1	20.4	0.1
butane	56.4	0.2	57.4	0.1	31.4	0.1	25.1	0.1	27.6	0.2
propene	49.8	0.1	50.0	0.1	24.9	0.1	22.5	0.1	24.5	0.1
water	46.2	0.7	16.5	0.1	13.6	0.1	46.2	0.7	16.5	0.1
methanol	42.6	0.9	31.2	0.1	25.5	0.5	43.2	0.8	30.9	0.6
ethanol	45.7	0.5	43.7	0.1	27.9	0.4	46.6	0.6	33.4	0.9
propanol	52.6	0.9	53.5	0.1	34.4	0.3	52.4	1.1	39.6	0.6

Table A5.3. Henry coefficients (mol · kg^{-1} · Pa^{-1}) of the gases in the structure and in the sites at 295 K. The second columns indicate the statistical error.

Molecules	Cu-BTC		T1		L2		L3		Windows	
argon	$4.6 \cdot 10^{-6}$	$2.5 \cdot 10^{-9}$	$3.1 \cdot 10^{-6}$	$4.1 \cdot 10^{-9}$	$1.3 \cdot 10^{-6}$	$1.6 \cdot 10^{-9}$	$8.8 \cdot 10^{-7}$	$1.3 \cdot 10^{-9}$	$3.2 \cdot 10^{-7}$	$1.4 \cdot 10^{-9}$
N_2	$4.0 \cdot 10^{-6}$	$6.6 \cdot 10^{-9}$	$2.4 \cdot 10^{-6}$	$7.4 \cdot 10^{-9}$	$1.1 \cdot 10^{-6}$	$1.1 \cdot 10^{-9}$	$8.2 \cdot 10^{-7}$	$8.9 \cdot 10^{-10}$	$1.4 \cdot 10^{-7}$	$6.3 \cdot 10^{-10}$
CO_2	$7.0 \cdot 10^{-5}$	$1.7 \cdot 10^{-7}$	$5.3 \cdot 10^{-5}$	$1.8 \cdot 10^{-7}$	$6.5 \cdot 10^{-6}$	$1.6 \cdot 10^{-8}$	$6.8 \cdot 10^{-6}$	$6.1 \cdot 10^{-8}$	$2.3 \cdot 10^{-7}$	$2.6 \cdot 10^{-9}$
O_2	$5.3 \cdot 10^{-6}$	$6.5 \cdot 10^{-9}$	$3.6 \cdot 10^{-6}$	$7.9 \cdot 10^{-9}$	$1.2 \cdot 10^{-6}$	$1.7 \cdot 10^{-9}$	$8.1 \cdot 10^{-7}$	$7.4 \cdot 10^{-10}$	$1.6 \cdot 10^{-7}$	$6.2 \cdot 10^{-10}$
methane	$1.8 \cdot 10^{-5}$	$3.6 \cdot 10^{-8}$	$1.5 \cdot 10^{-5}$	$3.8 \cdot 10^{-8}$	$3.0 \cdot 10^{-6}$	$4.4 \cdot 10^{-9}$	$1.9 \cdot 10^{-6}$	$3.7 \cdot 10^{-9}$	$7.2 \cdot 10^{-7}$	$2.6 \cdot 10^{-9}$
ethane	$9.8 \cdot 10^{-4}$	$1.2 \cdot 10^{-6}$	$9.5 \cdot 10^{-4}$	$1.2 \cdot 10^{-6}$	$2.2 \cdot 10^{-5}$	$2.4 \cdot 10^{-8}$	$8.8 \cdot 10^{-6}$	$2.0 \cdot 10^{-8}$	$1.3 \cdot 10^{-6}$	$7.6 \cdot 10^{-9}$
propane	$1.6 \cdot 10^{-2}$	$1.4 \cdot 10^{-4}$	$1.6 \cdot 10^{-2}$	$1.4 \cdot 10^{-4}$	$1.6 \cdot 10^{-4}$	$3.8 \cdot 10^{-7}$	$3.4 \cdot 10^{-5}$	$6.4 \cdot 10^{-8}$	$2.7 \cdot 10^{-6}$	$3.8 \cdot 10^{-8}$
butane	$3.6 \cdot 10^{-2}$	$8.4 \cdot 10^{-4}$	$3.5 \cdot 10^{-2}$	$8.3 \cdot 10^{-4}$	$1.2 \cdot 10^{-3}$	$3.9 \cdot 10^{-6}$	$1.2 \cdot 10^{-4}$	$3.3 \cdot 10^{-7}$	$1.5 \cdot 10^{-6}$	$4.7 \cdot 10^{-8}$
propene	$2.2 \cdot 10^{-2}$	$2.2 \cdot 10^{-4}$	$2.2 \cdot 10^{-2}$	$2.2 \cdot 10^{-4}$	$1.4 \cdot 10^{-4}$	$2.4 \cdot 10^{-7}$	$4.7 \cdot 10^{-5}$	$2.7 \cdot 10^{-7}$	$3.9 \cdot 10^{-6}$	$2.8 \cdot 10^{-8}$
water	$6.9 \cdot 10^{-3}$	$1.9 \cdot 10^{-3}$	$1.9 \cdot 10^{-6}$	$4.6 \cdot 10^{-9}$	$1.5 \cdot 10^{-6}$	$1.1 \cdot 10^{-8}$	$6.9 \cdot 10^{-3}$	$1.9 \cdot 10^{-3}$	$2.3 \cdot 10^{-7}$	$8.2 \cdot 10^{-9}$
methanol	$3.8 \cdot 10^{-3}$	$1.3 \cdot 10^{-3}$	$1.6 \cdot 10^{-4}$	$1.3 \cdot 10^{-6}$	$2.6 \cdot 10^{-5}$	$1.3 \cdot 10^{-6}$	$3.7 \cdot 10^{-3}$	$1.3 \cdot 10^{-3}$	$1.2 \cdot 10^{-5}$	$1.3 \cdot 10^{-6}$
ethanol	$1.4 \cdot 10^{-2}$	$2.7 \cdot 10^{-3}$	$3.3 \cdot 10^{-3}$	$2.4 \cdot 10^{-5}$	$1.1 \cdot 10^{-4}$	$5.1 \cdot 10^{-6}$	$1.1 \cdot 10^{-2}$	$2.7 \cdot 10^{-3}$	$1.4 \cdot 10^{-5}$	$4.6 \cdot 10^{-6}$
propanol	$8.2 \cdot 10^{-2}$	$3.7 \cdot 10^{-2}$	$1.5 \cdot 10^{-2}$	$2.3 \cdot 10^{-4}$	$6.8 \cdot 10^{-4}$	$3.7 \cdot 10^{-5}$	$6.5 \cdot 10^{-2}$	$3.7 \cdot 10^{-2}$	$4.8 \cdot 10^{-5}$	$3.5 \cdot 10^{-5}$

Table A5.4. -ΔU (kJ · mol^{-1}) of the gases in the structure and in the sites at 295 K. The second columns indicate the statistical error.

Molecules	Cu-BTC		T1		L2		L3		Windows	
argon	11.8	0.1	14.3	0.1	7.6	0.1	6.1	0.1	7.7	0.1
N_2	11.8	0.1	15.0	0.1	7.6	0.1	6.4	0.1	7.5	0.1
CO_2	23.1	0.1	25.1	0.1	14.5	0.1	15.9	0.1	12.5	0.1
O_2	12.8	0.1	15.5	0.1	7.9	0.1	6.1	0.1	7.6	0.1
methane	18.2	0.1	20.3	0.1	10.3	0.1	8.8	0.1	10.7	0.1
ethane	33.5	0.1	34.0	0.1	15.2	0.1	12.8	0.1	14.2	0.1
propane	43.2	0.1	43.5	0.1	19.0	0.1	14.8	0.1	18.0	0.1
butane	53.9	0.2	55.0	0.1	28.9	0.1	22.6	0.1	25.2	0.2
propene	47.3	0.1	47.6	0.1	22.5	0.1	20.0	0.1	22.1	0.1
water	43.7	0.7	14.1	0.1	11.1	0.1	43.7	0.7	14.0	0.1
methanol	40.1	0.9	28.7	0.1	23.1	0.5	40.8	0.8	28.5	0.6
ethanol	43.3	0.5	41.3	0.1	25.5	0.4	44.1	0.6	30.9	0.9
propanol	50.1	0.9	51.0	0.1	31.9	0.3	50.0	1.1	37.1	0.6

Table A5.5. ΔG (kJ · mol^{-1}) of the gases in the structure and in the sites at 295 K. The second columns indicate the statistical error.

Molecules	Cu-BTC		T1		L2		L3		Windows	
argon	-8.1	0.1	-7.1	0.1	-4.9	0.1	-4.0	0.1	-1.5	0.1
N_2	-7.7	0.1	-6.5	0.1	-4.5	0.1	-3.9	0.1	0.5	0.1
CO_2	-14.7	0.1	-14.1	0.1	-8.9	0.1	-9.0	0.1	-0.7	0.1
O_2	-8.4	0.1	-7.5	0.1	-4.9	0.1	-3.8	0.1	0.2	0.1
methane	-11.5	0.1	-11.0	0.1	-7.1	0.1	-5.9	0.1	-3.5	0.1
ethane	-21.2	0.1	-21.2	0.1	-11.9	0.1	-9.7	0.1	-5.1	0.1
propane	-28.0	0.1	-28.0	0.1	-16.8	0.1	-13.0	0.1	-6.8	0.1
butane	-30.1	0.1	-30.0	0.1	-21.6	0.1	-16.0	0.1	-5.4	0.1
propene	-28.9	0.1	-28.9	0.1	-16.5	0.1	-13.8	0.1	-7.6	0.1
water	-25.9	0.7	-5.9	0.1	-5.3	0.1	-25.9	0.7	-0.7	0.1
methanol	-24.4	0.8	-16.8	0.1	-12.4	0.1	-24.3	0.8	-10.4	0.3
ethanol	-27.7	0.5	-24.2	0.1	-15.8	0.1	-27.0	0.6	-10.6	0.7
propanol	-31.9	0.9	-28.0	0.1	-20.3	0.1	-31.2	1.1	-13.4	1.3

Table A5.6. ΔA ($kJ \cdot mol^{-1}$) of the gases in the structure and in the sites at 295 K. The second columns indicate the statistical error.

Molecules	Cu-BTC		T1		L2		L3		Windows	
argon	-5.6	0.1	-4.7	0.1	-2.5	0.1	-1.6	0.1	0.9	0.1
N_2	-5.3	0.1	-4.0	0.1	-2.1	0.1	-1.4	0.1	2.9	0.1
CO_2	-12.3	0.1	-11.6	0.1	-6.5	0.1	-6.6	0.1	1.7	0.1
O_2	-6.0	0.1	-5.0	0.1	-2.4	0.1	-1.4	0.1	2.6	0.1
methane	-9.0	0.1	-8.5	0.1	-4.6	0.1	-3.5	0.1	-1.1	0.1
ethane	-18.8	0.1	-18.7	0.1	-9.5	0.1	-7.2	0.1	-2.6	0.1
propane	-25.6	0.1	-25.6	0.1	-14.4	0.1	-10.5	0.1	-4.3	0.1
butane	-27.6	0.1	-27.5	0.1	-19.2	0.1	-13.6	0.1	-3.0	0.1
propene	-26.5	0.1	-26.4	0.1	-14.1	0.1	-11.4	0.1	-5.2	0.1
water	-23.5	0.7	-3.5	0.1	-2.8	0.1	-23.5	0.7	1.7	0.1
methanol	-22.0	0.8	-14.4	0.1	-9.9	0.1	-21.9	0.8	-7.9	0.3
ethanol	-25.3	0.5	-21.8	0.1	-13.3	0.1	-24.5	0.6	-8.2	0.7
propanol	-29.4	0.9	-25.5	0.1	-17.9	0.1	-28.8	1.1	-11.0	1.3

Table A5.7. ΔS ($J \cdot K^{-1} \cdot mol^{-1}$) of the gases in the structure and in the sites at 295 K. The second columns indicate the statistical error.

Molecules	Cu-BTC		T1		L2		L3		Windows	
argon	-20.9	0.1	-32.7	0.1	-17.4	0.1	-15.4	0.1	-29.2	0.1
N_2	-22.0	0.1	-37.4	0.1	-18.8	0.1	-16.8	0.1	-35.2	0.1
CO_2	-36.6	0.1	-45.6	0.1	-27.2	0.1	-31.5	0.1	-48.3	0.3
O_2	-23.1	0.1	-35.7	0.1	-18.7	0.1	-16.0	0.1	-34.6	0.1
methane	-31.2	0.1	-40.1	0.1	-19.2	0.1	-18.0	0.1	-32.7	0.1
ethane	-49.8	0.1	-52.0	0.1	-19.2	0.1	-18.9	0.1	-39.4	0.1
propane	-59.7	0.1	-60.9	0.1	-15.5	0.1	-14.6	0.1	-46.3	0.1
butane	-89.2	0.4	-93.0	0.4	-33.0	0.1	-30.6	0.1	-75.4	0.8
propene	-70.8	0.1	-71.6	0.1	-28.5	0.1	-29.4	0.1	-57.3	0.1
water	-68.6	1.5	-35.9	0.1	-28.1	0.1	-68.7	1.5	-53.5	0.3
methanol	-61.4	0.7	-48.7	0.2	-44.6	1.3	-64.1	0.7	-69.7	1.8
ethanol	-61.0	1.5	-66.1	0.1	-41.2	1.0	-66.4	2.2	-77.1	1.6
propanol	-70.0	3.6	-86.5	0.3	-47.7	1.0	-71.9	4.6	-88.6	5.2

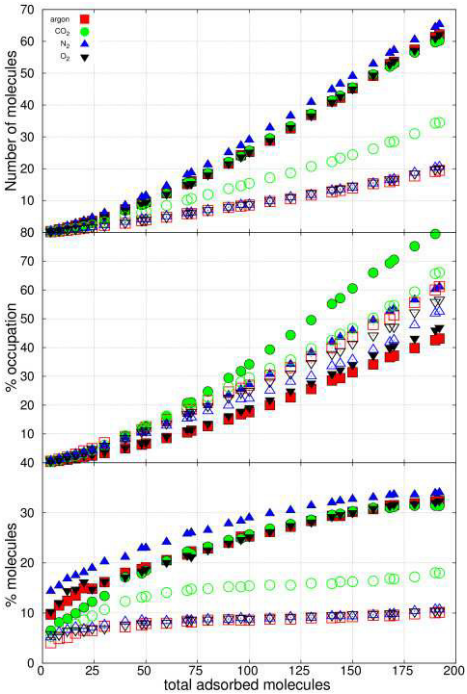

Figure A.5.1. Adsorption of argon (squares), carbon dioxide (circles), nitrogen (triangles), and oxygen (down triangles). Number of molecules adsorbed as a function of loading in the sites L_3 (full symbols) and L_w (empty symbols) of Cu-BTC (top), ratio of occupation of the site (center), and the fraction of the total adsorbed molecules in the structure (bottom).

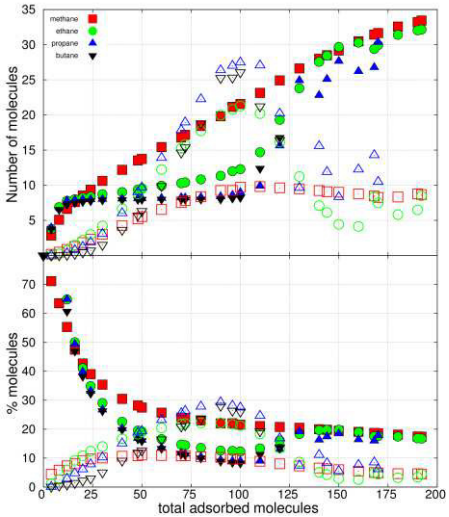

Figure A5.2. Adsorption of methane (squares), ethane (circles), propane (triangles), and butane (down triangles). Number of molecules adsorbed (top) as a function of loading in the sites T_1 (full symbols) and T_w (empty symbols) of Cu-BTC, and fraction of the total adsorbed molecules in the structure (bottom).

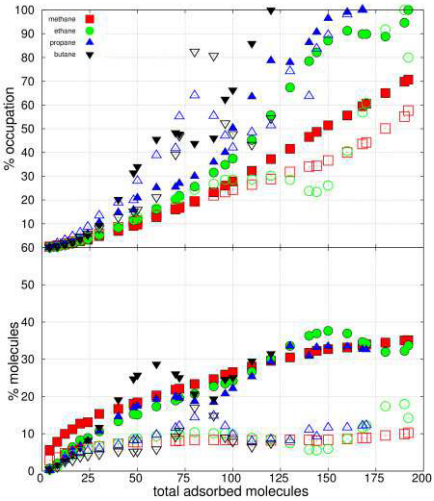

Figure A5.3. Ratio of occupation of the sites L_3 (full symbols) and L_w (empty symbols) of Cu-BTC.

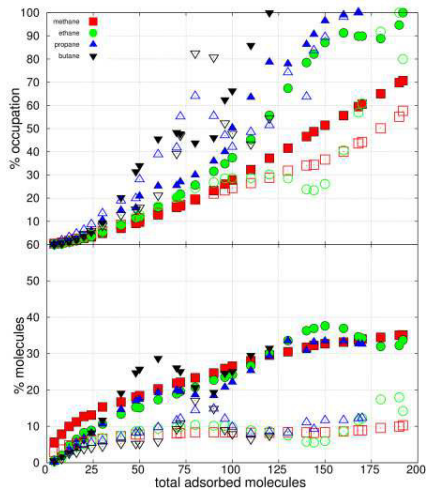

Figure A5.4. Adsorption of methane (squares), ethane (circles), propane (triangles), and butane (down triangles). Ratio of occupation of the sites L_3 (full symbols) and L_w (empty symbols) of Cu-BTC as a function of loading (top), and fraction of the total adsorbed molecules in the structure (bottom).

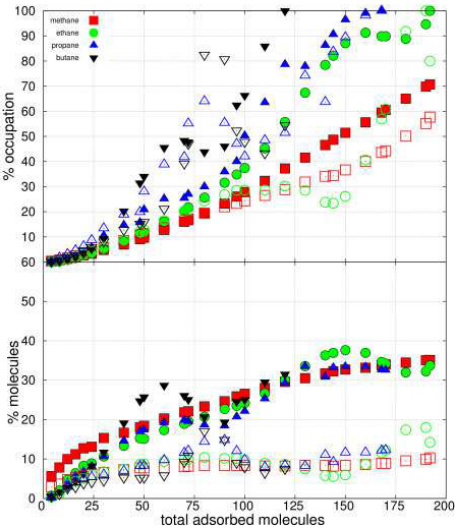

Figure A5.5. Adsorption of propane (squares), propene (circles), and propanol (triangles). Ratio of occupation of the sites T_1 (full symbols) and T_w (empty symbols) as a function of loading (top), and fraction of the total adsorbed molecules in the structure (bottom).

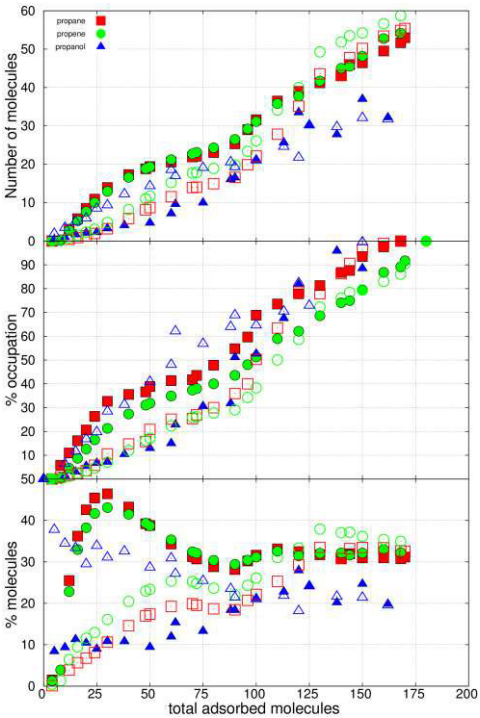

Figure A5.6. Adsorption of propane (squares), propene (circles), and propanol (triangles). Number of molecules adsorbed (top) as a function of loading in the sites L_2 (full symbols) and L_3 (empty symbols) of Cu-BTC, ratio of occupation of the site (center), and fraction of the total adsorbed molecules in the structure (bottom).

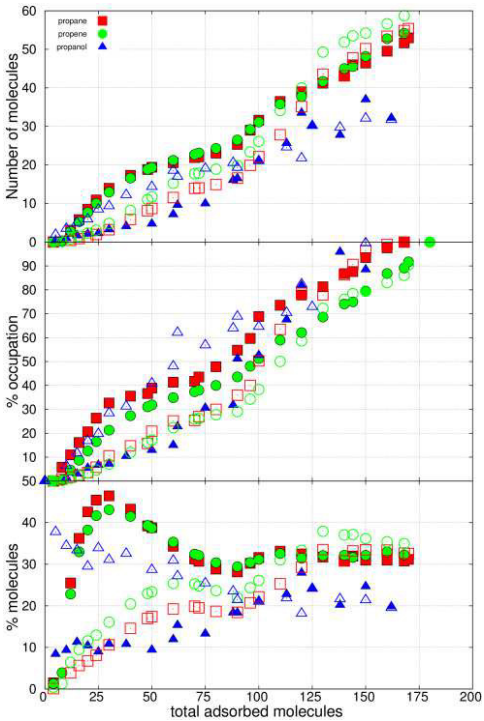

Figure A5.7. Adsorption of propane (squares), propene (circles), and propanol (triangles). Number of molecules adsorbed (top) as a function of loading in the sites L_2 (full symbols) and L_3 (empty symbols) of Cu-BTC, ratio of occupation of the site (center), and fraction of the total adsorbed molecules in the structure (bottom).

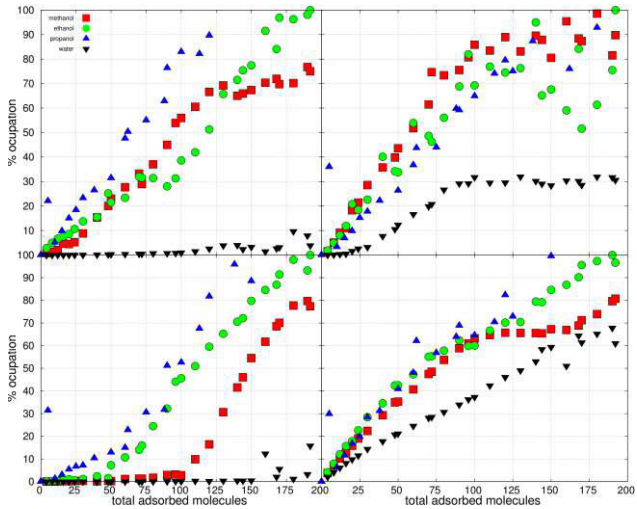

Figure A5.8. Adsorption methanol (squares), ethanol (circles), propanol (triangles), and water (down triangles) in the sites T_1 (top left), T_w (top right), L_2 (bottom left), and L_3 (bottom right) of Cu-BTC as a function of loading.

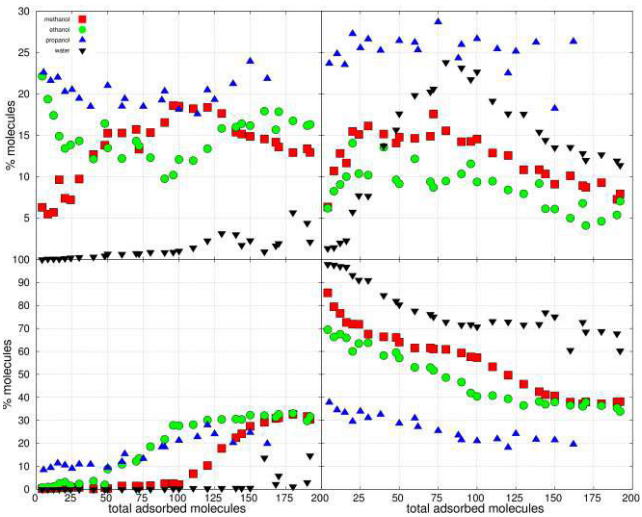

Figure A5.9. Fraction of molecules adsorbed of methanol (squares), ethanol (circles), propanol (triangles), and water (down triangles) in the sites T_1 (top left), T_w (top right), L_2 (bottom left), and L_3 (bottom right) of Cu-BTC as a function of loading.

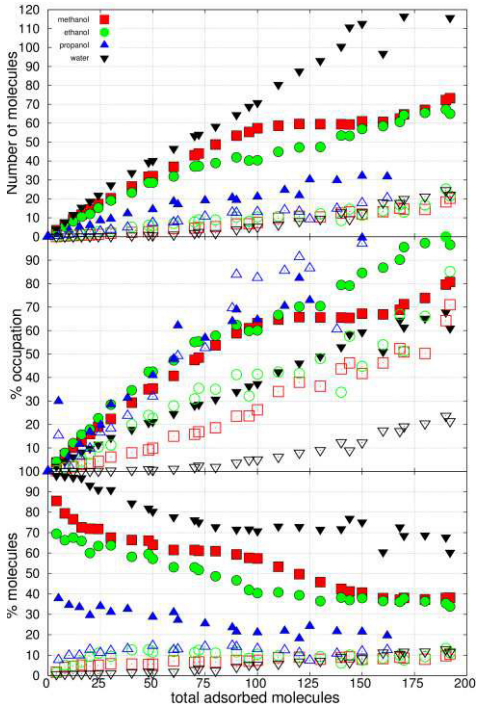

Figure A5.10. Adsorption of methanol (squares), ethanol (circles), propanol (triangles), and water (down triangles). Number of molecules adsorbed (top) as a function of loading in the sites L_3 (full symbols) and L_w (empty symbols) of Cu-BTC, ratio of occupation of the site (center), and fraction of the total adsorbed molecules in the structure (bottom).

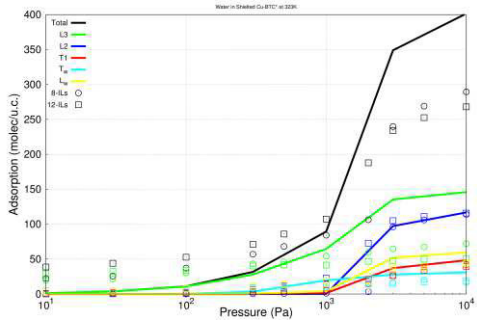

Figure A5.11. Adsorption of water on empty Cu-BTC (lines), Cu-BTC filled with 8 pairs of ILs (circles), and filled with 12 pairs of ILs (squares). In black the total adsorption, in green the adsorption in L_3, in blue the adsorption in L_2, in red the adsorption in T_1, in cyan the adsorption in T_w and in yellow the adsorption in L_w.

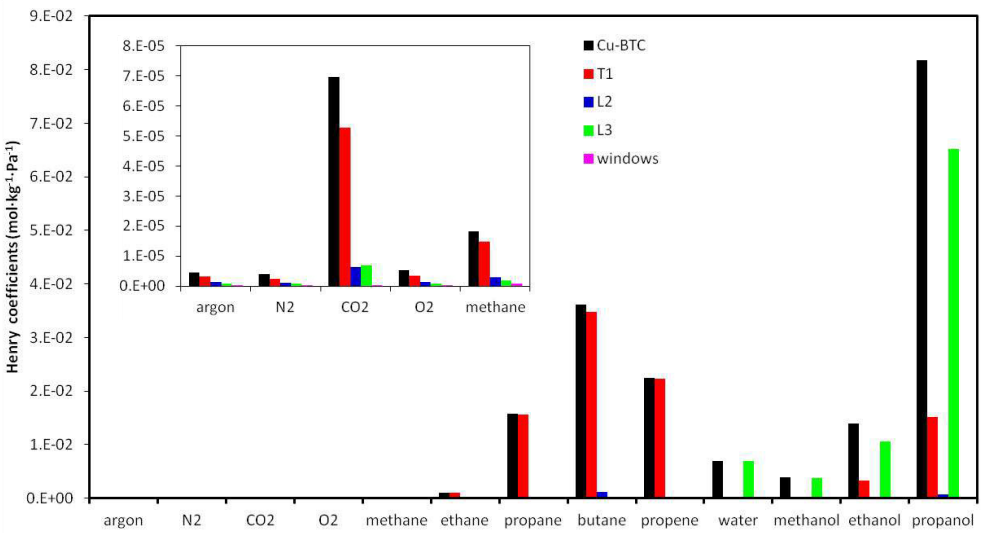

Figure A5.12. Henry coefficients (mol · kg^{-1} · Pa^{-1}) of the gases in the structure and in the sites at 295 K.

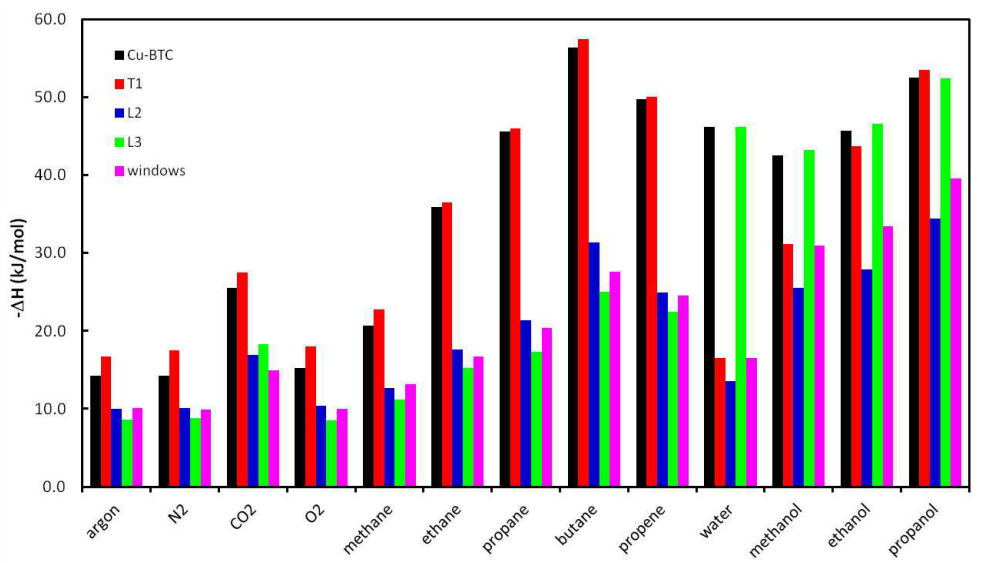

Figure A5.13. -ΔH (kJ · mol^{-1}) of the gases in the structure and in the sites at 295 K.

Appendix 6

Table A6.1. Lennard-Jones parameters and point charges for the adsorbent, adsorbates, and ionic liquids.

Atom types	**Epsilon/k_B (K)**	**Sigma (Å)**	**Charge (e^-)**	**Atom types**	**Epsilon/k_B (K)**	**Sigma (Å)**	**Charge (e^-)**
	Adsorbates				**Ionic Liquid**		
CH_3_ethanol	98.0	3.75	-	EMIM-C5	25.192	3.207	-0.13487
CH_2O_ethanol	46.0	3.95	0.265	EMIM-C4	25.192	3.207	-0.14717
O_ethanol	93.0	3.02	-0.7	EMIM-C2	25.192	3.207	-0.09121
H_ethanol	-	-	0.435	EMIM-N1	100.761	3.296	0.05941
O_water	89.516	3.097	-	EMIM-H3	3.93	2.616	0.22037
H_water	-	-	0.241	EMIM-H2	3.93	2.616	0.20999
Dummy_water	-	-	-0.241	EMIM-H1	23.175	1.604	0.21887
C_acetone	40.0	3.82	0.424	EMIM-N3	100.761	3.296	0.19371
O_acetone	79.0	3.05	-0.424	EMIM-C6	10.0761	4.054	-0.2508
CH_3_acetone	98.0	3.75	-	EMIM-H4,5,6	11.084	2.352	0.14516
O_ether	55.0	2.80	-0.5	EMIM-C7	10.076	4.054	0.10394
CH_3_ether	98.0	3.75	0.25	EMIM-H7,8	11.084	2.352	0.0555
Helium	10.9	2.64	-	EMIM-C8	27.709	3.875	-0.10455
	Cu-BTC			EMIM-H9,10,11	11.084	2.352	0.05858
MOF-Cu	2.518	3.114	1.248	Tf2N-N8	85.647	3.25	-0.66
MOF-O	48.19	3.03	-0.624	Tf2N-S1,2	125.951	3.55	1.02
MOF-C1	47.86	3,47	0.494	Tf2N-C50,51	33.251	3.5	0.35
MOF-C2	47.86	3.47	0.13	Tf2N-O1,2,3,4	105.799	2.96	-0.5
MOF-C3	47.86	3.47	-0.156	Tf2N-F1,2,3,4,5,6	26.702	2.95	-0.16
MOF-H	7.65	2.85	0.156				

Table A6.2. Computed helium void fraction, density of the framework considering the blocking and screening molecules as part of it (ρ*), and available pore volume using as framework density the value obtained for the bare Cu-BTC (PV) and ρ* (PV*).

	HVF	**ρ* (g/cm³)**	**PV (cm³/g)**	**PV* (g/cm³)**
Cu-BTC	0.759	0.879	0.863	0.863
Blocked	0.479	0.879	0.545	0.545
ILs (2)	0.523	1.163	0.595	0.449
ILs (4)	0.328	1.447	0.373	0.227
Shielded	0.653	0.896	0.743	0.728
Acetone	0.483	1.132	0.549	0.427
Dimethyl ether	0.518	1.080	0.589	0.480

Table A6.3. Adsorption energies (kJ/mol) plotted in Figure 1 (chapter 8) for water, acetone, and dimethyl ether. A negative sign corresponds to an exothermic process.

Cu-BTC	**Cu-BTC+1H_2O**	**Cu-BTC+2H_2O**
	-78.0	-153.2
	Cu-BTC+1$CO(CH_3)_2$	**Cu-BTC+2$CO(CH_3)_2$**
	-65.5	-122.2
0.0	**Cu-BTC+1$O(CH_3)_2$**	**Cu-BTC+2$O(CH_3)_2$**
	-66.3	-124.1
	Cu-BTC+H_2O+$CO(CH_3)_2$	**Cu-BTC+H_2O+$O(CH_3)_2$**
	-138.9	-139.7

Table A6.4. Adsorption energies (kJ/mol) for different adsorbates with different basis sets, 6-31G(d) and 6-311+G(d), and includig the dispersion correction, d3. The number in parenthesis refers to the number of adsorbate molecules for unit cell of Cu-BTC.

Adsorbate	**Previous results UB3LYP/ 6-31G(d)**	**New test UB3LYP/ 6-311+G(d)+d3**
Acetone (1)	-65.5	-67.9
Acetone (2)	-122.2	-125.3
Dimethyl ether (1)	-66.3	-75.9
Dimethyl ether (2)	-124.1	-143.3
H_2O (1)	-78.0	-74.6
H_2O (2)	-153.2	-144.8
H_2O and Acetone	-138.9	-136.9
H_2O and Dimethyl ether	-139.7	-145.1

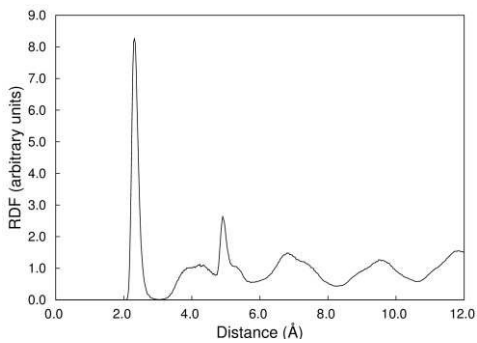

Figure A6.1. Radial distribution function copper-oxygen of water computed at 323 K.

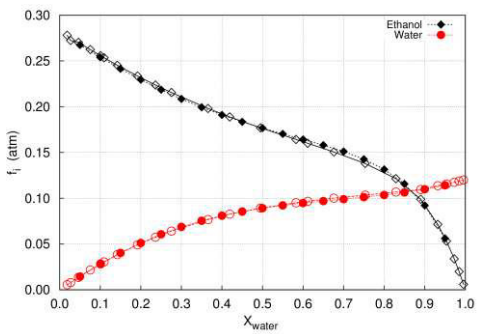

Figure A6.2. Fugacities obtained for the components that form the mixture ethanol-water at 323 K and 1 atm in the liquid phase. Red circles for water and black rhombus for ethanol. Open symbols correspond to experimental data and filled symbols to computed fugacities using Margules model for the activity coefficients.

Publications related to this thesis

Peer reviewed journals

- **Gutiérrez-Sevillano, J. J.**; Dubbeldam, D.; Bellarosa L.; López, N.; Liu, X.; Vlug, T. J. H.; and Calero, S. "Strategies to Simultaneously Enhance the Hydrostability and the Alcohol-Water Separation Behavior of Cu-BTC" *Journal of Physical Chemistry C*, 2013 (accepted)
- van Assche, T.; Duerinck, T.; **Gutierrez-Sevillano, J. J.**; Calero, S.; Baron, G.; and Denayer, J. "High Adsorption Capacities and Two-Step Adsorption of Polar Adsorbates on Cu-BTC Metal-Organic Framework" *Journal of Physical Chemistry C*, 2013 (accepted)
- Bellarosa, L.; **Gutiérrez-Sevillano J. J.**; Calero, S.; and López, N. "How ligands can improve the hydrothermal stability in the IRMOF family" *Physical Chemistry Chemical Physics.* 2013 (accepted)
- Deeg, K.; **Gutiérrez-Sevillano J. J.**; Bueno-Pérez R.; Parra, J. B.; Ania, C.; Doblare, M.; and Calero, S.; "Insights on the Molecular Mechanisms of Hydrogen Adsorption in Zeolites" *Journal of Physical Chemistry C*, accepted 2013 DOI: 10.1021/jp4037233
- **Gutiérrez-Sevillano, J. J.**; Martín-Calvo A.; Dubbeldam, D.; Calero, S.; and Hamad, "Adsorption of Hydrogen Sulfide on Metal-Organics Frameworks" *RSC Advance*, 2013 DOI: 10.1039/C3RA41682H 2013
- Balestra, S. R. G. ; **Gutiérrez-Sevillano J. J.**; Merkling P. J.; Dubbeldam, D.; and Calero, S. "Simulation study of structural changes in zeolite RHO" *Journal of Physical Chemistry C*, 2013, *117* (22), 11592–11599
- **Gutiérrez-Sevillano J. J.**; Vicent-Luna, J. M.; Dubbeldam D.; and Calero S. "On the Molecular Mechanisms for Adsorption in Cu-BTC Metal Organic Framework" *Journal of Physical Chemistry C*, 2013, *117* (21), 11357–11366
- De Lange M. F.; **Gutiérrez-Sevillano, J. J.**; Hamad, S.; Vlug, T. J. H.; Calero, S.; Gascon, J.; and Kapteijn, F.; "Understanding adsorption of highly polar vapors on mesoporous MIL-100(Cr) and MIL-101(Cr): Experiments and molecular simulations" *Journal of Physical Chemistry C,* 2013, *117* (15), 7613–7622
- **Gutiérrez-Sevillano, J. J.**; Calero, S.; Ania, C.; Parra, J. B.; Kapteijn, F.; Gascon, J.; and Hamad, S "Toward a Transferable Set of Charges to Model Zeolitic Imidazolate Frameworks: Combined Experimental–Theoretical Research" *Journal of Physical Chemistry C*, 2013, *117* (1), 466–471
- Calero S.; **Gutiérrez-Sevillano, J. J.**; and García-Pérez, E. "Effect of the Molecular Interactions on the Separation of Nonpolar Mixtures Using Cu-BTC Metal Organic Framework" *Microporous and Mesoporous Materials*, 2013, *165*, 79-83

- Ania, C. O.; Garcia-Perez, E.; Haro, M; **Gutiérrez-Sevillano, J. J.**; Valdes-Solis, T.; Parra, J. B.; and Calero, S. "Understanding Gas-Induced Structural Deformation of ZIF-8" *Journal Of Physical Chemistry Letters* 2012, *3* (9), 1159-1164

- **Gutiérrez-Sevillano, J. J.**; Caro-Perez, A.; Dubbeldam, D.; and Calero, S. "Molecular simulation investigation into the performance of Cu-BTC metal-organic frameworks for carbon dioxide-methane separations" *Physical Chemistry Chemical Physics,* 2011, *13* (45), 20453-20460

- Bueno-Pérez R.; García-Pérez E.; **Gutiérrez-Sevillano J. J.**; Merkling P. J.; and Calero S. "A Simulation Study of Hydrogen in Metal Organic Frameworks" *Adsorption Science and Technology*, 2010, *28*, 823-835

- **Gutiérrez-Sevillano J. J.**; Dubbeldam D.; Rey F.; Valencia S.; Palomino M.; Martín-Calvo A.; and Calero S. "Analysis of the ITQ-12 Zeolite Performance in Propane—Propylene Separations Using a Combination of Experiments and Molecular Simulations" *Journal of Physical Chemistry C*, 2010, *114*, 14907-14914

- **Gutiérrez-Sevillano, J. J.**; Balestra, S. R. G. ; Calero, S.; Hamad, S.; Rey F.; Valencia S.; Palomino M.; and Ruiz-Salvador, R. A.; "Enhanced dynamic flexibility in Ge containing zeolites: impact on diffusion" Submitted to *Angewandte Chemie*

- **Gutiérrez-Sevillano, J. J.**; Hamad, S.; Bellarosa, L.; López, N; and Calero, S.; "Effect of metal and oxygen substitutions on the adsorption in IRMOF-1" Submitted to *Journal of Physical Chemistry C*

- Vicent-Luna, J. M.; **Gutiérrez-Sevillano, J. J.**; Anta, J. A.; and Calero, S. "Strategies to Simultaneously Enhance the Hydrostability and the Alcohol-Water Separation Behavior of Cu-BTC" Submitted to *Journal of Physical Chemistry C*

Non-peer reviewed journals

- Martín-Calvo, A.; **Gutiérrez-Sevillano, J. J.**; and Calero, S. "Simulations studies on the adsorption and diffusion of gasses of environmental impact using Cu-BTC metal-organic framework" (7 pages). Conference Proceeding. EBA-9 & IBA-1, Recife (Brazil), 2012

- **Gutiérrez-Sevillano, J. J.** "La Simulación Molecular como Herramienta para estudiar procesos de Adsorción y Difusión en Cu-BTC". *Materiales en Adsorción y Catálisis,* 2011, *1*, 16-21